Analysis and Optimization of Interfaces in "Wide-Gap" Chalcopyrite-based Thin Film Solar Cell Devices

Von der Fakultät für Mathematik, Naturwissenschaften und Informatik
der Brandenburgischen Technischen Universität Cottbus-Senftenberg

zur Erlangung des akademischen Grades

Doktor der Naturwissenschaften
(Dr. rer. nat.)

genehmigte Dissertation

vorgelegt von

Master of Science in Chemistry

Roberto Félix Duarte

geboren am 13.11.1982 in Salvador Alvarado, Mexiko

Gutachter: Prof. Dr. Dieter Schmeißer

Gutachter: Prof. Dr. Marcus Bär

Gutachter: Prof. Dr. Hans-Werner Schock

Tag der mündlichen Prüfung: 23. April 2015

Abstract

The chemical and electronic structure of chalcopyrite absorber materials with different bulk band gap energies, E_g^{bulk}, [i.e., low-gap $Cu(In,Ga)Se_2$ (CIGSe, $E_g^{bulk} \sim 1.2$ eV) provided by Zentrum für Sonnenenergie- und Wasserstoff- Forschung Baden-Württemberg (ZSW) and wide-gap $CuInS_2$ (CIS, $E_g^{bulk} \sim 1.5$ eV) provided by Helmholtz Zentrum Berlin für Materialien und Energie GmbH (HZB) collaborators] and of buffer/absorber heterointerfaces based on these materials are studied with soft and hard x-ray spectroscopic techniques. Mechanisms that benefit (limit) the performance of low(wide)-gap chalcopyrite-based thin film solar cell devices are identified, the knowledge of which is used to develop surface tailoring treatments to optimize buffer/absorber heterointerfaces based on wide-gap chalcopyrites and improve the performance of resulting solar cell devices.

Photoemission spectroscopy (PES) elemental characterizations of the two investigated chalcopyrite absorber materials (i.e., CIGSe and CIS) reveal compositional-depth profiles. The changes detected in CIGSe include: a near surface Ga-depletion, a strongly Cu-poor surface and a strong presence of surface Na that (likely) occupies Cu vacancies. A similar Cu-deficiency is also detected for the CIS absorber. As a result of these variations in depth-composition, a significant widening of the band gap at the surface occurs (i.e., CIGSe, E_g^{surf}: 1.70 ± 0.2 eV and CIS, E_g^{surf}: 1.88 ± 0.2 eV) as evident in the evaluation of ultraviolet photoelectron spectroscopy (UPS) and inverse photoemission spectroscopy (IPES) measurements. Differences in the interaction of the CIGSe and CIS surfaces with the deposited buffer materials are also identified. The PES and modified Auger parameters reveal a strong intermixing at the studied buffer/absorber heterointerfaces based on CIGSe (i.e., CdS/CIGSe and ZnS/CIGSe). S $L_{2,3}$ x-ray emission spectroscopy (XES) measurements of CIGSe substrates submitted to CdS chemical bath deposition (CBD-CdS) treatments reveal the formation of In_2S_3 and defect-rich/nanostructured CdS at the interface, compounds with presumably higher band gap values than the measured E_g^{surf} for CIGSe. S $L_{2,3}$ XES spectra of CIGSe substrates submitted to ZnS chemical bath deposition (CBD-ZnS) treatments show similar findings: e.g., the formation of $(Zn,In)(S,Se)_2$ chemical analogs. Similar PES and XES measurement series show that the CdS/CIS heterointerface is more abrupt, with no detected interface chemical species. Direct measurement of the band alignment of these three heterointerfaces reveals: an ideal conduction band offset (CBO) configuration for CdS/CIGSe

(i.e., CBO: +0.11 ± 0.25 eV), a spike CBO configuration for ZnS/CIGSe (i.e., CBO: +1.06 ± 0.4 eV), and a highly unfavorable cliff CBO configuration for CdS/CIS (i.e., CBO: -0.42 ± 0.25 eV). The performance of solar cell devices corresponding to these heterointerfaces is correlated to their CBO configurations.

Two surface tailoring approaches intended to optimize the CBO configuration of the CdS/CIS heterointerface are presented. The first method is based on rapid thermal processing (RTP) selenization treatments of KCN-etched CIS absorbers, attempted to exchange of Se for S in the treated samples. The idea behind this approach is to prepare the surface of a wide-gap chalcopyrite absorber so that it interacts with CdS to form a more favorable heterointerface, such as the heterointerfaces within low-gap chalcopyrite devices. X-ray fluorescence analysis (XRF) and PES measurements of RTP-treated CIS samples (with the used set of RTP-parameter ranges) show a greater treatment effect at the surface of the sample compared to the bulk (i.e., surface [Se]/[S+Se] range: 0.23 ± 0.05 to 0.83 ± 0.05, compared to bulk [Se]/[S+Se] range: 0.01 ± 0.03 to 0.24 ± 0.03). Tuning of the Cu:In:(S+Se) surface composition from a Cu-poor 1:3:5 to a 1:1:2 stoichiometry is also observed in RTP-treated CIS absorbers with lower to higher surface Se contents, respectively. UPS measurements show a shift in valence band maximum (VBM) toward the Fermi level, E_F, in samples with higher surface Se content (i.e., -0.88 ± 0.1 to -0.51 ± 0.1 eV), as expected for a reduction in E_g^{surf} produced by exchange of Se for S. Ultraviolet-visible spectrophotometry reveals a reduction in the optical (bulk) band gap of samples with greater Se incorporation (i.e., from 1.47 ± 0.05 to 1.08 ± 0.05 eV), allowing for a working window for optimization purposes.

The second optimization approach involves surface functionalization of KCN-etched CIS absorbers with dipole-charge-inducing self-assembled monolayers (SAM) based on benzoic acid derivatives and thiol molecules. The introduction of dipole charges between the CdS/CIS heterointerface can tune the relative alignment of the electronic bands composing the electronic structure of the heterointerface; the use of a suitable dipole-inducing SAM could correct the CBO misalignment in the CdS/CIS heterointerface. UPS measurements of the secondary electron cut-off region of CIS samples treated with the selected set of dipole-inducing SAMs show a work function modulation of CIS (i.e., 4.4 ± 0.2 eV to 5.2 ± 0.2 eV). Small improvements in solar cell parameters of solar cell devices based on SAM-modified heterointerfaces are measured.

An overview of the performance of various chalcopyrite(kesterite)-based solar cells in relation to the electronic properties of their corresponding buffer/absorber heterointerface suggests that optimization approaches extending beyond the buffer/absorber heterointerface may be required to further materialize gains in performance in wide-gap chalcopyrite-based thin film solar cell devices.

Zusammenfassung

Die chemische und elektronische Struktur von Chalkopyrit-Absorbermaterialien mit verschiedenen Bandlückenenergien, E_g^{bulk}, und von Puffer/Absorber Grenzflächen wurde mittels verschiedener spektroskopischer Methoden mit weicher und harter Röntgenstrahlung untersucht. Die Arbeit konzentriert sich im Wesentlichen auf die Untersuchung entsprechender Schichtstapel basierend auf Chalkopyritabsorbern mit *kleiner* [$Cu(In,Ga)Se_2$ (CIGSe, $E_g^{bulk} \sim 1.2$ eV)] und *großer* [$CuInS_2$ (CIS, $E_g^{bulk} \sim 1.5$ eV)] Bandlücke welche durch das Zentrum für Sonnenenergie- und Wasserstoff-Forschung Baden-Württemberg (ZSW) bzw. durch das HZB Institut für Technologie bereitgestellt wurden. Das Ziel der Arbeit ist es, insbesondere die ober- und grenzflächenbezogenen Besonderheiten der Chalkopyritabsorberstrukturen mit kleiner bzw. großer Bandlücke zu identifizieren die die Bauteileigenschaften bestimmen. In einem nächsten Schritt wurde diese Einsicht dazu verwendet mittels Oberflächenbehandlungen die Absorberoberfläche und damit die Puffer/Absorber-Grenzflächen speziell von Chalkopyriten mit großer Bandlücke gezielt zu optimieren, um so die Leistungsfähigkeit der resultierenden Solarzellen zu verbessern.

Mithilfe von anregungsenergieabhängiger Photoelektronenspektroskopie (PES) wurde die Oberflächenkomposition der untersuchten Chalkopyrit-Absorbermaterialien (d.h., von CIGSe und CIS) „tiefenaufgelöst“ bestimmt. Beiden Materialien zeigen tiefenabhängig Kompositionsprofile. Für CIGSe konnte eine signifikante Oberflächeverarmerung von Ga und Cu sowie die Anwesenheit von Na nachgewiesen werden. Eine ähnliche Cu-arme Oberflächenkomposition wurde für CIS-Absorber festgestellt. Diese Kompositionsprofile resultieren in eine ausgeprägte Aufweitung der Oberflächenbandlücke [CIGSe: $E_g^{surf} = (1.70 \pm 0.20)$ eV und CIS: E_g^{surf}: $(1.88 \pm 0.20$ eV)], wir durch die direkte E_g^{surf} Messung mittels Ultraviolett-Photoelektronenspektroskopie (UPS) und inverser Photoelektronenspektroskopie (IPES) gezeigt werden konnte. Unterschiede in der Interaktion der CIGSe- und CIS-Oberflächen mit verschiedenen Puffermaterialien wurden ebenfalls identifiziert. Mithilfe von PES und insbesondere durch die Analyse der modifizierten Auger-Parameter konnte eine starke Durchmischung an den CdS/CIGSe und ZnS/CIGSe Puffer/Absorber-Grenzflächen identifiziert werden. Zusätzlich konnte durch Röntgenemissionsspektroskopie (XES) – Messungen an der S $L_{2,3}$ Kante die Ausbildung einer Grenzflächenspezies an der CdS/CIGSe Grenzfläche nachgewiesen werden, die am besten durch eine Mischung aus In_2S_3 und defektreichen/nanokristallinem CdS beschrieben werden kann. Auf der Basis von S $L_{2,3}$ XES

Spektren von ZnS/CIGSe Proben ergibt sich für diese Grenzfläche ein ganz ähnliches Bild: die Bildung einer $(Zn,In)(S,Se)_2$ – artigen Grenzflächenspezies. Ähnliche PES- und XES-Messungen an CdS/CIS Proben zeigen keine signifikante Interaktion an der Puffer/Absorber-Grenzflächen und eine in diesem Sinn abruptere Grenzfläche. Direkte Messung der Bandanpassung an diesen drei Grenzflächen mittels PES, UPS, und IPES ergibt: einen idealen Leitungsbandversatz (CBO) für die CdS/CIGSe Grenzfläche [$\mathrm{CBO}_{\mathrm{CdS/CIGSe}}$ = (0.11 ± 0.25 eV)], ein „spike“-artiges CBO für die ZnS/CIGSe Grenzfläche [$\mathrm{CBO}_{\mathrm{ZnS/CIGSe}}$ = (1.06 ± 0.4 eV)] und ein sehr ungünstiges „cliff“-artiges CBO für die CdS/CIS Grenzfläche [$\mathrm{CBO}_{\mathrm{CdS/CIS}}$ = (-0.42 ± 0.25 eV)]. Zudem konnte gezeigt werden, dass die Bauteileigenschaften der entsprechenden Solarzellen mit den ermittelten CBO in Verbindung steht: η(CdS/CIGSe) > η(ZnS/CIGSe) >> η(CdS/CIS).

Zwei Oberflächenbehandlungen des CIS Absorbers zur gezielten Optimierung des CBO an der CdS/CIS Grenzfläche wurden vorgestellt. Das erste Verfahren basiert auf einer Selenisierung der KCN-geätzten CIS Absorber durch schnelles Aufheizen in einer Se-Atmosphäre. Das Ziel hierbei war es das Schwefel in der CIS Oberfläche durch Selen zu ersetzen, um die Oberfläche des Chalkopyrit-Absorbers mit großer Bandlücke so zu modifizieren, dass er mit dem CdS Puffer eine ähnliche (→ günstigere) Grenzfläche bilden kann, wie die die für den CdS/CIGSe Schichtstapel festgestellt wurde. Volumensensitive Röntgenfluoreszenzanalyse (XRF) und oberflächensensitive PES Messungen der selenisierten CIS Proben zeigen in der Tat einen höheren Selenisierungsgrad an der Oberfläche im Vergleich zum Volumen des Absorbers (PES: $0.23 \pm 0.05 \leq [Se]/[S + Se] \leq 0.83 \pm 0.05$; XRF: $0.01 \pm 0.03 \leq [Se]/[S + Se] \leq 0.24 \pm 0.03$). Zudem konnte festgestellt werden, dass sich die Cu:In:(S + Se) Oberflächenzusammensetzung der selenisierten Absorber von 1:3:5 zu einer stöchiometrischen 1:1:2 Komposition mit zunehmendem Selenisierungsgrad ändert. Simultan wird eine Verschiebung des Valenzbandmaximums (VBMs) zum Fermielevel [(-0.88 ± 0.10 → (-0.51 ± 0.10 eV)] beobachtet, was durch eine E_g^{surf} Verringerung – induziert durch den beobachteten S-Se Austausch – erklärt werden konnte. Die Überprüfung der Volumenbandlücke (E_g^{bulk}) mittels UV-VIS-Spektrophotometrie bestätigte in der Tat eine Verringerung der Bandlücke von selenisierten CIS Proben mit grösserem Se-Gehalt [(1.47 ± 0.05) → (1.08 ± 0.05 eV)]. Dies zeigt, dass durch diesen Ansatz die optoelektronischen Eigenschaften von (selenisierten) CIS Absorbern in einem großen (Optimierungs-)Fenster gezielt eingestellt werden können.

Der zweite Ansatz beruht auf der Oberflächenfunktionalisierung von KCN-geätzten CIS-Absorber mit selbstorganisierten Monolagen (SAM) organischer Moleküle auf der Basis von Benzoesäurederivate und Thiolen die Dipolladungen induzieren können. Das Ziel hierbei ist es durch das Einbringen von Dipolladungen an der CdS/CIS Grenzfläche die elektronische Grenzflächenstruktur (also die Bandanpassung) zu optimieren. Durch die Verwendung eines geeigneten Dipol-induzierenden SAMs könnte so das ungünstige negative CBO an der der CdS/CIS Grenzfläche korrigiert werden. UPS Messungen an verschieden funktionalisierten CIS Oberflächen zeigten in der Tat eine Modulation der Austrittsarbeit von (4.4 ± 0.2) eV bis (5.2 ± 0.2 eV). Der Fakt, dass bereits bei diesen Vorversuchen eine Verbessrung der Bauteileigenschaften von Solarzellen basierend auf entsprechend funktionalisierten CIS Absorbern gezeigt werden konnte zeigt das Potential dieses Optimierungsansatzes.

Die Korrelation der Bauteileigenschaften von verschiedenen Chalkopyrit-Solarzellen zur elektronischen Struktur (→ CBO) der entsprechenden Puffer/Absorber Grenzfläche (festgestellt in dieser Arbeit und dokumentiert in der Literatur) legt nahe, dass zukünftige Optimierungsansätze, die sich nicht ausschließlich auf die Puffer/Absorber Grenzfläche konzentrieren, erforderlich sein können, um weitere Leistungssteigerungen in Dünnschichtsolarzellen auf der Basis von Chalkopyriten mit großer Bandlücke zu erzielen.

Table of Contents

1 Introduction

1.1 Motivation

The need to use renewable energy sources to meet the growing energy demands of human society is unequivocal. As human population and the degree of industrialization in the world continue to increase, the fossil fuel reserves upon which the world so heavily relies are increasingly strained. Moreover, their accelerated rate of consumption takes an alarming toll on the global environment and increasingly threatens the stability of our planet.

Solar energy is an ideal candidate to play a significant role in the diverse energy supply needed for a sustainable fossil-fuel-free economy. Sunlight is a reliable and abundant source of clean energy available throughout the world. In fact, an amount of energy equivalent to the total annual energy consumption of human beings is received each hour by the earth from the sun [1]. Photovoltaics (PV) is a means of harnessing this energy by directly converting sunlight into electricity. Solar cell devices absorb incoming sunlight and generate electron-hole (i.e., charge carrier) pairs that are separated so that the different charge carriers reach the external contacts of the device and are subsequently transported through an external circuit, where this energy can be consumed. A key parameter of the light-absorbing part (hereafter, referred to as the absorber) of the solar cell device is its band gap (E_g), the energetic minimum for the photo-generation of an electron-hole pair. Although the principles behind PV have for long been observed (i.e., the photovoltaic effect was first described by Edmund Becquerel in 1839 [2], while the photoelectric effect was first reported by Heinrich Hertz in 1887 [3]), they involve complex, quantum-mechanical phenomena. The succesful implementation of PV applications did not begin until a more solid theoretical framework had been established. It was not until the 1950s that the first modern solar cell devices were produced by Bell Labs [4]. These devices were Si-based and exhibited solar energy conversion efficiencies (η) of ~ 6%. Ever since, crystalline Si wafer-based photovoltaics have dominated solar cell technology mostly due to the high utilization of this material in the microelectronics industry.

At first, conventional Si wafer-based solar modules were produced from silicon that did not meet the high control requirements for microelectronic applications. Due to the low absorption coefficient of Si (an indirect semiconductor), relatively thick absorber layers (~200 μm) are needed in these first-generation solar cell devices, which translates into a higher material consumption. Moreover, the material quality standards for PV applications are lower than for microelectronics applications; however, a very pure and pristine crystal structure is still needed for photo-generated carriers to reach the solar cell contacts (i.e., to minimize recombination losses). Growing demands for high-efficiency in PV applications, in conjunction with widespread deployment and rising material costs, no longer make the use of the undesirable surpluses of the microelectronics industry as a source of Si viable. Instead, solar-grade monocrystalline Si (c-Si) or multicrystalline Si (mc-Si) is produced by high-energy processes, such as Czochralski-grown ingots or block-casting of molten Si, respectively. Although solar cell devices based on material produced from these processes achieve high conversion efficiencies (i.e., record module efficiencies, η, are c-Si: 22.9%; and mc-Si: 18.5% [5]), the resulting high material production expenses (ranging from 40-50% of the final module cost [6]) greatly limit further cost reduction.

In an effort to reduce solar module production costs (by minimizing material and energy usage), the development and optimization of thin film solar cells have been advanced over the last decades. In these second-generation solar cells, a thin absorber layer (~ a few μm) of a direct semiconductor is deposited on a carrier substrate [i.e., soda lime glass (SLG), polyimide, etc.]. One of the most successfully developed types of thin film solar cells uses chalcopyrites [$Cu(In_{1-x}Ga_x)(S_ySe_{1-y})_2$, CIGSSe] as the absorber material {other successfully employed absorber materials used in thin film solar cells include: cadmium telluride (CdTe) and, recently, kesterites [$Cu_2ZnSn(S,Se)_4$, CZTSSe]} and is typically stacked in the following p-n heterojunction configuration (from top to bottom): n-type ZnO window/n-type buffer layer/p-type chalcopyrite absorbers/Mo-coated SLG. Chalcopyrite-based thin film solar cells have already surpassed power conversion efficiencies, η, of 20% on the laboratory-scale (record η: 21.7% [7]) and have a theoretical maximum efficiency of nearly 30% for a single p-n junction solar cell under the terrestrial solar spectrum (i.e., the theoretical optimum absorber E_g for solar energy conversion is ~1.4 eV [8]).

One of the advantages of the $Cu(In_{1-x}Ga_x)(S_ySe_{1-y})_2$ (CIGSSe) alloy system is that by changing the elemental x and y composition of the absorber, its optical (i.e., bulk) E_g can be varied between 1.04 eV (for $x = 0$, $y = 0 \rightarrow CuInSe_2$, CISe) and 2.53 eV (for $x = 1$, $y = 1 \rightarrow CuGaS_2$, CGS) [9]. Therefore, it is possible to engineer the bulk E_g of the absorber values to be optimal for solar energy conversion. However, the highest efficiency chalcopyrite-based thin film solar cells achieved so far (over 20% on laboratory-scale [7,10]) are based on

$Cu(In_{1-x}Ga_x)Se_2$ (CIGSe) absorbers with a composition of around x = 0.3, which results in a E_g of ~ 1.2 eV. Despite having an E_g which is better matched to the terrestrial solar spectrum, efficiencies of "wide-gap" chalcopyrite-based thin film solar cells (i.e., chalcopyrite absorbers with E_g > 1.25 eV) are generally much lower than their "low-gap" counterparts. For example, solar devices based on $CuInS_2$ (CIS, E_g = 1.54 eV) and $CuGaSe_2$ (CGSe, E_g = 1.68 eV) absorbers are currently limited to around 12% and 10% in efficiency [11,12], respectively.

Advances in solar conversion efficiencies of chalcopyrite-based devices have been primarily realized through empirical approaches in the synthesis process. However, the design of chalcopyrite-based thin film solar cells requires accounting for the effects of conjoining material layers with different chemical and electronic properties at each of the heterointerfaces (in contrast to the homojunction-based conventional Si wafer-based solar cells). Stresses arising from resulting non-optimized heterointerfaces can lead to an increased presence of interface defects that can act as recombination centers for photo-generated carriers, as appears to be the case in wide-gap chalcopyrite devices. For example, studies have reported that the location of dominant recombination losses is different for low- and wide-gap chalcopyrite-based solar cells (with CdS buffer layers) [13,14]. For low-gap chalcopyrites used in high-performing devices, carrier recombination takes place mainly in (near) the bulk of the absorber [13]. In contrast, the dominant carrier recombination for wide-gap chalcopyrite-based devices mainly occurs at the buffer/absorber heterointerface [14]. These findings can also be correlated to the (directly-measured) electronic structure of similar heterointerfaces. An ideal conduction band alignment forms between the CdS buffer layer and low-gap chalcopyrite absorbers, which minimizes recombination losses at the heterointerface [15]. In contrast, the only directly-measured electronic structure reported for a heterointerface based on a wide-gap chalcopyrite absorber [i.e., $Cu(In,Ga)S_2$, CIGSe] and CdS (i.e., the CdS/CIGS heterointerface) revealed a highly unfavorable conduction band offset [16], which reduces the recombination barrier at the heterointerface and detrimentally affects the resulting solar cell performance.

A better understanding of the chemical and electronic properties of the heterointerfaces of (wide-gap) chalcopyrite-based solar cell devices is necessary to identify performance limiting mechanisms. Then, knowledge-based interface tailoring targeting such processes can be used as optimization routes to reach the potential of wide-gap chalcopyrite-based PV.

1.2 Dissertation Organization

The goal of this dissertation is to advance the current state of knowledge regarding the chemical and electronic structures of buffer/absorber heterointerfaces based on low- and wide-gap chalcopyrites (specifically CIGSe and CIS, respectively). Models for performance-loss mechanisms present in wide-gap chalcopyrite-based devices are derived from the characterization. Based on these results, two suitable heterointerface modifications are developed and tested.

The work is presented in this dissertation in the following order:

Chapter 2 overviews the physical principles behind the operation of solar cell devices. The configuration of thin film chalcopyrite-based solar cell devices and the function of the various layers are further explained, as well as the limiting mechanisms potentially acting on them.

Chapter 3 covers the working principles behind the spectroscopic techniques employed in this dissertation.

Chapter 4 presents the chemical and electronic properties of the CdS/- and ZnS/CIGSe heterointerface formations in (low-gap) high-efficiency chalcopyrite-based solar cells. The findings in this chapter are meant to establish a benchmark picture of the chemical and electronic structure of high-efficiency chalcopyrite-based solar devices. The study of the chemical structure formation of the two different heterointerfaces is performed via x-ray photoemission spectroscopy (XPS) and x-ray emission spectroscopy (XES). The electronic structures of the heterointerfaces are directly probed by combining ultraviolet photoelectron spectroscopy (UPS) and inverse photoemission spectroscopy (IPES). Following the same methodology, Chapter 5 presents the directly measured chemical and electronic properties of the CdS/CIS heterointerface, a wide-gap chalcopyrite-based buffer/absorber heterointerface. A comparison of the results presented in Chapters 4 and 5 serves to identify performance loss mechanisms in wide-gap chalcopyrite-based solar cell devices, the knowledge of which will guide the way in the development of interface property optimization treatments.

Chapter 6 shows the results of the first interface tailoring approach: a selenization treatment of CIS absorbers performed to incorporate into the treated CIS samples interface mechanisms found in low-gap chalcopyrite-based heterointerfaces and help improve the overall performance of resulting solar cell devices. The evolution of the chemical structure at the surface and the bulk of the treated samples is determined by XPS and x-ray fluorescence analysis (XRF). The electronic and optical properties of the treated samples are probed by UPS and ultraviolet-visible (UV-Vis) spectrophotometry.

Chapter 7 compiles the results of directly measured heterointerface electronic structures formed by chalcopyrite and kesterite (a chemically-related material also used in PV) absorbers of various bulk E_g (E_g^{bulk}) values onto which CdS had been deposited. Findings in Chapters 4 and 5 are included in this analysis. An interpretation of the influence of various electronic structure parameters on the performance of the resulting solar cell devices is provided.

Chapter 8 shows the results of the second interface modification involving the insertion of dipole-charged organic self-assembled monolayer (SAM) compounds between the CdS/CIS heterointerface, in order to modulate the alignment of the heterointerface electronic structure. Changes in surface chemical structure are analyzed using XPS. The magnitude and polarity of the deposited surface dipoles are determined by monitoring induced changes in work function (Φ) of the treated samples, derived from UPS secondary electron cut-off spectra.

Chapter 9 summarizes the findings of the previous chapters in this dissertation. Furthermore, it concludes by giving an outlook regarding future work related to this dissertation.

2 Chalcopyrite-based Thin Film Solar Cells

In this chapter, a concise overview of the physical principles behind solar cell device performance is presented. Current density-voltage (*j*-V) curve characterization is introduced along with important solar cell performance parameters that can be obtained from this method. Each component layer in chalcopyrite-based solar cells and the role it plays in the device is described. The possible loss mechanisms occurring throughout the device are also discussed, with a special emphasis on carrier recombination in the absorber layer and at the buffer/absorber interface.

2.1 Physical Principles of Solar Cell Device Performance

A solar cell device is designed so that photons with sufficient energy (i.e., $h\nu \geq E_g$, where h is Planck's constant and ν is the frequency of the photon's electromagnetic wave) create electron-hole (i.e., charge carrier) pairs in the absorber material. However, photo-generation of charge carriers is not the only relevant factor affecting the electric output; the carriers must be separated to reach the contacts of the solar device and be transported through the external circuit. Carriers move freely throughout a semiconductor material [i.e., electrons in the conduction band (CB) and holes in the valence band (VB) of the material], however, in the absence of an external force, the carrier movement is random due to constant collisions with lattice atoms. Without an effective carrier separation mechanism, the overwhelming majority of generated carriers would recombine without reaching the device's contacts. In thin film solar cells, the separation of charge carriers is carried out by a built-in field, V_{bi}, formed by a p-n junction.

A p-n junction can be assembled by oppositely doping different regions of a semiconductor material (i.e., p-n homojunction) or by joining a p-type and an n-type semiconductor material (i.e., p-n heterojunction). In the heterojunction configuration, placing a p-type and an n-type material together induces a transfer of charge carriers due to the carrier concentration gradients (i.e., electrons from the n-type side diffuse into the p-type side and holes from the p-type side diffuse into the n-type side). This diffusion of charge carriers produces an electric field between the immobile positively-charged uncompensated donor states in the n-type side of the junction and the immobile negatively-charged uncompensated acceptor states in the p-type side. In the presence of an electric field, electrons are accelerated in the direction opposite the electric field (i.e., repelled), whereas holes are accelerated in the direction of the field (i.e., attracted). The movement of carriers due to the effect of this electric field is referred to as drift transport. Moreover, the diffusion of charge carriers across the junction continues until the force of the carrier concentration gradient is counterbalanced by the potential build up, V_{bi}.

According to the depletion-approximation model proposed by Schottky [17], a positively-charged region in the n-type side (of thickness x_n from the heterojunction) and a negatively-charged region in the p-type side (of thickness x_p from the heterojunction) are formed, which are completely void of charge carriers. This portion of the solar cell device is termed the space charge region (SCR) and the neutral remainder of the solar device is called the quasi neutral region (QNR). From this model, it follows that i) minority charge carriers (i.e., holes in the n-type side and electrons in the p-type side) are swept across the SCR as a result of the V_{bi}; and that current flows across the SCR (i.e., carrier diffusion or drift transport) are dependent on minority carrier recombination in the QNR. Due to asymmetric doping in the chalcopyrite-based solar cells (as will be explained in Sect. 2.3), the SCR in this type of device is located to a large extent inside the absorber layer. Consequently, the potential drop at the p-type side of the junction is a good approximation of the V_{bi}. Changes in local charge neutrality, charge density, electric field and potential predicted by the depletion-approximation model are depicted in Fig. 2.1.

Under illumination, the charge carrier density in the p-type material increases, generally leading to a higher transfer of minority carriers (i.e., electrons) across the SCR. In short circuit conditions (i.e., the front and back contacts of the device are connected), the higher drift transport does not result in a charge carrier build up in the QNR because the external circuit supplies an exit flow for the charge carriers. The resulting electrical current (density) is referred to as, I_{SC} (j_{SC}).

If photo-generated carriers are prevented from exiting the solar device (i.e., in the absence of an external source or by applying an external bias between the device contacts), charge begins to build up begin in the QNR of the p-type side (i.e., a positive hole-induced charge) and the n-type side (i.e., a negative electron-induced charge) of the heterojunction, inducing an electric field opposing the existing V_{bi}. Because the V_{bi} acts as a barrier for the concentration-gradient-related diffusion of carriers across the p-n junction (i.e., the forward bias diffusion current), the formation of an opposing electric field decreases the effective electric field at the

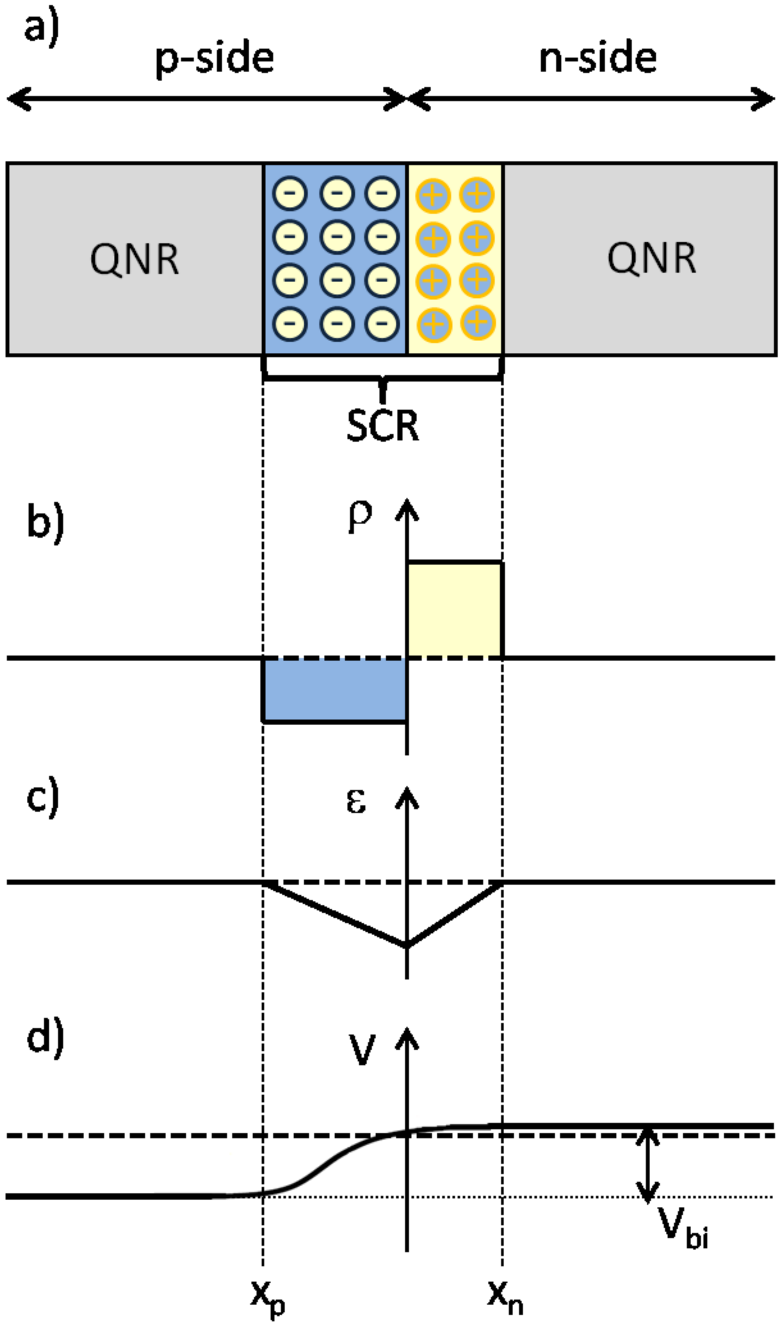

Figure 2.1 Schematic diagrams showing changes in (a) local charge neutrality, (b) charge density, ρ, (c) electric field, ε, and (d) potential, V, across a p-n junction predicted by the depletion approximation model (as adopted from [18]).

junction, establishing a new equilibrium voltage, allowing an increase in diffusion current. The current (density) produced by the solar cell device then becomes the difference between the light-generated current, I_L (j_L), and the forward bias diffusion current. The bias at which the forward bias diffusion current actually offsets the drift transport of photo-generated carriers (i.e., a state of no net current) is referred to as open circuit voltage, V_{OC}.

2.2 *j*-V Characterization of Solar Cell Devices

The current density-voltage (*j*-V) characteristics of a p-n junction as a function of an applied voltage in dark conditions has been formulated by Shockley (in what is known as the ideal-diode equation [19]) as follows:

$$j(V) = j_{01}\left[e^{\left(\frac{qV}{kT}\right)} - 1\right] \qquad (2.1),$$

where j_{01} is the saturation current density, q is the elementary charge unit, k is the Boltzmann constant and T is the temperature of the device.

The j_{01} value depends on the properties of the semiconductors composing the heterojunction and can be described by the following equation:

$$j_{01} = \left(\frac{qD_p}{L_p}p_n + \frac{qD_n}{L_n}n_p\right) \qquad (2.2),$$

where p_n and n_p are the minority carrier concentrations (i.e., the hole concentration in the n-type material and the electron concentration in the p-type material), D_p and D_n are the charge carrier diffusion coefficients and L_p and L_n are the carrier diffusion lengths.

As mentioned in Sect. 2.1, illumination of the solar cell will create a surge of charge carriers. These photo-generated carriers will either recombine or, if separated by the electric field of the SCR, will increase the current density output of the diode by j_L. Superimposing both of these current densities, one obtains:

$$j(V) = j_{01}\left[e^{\left(\frac{qV}{kT}\right)} - 1\right] - j_L \qquad (2.3)$$

From eqn. (2.3), several important parameters of solar cell performance can be derived. The j_{SC} can be reached by setting the voltage to zero (i.e., V = 0) in eqn. (2.3). If it is assumed that j_L is constant and independent of voltage across the junction, then:

$$j_{SC} = j_L \qquad (2.4)$$

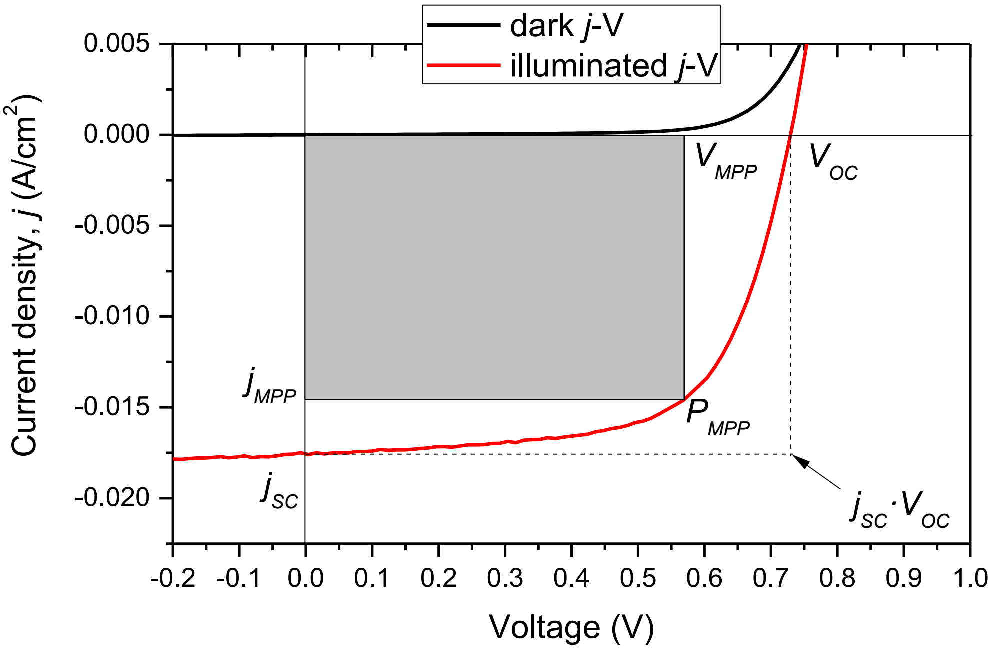

Figure 2.2 *j*-V characteristics of a solar cell. The different labeled solar cell parameters are explained in the text. The area of the P_{MPP} rectangle is gray-shaded for comparison purposes.

Likewise, the V_{OC} can be calculated by setting the current density of the solar cell to zero (i.e., $j = 0$, there is no net current flow through the device under open circuit conditions). Thus, getting:

$$V_{OC} = \frac{kT}{q} ln\left(\frac{j_L}{j_{01}} + 1\right) \qquad (2.5)$$

Fig. 2.2 shows the *j*-V characteristics under dark and illuminated conditions. The j_{SC} and the V_{OC} are the largest current density and voltages that a solar cell can sustain. However, the power of the solar cell is zero at both these points. The maximum power point of a solar cell, P_{MPP}, can be graphically expressed as the largest rectangle that can be fitted within the *j*-V curve of the solar cell, as shown by the gray-shaded rectangle in Fig. 2.2. The relation between the P_{MPP} [which is the product of the current density and voltage at the maximum power point of the *j*-V curve (j_{MPP} and V_{MPP}, respectively)] and the product of the j_{SC} and V_{OC} of a solar cell is denoted by another parameter, the fill factor, *FF*, or:

$$FF = \frac{j_{MPP} \cdot V_{MPP}}{j_{SC} \cdot V_{OC}} \qquad (2.6)$$

In this respect, the *FF* assesses the squareness of the *j*-V response.

Because the purpose of solar cell devices is to produce an electrical output, the most important solar cell performance parameter is the power conversion efficiency, η, defined as the ratio between the P_{MPP} and the incoming irradiative power, P_{in}. From eqn. (2.6), P_{MPP} can be expressed as the product of the product of the j_{SC}, V_{OC}, and FF, which leads to the following equation:

$$\eta = \frac{P_{MPP}}{P_{in}} = \frac{j_{SC} \cdot V_{OC} \cdot FF}{P_{in}} \qquad (2.7)$$

The efficiencies of solar cell devices for terrestrial applications are typically tested using the AM1.5 solar spectrum at 25 °C as standard measurement conditions. The AM1.5 illumination represents the solar radiation after traversing 1.5 times the atmosphere, simulating sunlight that strikes a surface at sea level with a 48.2° incidence (1000 W/m^2).

2.3 Device Structure

Chalcopyrite-based thin film solar cells typically consist of five stacked layers supported by a glass substrate, as illustrated in Fig. 2.3. A description of each of these layers is presented in this section in order of synthesis. The absorber layer is the p-type semiconductor, which along with the n-type buffer and the two ZnO layers, form the p-n junction of the solar cell device.

Soda lime glass (SLG) is a common substrate material due to its availability and low-cost. A Mo layer is added to the top of the substrate, by sputtering or evaporation, and serves as the back contact of the solar cell device. SLG continues to be the substrate material of choice because a thermally-activated Na diffusion through the Mo layer occurs during the chalcopyrite synthesis process, which conveys beneficial effects to absorber growth and ultimately device performance [20,21]. Although other substrate materials can be used to provide specific device properties (i.e., Ti and polyimide foils allow for the fabrication of flexible solar cell devices), Na-containing precursors must then be added to produce similar desirable Na-related effects and high efficiencies [22,23].

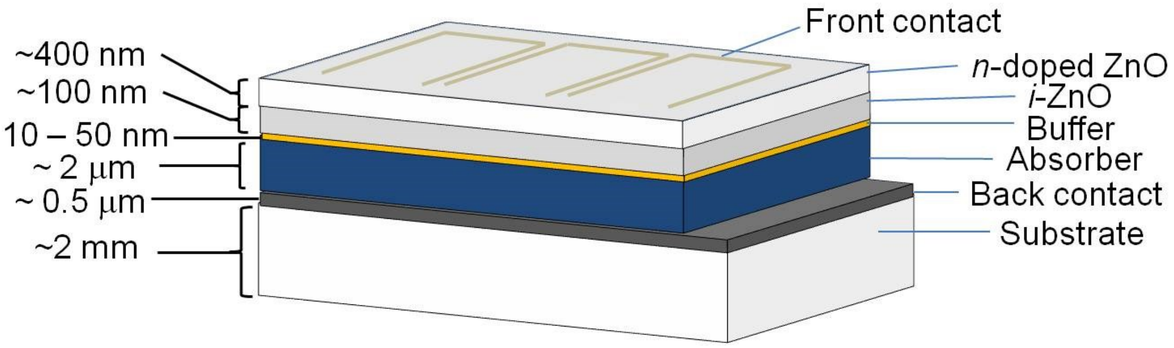

Figure 2.3 The layer configuration of a chalcopyrite-based thin film solar cell (not to scale). The approximate thickness of each layer is also included.

The chalcopyrite absorber is deposited atop the Mo-coated substrate. $Cu(In_{1-x}Ga_x)(S_ySe_{1-y})_2$ are tetrahedrally bonded semiconductor compounds with a $A^IB^{III}C^{VI}$ structure. In accordance to the Grimm-Sommerfeld rule [24], each atomic site has on average 4 valence electrons. As mentioned in Ch. 1, the E_g^{bulk} of the absorber layer can be tuned from 1.04 – 2.53 eV by changing the elemental x and y composition. This effect has been attributed to two mechanisms relating to the chalcopyrite crystal lattice [25]. The first reason pertains to p-d repulsions forming between the valence states of the anion (i.e., S 3p and Se 4p states) and the Cu 3d orbitals, which lowers E_g. These p-d repulsions explain the significantly lower E_g of chalcopyrite semiconductors compared to their II-VI binary structural analogs [e.g., Cd(S,Se) and Zn(S,Se) compounds], which exhibit lower p-d state repulsions [25]. The second reason pertains to anion displacement in the chalcopyrite lattice due to differences in bonding lengths as a result of variations in atomic sizes of the B^{III} cation. In common-anion chalcopyrites, which exhibit similar p-d repulsive states, the E_g of the material is inversely related to size of the B^{III} cation.

If an isovalent atom replaces one of the chalcopyrite lattice atoms so that the four-electron-per-atomic-site rule is conserved, the new compound continues to be considered a chalcopyrite phase. However, a defect compound is formed with incorporation of non-isovalent atoms, in which case, the formation of vacancy sites will maintain charge neutrality. One of the predominant site defects in chalcopyrites involves the formation of copper vacancies, V_{Cu}, which can affect the E_g (i.e., increase it) and doping level (i.e., n-type conversion) of the material [26]. In fact, one of the reported benefits of SLG-originated Na diffusion is to occupy these V_{Cu} sites and prevent non-isovalent atoms from occupying them (i.e., antisite prevention) [27,28].

In this dissertation, CIGSe and CIS absorbers with E_g^{bulk} values of 1.2 and 1.5 eV, respectively, are investigated. The CIGSe samples were prepared in a Zentrum für Sonnenenergie- und Wasserstoff- Forschung Baden-Württemberg (ZSW) high-efficiency solar cell production line. The synthesis involved an in-line multi-stage co-evaporation of Cu, In, Ga and Se on Mo-coated SLG substrates [29]. The CIS samples were prepared by Helmholtz Zentrum Berlin für Materialien und Energie GmbH (HZB) collaborators by co-deposition of Cu and In on Mo-coated SLG substrates, followed by sulfurization in a rapid thermal process (RTP) line [30]. Prior to the sulfurization step, the deposited precursors are strongly Cu-rich (i.e., [Cu]/[In] = 1.8) [30]. The sulfurization process produces a uniform CIS layer with excess Cu producing a Cu_xS capping surface phase. Before subsequent solar cell synthesis steps can be conducted, this Cu_xS phase is selectively removed via a KCN etching treatment; the etching rate of Cu-S phases is 10^5 times larger than that of CIS [31].

A relatively thin layer (several tens of nm) of a n-type semiconductor, referred to as the buffer layer, is deposited between the absorber and the window layers. An ideal buffer material would meet the following criteria: i) it should be a n-type material in order to form the p-n junction with the absorber layer; ii) it should possess a wide E_g (relative to the absorber material) to maximize light transmission into the absorber layer; iii) it should passivate potential shorting paths and trap surface states; iv) it should improve the energy band alignment between the absorber and the window layers; v) it should be a non-toxic material. Moreover, the buffer layer may protect the surface of the absorber by preventing the formation of metallic phases as a result of the high-energy ion sputtering process involved in the deposition of the ZnO window layers.

Until recently, record solar cells had consistently included CdS (E_g = 2.5 eV [32]) as the buffer material, which in this case is typically deposited through a wet chemical step. At first, it seemed that replacing this buffer material with a more transparent one (i.e., a wider-E_g material such as ZnS, ZnO, etc.) should improve the efficiency conversion factor of resulting solar devices. Moreover, the chemical bath deposition (CBD) step from a production stand is not ideal because it interrupts the vacuum-based synthesis sequence (although the exposure of the absorber´s surface to ammonia during the early stages of the CBD process generates a cleaning effect) [33]. However, until recently [7], buffer replacement efforts had continued to be unable to produce solar cell devices that meet the efficiencies achieved by devices including the standard CdS layer. Such outcomes suggest that in high-efficiency chalcopyrite-based solar cell devices CdS, or its wet chemical deposition approach, performs a vital part in the formation of an optimal buffer/absorber heterointerface.

Two layers of ZnO (E_g = 3.4 eV [34]), deposited on top of the buffer layer by rf-magnetron sputtering, act as the window layer of the thin film solar cell device. The first deposited ZnO layer is intrinsically-doped (i-ZnO) and serves as a dopant barrier for the second highly-doped ZnO:Al layer. The high doping concentration of the ZnO:Al layer provides an asymetrically-doped character to the p-n junction, with the donor concentration, N_D, greatly outweighing the acceptor concentration, N_A, (i.e., $N_D >> N_A$) in the absorber. This setting ensures that the effect of the V_{bi} spans mostly within the p-type side of the junction, as mentioned in Sect. 2.1. Another feature of the window layer is its light scattering properties, which extends the light trajectory across the absorber layer and enhances the probability of light absorption.

The front contact of laboratory-scale solar cell devices is a metallic grid consisting of a thin Ni layer (~ 10 nm) and a layer of Al (~ 1 μm). Although Al is the actual ohmic contact of the device, the purpose of the Ni layer is to prevent the oxidation of Al by contact with ZnO.

2.4 Band Offsets

The flux of charge carriers in a p-type and n-type materials resulting from p-n junction formation (i.e., joining together of these materials) was described in Sect. 2.1. The related changes in electronic band alignment in these materials with the formation of the heterojunction are now discussed.

The energy band diagrams of a p-type and n-type semiconductors that are separated are shown in Fig. 2.4 (a). The relative position of the Fermi level, E_F, within the E_g is related to the doping types of the material, which is associated with charge carrier concentrations. In this figure, the work function, Φ, of a material is shown to be the energy difference between the E_F and the vacuum level, E_{Vac}. Moreover, the electron affinity, χ, of a material is the energy difference between its conduction band minimum (CBM) and the E_{Vac}. The E_{Vac} is defined as the energy of a stationary electron in vacuum that is completely free from the crystal and electrostatic potentials of a material [35]. Because an electron inside a material must first reach its surface in order to escape from it, the energetic distance of the electronic band alignment of a material to the E_{Vac} depends on the surface electronic properties of the

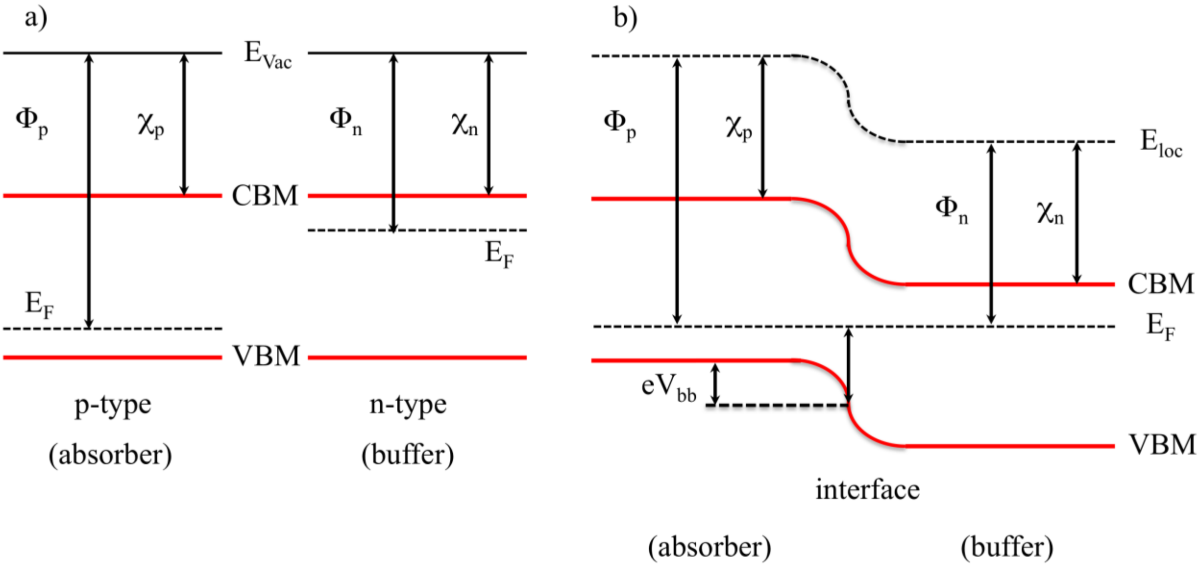

Figure 2.4 Energy band diagram of a) a p-type and a n-type semiconductor separated from each other and b) joined together to form a p-n junction. eV_{bb} stands for the maximum band bending at the absorber.

material. (In this respect, the Φ and χ of a material are surface-related properties.) However, a concept refered to as the local vacuum level, E_{loc}, is ocassionally used in literature to address the effect of electrostatic potential on the energy band alignment inside materials (heterojunctions). E_{loc} is defined as the energy of a stationary electron that is free from the influence of a material's crystal potential and is presented by adding the χ value above the CBM of a material [35].

Differences in E_{Vac} and E_{loc} are shown in Fig. 2.4 (a), (b). The reference E_{Vac} for both materials in Fig. 2.4 (a) is the same. When two materials with different electronic properties (i.e., Φ and/or χ) are joined, as seen in Fig. 2.4 (b), a built-in field is formed that brings the E_F to the same level across the whole junction. The relocation of the energy bands to produce a common E_F level causes the E_{loc} to change along the different components of the heterojunction. This re-alignment also induces a bending of the electronic bands near the interface of the formed heterojunction, which in chalcopyrite-based thin film solar cells is more prominent at the absorber side due to the assymetrically-doped character of the p-n junction. The maximum band bending, eV_{bb}, that can take place in the absorber layer [i.e., the energetic difference between the E_F level and the absorber's VBM outside the SCR of the solar cell p-n junction and the E_F level and the VBM at the absorber's surface, as shown in Fig. 2.4 (b)] is reported to influence the maximum photovoltage of a chalcopyrite-based solar cell device. In this particular illustration, there is no discontinuity shown in the heterointerface

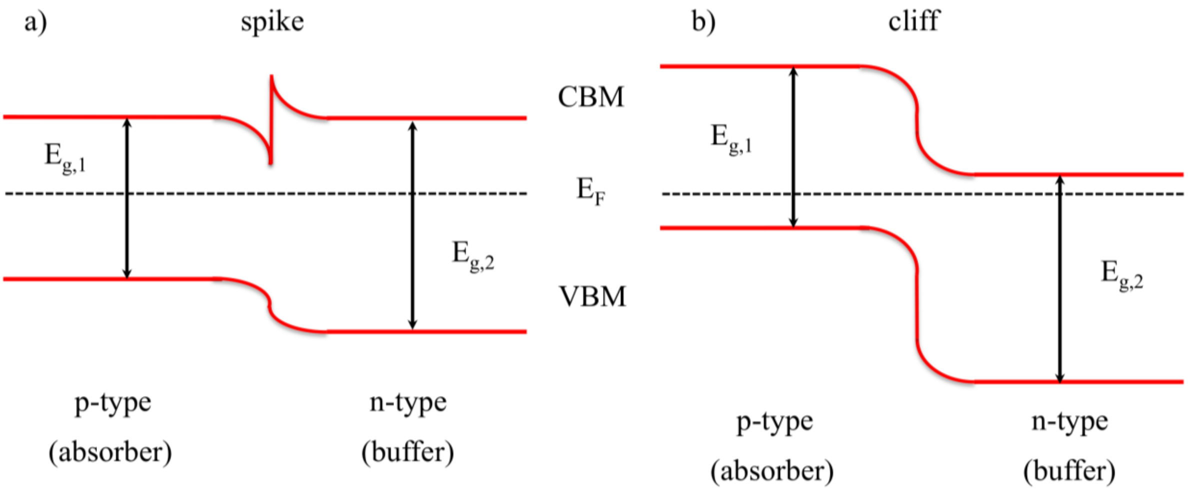

Figure 2.5 Band alignment of a heterointerface with a) a spike-like and b) a cliff-like CBO configuration. $E_{g,1}$ and $E_{g,2}$ stand for the band gap of the p-type and n-type materials, respectively.

conduction (valence) band alignment [i.e., flat conduction and valence band offset (CBO and VBO) configurations]. However, diverse material combinations of p-n junctions often produce discontinuities in the CB and VB due to differences in χ and E_g between the component semiconductors.

In this dissertation, a positive buffer/absorber heterointerface CBO (VBO) refers to a band alignment in which the CBM (VBM) of the buffer is energetically higher than the CBM (VBM) of the absorber (i.e., a spike-like configuration). Likewise, a negative buffer/absorber heterointerface CBO (VBO) refers to a band alignment in which the CBM (VBM) of the buffer is energetically lower than the CBM (VBM) of the absorber (i.e., a cliff-like configuration). Fig. 2.5 (a),(b) show the qualitative alignment of both configurations.

As mentioned in Sect. 2.1, drift current depends on the concentration of the minority charge carrier. Electrons, which are transported in the CB, are the minority charge carrier at the absorber layer (i.e., the site for photo-generation of charge carriers). Therefore, the buffer/absorber CBO configuration is considered to play a critical role in the performance of chalcopyrite-based thin film solar cells. Based on device simulations, the optimal CBO range is reported to be 0-0.4 eV [36,37]. Higher CB misalignments block carrier transport across the absorber/buffer heterointerface. Even a small negative CBO configuration (i.e., -0.1 eV) is predicted to significantly decrease the V_{OC} of resulting solar cell devices by reducing the interface carrier recombination barrier (more details are presented in the next section) [36,37].

These cases highlight the significance of accurately determining band alignment offsets in heterointerfaces. A common method used to indirectly estimate CBO values involves finding first the VBO of the investigated heterointerface, which can be directly determined via photoemission characterization (more details provided in Sect. 3.1), and then calculating the CBO from the following equation:

$$\text{CBO} = \text{VBO} + E_g^{\text{buffer}} - E_g^{\text{absorber}} \qquad (2.8)$$

where E_g^{buffer} and E_g^{absorber} are the E_g values of the buffer and absorber materials, respectively. Reference E_g^{bulk} values are often used for E_g^{buffer} and E_g^{absorber}, which assumes that i) the E_g at the surface (E_g^{surf}) is the same to that of the bulk and that ii) the interface is abrupt (i.e., no chemical intermixing nor formation of new interface chemical species occurs). As will be shown in this work, these conditions are frequently not met in chalcopyrite-based heterointerfaces, which lead to inaccurate assessments.

2.5 Loss Mechanisms

An overwhelming fraction of the energy absorbed as photons (i.e., $h\nu \geq E_g$) by a solar cell device is lost in the generation of charge carriers, the separation of said carriers and the their transport to the contacts of the device and through the device's external circuit. Due to the energetic loss mechanisms acting upon each of these mentioned steps, the theoretical conversion efficiency maximum for a single p-n junction is close to 30% [8]. For chalcopyrite-based thin film solar cells, energy leak sources can be found throughout the spatial geometry of the device. High E_g semiconductor materials (compared to the E_g of the absorber layer) are used to make the window of the solar cell, which effectively shifts most of the photo-generation of charge carriers into the absorber layer. However, light absorption cannot be entirely prevented at the window and buffer layers, resulting in light transmission losses. Of the amount of photons that reach the absorber layer, the ones with an energy equal to or higher than the E_g of the absorber material create charge carrier pairs, however, excess photon energy (i.e., the fraction of energy higher than the E_g of the absorber) is lost by relaxation mechanisms. Recombination losses reduce the carrier concentration that ends up reaching the contacts of the solar device. The presence of structural anomalies that decrease the shunt resistance, R_{sh}, of the solar cell (i.e., pin-holes that traverse the entire absorber layer or voids at the back contact) can open shorting paths. In addition to the intrinsic resistivity of

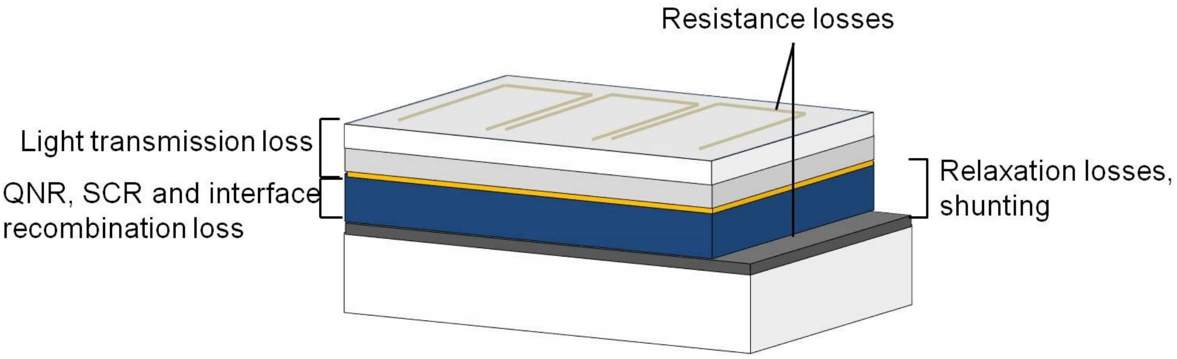

Figure 2.6 Common conversion loss mechanisms in chalcopyrite-based thin film solar cells with respect to spatial device geometry.

the different semiconductor layers in the solar device, a series resistance, R_s, is formed between the contacts of the device and the external circuit, which results in effective electronic losses. Fig. 2.6 depicts the region of occurrence of the common loss mechanisms undergone by chalcopyrite-based solar cells.

As mentioned in Ch. 1, thin film solar devices based on low-E_g chalcopyrite absorbers are well on their way to meet their full conversion efficiency potential (with record laboratory scale devices already achieving $\eta = 21.7$ % [7]), whereas solar devices based on wide-E_g chalcopyrites significantly lag behind. The location of dominant carrier recombination within the device geometry has been identified as one of the most significant differences in loss mechanisms between both types of chalcopyrite-based devices [13,14]. Such variation can be correlated to the band alignment of the buffer/absorber heterointerface.

Fig. 2.7 (a),(b) shows the qualitative carrier recombination loss routes undergone in chalcopyrite-based buffer/absorber heterointerfaces with spike- and cliff-like CBO configurations, respectively. According to the location at which they take place, these losses can be referred to as: i) bulk, ii) SCR, and iii) interface recombinations.

Under the ideal-diode model discussed in Sect. 2.1, it is presumed that the SCR is depleted of charge carriers, to which it follows that carrier recombinations do not occur in this region. These assumptions are acceptable for conventional Si wafer-based solar cell devices because the SCR-width is negligible compared to the carrier diffusion lengths [38]. For thin film solar cells, the widths of their SCR and QNR, and the carrier diffusion lengths are within the same order of magnitude [39], making the no-SCR-carrier-recombination assumption invalid.

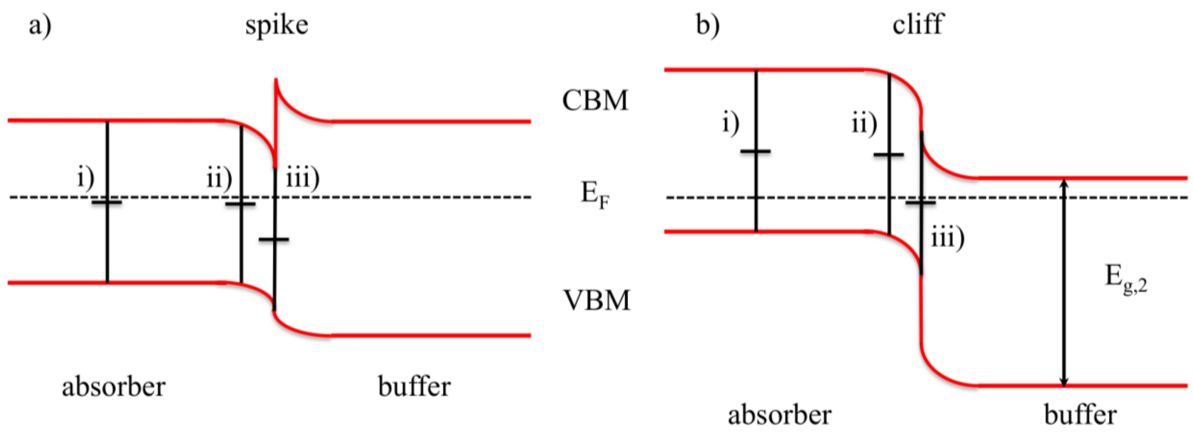

Figure 2.7 Recombination paths for buffer/absorber heterointerfaces with a) spike-like and b) cliff-like CBO configurations with respect to region of occurrence: i) bulk, ii) SCR and iii) interface. The middle of the E_g is represented by horizontal dividers on the recombination path lines.

Based on the Shockley-Read-Hall (RSH) model [40], maximum recombination occurs where the E_F lies at the middle of the E_g [signaled by the horizontal dividers in Fig. 2.7 (a),(b)], the location at which the electron density, n, equals the hole density, p [40,41]. In a buffer/absorber heterointerface with a spike-like or a flat CBO configuration, such condition (i.e., n = p) is satisfied within the SCR, as pointed out in Fig. 2.7 (a). This conclusion is in agreement with reports of bulk- (SCR-) dominant recombination losses in low-E_g chalcopyrite-based solar devices, which have been found to possess flat CBO configurations [15].

If a buffer/absorber heterointerface has a cliff-like CBO configuration, the energetic barrier preventing electrons at the CB of the buffer from recombining with holes of the VB of the absorber is reduced at the interface, as illustrated in Fig. 2.7 (b). In such conditions, interface recombination [i.e., path (iii)] may become the dominant recombination loss mechanism and may restrain increases in V_{OC} expected of absorbers with wider E_g. A main objective of this dissertation is to determine whether such a limiting mechanism is present in wide-E_g chalcopyrite-based thin film solar cell devices.

3 Experimental Methods

In this chapter, the spectroscopic techniques employed in this dissertation are explained. Photoemission spectroscopy is the principal characterization technique used, through which the surface chemical and electronic structure of semiconductor samples can be determined. The chemical properties of samples in the near-bulk region are probed via soft x-ray emission spectroscopy. X-ray fluorescence analysis is carried out to assess the bulk elemental compositions of materials, and ultraviolet-visible spectrophotometry is conducted to assess the optical (bulk) E_g of materials. The pertinent data analysis for each spectroscopic technique, as well as various sample preparation steps used in this work, are also presented.

3.1 Photoemission

Photoemission spectroscopy (PES) is an analytical technique used for characterization of chemical and electronic properties of solid surfaces. The basis of this spectroscopic technique is the external photoelectric effect, which was first experimentally discovered by Heinrich Hertz [4], and later explained by Albert Einstein [42]. In direct PES, an excitation source irradiates a sample with photons of a known energy and excites electrons from occupied electronic states above the vacuum level. Information related to the occupied density of states (DOS) can be derived from the kinetic energy (KE) of the excited photoelectrons. Complementarily, inverse photoemission spectroscopy (IPES) probes the unoccupied DOS of sample by targeting it with low-KE electrons, which relax into unoccupied states in the conduction band (CB) of the sample and emit photons in the process. By combining PES (i.e., more specifically, ultraviolet photoelectron spectroscopy [UPS]) and IPES, it is possible to directly assess the surface electronic structure of a material, E_g^{surf}.

3.1.1 Direct Photoemission

In the photoemission event, an incident photon with energy hν excites an N-electron system from an initial state $\left|\psi_i\right\rangle$ to a final state $\left|\psi_f\right\rangle$. In this process, one electron is excited from its ground state to a state above the vacuum level. The probability for this transition, $P_{\mathrm{i}\rightarrow\mathrm{f}}$, can be calculated by Fermi's Golden Rule:

$$P_{i \to f} \propto \left| \left\langle \psi_f \left| \hat{H} \right| \psi_i \right\rangle \right|^2 \delta\left(E_f - E_i - h\nu \right), \qquad (3.1)$$

where δ describes the energy conservation law, $\hat{H}$ is the transition operator, and E_f and E_i are the energies of the final and initial states, respectively [43].

Under the Koopmans theorem (i.e., the frozen orbital approximation) [43,44], it is assumed that orbitals of the initial (i.e., N-electron system) and final (i.e., N-1-electron system) are identical. For the photoemission process, in which the initial state is an electron in a ground state with binding energy, BE, and the final state is a free electron with kinetic energy, KE, the δ-function only allows transitions with the following relation:

$$\mathrm{KE} = h\nu - \mathrm{BE} - \Phi \qquad (3.2),$$

where Φ is the work function of the system (i.e., due to the free electron nature of the final state). Using an excitation source, PES measures the count of emitted photoelectrons versus the KE of the photoelectrons. Depending on the excitation energy, PES is also referred to as x-ray photoelectron spectroscopy (XPS) or UPS. Fig. 3.1 illustrates the photoemission process.

PES measurements are carried out in ultra-high vacuum (UHV; $p < 10^{-9}$ mbar) conditions for the following reasons: i) changes to sample surface composition (i.e., surface oxidation or adsorption of surface contaminants) need to be minimized in order to reach meaningful conclusions; ii) it is necessary that photoelectrons ejected from the sample do not lose their KE through collisions with particles *en route* to the electron analyzer; and iii) components of the experimental apparatus require UHV conditions for proper operation (i.e., the x-ray source and electron analyzer).

The nomenclature for PES lines, in spectroscopic notation, is: element, principal quantum number, and the orbital angular momentum quantum number in letter form (i.e., S 2s). If a probed line exhibits a spin-orbit splitting, the total angular momentum quantum number ($j = l+s$) is given as a subscript (i.e., In $3d_{3/2}$).

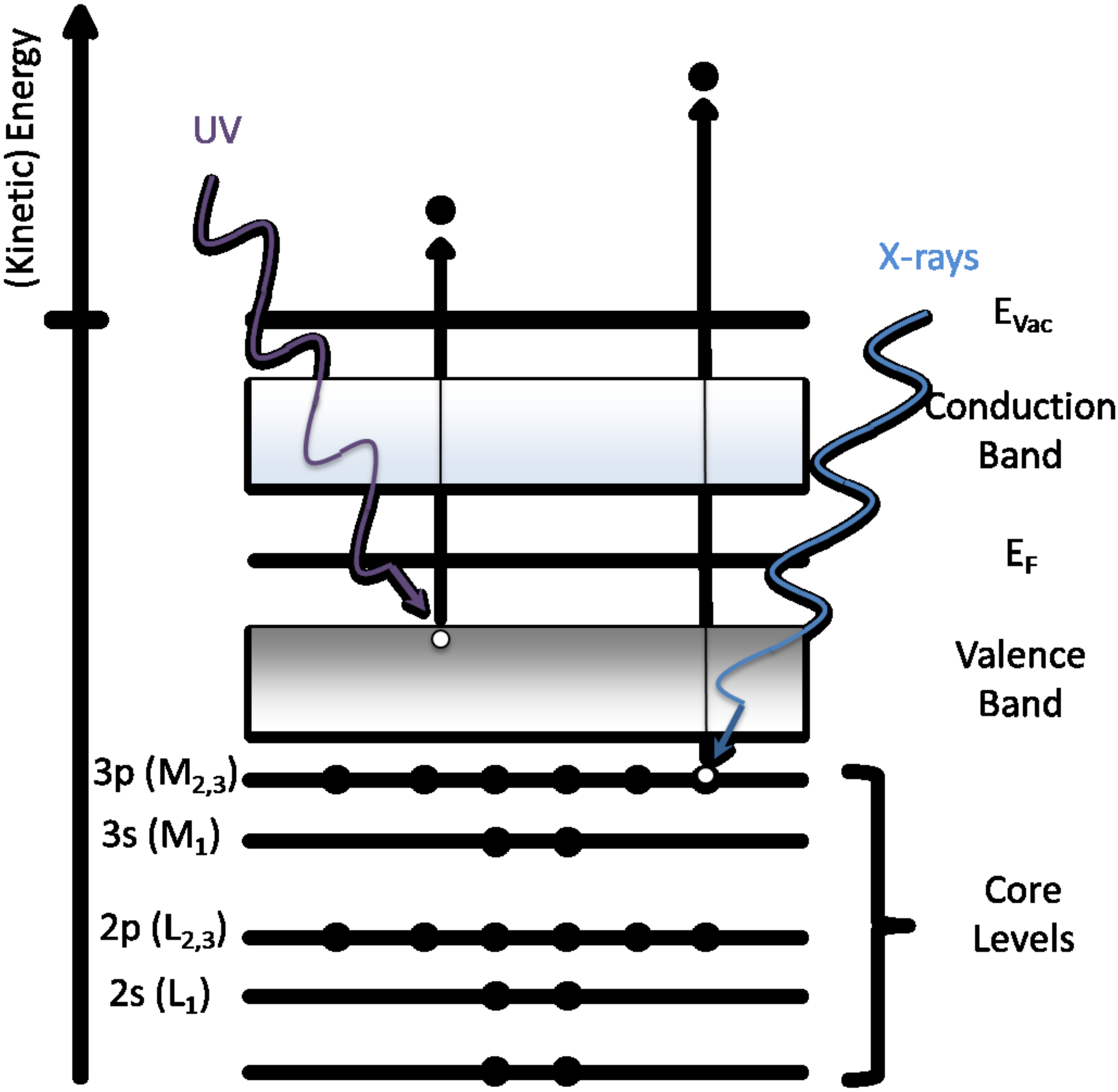

Figure 3.1 Schematic of the photoemission process. X-ray or UV photons excite electrons from different electronic levels of the sample above the vacuum level, E$_{Vac}$. The kinetic energy of the resulting photoelectrons is measured by an electron analyzer in photoemission spectroscopy. The nomenclature of the most common electronic (sub)shells investigated in this dissertation are given in atomic (x-ray) notation. Differences in energy levels due to spin-orbit splitting are not shown.

Because each element has its own electronic configuration with unique binding energies for each of its electronic states, PES is a valuable spectroscopic technique that allows for the identification of elements and evaluation of their surface coverage on a sample. (Reasons underlying the probing limits of PES to the surface of a sample are addressed below.) The detected intensity of a PES line, I (in photoelectrons per second), can be defined as [45]:

$$I = nf\sigma\theta y\lambda AT \qquad (3.3),$$

where n is the atomic density of the probed element (in atoms per cm^3), f is the x-ray excitation flux (in photons per cm^2-s), σ is the photoionization cross section of the probed electronic subshell (in cm^2), θ is the instrumental angular efficiency factor based on the angle between the path of the incoming photon and the detected photoelectron, y is the photoelectric process efficiency, λ is the inelastic mean free path (IMFP) of the probed photoelectrons in the material, A is the probed sample area, and T is the transmission function of the electron analyzer.

The surface ratio of two elements, $\frac{n_1}{n_2}$, in a sample can be obtained as follows [45]:

$$\frac{n_1}{n_2} = \frac{I_1 / S_1}{I_2 / S_2} \qquad (3.4),$$

where S_x is the atomic sensitivity factor.

Likewise, the elemental composition fraction, C_x, of a sample can be determined as follows [45]:

$$C_x = \frac{n_x}{\sum n_i} = \frac{I_x / S_x}{\sum I_i / S_i} \qquad (3.5)$$

For measurements of the same sample carried out under the same experimental settings, $S_x = \sigma_x \lambda_x T_x$ in eqns. (3.3) and (3.4). Reference σ values for a given excitation energy are used to account for differences in photoionization cross section of the probed electronic subshells [46,47]. The transmission function of the electron analyzer (T) is determined by normalizing a measured survey spectrum of a sputter-cleaned Ag foil to match the background of an absolute reference Ag spectrum, as explained in ref. [48]. Normalization by inelastic mean free path of the detected electrons (λ) is now explained.

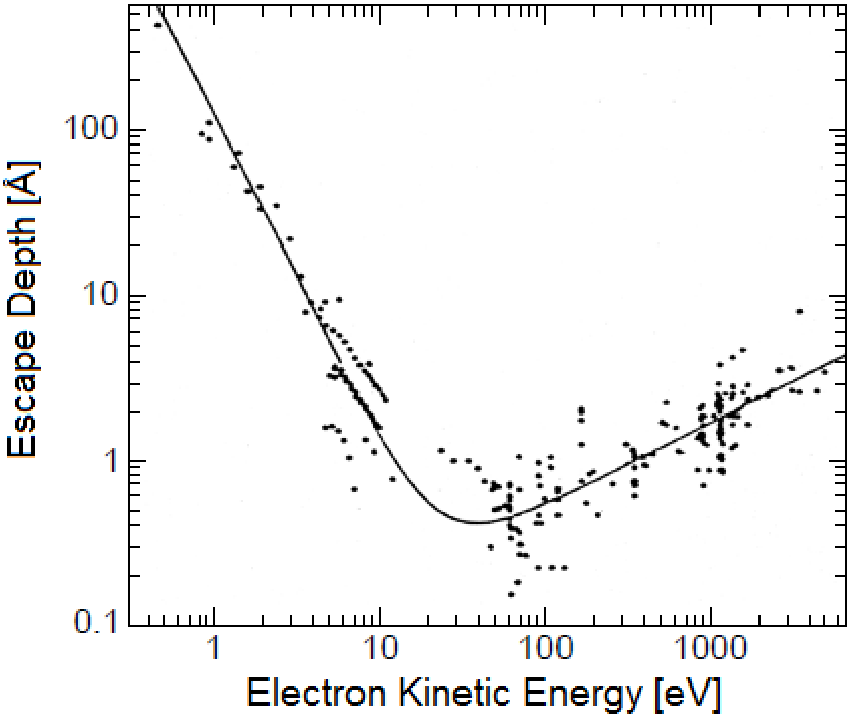

Figure 3.2 Universal curve of the inelastic mean free path of electrons in a solid as a function of electron kinetic energy (adapted from ref. [49]).

The intensity of a PES line is related to the number of photoelectrons that are not inelastically scattered as they exit the sample. The fraction of unscattered electrons shows an exponential decay as a function of path length. The distance λ at which the number of electrons is reduced to 1/e of its original value is referred to as its inelastic mean free path (IMFP). Although the λ is dependent on the material, the relation of the λ and the KE of an electron shows a similar qualitative trend in a large number of solids, expressed by the so-called universal curve, as shown in Fig. 3.2 [49]. The surface-sensitive nature of PES is, thus, linked to the short λ values of the detected photoelectrons. By increasing the employed excitation energies, it is possible to change the information depth (ID) of the measurements. In this dissertation, the ID is considered to be 3λ, a path length at which approximately 95% of electrons are scattered. The employed λ values were calculated by the TPP-2 formula using the Quases-Tourgaard computer code [50,51].

Because the chemical environment of a sample may influence the BE position of a PES line of a given element (i.e., chemical shift), PES can also be used to assess the chemical state of a given element found on the surface of a sample. This phenomenon is predicted by eqn. (3.1). E_i is different for various chemical states of a given element due to changes in electronic configuration (i.e., due to bond formation, redox effects, etc.). E_f is affected by interactions between the core hole and the emitted electron. In this respect, the chemical environment of an atom directly influences the lifetime of the core hole and the partial shielding that the other electrons in the samples will exert on the core hole. Moreover, the natural line width of PES core level lines is directly related to the core hole lifetime, as denoted by the Heisenberg uncertainty principle.

3.1.2 X-ray Excited Auger Electron Spectroscopy

During PES measurements, two types of spectral lines can be detected that are related to different emission processes following x-ray excitation: i) photoemission lines and ii) Auger lines [49]. After the absorption of a photon results in the emission of a photoelectron, a core hole is left behind, which is filled by an outer-level (i.e., lower BE) electron. The energy difference between the electronic states involved in this relaxation step is conserved by the emission of either a photon (i.e., fluorescence) or another electron, referred to as an Auger electron. The dominant relaxation mechanism for relatively shallow core levels is the latter process (i.e., Auger decay). Because the Auger transition depends on the BE of the three involved electronic states, the KE of Auger electrons is independent of the excitation energy. The detection of Auger electrons in PES measurements is referred to as x-ray excited Auger electron spectroscopy (XAES). The nomenclature of XAES lines, in x-ray notation, is: element, the three principal quantum numbers of the electrons participating in the process and a subscript representing the angular momentum, spin quantum number, and their coupling (i.e., Cu $L_3M_{45}M_{45}$). The XAES process for the Cu $L_3M_{45}M_{45}$ transition is depicted in Fig. 3.3.

XAES line shapes are very sensitive to changes in chemical environment because relaxing and/or emitted Auger electrons often originate from valence electrons [i.e., Cu M_{45}(3d) are valence electrons]. Moreover, chemical shift effects also apply to Auger electrons.

The modified Auger parameter (α^*) is a powerful tool to ascertain the chemical environment of a detected element [45,52]. It combines the chemical shift effect of XPS core line and XAES Auger line measurements and is calculated as follows [45,52]:

$$\alpha^* = BE_{PES} + KE_{XAES} \tag{3.6}$$

Because α^* are the sum of PES and XAES lines (in BE and KE, respectively), α^* values are not affected by sample surface charging or band-bending effects. Reference α^* values for different compounds using the most intense XPS and XAES lines of a given element can be found in literature [45,52,53].

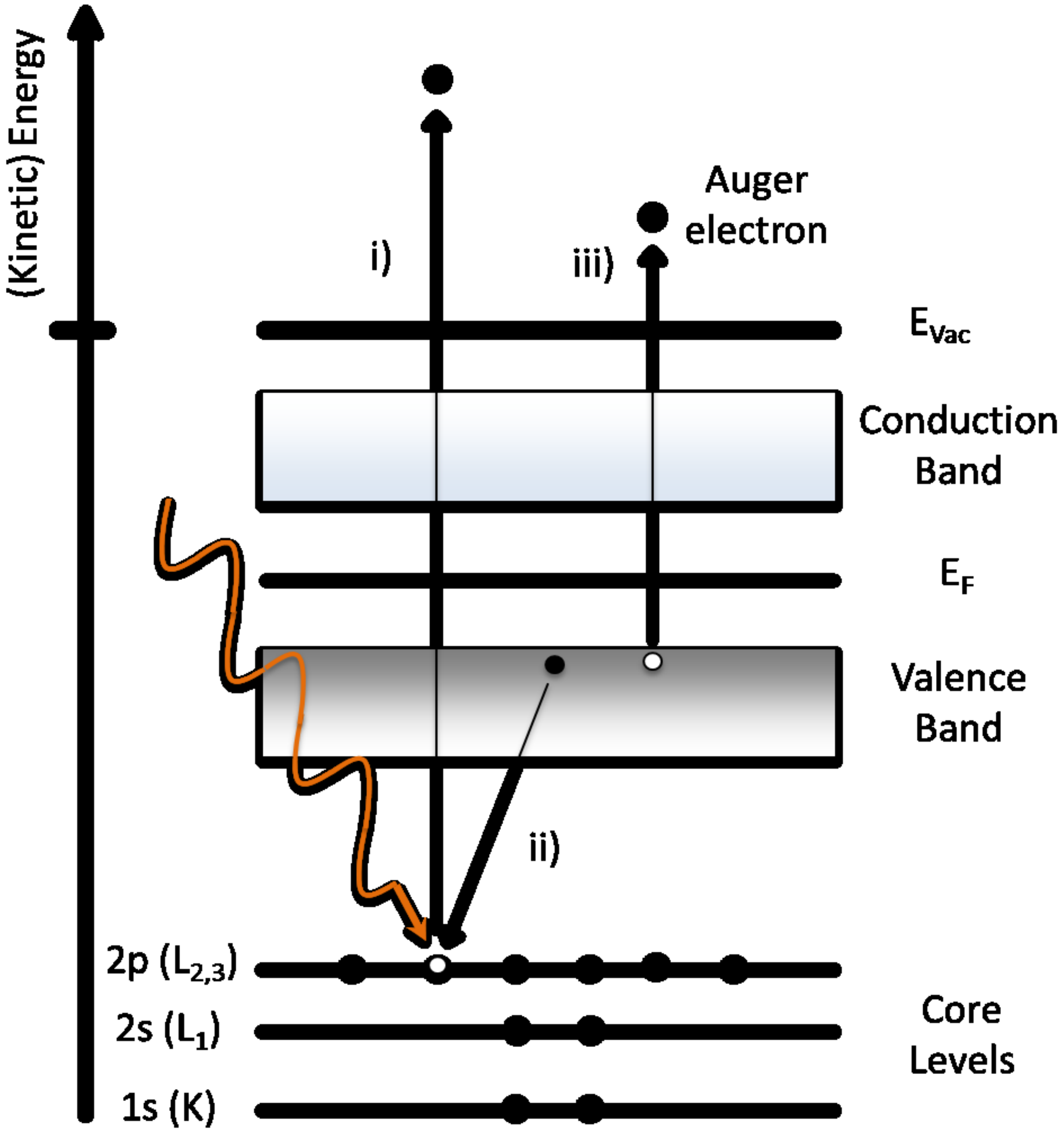

Figure 3.3 Schematic of the three steps involved in the x-ray excited Auger $L_3M_{45}M_{45}$ transition for a copper atom. i) Photoemission of an electron from an $2p_{3/2}$ (L_3) subshell creates a core hole. ii) The core hole is filled by the relaxation of an electron from a 3d (M_{45}) subshell (i.e., a valence electron). iii) The energy difference of the two electronic levels is liberated by the emission of a second 3d (M_{45}) subshell electron (i.e., Auger electron).

3.1.3 Instrumentation

For XPS measurements, Mg K_α and Al K_α (i.e., hν = 1253.6 and 1486.6 eV, respectively) excitations (i.e., generated via high-energy electron bombardment of Mg and Al anodes, respectively) are used for characterization of core levels. These x-ray photons can traverse several hundred nm inside probed materials; therefore, their attenuation can be neglected when considering the ID of XPS measurements. In this work, these excitation energies were generated with a XR50 SPECS twin anode x-ray source. Because the beams are not monochromatized and a minute fraction of the produced photons have energies slightly higher than the characteristic excitation energy, sets of minor peaks are found at lower BEs relative to XPS core level lines (i.e., satellite energy lines) [45]. The intensity and location of these lines are related to the anode material.

For the probing of valence band states, ultraviolet excitation energies (i.e., generated by a gas discharge lamp) are used instead due to higher cross section values and higher resolution. In this work, the He I (i.e., hν = 21.2 eV) excitation is employed for UPS measurements, although photon energies within the 4-150 eV range are suitable [43,52]. The work function, Φ, of a sample can also be determined via UPS, as follows:

$$\Phi = h\nu - (E_{k,F} - E_{k,min}) \qquad (3.7),$$

where $E_{k,min}$ is the KE of the slowest emitted electrons of the sample and $E_{k,F}$ is the KE of the Fermi edge.

The KE of photoelectrons, with respect to the Fermi energy, E_F, is measured via a concentric hemispherical analyzer (CHA) [43,52]. The general configuration of this type of electron analyzer is depicted in Fig. 3.4.

The principal component of a CHA consists of two metal hemispheres (i.e., one shaped concave and the other convex) with coincidental curvature centers. Electrons enter the gap between the hemispheres through an entrance slit, the width of which influences the overall spectral resolution and count rate (i.e., the number of electrons reaching the detector of the CHA) of the measurements. The inner and outer hemispheres are submitted to a positive and negative bias, respectively, a setting permitting only electrons within a narrow energy window

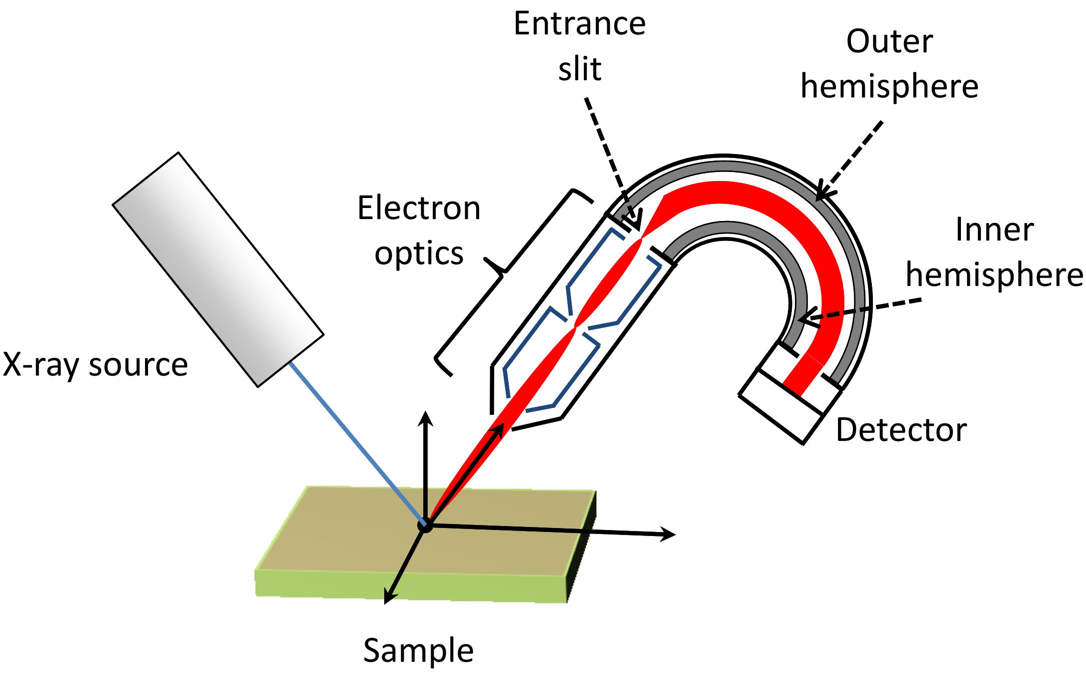

Figure 3.4 Schematic of the PES experimental setup.

(i.e., centered on pass energy, E_{pass}) to exit the hemispheres and reach the multichanneltron detector (MCD). [If electrons passing through the entrance slit are traveling too fast (i.e., high KE), they collide with the outer hemisphere; if they are traveling too slow (i.e., low KE), they become drawn into the inner hemisphere.] Like the entrace slit width, the E_{pass} is a relevant parameter to control the resolution and count rate of a measurement.

The instrumental energy resolution ($\Delta E/E_0$) of a CHA can be expressed as follows [52]:

$$\frac{\Delta E}{E_0} = \frac{s \cdot E_{pass}}{2r} \qquad (3.8),$$

where s is the entrance slit width (in mm) and r is the CHA hemisphere radius.

The CHA used for soft x-ray measurements is a SPECS PHOIBOS 150 MCD (i.e., UPS and XPS, for lab-based measurements; PES at the SALSA endstation in Beamline 8.0.1 at the ALS). For hard x-ray PES (HAXPES) measurements, a VG SCIENTA R4000 electron analyzer is used in Beamline BL15XU at SPring-8 in Hyōgo, Japan.

The energy scale of the lab-based electron analyzer (i.e, for XPS measurements) is calibrated by measuring the Ag $3d_{5/2}$, Au $4f_{7/2}$, and Cu $2p_{3/2}$ PES lines of the corresponding sputter-cleaned metal foils. The measured KE values are then linearly fitted to reference values of these core levels, yielding an energy scale correction (as explained in ref. [52]). The energy scales of PES (HAXPES) measurements at synchrotron facilities are calibrated (so that variations in hν can be accounted for) by measuring the Au 4f and the Fermi edge of an Au reference sample.

3.1.4 Curve Fit Analysis

Curve fit analysis was used to determine the intensity and the number of spectral contributions (i.e., derived by different chemical species) in a measured PES line. This method involves fitting a measured spectrum with a set of theoretical curves to model the acquired data with a calculated spectrum (i.e., the fit line). In the present dissertation, curve fits are carried out using Voigt profiles with a linear background. The Voigt function is widely used in all branches of spectroscopy because it incorporates Gaussian and Lorentzian functions in the lineshape of the curve [54,55]. The Gaussian component simulates peak broadening due to experimental origins (i.e., excitation energy line width and instrumental origins). Broadening arising from the transitional changes involved in the spectroscopic technique (i.e., the uncertainty principle) are described by the Lorentzian component. Because both of these types of functions are symmetric, a convolution of both functions (i.e., the Voigt function) is symmetric; therefore, the maximum point of the Voigt curve is located at the center. The full-width-half-maximum (FWHM) of the Gaussian function contribution is used to indicate the experimental resolution of the measurement.

The curve fit analysis is conducted by iterative fitting by the least-squares method with the Fityk software [56]. The chi-square (χ^2) value, which qualifies the validity of the fit, is related to the square of the fit residuum (i.e., the difference between the measured spectrum minus the fit). Certain constraints are used to attain a meaningful physical interpretation of the curve fits. For example, the spin-orbit splitting ratio is accounted for when fitting spin-orbit doublet peaks, as follows [45]:

$$\frac{I_{nl_{l+s}}}{I_{nl_{l-s}}} = \frac{l+s+\frac{1}{2}}{l+s-\frac{1}{2}} \qquad (3.9),$$

where n is the principal quantum number, l is the angular momentum quantum number, s is the spin ½, and I is the intensity of the respective nlj peak, where j is the total angular momentum quantum number.

The spin-orbit separation energy is used as another fitting constraint. For measurements of a given photoemission line in a sample series using the same excitation energy and electron analyzer settings, spectra are simultaneously fitted, and the FWHM of the curve fit peaks are coupled to the same value. Finally, the number of employed fit peaks are minimized; additional peaks are only used if a physical reason is found (i.e., peak broadening due to the presence of new chemical species).

3.1.5 Inverse Photoemission

As suggested by its name, inverse photoemission spectroscopy (IPES) is the time-reversal of the PES process. Probed samples are targeted with electrons, which fall into unoccupied electronic states in the CB of the sample. The energy difference between the electron energy levels above the vacuum level of the sample and the electronic states filled in the CB is emitted as a photon. The IPES process is depicted in Fig. 3.5.

The cross section for the IPES process (σ_{IPES}) is several orders of magnitude lower than the cross section for the PES process (σ_{PES}). The ratio of these cross sections can be expressed by the following formula [57]:

$$\frac{\sigma_{IPES}}{\sigma_{PES}} = \left(\frac{\lambda_e}{\lambda_p}\right)^2 \qquad (3.10),$$

where λ_e and λ_p are the de-Broglie wavelengths of the electron and photon absorbed in the IPES and PES processes, respectively. For electrons and photons energy of 10 eV, the $\sigma_{IPES}/\sigma_{PES}$ ratio is around 10^{-5} [57]. This less favorable parameter accounts for the greater difficulty and longer measurement times involved in IPES experiments, compared to PES.

In this work, IPES measurements were carried out in the laboratory facilities of the group of Prof. Clemens Heske at the University of Nevada, Las Vegas. The detection of emitted photons is carried out in isochromat mode as a function of the electron kinetic energy (i.e., photons of a specific energy are counted by a narrow band pass detector). The employed photon detector acts similar to a Geiger-Müller counter, using a SrF_2 window as an entrance to a tube containing a high-voltage rod and an Ar:I_2 environment. The SrF_2 entrance window sets the upper energy detection limit to 9.8 eV by preventing the transmission of photons of higher energy into the detector tube [58]. The lower energy limit is the photoionization threshold of molecular iodine (i.e., 9.37 eV [59]), as shown in the following reaction:

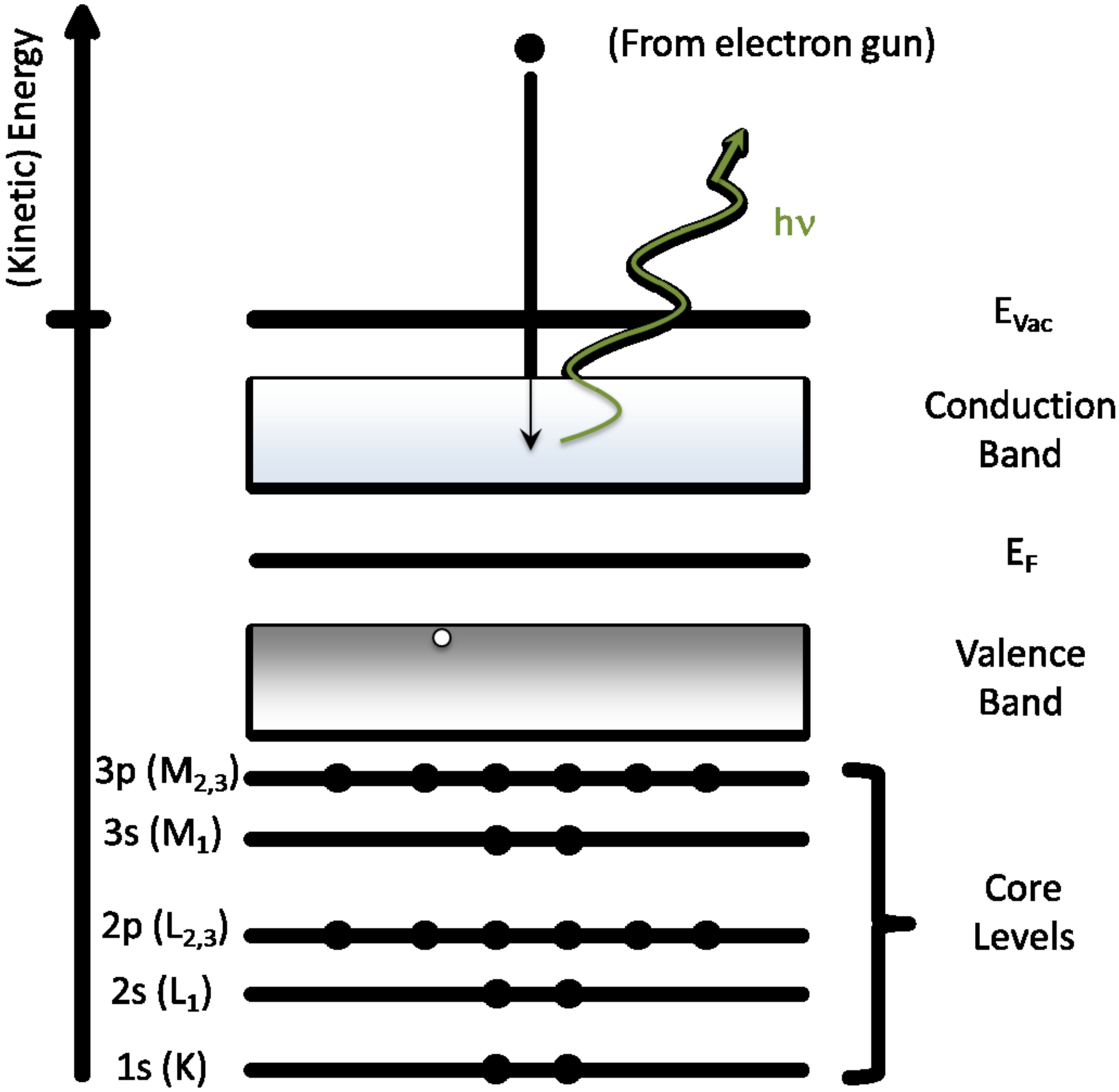

Figure 3.5 Schematic of the inverse photoemission process. A sample is bombarded with electrons, which fall into unoccupied states in the conduction band of the sample. This relaxation step results in the emission of a photon, the energy of which is the difference between the electron energy levels above E_{Vac} of the sample (i.e., the kinetic energy) and the electronic state that is filled in the conduction band. Measurements are carried out in isochromat-mode. (More details are provided in the text.)

$$I_2 + h\nu \rightarrow I_2^- + e^-$$

The kinetic energy of the impinging electron beam, produced by filament thermoionic emission with a low-energy gun (STAIB), is varied from 6-16 eV.

Energy calibration is carried out by measuring the Fermi edge of a sputter-cleaned Au foil. The energy scale of all subsequent spectra are referenced to this measured E_F level. The experimental resolution of the used IPES setup is ~ 0.4 eV.

3.1.6 Combining UPS and IPES

A direct evaluation of the E_g^{surf} of a material can be performed by combining the electronic state probing capabilities of UPS (i.e., occupied DOS profile) and IPES (i.e., unoccupied DOS profile). Based on the universal curve of electron IMFP vs electron KE shown in Fig. 3.2, the ID of both techniques is confined to surface depth of ~ 2-3 nm (i.e., the electron KE range for IPES measurements is 6-16 eV; the KE of photoelectrons derived from the VBM edge is ~ 20 eV [using He I radiation]). The energies of the VBM and CBM are determined by linear approximation of the leading edges of the UPS and IPES spectra, respectively. The use of this linear extrapolation method has been experimentally justified in several works [15,16].

Because the elemental composition of a sample may change at the surface relative to the bulk (as addressed in Sect. 2.3 for chalcopyrite absorbers), the electronic properties of the sample can also exhibit depth variations. Moreover, heterointerface band offsets, which can play a major role in the carrier transport of a thin film solar cell device (as explained in Sect. 2.4), are influenced by the chemistry of the two materials forming the heterointerface. A direct measurement of the surface VBM and CBM of these materials is necessary, not only to assess the electronic properties of the materials, but to better understand the physics of the device.

3.2 Synchrotron-based Spectroscopy

A significant portion of the measurements presented in this work was carried out at synchrotron light sources. These special experimental facilities provide energy-tunable, high-brilliance photon beams that allow to conduct spectroscopic techniques that are not possible under standard laboratory settings. In this section, a brief overview of the infrastructure found in synchrotron light sources is presented. An explanation of the general layout of the specific beamlines used in this work is followed. The physical principles behind the synchrotron-based x-ray spectroscopic technique, along with the pertinent evaluation method, is also covered.

3.2.1 Synchrotron X-ray Sources

Synchrotron light sources consist mainly of a storage ring in which charged particles (i.e., electrons in the case of the light sources used for experimental campaigns for the present work) are kept circulating at near light speeds [60]. In order to propel the charged particles to such relativistic speeds, a particle beam is first formed in a linear accelerator and then shaped into particle bunches that are accelerated in a booster ring prior to insertion into the storage ring. The shaping and acceleration of the beam bunches are achieved by using klystrons as high radio frequency power sources in the booster ring. After insertion in the storage ring, the path of the particle bunches is prevented from colliding with the walls of the storage ring by way of bending magnets.

When a magnet forces the bunches to bend their trajectory, the traveling particles are accelerated toward the center of the bending curve path, resulting in radiation emission. Because the speed of the bunches is close to the speed of light, the Lorentz factor, γ, becomes highly relevant to describe the shape and direction of the synchrotron radiation emission. γ is defined as follows [60]:

$$\gamma \equiv \frac{1}{\sqrt{1-\frac{v^2}{c^2}}} \qquad (3.11),$$

where v is the velocity of the particle and c is the speed of light in vacuum.

A representation of the radiation emissions arising from the path alteration of a charged particle traveling through a constant magnetic field at non-relativistic and relativistic speeds is depicted in Fig. 3.6 (a),(b), respectively [61]. In the relativistic event, the radiation is emitted as a tangential cone, relative to the path of the particle, with an angle $\alpha \cong \frac{1}{2\gamma}$ [60,61].

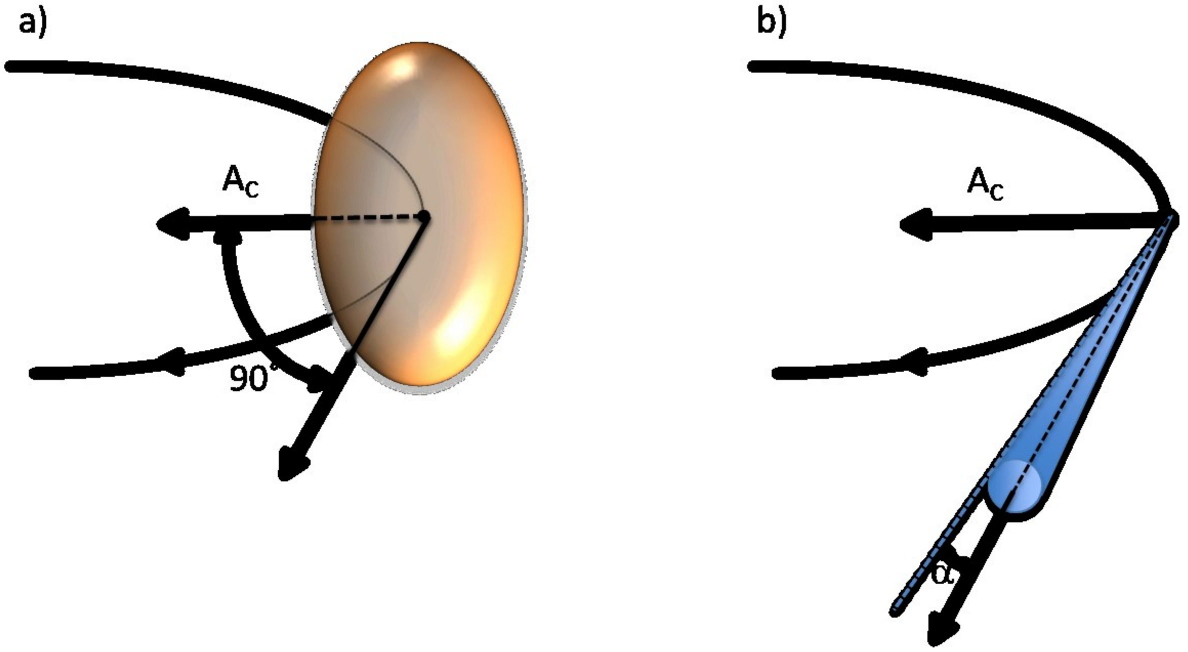

Figure 3.6 Representation of radiation emissions arising from path alterations of an electron traveling through a constant magnetic field at (a) non-relativistic and (b) relativistic speeds (adapted from ref. [61]). A$_C$ is the acceleration that is exerted on the electron towards the center of is modified curved path in these events.

This radiation is directed through beamlines to the experimental endstation. (In order to compensate for energy losses associated with these radiation emissions, the particle bunches are re-energized by klystrons in the storage ring.) The energy spectrum of the synchrotron radiation is very broad, encompassing the whole electromagnetic spectrum [60]. The critical photon energy, E_c, defined as the photon energy that divides the synchrotron radiation emission into two parts of equally radiated power, is related to the magnetic density flux, B_0, of the bending magnet as follows [60]:

$$E_c = \frac{3e\hbar B\gamma^2}{2m} \qquad (3.12),$$

where e and m are the charge and mass of the emitting particles, respectively.

For synchrotron light sources using electrons as charged particles, eqn. (3.12) can be expressed as follows:

$$E_c\,[\text{keV}] = 0.665 \cdot E_r^2\,[\text{GeV}] \cdot B[\text{T}] \qquad (3.13),$$

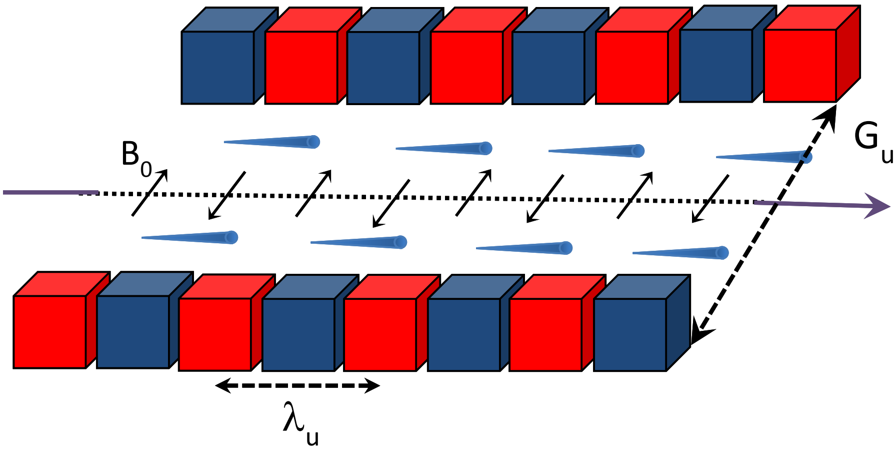

Figure 3.7 Schematic of an insertion device consisting of pairs of permanent magnets with alternating polarity (adapted from ref. [60]). The configuration of the alternating magnetic field densities, B_0 (black arrows), the induced changes in path of the electron bunches (purple), and the direction of the resulting radiation emission (blue cones) is shown. Parameters λ_u and G_u are also indicated.

where E_r is the specific ring energy of the synchrotron light source and the expression $\gamma = E_r/mc^2$ is used. From eqn. (3.13), it is clear that a higher E_r yields a higher E_c. The Advanced Light Source (ALS) in Berkeley and SPring-8 in Hyōgo have storage rings with E_r values of 1.9 GeV and 8 GeV, respectively.

In order to increase the brilliance of the synchrotron radiation (and even to discriminate for photons of a specific energy) reaching the endstation, insertion devices are included in the straight sections of the storage ring. Fig. 3.7 illustrates the working principles of these devices, consisting of stacks of pairs of permanent magnets with alternating polarity. The distance between magnets of the same polarity determines the undulator frequency, λ_u. The distance between two arrays of magnets is referred to as the undulator gap, G_u.

As the particle bunch passes between the magnet arrays of the insertion device, its path becomes affected by the fields, B_0, of the magnet pairs, making the path oscillate by the alternating magnetic configuration. With every oscillation, radiation is emitted, some of which may constructively interfere along the gap of the insertion device and significantly increase the intensity of photons of a specific energy [60].

Whether an insertion device is capable of inducing constructive interference in the synchrotron emission cones is related to the non-dimensional magnetic strength, K, defined as [60]:

$$K \equiv \frac{eB_0\lambda_u}{2\pi mc} = 0.9337 \cdot B_0[T] \cdot \lambda_u[cm] \qquad (3.14)$$

If factor K >>1, the large amplitude of the oscillations mean that radiation emission cones are too spatially distant to interfere with each other. In this case, the insertion device is referred to as a wiggler. Although the emission intensities produced by wigglers are several orders of magnitude higher than the emission intensities produced by a bending magnet, the emissions from both types of devices are similar: a smooth, continuous spectrum over a broad energy range.

If factor K < 1, the radiation emission cones produce a constructive interference that significantly raises the intensity of photons with wavelength, λ_n, and its higher harmonics, as expressed in the following equation [60]:

$$\lambda_n = \frac{\lambda_u}{2n\gamma^2}\left(1 + \frac{K^2}{2} + \alpha^2\gamma^2\right) \qquad (3.15),$$

where the last term (i.e., $\alpha^2\gamma^2$) highlights an angular dependence of the wavelength with α. In this case, the insertion device is referred to as an undulator. Eqn. (3.15) can also be expressed in terms of photon energy, as follows:

$$E_n[keV] = \frac{0.9496 \cdot n \cdot E_r^2[GeV]}{\lambda_u[cm]\left(1 + \frac{K^2}{2} + \alpha^2\gamma^2\right)} \qquad (3.16)$$

To set an undulator to produce constructive interference and, therefore, increased intensity of a specific energy, the magnetic field density, B_0, is varied by changing G_u. The generated synchrotron radiation is guided through a beamline to the experimental endstation. The beamline incorporates optical elements to direct and filter the beam for the desired excitation energy, as well as components to record the intensity of the excitation beam. Specific details of the beamlines used for experimental campaigns pertaining to this work will be now given.

X-ray emission spectroscopy (XES) and PES measurements were conducted on Beamline 8.0.1 at the ALS, Lawrence Berkeley National Laboratory [62]. (The physical principles of XES are discussed in Sect. 3.2.2.) The layout of the beamline is shown in Fig. 3.8. A U5.0 undulator with 89 magnetic pole pairs and a λ_u of 5.0 cm is employed. X-ray photons with an

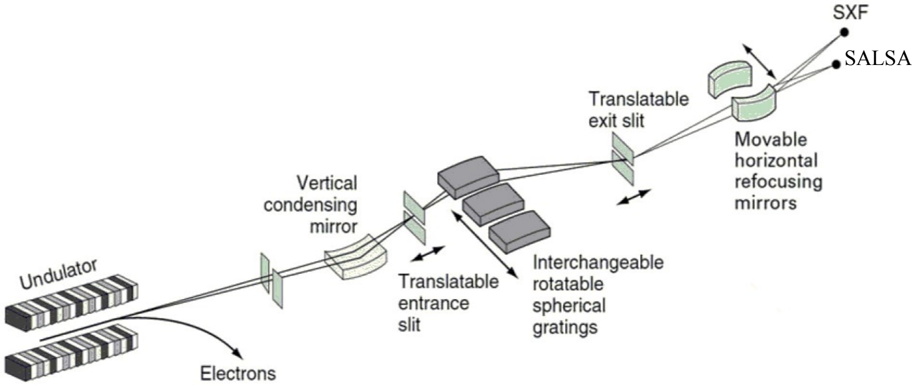

Figure 3.8. Schematic of Beamline 8.0.1 layout at the ALS (taken from ref. [62]).

energy range of 65-1409 eV can be produced by using the first, third and fifth harmonics of the undulator [62]. The beam light is focussed by way of a vertical condensing mirror to the monochromator component of the beamline, which is formed by a translatable entrance slit, a spherical grating monochromator (SGM) and a translatable exit slit. These three parts are arranged to form a Rowland circle geometry. Energy monochromatization in an 80 to 1400 eV range is accomplished by x-ray diffraction with one of the three interchangeable ruled gratings of the SGM (i.e., 150, 380 and 925 lines/mm) [62]. The exiting monochromatized beam then is focussed onto an endstation [i.e., the Soft X-ray Fluorescence (SXF) spectrometer endstation or the Solid and Liquid Spectroscopic Analysis (SALSA) endstation] by using a horizontal refocussing mirror.

XES measurements were conducted using the SXF endstation, a schematic of which is shown in Fig. 3.9. The endstation consists of a UHV (analysis) chamber attached to an x-ray spectrometer (also under UHV conditions). The analysis chamber is equipped with a 4-axis manipulator, onto which the sample is mounted, that facilitates positioning the sample in line with the beamspot. Emission photons pass through an entrance slit located between the analysis chamber and the x-ray spectrometer. The x-ray spectrometer consists of a SGM with 4 interchangeable gratings (for an energy range of 40-1000 eV) and a 2D channel plate detector mounted on a movable table [63,64]. The positions of i) the entrance slit, ii) the SGM and iii) the 2D detector are arranged to form a Rowland geometry. Moreover, the use a 2D detector allows to record a spatially-resolved image of the x-ray emissions. By tilting the channel plate, the width of the energy window of the measurement can be varied. An energy-resolved spectrum is attained by processing the detector image with a user interface software

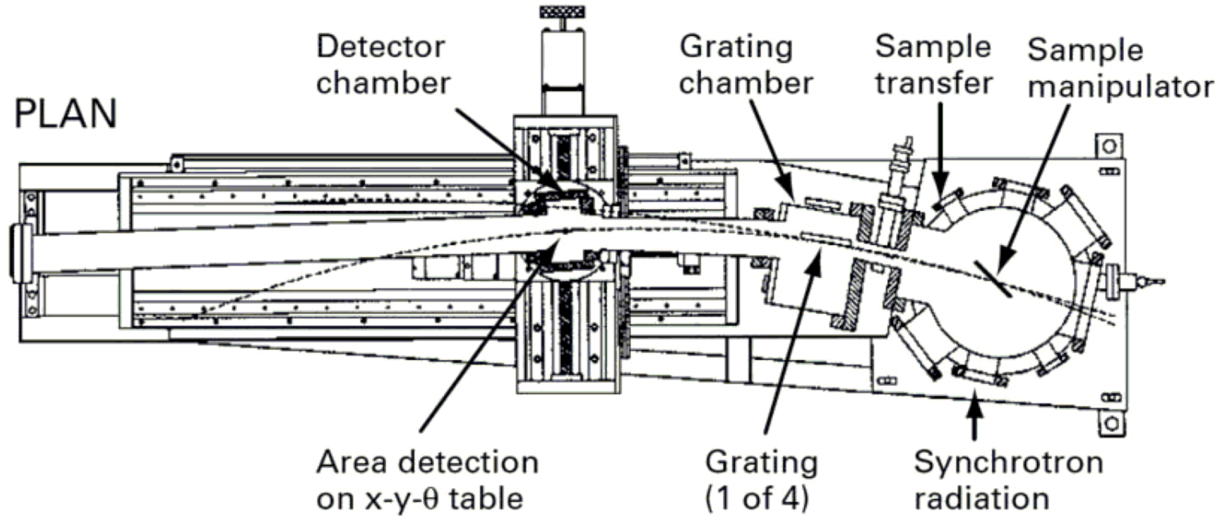

Figure 3.9 Schematic of the experimental setup of the SXF endstation at the ALS Beamline 8.0.1 (taken from ref. [64]).

(ALS sxedaq [65]). More details on this procedure and the energy calibration of the produced emission spectra are discussed in Sect. 3.2.3.

PES measurements were conducted at the SALSA endstation on the same beamline, which is equipped with a SPECS PHOIBOS 150 MCD electron analyzer [66]. Detection of photoelectrons is carried out at normal incidence. The energy scale is calibrated by measuring the Au 4f and the Fermi edge of an Au reference sample.

HAXPES measurements were performed on Beamline BL15XU at SPring-8 in Hyōgo, Japan [67,68]. The layout of this beamline is shown in Fig. 3.10 [67]. A helical undulator with 102 magnetic dipole pairs and a λ_u of 4.4 cm is used in this beamline. A double crystal monochromator (DCM) based on Bragg reflections on a pair of Si (111) or Si (311) crystals is used to monochromatize beam energies on a 2 – 36 keV range. The beam then passes through a channel cut sub-monochromator [i.e., Si(111), Si(200) and Si(311) crystals] in order to obtain highly monochromatic light, which is then focussed onto the endstation by using total reflection mirrors and a toroidal refocussing mirror. The endstation uses a VG SCIENTA R4000 electron analyzer. Detection of photoelectrons is carried out at normal incidence. The energy scale is also calibrated by measuring the Au 4f and the Fermi edge of an Au reference sample.

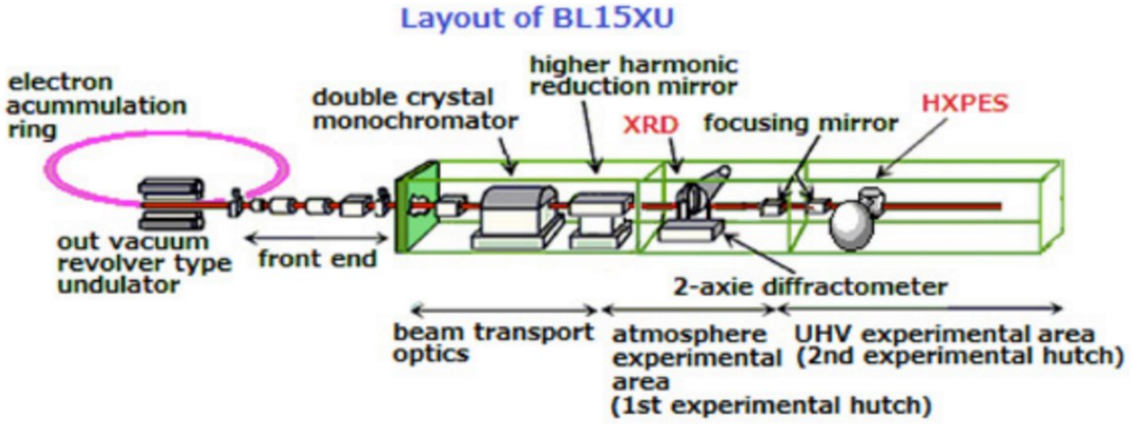

Figure 3.10. Schematic of the experimental setup of the Beamline BL15XU at SPring-8 (taken from ref. [67]).

3.2.2 X-ray Emission Spectroscopy

As mentioned in Sect. 3.1.2, the two competing processes for core hole relaxation are: (i) non-radiant Auger decay and (ii) radiant fluorescence (i.e., photon emission). The Auger decay process has already been explained. In the fluorescence process, the core hole is also filled by an electron from an outer energy level; however, conservation of energy is satisfied by the emission of an x-ray photon with the energy difference between the two involved electronic states (i.e., the core hole and the outer energy level). The intensity, I, of the x-ray emission of energy, $h\nu_{em}$, is governed by the following form of the Fermi's golden rule [similar to eqn. (3.1)][69]:

$$I(h\nu_{em}) \propto \left|\left\langle \psi_i \middle| \hat{H} \middle| \psi_f \right\rangle\right|^2 \delta\left(E_f - E_i - h\nu\right) \qquad (3.17)$$

In eqn. (3.17), it is assumed that the photon absorption and photon emission processes are independent of each other, as the photoelectron becomes a free electron (i.e., it is excited above the E_{Vac} level of the sample) and the fluorescence step depends on the decay of the excited core hole state. Moreover, only outer energy levels that obey the dipole selection rule, $\Delta l = \pm 1$, participate in the relaxation transition. A schematic diagram of this process is shown in Fig. 3.11.

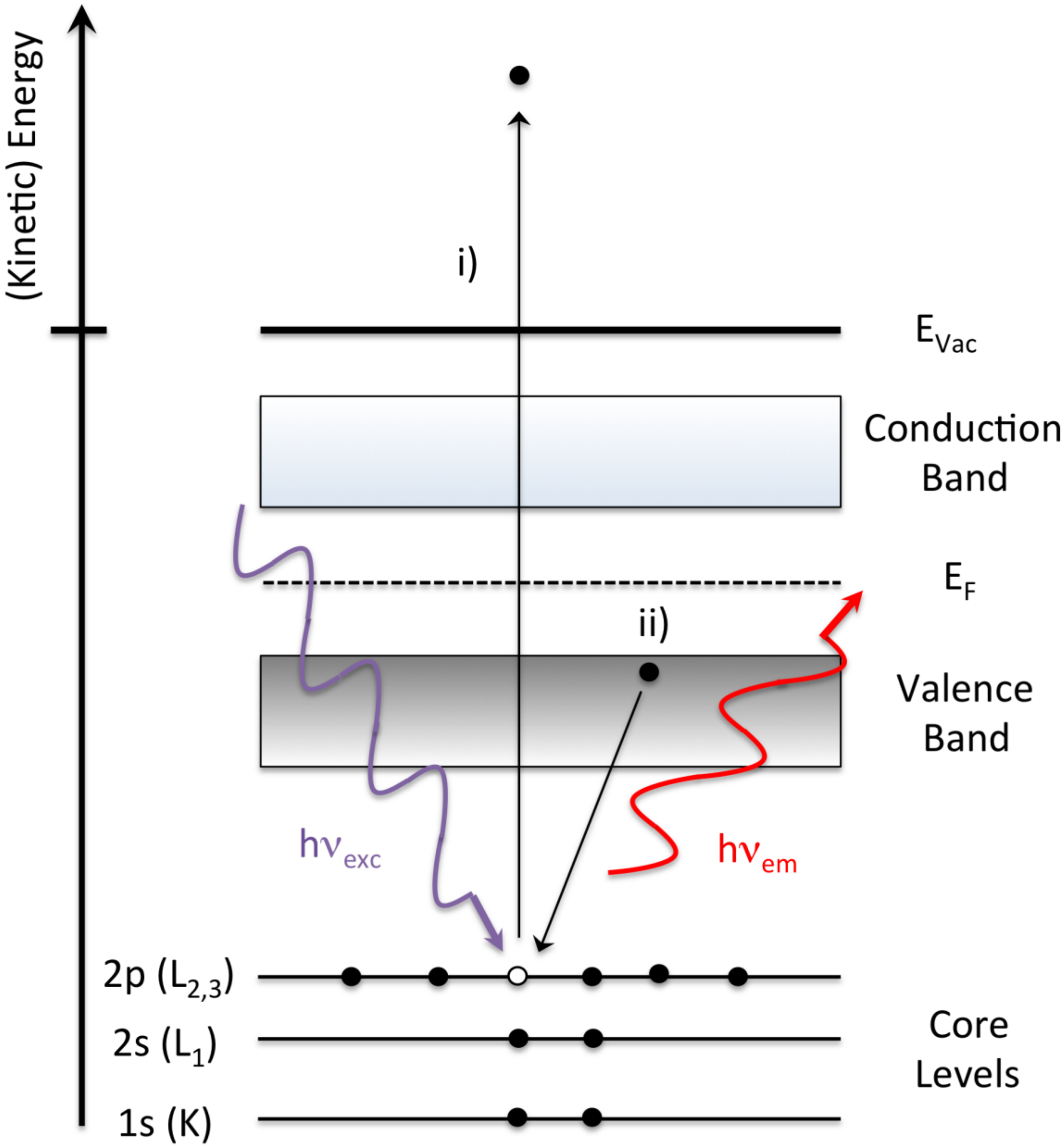

Figure 3.11 Schematic of the two steps involved in the $L_{2,3}$ x-ray emission process. i) Photoemission of an electron from an 2p ($L_{2,3}$) subshell creates a core hole. ii) The core hole is filled by the relaxation of an outer level electron (i.e., in this case, a valence electron), with the energy difference of the two electronic levels emitted as a photon. Step ii) follows the dipole selection rule.

By using an appropriate excitation energy, x-ray emission spectroscopy (XES) measurements can be designed to probe a specific element line edge (i.e., rapid increase in x-ray emission due to energy matching with the excitation of a particular electronic level). An element-specific (partial) picture of the occupied DOS can be attained. (The dipole selection rule restricts the electronic states allowed in the relaxation process to only a subset of all occupied states).

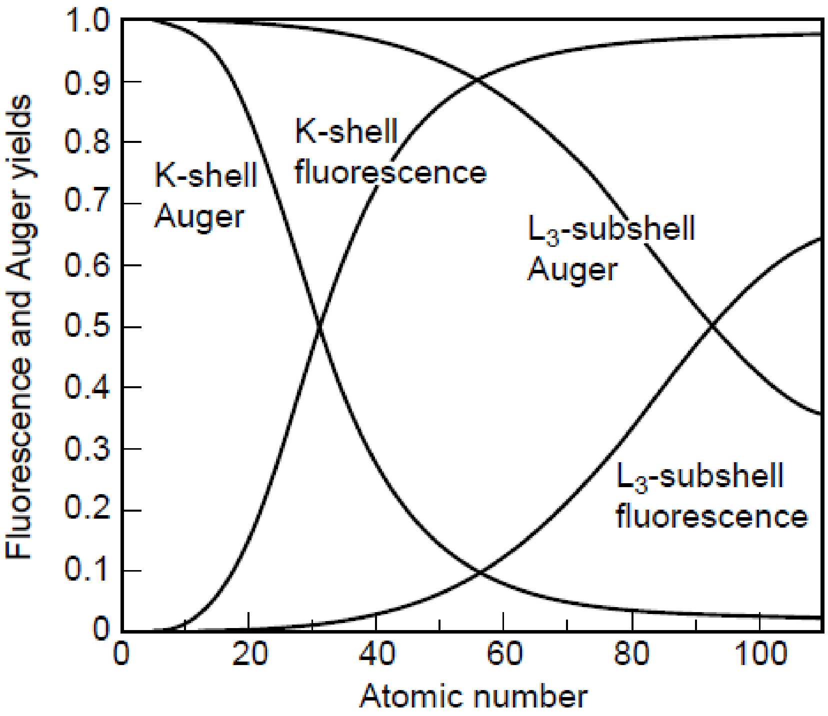

Figure 3.12 Yields of the fluorescence and Auger relaxation processes for K-shell and L_3-subshell core holes (as taken from ref. [60]).

The nomenclature for x-ray emission spectra, in x-ray notation, is: element, the principal quantum number of the excited core level and a subscript representing the angular momentum, spin quantum number, and their coupling (i.e., S $L_{2,3}$).

Like the electrons in photoemission processes, photons become exponentially attenuated while traversing a material so XES intensity is affected by the attenuation of the incoming and outgoing photons (i.e., at the excitation and emission energies, respectively). Databases of the attenuation lengths of x-rays of various energies through different materials can be used to calculate the effective attenuation length of a particular XES line [70]. Compared to PES, the higher effective attenuation lengths of XES measurements allow for a more bulk-sensitive sample characterization.

For decades, the scope of XES experiments was limited by the low fluorescence relaxation yields of light elements. The probability or relative yield of fluorescence, compared to Auger decay, as the core-hole-relaxation mechanism for the K shell and L_3 subshell is shown in Fig. 3.12, as taken from ref. [60]. In elements with a low atomic number, z (i.e., z < ca. 30 for the K shell; z < ca. 90 for the L_3 subshell), Auger decay is the dominant transition. Recent developments on high-brilliance light source facilities and high-sensitivity spectrometers have allowed the implementation of XES experiments to a timescale comparable to other laboratory x-ray-based spectroscopic techniques (i.e., XPS and XAES).

3.2.3 XES Energy Calibration

As mentioned in Sect. 3.2.1, a custom software is used to convert the SXF spatially-resolved detector images into energy-resolved x-ray emission spectra [65]. The program allows to view the effects of changing the parameters of the spectrometer's optical geometry (i.e., detector energy, detector tilt angle, and the angle between the detector normal and the Rowland circle radius) on the shape of the converted spectrum. By using the program on an XES measurement of a reference sample (i.e., a spectrum that exhibits distinct peaks at well-established emission energies throughout the measured energy window), the set of optical parameters can be obtained to correct for the grazing effects of the curved SGM gratings and calibrate the emission energy scale. The obtained parameter set can then be applied to subsequent measurements with the same settings to produce highly reliable spectral conversions and calibrations.

3.2.4 Principal Component Analysis

Principal component analysis (PCA) is a numerical technique that uses single value decomposition to determine the number of independent contributions to a data set [71-73]. When a series of spectra taken at a particular edge are input to the PCA routine, the output is a set of eigenvectors equal to the number of input spectra. PCA requires as input a series of *m* spectra, each having *n* data points. The spectra are placed in an *nxm* matrix, here designated as **A.** This matrix is then decomposed as follows:

$$\overleftrightarrow{A} = \overleftrightarrow{U} \cdot \overleftrightarrow{V} \cdot \overleftrightarrow{W}^t \qquad (3.18),$$

where **U** is an *nxm* matrix of eigenvectors, **V** is diagonal *mxm* matrix of eigenvalues, and $\mathbf{W}^t$ is an *mxm* matrix of scaling coefficients. All of the spectra in the original data set can be expressed as a superposition of the individual eigenvectors. The usefulness of PCA comes from the fact that not all of the eigenvectors are needed to reproduce the spectra if they have any similarities in their compositions. Therefore, by systematically removing each eigenvector from the equation and attempting the reconstruction of the measured spectra, the minimum number of necessary eigenvectors can be determined. This number is equal to the minimum number of individual spectral signatures needed to reproduce the spectra of the measured mixtures, and therefore is equal to the number of individual components in the mixture. Measured spectra of reference samples are tested via target transformation to identify whether they are components of the analyzed data set. A best-fit line (i.e., transformation) from a linear combination of the eigenvectors determined from the PCA reconstructions is carried out. A high quality match between the measured candidate spectrum and its respective transformation confirms it to be a fundamental component of the investigated data set. After identifying all spectral components, a quantification of their individual contributions to the mixture is possible by submitting the data set to a least-squares fitting analysis using the reference spectra.

3.3 X-ray Fluorescence Analysis

High-resolution XES is used to obtain a partial DOS picture of occupied states of a given element in a sample, but another more frequently used analytical technique based on fluorescence is x-ray fluorescence analysis (XRF), by which the bulk elemental composition of materials can be determined based on relative peak intensities. Fluorescence lines with high intensities (relative to the intensities of principal emission lines of a given element) and with emission energies that do not overlap with other lines of elements potentially present in the sample are typically used for XRF analysis. In general, higher excitation and probed emission energies are employed for XRF than for XES, meaning that the higher effective attenuation lengths for XRF measurements yield higher intensity signals. Moreover, the selected emission lines often have natural line widths of several eV (i.e., the natural line width of In K_α, which is used for elemental bulk analysis of CIS substrates in Ch. 6, is ~ 11 eV [74]), indicating lower detector energy resolution requirements for XRF. For these reasons, the experimental set-up needed for XRF runs is much simpler than for XES, allowing XRF to be a laboratory-based spectroscopic technique.

XRF measurements presented in this work were performed on a wavelength-dispersive XRF spectrometer (Rigaku WD-XRF ZSX Primus II [75]) with an end-window-type Rh-target x-ray source. A LiF(200) crystal setup was used for wavelength dispersion of the emitted fluorescent x-ray lines, along with a P10-gas flow proportional counter (PC) and scintillation counter (SC) detector systems. The Cu K$_\alpha$, In K$_\alpha$, S K$_\alpha$ and Se K$_\alpha$ lines of the samples were analyzed.

3.4 Ultraviolet-visible Spectrophotometry

Ultraviolet-visible spectrophotometry (UV-Vis) can be used to determine the optical (bulk) band gap of a semiconductor material by monitoring the absorption of incoming light as a function of photon energy [73]. A rapid rise in light absorption signals the excitation of electrons from the valence band to the conduction band of the material. In UV-Vis runs, absorption is typically linked to the light transmittance, T, (i.e., the fraction of incident light of a given wavelength traversing a sample) of the measurement, as follows [76]:

$$T = e^{-\alpha \cdot x} \qquad (3.19),$$

where α is the absorption coefficient of the sample, and x is the sample thickness.

The E_g of the material is then related to its α through the following equation [76]:

$$\alpha h\nu = C\,(h\nu - E_g)^m \qquad (3.20),$$

where hν is the photon energy, C is a proportionality constant and m is a coefficient that depends on the absorption transition type (i.e., 1/2 for a direct allowed transition and 2 for an indirect allowed transition).

Because of the design (multilayers of different materials) and thickness of the studied absorber substrates, UV-Vis analysis based on transmittance measurements are not a suitable approach for E_g^{bulk} evaluation. Instead, UV-Vis measurements of samples were carried out in reflection mode in this work. Under the Kubelka-Munka model [77], a reflectance transformation, $F(R_\infty)$, can be computed that is proportional to $\alpha h\nu$ in a sample sufficiently thick so that neither the sample thickness nor the sample holder influence the reflectance measurement (i.e., “infinitely” thick sample), as follows:

$$F(R_\infty) \equiv \frac{(1-R_\infty)^2}{R_\infty} \qquad (3.21),$$

where R_∞ is the reflectance of the “infinitely” thick material.

By substituting $\alpha h\nu$ in eqn. (3.20) with $F(R_\infty)$ of eqn. (3.21) for a direct allowed transition, the following equation is reached:

$$[F(R_\infty)\cdot h\nu]^2 = C_2(h\nu - E_g) \qquad (3.22),$$

where C_2 is also a proportionality constant.

Assessment of the optical E_g was carried out by linear extrapolation of the leading edge of the transformed $[F(R_\infty)\cdot h\nu]^2$ vs photon energy, $h\nu$, plots [i.e., the $h\nu$ at which $[F(R_\infty)\cdot h\nu]^2$ becomes zero].

Reflectance spectra were measured on a Perkin-Elmer Lambda 950 UV/Vis/NIR spectrophotometer [78]. Tungsten-halogen and deuterium lamps were used as excitation sources. The UV-Vis portions of the spectra were detected via a photomultiplier. The near-infrared (NIR) portions of the spectra were recorded through a Peltier-cooled PbS detector setup.

3.5 Sample Treatment

In this section, an overview of the different types of surface treatments (modifications) performed in this dissertation is presented.

3.5.1 Wet Chemical Treatments

As mentioned in Sect. 2.3, a couple of wet chemical treatments are employed in this work to form the investigated buffer/absorber heterointerface: i) KCN etching of CIS absorbers and ii) chemical bath deposition (CBD) of the buffer.

For removal of Cu_xS capping surface phases of CIS absorbers, substrates were etched for 3 min in a 1.5 M aqueous KCN solution, followed by extensive washing of the etched substrates with deionized water to remove KCN traces.

For deposition of CdS layers, samples were introduced into a chemical bath consisting of standard solutions of Cd-acetate [0.0013 M], ammonia [1 M] and thiourea [0.12 M] at 60 °C

[33]. To vary the thickness of the deposited CdS layers, CBD times ranged from 0.5 – 7.0 min.

Samples described in Ch. 8 are treated with millimolar concentration solutions (i.e., 1, 5, 10 and 20 mM) of selected benzoic acid derivative and alkanethiol self-assembled monolayers (SAM) using acetonitrile and ethanol as solvents, respectively. Treatment of samples in SAM solutions lasted 12 hours and were carried out inside a N_2-filled glovebox directly attached to the surface analysis system.

3.5.2 Ion Treatment

As a final preparation step for the measurement of sample surfaces, low energy ion treatments were conducted to remove surface contaminants. A high-purity inert gas (i.e., Ar, >99.999 %) was used to produce an ion beam targeting the surface sample, in order to prevent reactions between the impinging ions and the sample. The ion treatments produce an exchange of energy and momentum between the colliding ions and the atoms of the sample´s surface, inducing collision cascades in the sample. When recoils of the collision cascades reach the surface of the sample with energies greater than the energy binding the surface atoms (adatoms) to the material, atoms (adatoms) are ejected from the sample (i.e., sputtered) [79]. The kinetic energy of ion treatments conducted on absorber substrates was confined to a 50-250 eV range in order to maintain the ion beam energy exchange below the sputter energy threshold [49] and prevent damage of the sample. Higher ion kinetic energies were allowed for the cleaning of metal foils. Ion treatments were conducted with either a Vacuum Generator Ex05 or Nonsequitur Technologies 1402 ion source [80,81].

3.5.3 Rapid Thermal Processing

The RTP-chamber setup for the sulfurization step of CIS precursors (see Sect. 2.3) and the selenization of CIS substrates for sample tailoring purposes (see Ch. 6) is illustrated in Fig. 3.13. These reactions are carried out inside a cylinder consisting of a graphite ring, sealed by two quartz membranes. (This assembly is referred to as a graphite box.) The graphite box is supported by a quartz table (not shown in the diagram), which is fastened to the chamber walls. A port in the graphite box is opened/closed by a motor valve for pumping/venting purposes. Two sets of lamps are positioned at the top and bottom of the graphite box, which act as heating sources. According to ref. [82], the heating rate of the lamps can be set up to 8.6 K/s, as measured by thermocouples placed 1 mm away from the lamps. The temperature of the treated samples can be monitored by another thermocouple inside the graphite box. The baseline pressure of the RTP-chamber (graphite box with an open port) is lower than 10^{-3} mbar. The pressure inside the graphite box during RTP treatments is estimated to range from 10^{-3} - ~ 10 mbar. An exact pressure quantification cannot be made because the graphite box is not perfectly hermetic.

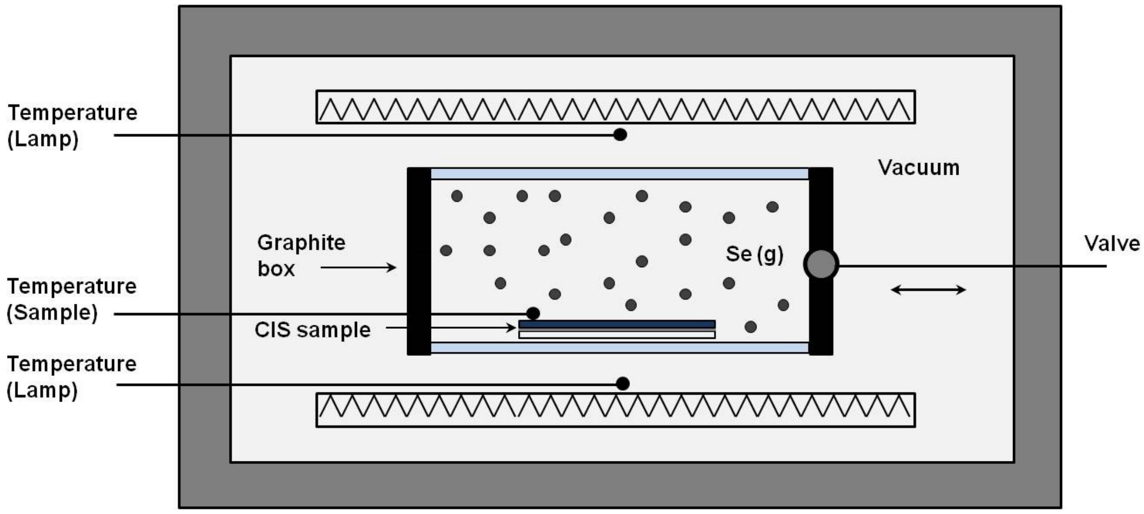

Figure 3.13 Schematic of the RTP-chamber used for the selenization experiments of CIS substrates in Ch. 6, adapted from [82].

4 Characterization of CdS/Cu(In,Ga)Se_2 and ZnS/Cu(In,Ga)Se_2 Heterointerfaces

4.1 Introduction

Solar cells based on Cu(In,Ga)Se_2 (or CIGSe) absorbers have already surpassed the 20%-efficiency milestone on laboratory scale [7,10] and 15.7 % for large area modules [5]. As was explained in Ch. 2, this type of thin film solar cell is commonly stacked in the following p-n junction device configuration (from top to bottom): n-type ZnO window layer/buffer layer/p-type chalcopyrite absorber/Mo covered soda-lime glass (SLG) back contacts [20,21]. Until recently, the highest performing CIGSe solar cells are generally attained with a CdS buffer layer. Using a material more transparent than CdS as a buffer layer, such as ZnS, should increase the efficiency of chalcopyrite-based devices by increasing the light that reaches the absorber film. However, efforts to improve device efficiencies through this approach had proven unsuccessful. This indicates that, in the case of CIGSe-based solar devices, the CdS buffer layer and/or the buffer deposition process play an important role in the formation of a suitable buffer/absorber heterointerface.

In order to push CIGSe solar cell efficiencies towards their theoretical maximum, a better understanding of the chemical and electronic structures of junctions formed between different buffer layers and absorber materials and, subsequently, the correlation to their respective device properties is necessary. Knowledge gained through such investigations can open new routes for optimization of chalcopyrite-based solar cell devices. For this reason, the chemical and electronic properties of high-perfomance CdS- and ZnS/CIGSe heterointerfaces are here presented.

4.2 Experimental Details

The sample sets were produced in a ZSW high-efficiency, small-area solar cell production line [29]. The CIGSe absorbers were synthesized by co-evaporation of Cu, In, Ga and Se on Mo-covered SLG back contacts. Deposition of the CdS and ZnS buffer layers was carried out by CBD, as mentioned in Sect. 2.3. (The specific details of the chemical bath protocol used in the ZSW production line can be found in ref. [29].) By varying the duration of the chemical bath, sample series of CIGSe absorbers with varying buffer thicknesses were produced. For the CdS/CIGSe sample series, the CBD-treatment times were varied between 0 and 10 minutes. For the ZnS/CIGSe sample series, they were varied between 0 and 15 minutes. The samples were shipped to the HZB after being sealed in an inert atmosphere in order to minimize exposure to air. Upon arrival at the HZB, they were stored in an ultra-high vacuum (UHV) chamber until their characterization via the surface-sensitive XPS and XAES techniques. Similar sample packing precautions were employed for the transport of samples outside the HZB (i.e., for IPES measurements in the laboratory facilities of the group of Prof. Clemens Heske at the University of Nevada, Las Vegas). Prior to bulk-sensitive XES characterization at the ALS, samples were briefly exposed to air while being introduced into the UHV beamline.

The surface-sensitive XPS and XAES characterizations of the CdS/CIGSe and ZnS/CIGSe sample series were mostly carried out at the HZB employing a SPECS PHOIBOS 150MCD electron analyzer using Mg and Al K_α excitation energies. Further PES measurements were conducted at the ALS Beamline 8.0.1 using the SALSA endstation [66] and the SPring-8 BL15XU beamline [67,68]. This combination of experimental techniques allowed for the use of a 150 – 5950 eV excitation energy range in PES measurements. For XES characterization, experiments were performed at ALS Beamline 8.0.1 using the Soft X-ray Fluorescence (SXF) endstation [62-64]. Cd $M_{4,5}$ and In $M_{4,5}$ XES measurements were performed on the CdS/CIGSe sample series using a 500-eV excitation energy. Zn $L_{2,3}^{III}$ and In $M_{4,5}$ XES measurements were carried out on the ZnS/CIGSe samples series using a 550-eV excitation energy. The Se $M_{2,3}$/S $L_{2,3}$ XES spectra were measured with a 200-eV excitation energy. All excitation energies were chosen to avoid resonant excitation effects.

UPS measurements were conducted with a He discharge lamp using the He I excitation source. The inverse photoemission spectroscopy (IPES) experiments were carried out with a low energy STAIB electron gun and a Geiger-Müller-like photon detector with an SrF_2 window and an $Ar:I_2$ gas [57-59]. To remove adsorbates from sample surfaces, the investigated sample series were submitted to mild Ar^+ ion treatment (kinetic energy upto 250 eV) for short time periods (of 30 min cycles).

4.3 Cu(In,Ga)Se_2 Absorber

In the following section, the characterization of the chemical and electronic structure of the CIGSe absorber will be presented. This starting point will serve as an appropriate foundation for subsequent heterointerface characterizations, in Sections 4.4 and 4.5, based on this absorber. First, attention is given to surface-sensitive PES experimental results. Then, direct measurements of the surface band gap of the CIGSe absorber are presented and discussed.

4.3.1 Surface Chemical Structure

Fig. 4.1 shows the XPS survey spectra of all samples in the CBD-CdS series, along with respective peak identification. (Although for now only the CIGSe absorber will be considered.) The XPS survey spectrum of the bare CIGSe absorber displays the photoemission lines of the signature absorber elements (i.e., Cu, In, Ga, and Se). Na-related lines can also be observed, which are attributed to Na-diffusion from the SLG back contact to the front surface of the CIGSe absorber, a well-reported phenomenon [20,21]. The elemental surface composition of the absorber was quantified by evaluating the intensity of the Cu $2p_{3/2}$, In $3d_{3/2}$ (the In $3d_{3/2}$ peak was preferred over the In $3d_{5/2}$ peak in order to avoid the overlapping of Mg $K_{\alpha 3,4}$ excitation satellites with the In $3d_{5/2}$ peak), Ga $2p_{3/2}$, and Se $3d_{5/2}$ core level peaks, as determined by the curve fit analysis of the spectra. (These spectra are shown, with the curve fits, in Fig. 4.6, along with spectra of the rest of the samples in the CBD-CdS series.) The peak intensities of the XPS core levels were normalized to account for differences in inelastic mean free path (λ) [50,51], photoionization cross section (σ) [46,47], and the transmission function of the electron analyzer (T) [48].

The detected surface composition of the absorber is Cu:(In+Ga):Se = 0.10:0.30:0.60, close to the 1:3:5 stoichiometry reported for other high-efficiency CIGSe absorber surfaces [20,28,83]. Moreover, including the surface Na content in the evaluation yields a (Cu+Na):(In+Ga):Se = 0.18:0.27:0.55, close to a 1:1:2 stoichiometry. These findings indicate that the absorber surface is Cu-poor and suggest that the diffused Na may fill surface Cu-vacancies [27,28]. Because the Cu and Na surface contents are comparable (i.e., 0.10 and 0.08, respectively), the formation of surface Na-Cu-In-Ga-Se phases, such as $Na_2Cu_2(In+Ga)_5Se_{11}$, cannot be excluded [28,84,85]. The effect of the surface Cu-depletion on the surface band gap (E_g) of the CIGSe absorber will be discussed in Sect. 4.3.3.

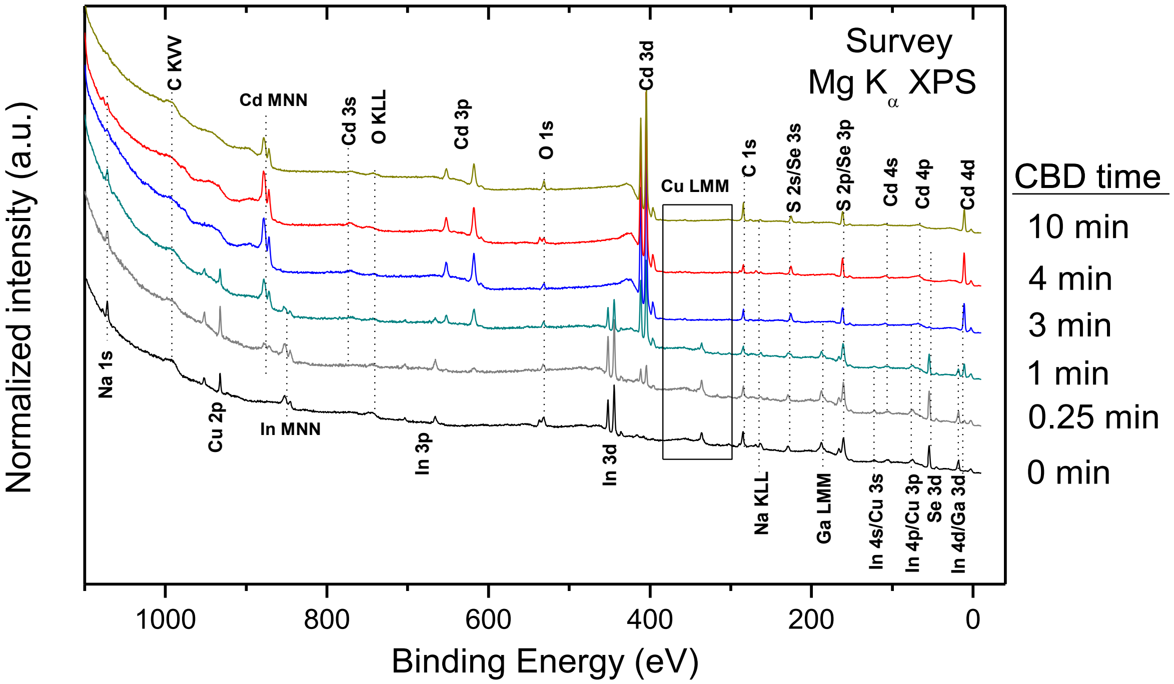

Figure 4.1 XPS survey spectra of the CdS/CIGSe sample series prepared with different CBD times. Vertical offsets are added for clarity.

Another potential surface feature is noticed after calculating the [Ga]/[In+Ga] ratio of the absorber using pairs of Ga and In core level peaks with different information depths. [As explained in Sect. 3.1.1, we define the information depth (ID) as the depth from which virtually all (~ 95%) of detected photoelectrons originate, equivalent to 3λ.] The [Ga]/[In+Ga] ratio calculated with the Ga $2p_{3/2}$ and In $3d_{3/2}$ line pairs (the IDs of the Ga $2p_{3/2}$ and In $3d_{3/2}$ lines are 2 ± 1 and 3 ± 1 nm), and with the Ga $3d_{5/2}$ and In $4d_{5/2}$ line pairs (the IDs of the Ga $3d_{5/2}$ and In $4d_{5/2}$ lines are both 7 ± 1 nm) are 0.25 ± 0.05 and 0.42 ± 0.03, respectively. The lower [Ga]/[In+Ga] ratio found for the line pair with the smaller ID suggests a depth-dependent Ga grading near the surface of the CIGSe absorber. This topic is addressed in the following subsection.

4.3.2 In and Ga Depth-Profile Analysis

Photoelectron spectroscopy (PES) measurements were carried out on the CIGSe absorber at different excitation energies as a means to control the ID, which is governed by the kinetic energy of the photoelectron. The excitation energies ranged from 150 – 5950 eV. Calculating the λ of CIGSe for the selected excitation energies leads to an effective probing ID range between 1.7 – 24.4 nm for the set of conducted experiments [50,51]. The In 4d/Ga 3d region was measured with the selected excitation energies. Because of the energetic proximity of the

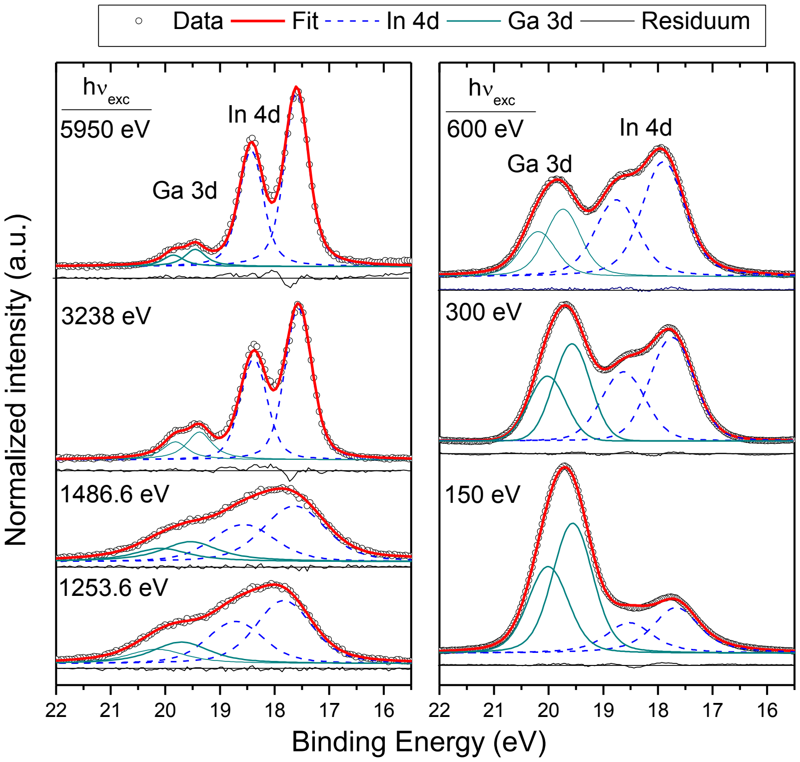

Figure 4.2 (a) and (b) PES detail spectra of the In 4d/Ga 3d region of the CIGSe sample, including fits, as measured with various excitation energies. Vertical offsets are added for clarity.

In 4d/Ga 3d peaks, signal changes associated with differences of λ and of the electron analyzer's transmission function for a given excitation energy are negligible. This arrangement considerably simplifies the analysis because the PES core level intensities need to be only normalized by their respective photoionization cross section [46,47].

Fig. 4.2 (a) and (b) show the results of this curve fit analysis. Spectra measured with 1253.6 and 1486.6 eV excitation energies are significantly broader than the others, ascribed mainly to larger x-ray line widths resulting from the non-monochromatized lab-based excitation source. As explained in Sect. 3.1.4, each of the measured In 4d/Ga 3d spectra was fitted using Voigt profile functions along with linear backgrounds, the peaks of a given spin-orbit doublet were constrained to share the same FWHM, and the intensity ratio of the peaks in a doublet were set to obey the $2j+1$ multiplicity rule [i.e., eqn. (3.9)]. The relative increase of the Ga 3d signal with lower excitation energies does not necessarily mean a Ga-enrichment in the region nearest the absorber surface: the relative intensities of the In 4d and Ga 3d lines in Fig. 4.2 are greatly affected by changes of σ as a function of excitation energy. Photoionization of Ga 3d electrons is favored over In 4d electrons with lower energies of the selected excitation range

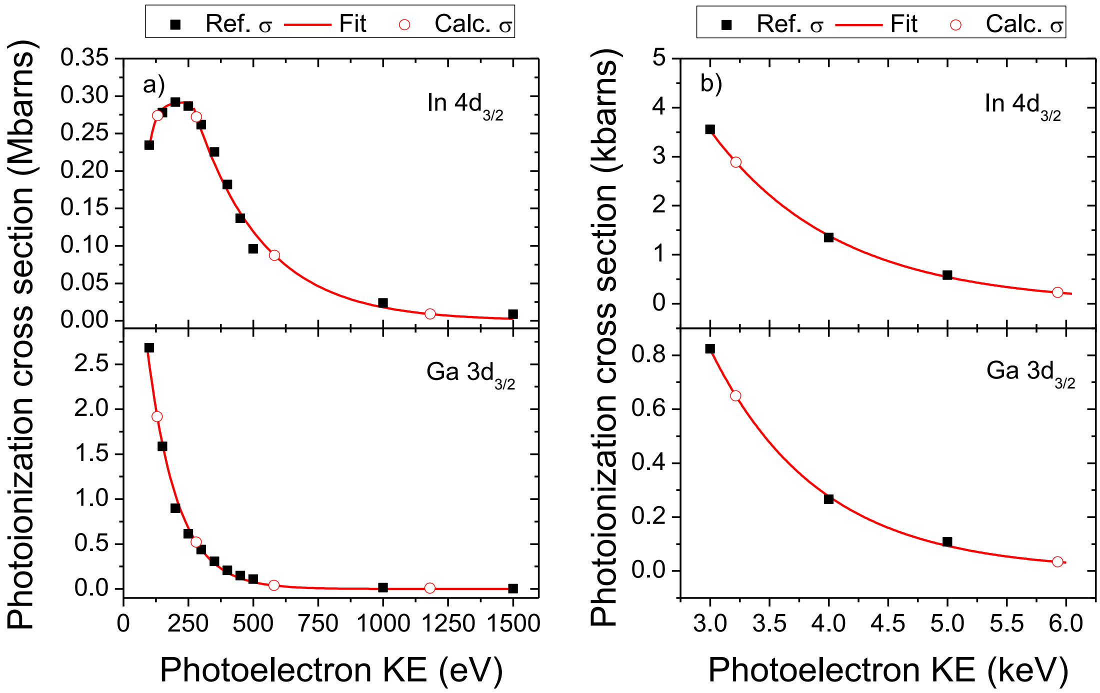

Figure 4.3 Theoretical photoionization cross sections of the In $4d_{3/2}$ and Ga $3d_{3/2}$ core levels at (a) 100-1500 eV and (b) 3-6 keV photoelectron kinetic energy ranges, respectively.

[47,86,87]. {The as-measured (i.e., unnormalized) [Ga]/[In+Ga] ratio is shown in Fig. 4.4.} This effect will be discussed in more detail shortly.

In order to calculate the depth-resolved [Ga]/[In+Ga] ratio, the photoionization cross sections of the In $4d_{3/2}$ ($\sigma_{\text{In 4d}}$) and Ga $3d_{3/2}$ ($\sigma_{\text{Ga 3d}}$) core levels were obtained for the used excitation energies (e.g., as a function of the resulting photoelectron kinetic energy), as described in ref. [47]. Included in the necessary photoionization σ values is a correction for the angular distribution of the emitted photoelectrons, which is dependent on the measurement geometry due to the polarization of the x-ray (more details are presented in ref. [47]), the following angular parameters were introduced in eqn. (3) of ref. [47]: α:0°, θ:90°, ϕ:180°, for the ALS-based measurements (i.e., 150-600 eV excitation energy range); α:0°, θ:0°, ϕ:90°, for the SPring-8-based measurements (i.e., 3238 and 5950 eV excitation energies). Fig. 4.3 (a) and (b) show reference σ (i.e., Ref. σ, black filled squares) for In $4d_{3/2}$ and Ga $3d_{3/2}$ as a function of photoelectron kinetic energy. The σ values show an exponential decay as a function of photoionization energy, with the exception of $\sigma_{\text{In 4d}}$ in the 100 – 250 eV range. This shift in σ trend is ascribed to a Cooper minimum (i.e., a σ minimum for particular orbitals [86]), a quantum effect, which for $\sigma_{\text{In 4d}}$ occurs around 130 eV [87]. The Ga 3d to In 4d signal ratio has been reported to be at its maximum (i.e., $\sigma_{\mathrm{Ga\ 3d}}/\sigma_{\mathrm{In\ 4d}} \sim 14$, in free elemental conditions) at approximately this energy [87]; however, in solids the drop in σ value due to Cooper minima are in general reported to be less pronounced [86]. The reference σ values (i.e., Ref. σ, black filled squares) were fitted as an exponential function of excitation energy (red line), allowing for the interpolation (extrapolation for the photoelectrons with the highest kinetic energy) of the σ values at the excitation energies of interest (i.e., Calc. σ, red hollowed circles).

Fig. 4.4 (a) shows the [Ga]/[In+Ga] ratio profiling analysis as a function of ID normalized to respective σ values (black squares). [The as-measured (i.e., unnormalized) [Ga]/[In + Ga] intensity ratio is also shown (red hollow circles)]. The reported average XRF-probed bulk [Ga]/[In+Ga] composition of absorbers produced by the same ZSW production line (e.g., 0.30 – 0.35) is also displayed as the gray-shaded area [29]. The [Ga]/[In+Ga] value ascertained for the deepest profiling ID is slightly above the reported bulk value, but it changes as the ID decreases. This fluctuation is consistent with the compositional grading design of the CIGSe absorber, aiming at accumulating a higher Ga content at the front (as observed for IDs between 7 – 15 nm) and back of the absorber [29]. Probed IDs lower than 5 nm (i.e., hν = 600 eV) show a continuous drop in the assessed [Ga]/[In+Ga] composition, which could be interpreted as a strong In-enrichment in the region nearest the absorber surface. A comparison of all the unnormalized and normalized [Ga]/[In+Ga] ratios in Fig. 4.4 reveals that the σ-correction yields a drastic trend inversion, especially at shorter IDs. This strong impact on the [Ga]/[In+Ga] ratio profiling analysis may raise concerns about the validity of the employed σ's. However, in order for the lowest obtained [Ga]/[In+Ga] ratio (i.e., from the spectrum of the 150 eV excitation energy) to equal the lower bound of the of the XRF-probed bulk average (i.e., 0.30), the calculated $\sigma_{\mathrm{In\ 4d}}$ would have to be greater by a factor of 1.43 ($\sigma_{\mathrm{In\ 4d}} \sim$ 0.4 Mbarns). For this to be so, no drop at all should be observed in the $\sigma_{\mathrm{In\ 4d}}$ values of the lower excitation energy range (i.e., nearly complete absence of the Cooper minimum).

Furthermore, results of the chemical structure of absorber samples treated to represent the early stages of the CdS/CIGSe and ZnS/CIGSe heterointerface formations (considered in greater detail in Sections 4.4.5 and 4.5.5, respectively) favor a Ga-depleted surface scenario. Similar In-rich surfaces can be expected of high-performing CIGSe absorbers from other production lines, which employ In-termination steps at the end of their absorber growth process [83,88].

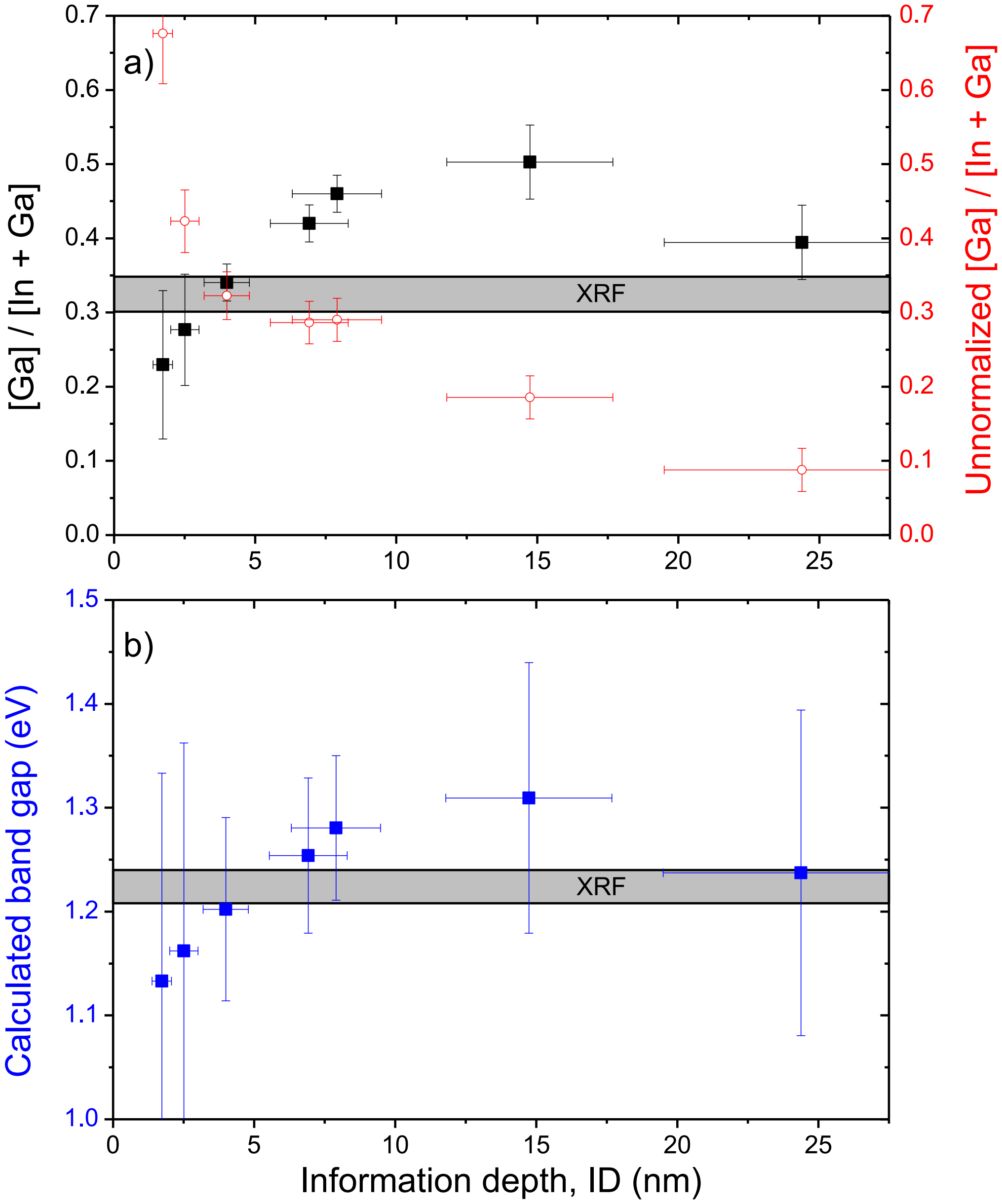

Figure 4.4 (a) Depth-resolved [Ga]/[In+Ga] ratio as a function of probing information depth (ID). The unnormalized [Ga]/[In+Ga] values were not corrected by respective photoionization cross sections, computed and illustrated in Fig. 4.3. (b) Calculated bulk E_g values expected for the [Ga]/[In+Ga] ratios in (a), as computed from ref. [9].

Fig. 4.4 (b) shows theoretical E_g^{bulk} values expected for the [Ga]/[In+Ga] ratios in Fig. 4.4 (a), as computed from ref. [9]. The use of similar calculations to indirectly determine band alignment offsets in heterointerfaces, which many times entail assumptions that cannot be corroborated, is often encountered in literature. (For example, for the E_g calculations in Fig. 4.4 (b), it needs to be assumed that the absorber has uniform Cu and Se contents throughout the investigated depth; a conjecture that is dismissed by the detected Cu-poor surface.) This in turn can lead to erroneous assessments. Based solely on Fig. 4.4 (b), it could be wrongfully concluded that there is a reduction in E_g at the surface of the absorber compared to the bulk due to the detected surface Ga-depletion. These calculated E_g values will, however, serve as a point of comparison for the directly measured E_g^{surf} of the absorber, considered in the next subsection.

4.3.3 Surface Electronic Structure

The E_g^{surf} of the CIGSe absorber is directly determined by combining UPS and IPES: UPS and IPES are employed to determine the positions of the VBM and CBM, respectively, as discussed in Sect. 3.1.6.

Due to the surface sensitivity of the spectroscopic techniques used in this study, removal of adsorbed carbon- and oxygen-containing surface species is imperative when measuring the E_g^{surf} of samples. The samples were first immersed for 1 min in aqueous ammonia (~1M) solution at room temperature, then rinsed with deionized water. This wet chemical cleaning treatment was carried out inside a dry-N_2 glove box directly attached to the surface characterization system. Inside the UHV chamber, they were submitted to low-energy Ar^+ ion treatments to desorb remaining surface contaminants.

In Fig. 4.5, the UPS and IPES spectra of the bare CIGSe are shown in the course of two steps of Ar^+ ion treatments. As the Ar^+ treatment time (and/or energy) increases, a reduction of the E_g^{surf} occurs. This is mainly due to a movement of the VBM towards the E_F, resulting from Cu 3d-derived states (e.g., ~ -3 eV) being more prominent [16,83]. After two steps of Ar^+ ion treatment (i.e., Fig. 4.5, top), the VBM and CBM positions are determined to be -0.88 ± 0.1 eV and 0.82 ± 0.15 eV, respectively. From these results, the E_g^{surf} of the examined CIGSe absorber is assessed to be 1.70 ± 0.2 eV, significantly higher than the calculated E_g shown in Fig. 4.4 (b) or the reported E_g^{bulk} of the absorber (i.e., ~ 1.2 eV) [29]. Additionally, the surface of the investigated absorber may be slightly n-type, as indicated by the (slightly) closer proximity of the E_F to the CBM. Although past studies have established that chalcopyrite absorbers are characteristic of larger surface E_g when compared to their respective E_g^{bulk} values [15,16,83,89], such a wide E_g^{surf} has not been reported for a sulfur-free absorber. In fact, the here determined E_g^{surf} for the CIGSe absorber is comparable to the reported surface E_g for $Cu(In,Ga)S_2$ (i.e., 1.76 ± 0.15 eV), the sulfide counterpart of the studied chalcopyrite (expected to have a significantly larger E_g) [16]. The measurement of further Ar^+ ion cycles to confirm such large E_g^{surf} was not possible.

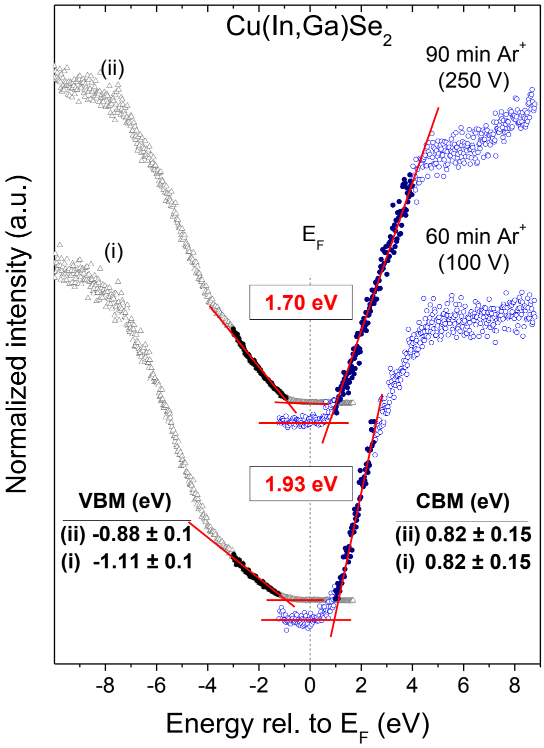

Figure 4.5 He I UPS and IPES spectra of the CIGSe sample after the indicated mild Ar$^+$ ion treatments. Linear extrapolations of the respective edges are shown in red lines. Measured E_g^{surf} values are shown in the rectangular insets. The experimental uncertainty of the assessed E_g^{surf} is ± 0.2 eV.

However, the validity of the obtained E_g^{surf} value is supported by the strong surface Cu-deficiency of the absorber. This state was detected by the XPS analysis and can be observed in the weak intensity of the Cu 3d-derived states in the UPS spectra of the bare absorber (see Fig. 4.5). Considering that the XPS results show a 10 % Cu surface composition for the studied absorber, it would be reasonable to predict a E_g^{surf} value close to that of β-In$_2$Se$_3$ (i.e., tetrahedral phase), reported to be 1.55 eV for thin films [90], which borders the lower-bound margin of error of the absorber's measured E_g^{surf} value. Although the Ga content is expected to be low on the surface of the absorber [based on the already presented Ga/(In+Ga) depth-profile analysis], any amount of Ga would increase the E_g^{surf} value [9], bringing the values closer to a match. The effect such a widened E_g near the interface may play on the performance of its respective solar cell will be discussed in more detail in Ch. 7.

4.4 CdS/Cu(In,Ga)Se₂ Heterointerface

In the following section, the characterization of the chemical and electronic structure of the CdS/CIGSe heterointerface is presented. First, attention is given to surface-sensitive PES and XAES experimental results. These results are then complemented by XES measurements that lead to a more complete understanding of the studied heterointerface formation. In the final part of this section, direct measurements of the electronic band alignment of the CdS/CIGSe heterointerface are presented and discussed.

4.4.1 Surface Chemical Structure and Buffer Growth

In this subsection, the results of surface-sensitive PES and XAES measurements are discussed in an attempt to ascertain the surface chemistry of the investigated heterointerface as a function of CBD-treatment time.

Fig. 4.1 shows the XPS survey spectra of the investigated samples, along with respective peak identification. The XPS survey spectrum of the bare CIGSe absorber was discussed in Sect. 4.3.1. Samples treated with CBD-CdS times exhibit additional Cd- and S-related photoemission lines in their XPS survey spectra, which intensify as a function of CBD-treatment time. At the same time, the signal of the absorber-related XPS lines decreases in these samples. These changes both result from growth of the buffer layer on top of the CIGSe substrate: as the buffer layer becomes thicker, the attenuation of the CIGSe-derived photoemission lines is greater. An exception to this trend is found for the sample with the first CBD-treatement time (i.e., 0.25 min), in which the intensities of the absorber-related lines actually increase. This effect is attributed to a cleaning of the absorber surface induced by the chemical bath prior to the onset of buffer deposition [33,91]. All these effects are clearer in the detail XPS spectra of selected core levels of absorber- and buffer-related elements, presented in Fig. 4.6 along with peak fits. [The signal detected in Fig. 4.6 (c) for samples (iv) – (vi) is ascribed to a Cd MNN plasmon background rather than Cu $2p_{3/2}$ intensity.]

By assuming that the cleaner surface of the 0.25 min CBD-CdS/CIGSe sample better represents a bare surface of the CIGSe absorber (as indicated by the higher intensity of the absorber-related photoemission lines), the observed attenuation of the absorber-related lines of samples with longer CBD-CdS treatment periods could be used to estimate the effective thickness of their buffer layers. The measured intensity, I^{sub}, attenuated due to coverage of the

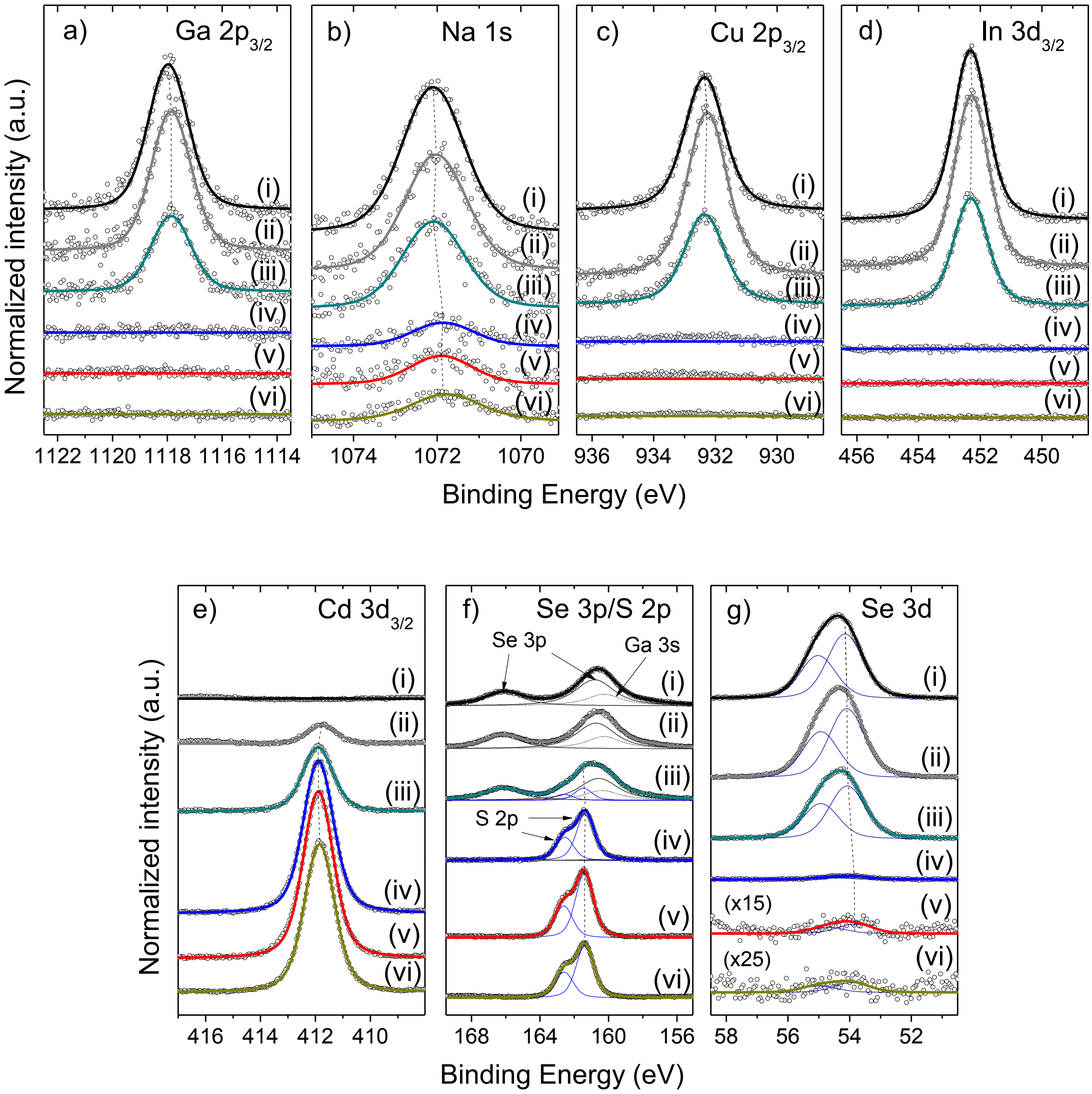

Figure 4.6 XPS detail spectra of the (a) Ga $2p_{3/2}$, (b) Na 1s, (c) Cu $2p_{3/2}$, (d) In $3d_{3/2}$, (e) Cd $3d_{3/2}$, (f) Se 3p/S 2p, and (g) Se 3d regions of the CdS/CIGSe sample series, as normalized to background intensity. The following CBD times were used: (i) 0, (ii) 0.25, (iii) 1, (iv) 3, (v) 4, and (vi) 10 min. Dashed lines indicate peak centers determined by curve fit analysis. All spectra were measured using Mg K_α excitation. Vertical offsets are added for clarity.

absorber surface by a buffer layer of thickness, *d*, can be described by the following formula:

$$I^{sub}(d) = I^{sub}_{ref} \cdot e^{-d/\lambda} \qquad (4.1),$$

where I^{sub}_{ref} is the intensity of the bare substrate, and λ stands for the photoelectron inelastic mean free path (IMFP).

Similarly, the increase in intensity of buffer-related photoemission lines, I^{cov}, as a function of the buffer thickness, d, can be described by the following formula:

$$I^{cov}(d) = I^{cov}_{ref} \cdot (1 - e^{-d/\lambda}) \qquad (4.2),$$

where I^{cov}_{ref} is the saturated intensity of a sufficiently thick buffer layer.

Due to the initial cleaning effect of the chemical bath and the complete attenuation (saturation) of the signal of absorber-(buffer-)related photoemission lines for samples with CBD times ≥ 3 min, it was only possible to calculate the effective buffer thickness of the 1 min CBD-CdS/CIGSe sample. {Traces of Se are still seen in the spectrum of the 10 min CBD-CdS/CIGSe sample in Fig. 4.6 (g), indicating diffusion of Se into the buffer layer. Similar Se-S intermixing has been reported in previous CdS/CI(G)Se heterointerface studies [15,92,93]. The effects on the formation of the interface chemical structure will be discussed later.} Table 4.1 shows the results of this evaluation. The average estimated buffer thickness after 1 min is 0.9 ± 0.3 nm.

Table 4.1 Effective buffer thicknesses, d (in nm), of the CdS CBD-treated sample series. λ values are also reported in nm and were obtained from refs. [50,51]).

CBD (min)	Ga 2p (I/I_0)	$d_{Ga\ 2p}$ ($\lambda = 0.56$)	Cu 2p (I/I_0)	$d_{Cu\ 2p}$ ($\lambda = 0.89$)	In 3d (I/I_0)	$d_{In\ 3d}$ ($\lambda = 1.67$)	Se 3d (I/I_0)	$d_{Se\ 3d}$ ($\lambda = 2.24$)	Cd 3d (I/I_0)	$d_{Cd\ 3d}$ ($\lambda = 1.74$)	S 2p (I/I_0)	$d_{S\ 2p}$ ($\lambda = 2.11$)
0.25	1	-	1	-	1	-	1	-	0.15	-	1	-
1	0.49	0.4 ± 0.1	0.44	0.7 ± 0.2	0.50	1.2 ± 0.2	0.59	1.2 ± 0.2	0.43	1.0 ± 0.2	0.36	1.0 ± 0.2
3	0	-	0	-	0	-	0.03	7.7 ± 1.5	1.15	-	1.24	-
4	0	-	0	-	0	-	0.01	-	1.29	-	1.40	-
10	0	-	0	-	0	-	0.01	-	1	-	1	-

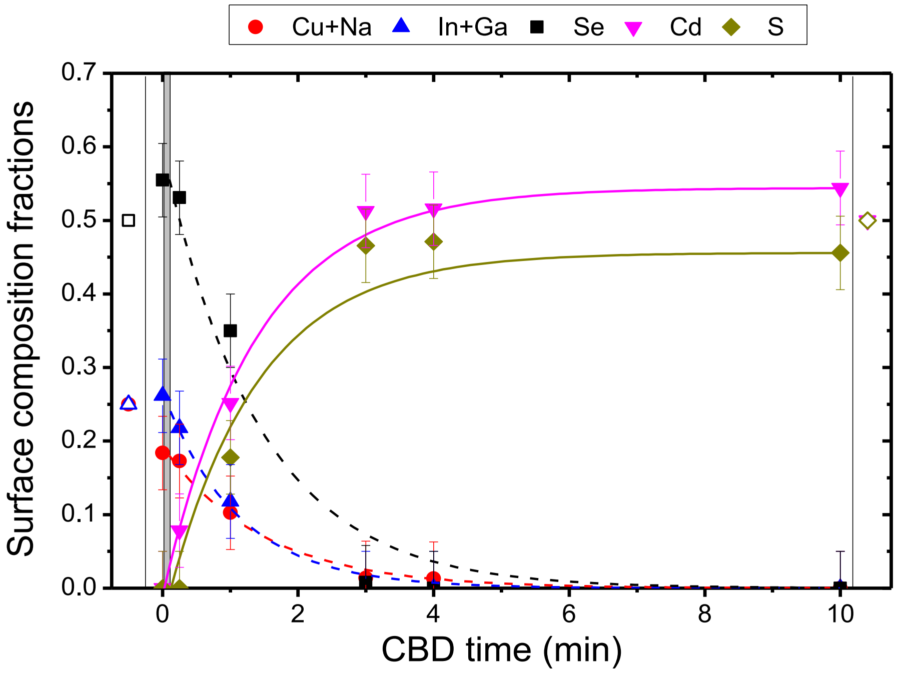

Figure 4.7 Composition from the XPS spectra of the investigated sample series as a function of CBD-CdS time. Changes in surface composition were fitted by an exponential as a function of CBD time to show the decrease (dashes lines)/increase (solid lines) of the respective elements. The gray-shaded area indicates the onset of the buffer deposition, as determined by the XPS analysis. The hollow icons at the left and right extremities of the figure represent stoichiometric 1:1:2 and 1:1 compositions expected for the absorber and 10 min CBD-CdS/CIGSe samples, respectively.

The photoemission intensity of the absorber elements is found to decrease exponentially as a function of CBD time; this occurence is demonstrated by the line fits of the respective element surface fractions. Complementing this finding, the surface concentration of the buffer lines show an asymptotic growth trend. These observed patterns are consistent with a uniform layer-by-layer (i.e., Frank-van der Merwe) growth mode of the deposited buffer and are predicted by eqn. (4.1) and (4.2) [94,95]. No perceptible change in photoemission intensity is observed past 3 min of CBD-treatment, confirming earlier assumptions of a complete coverage of the absorber surface by the buffer layer [i.e., of a thickness greater than the information depth (ID) of the analyzed XPS core levels]. Furthermore, samples treated with these CBD times show surface compositions of Cd:S = 1:1 ratio (within the margin of error), as expected of stoichiometric CdS. Moreover, the relative surface elemental fractions of CBD-CdS/CIGSe were fitted (i.e., the fractions of the CIGSe absorber are excluded from the fits) to estimate the CBD latency period (i.e., the time prior to the onset of buffer deposition). For this purpose, the functions of the line fits of the fractions of absorber-related elements (pairs) (i.e., Cu+Ga, In+Ga and Se dashed lines) were used to compute the CBD time at which the surface fractions of each absorber-related element (pairs) still equals the fraction found for the untreated CIGSe sample (i.e., the CBD time after which the elemental fractions start to decrease). The x-intercept of the functions of the line fits of the fractions of buffer-related elements (i.e., Cd and S solid lines) were calculated to determine the CBD time at which the surface fractions of the buffer-related elements start to increase due to CdS deposition. Table 4.2 summarizes the results of these calculations. The average onset of buffer deposition was determined to be 0.07 ± 0.05 min (i.e., 4.2 ± 3 s). In order to assess the chemical environment of the deposited buffer layer during the early stages of the buffer deposition, further studies combining the XPS and X-ray-excited Auger electron spectroscopy (XAES) techniques will be presented later in this section.

Table 4.2 Estimation of the onset of CdS deposition

Elements	Surface composition (at CBD = 0 min)	Fit line formula (x stands for CBD time)	Buffer deposition onset (min)
Cu + Na	0.18 ± 0.05	$0.19 * e^{-x/1.47}$	0.07 ± 0.05
In + Ga	0.27 ± 0.05	$0.27 * e^{-x/1.11}$	0.02 ± 0.05
Se	0.55 ± 0.05	$0.60 * e^{-x/1.43}$	0.10 ± 0.05
Cd	0	$0.544-(0.55 * e^{-x/1.39})$	0.02 ± 0.05
S	0	$0.46-(0.50 * e^{-x/1.34})$	0.12 ± 0.05

4.4.2 Cd Modified Auger Parameter Analysis

Next, changes in the chemical composition of the buffer layer throughout the CBD process are discussed. As mentioned in Sect. 3.1, chemical shifts are in general more pronounced in XAES lines than in PES core levels. However, when both of these shifts are considered, as in the case of the modified Auger parameter method, a powerful tool for the identification of chemical states can be implemented [45,52]. In the present analysis, attention is, at first, directed to changes in the Cd $M_{45}N_{45}N_{45}$ XAES line as a function of CBD time. Afterwards, consideration is given to the evolution of the modified Auger parameter (α^*) of Cd of the investigated sample series. The Cd α^* values were derived by using the Cd $3d_{3/2}$ XPS core level and the Cd $M_4N_{45}N_{45}$ XAES line of the respective samples. (The Cd $3d_{3/2}$ peak was preferred over the Cd $3d_{5/2}$ peak in order to avoid the overlapping of Mg $K_{\alpha 3,4}$ excitation satellites with the Cd $3d_{5/2}$ peak).

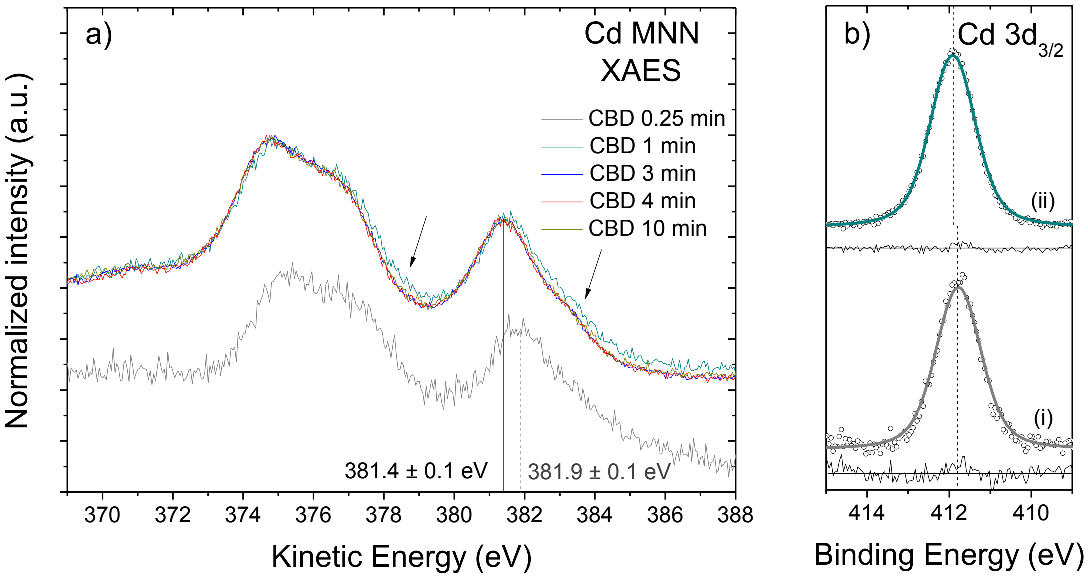

Figure 4.8 (a) Cd $M_{45}N_{45}N_{45}$ XAES lines of CBD-CdS/CIGSe sample series, labeled by CBD time. Arrows highlight the broader region of the XAES line of the 1 min CBD-CdS/CIGSe sample. (b) Cd $3d_{3/2}$ XPS detail spectra, normalized to maximum intensity, of the (i) 0.25 min and (ii) 1.0 min CBD-treated samples. All spectra were measured using Mg K_α excitation. Vertical offsets are added for clarity.

Fig. 4.8 (a) displays the Cd $M_{45}N_{45}N_{45}$ (MNN) XAES line of each CBD-CdS/CIGSe sample in the investigated series, normalized to the maximum intensity value of every spectrum. The spectrum of the 0.25 min CBD-CdS/CIGSe sample (its Cd $M_4N_{45}N_{45}$ XAES line is located at a KE of 381.9 ± 0.1 eV) is shifted compared to the rest of the measured spectra (their Cd $M_4N_{45}N_{45}$ XAES line are located at a KE of 381.4 ± 0.1 eV), and the shape of the Cd MNN line for the 1.0 min CBD-CdS/CIGSe sample is broader than the ones of samples with longer CBD treatments (pointed out by the arrows). The Cd MNN lines of samples with 3 min and longer CBD times are identical. These observations suggest the following possibilities: first, the 0.25 min CBD-CdS/CIGSe sample may be in a different chemical state than the rest of the samples; second, the broader shape observed in the spectrum of the 1.0 min CBD-CdS/CIGSe sample appears to be the result of two overlapping Cd MNN lines, each derived from different Cd chemical species. In order to confirm the validity of this assumption, an appropriately weighted fraction of the 10 min CBD-CdS/CIGSe sample Cd MNN line (i.e., the sample with the thickest CdS layer) was subtracted from the spectrum in question, while not allowing the difference to fall into a negative intensity. The results of this evaluation are depicted in Fig.

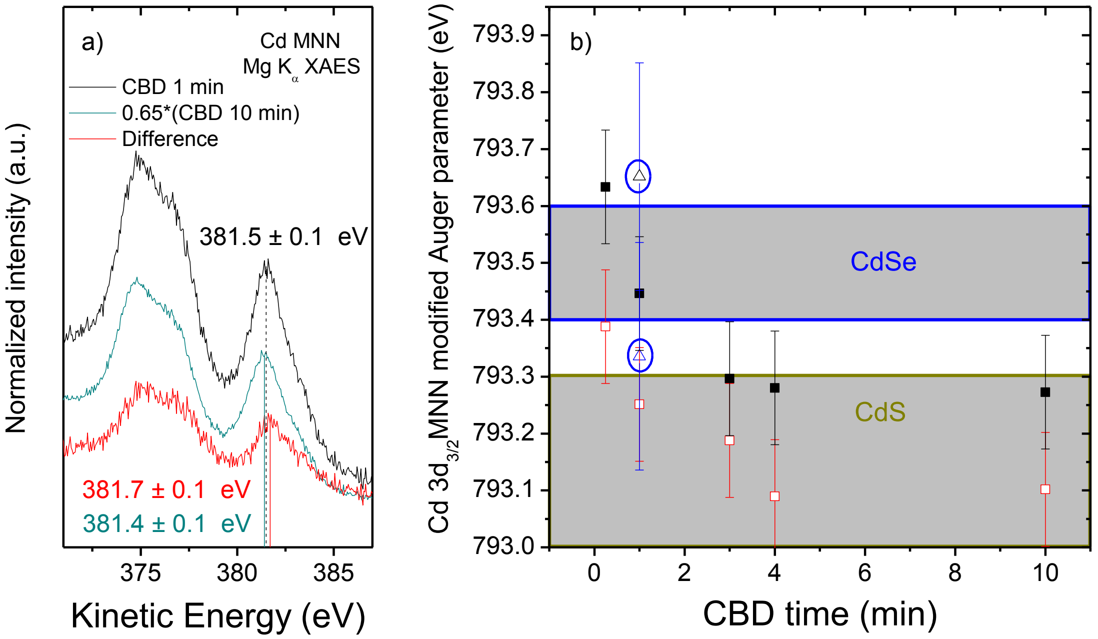

Figure 4.9 (a) Cd $M_{45}N_{45}N_{45}$ XAES line of the 1 min CBD-CdS/CIGSe sample together with a weighted spectrum of 10 min CBD-CdS/CIGSe sample and the corresponding difference (1 min – 0.65 * 10 min). (b) Cd modified Auger parameter (α*) of the CBD-CdS/CIGSe sample series shown as a function of CBD time. The encircled triangles indicate the α*-values obtained by using the KEs of the two Cd MNN contributions into which the 1 min CBD-CdS/CIGSe sample spectrum was decomposed. The red hollow squares are Cd α*-values of another set of independently-measured CBD-CdS/CIGSe sample series produced by the same ZSW production line (more details can be found in the text).

4.9 (a). The difference spectrum resembles the shape of a Cd MNN line, and the energetic position of the attained new Cd MNN line is close to that of the 0.25 min CBD-CdS/CIGSe sample. Earlier, the effective thickness of the buffer layer of the 1 min CBD-CdS/CIGSe sample was estimated to be 0.9 ± 0.3 nm. The λ of the Cd MNN line (KE ~ 382 eV) is 0.99 nm [50,51]. If a new Cd chemical species were present on the surface of the 1.0 min CBD-CdS/CIGSe sample, it would not be sufficiently thick to completely attenuate the signal of the first-formed Cd chemical species (i.e., the one observed for the 0.25 min CBD-treated sample). Such a scenario appears to agree with the data evaluation shown in Fig. 4.9 (a). The existence of two Cd chemical environments in samples treated during the early stages of the CBD process is indicated.

The computed Cd α* values for the investigated sample series are presented in Fig. 4.9 (b), along with reported Cd α* values for CdS and CdSe [45,52,53,96-98]. The samples treated with shorter CBD times (i.e., 0.25 min and 1 min) show Cd α* values above the range reported for CdS. In the case of the 0.25 min CBD-CdS/CIGSe sample, its computed Cd α* lies slightly above the reported range of values for CdSe. In the case of the 1 min CBD-CdS/CIGSe sample, its computed Cd α* (using the as-measured XAES line) would lie within the reported range of values for CdSe, as denoted by the black square in Fig. 4.9 (b). However, if the values obtained from the two Cd XAES lines derived from the spectrum analysis are employed [as denoted by the circled triangles in Fig. 4.9 (b)], the higher KE-shifted line yields a Cd α* above the reported range of values for CdSe (just like the obtained Cd α* for the 0.25 min CBD-CdS/CIGSe sample), whereas the lower KE-shifted line results in a Cd α* between reported values for CdSe and CdS. [Note that no indication of a second contribution was observed in the curve fit of the Cd $3d_{3/2}$ XPS line of the 1 min CBD-CdS/CIGSe sample, as shown in Fig. 4.8 (b)]. Moreover, all of the calculated Cd α* for samples with CBD times of at least 3 min are seen to fall in the range of reported Cd α* values for CdS, as expected of samples with thicker CdS layers. Thus, the modified Auger parameter analysis suggest the formation of interfacial CdSe, as well CdS, during the early stages of the CdS/CIGSe heterointerface formation. This interpretation is consistent with the curve fit analysis of the Cd $3d_{3/2}$ and the Se 3p/S 2p regions (see Fig. 4.6). Whereas Cd is present in samples with 0.25 and 1.0 min CBD treatments, S could only be confirmed for the 1.0 min CBD-CdS/CIGSe sample. The red hollow square in Fig. 4.9 (b) are data points of a different CBD-CdS/CIGSe sample series produced by the same ZSW production line using the same CBD times employed for the currently investigated sample series. The samples were independently measured (and the spectra were provided) by the group of Prof. Andreas Klein of the Surface Science Division of the Institute of Materials Science of the Technische Universität Darmstadt. Differences in Cd α* values for the two sets may be associated with variances in sample handling, experimental measurement setups and/or electron analyzer calibration methods. However, the general trend in the Cd-α*-value evolution as a function of CBD time is observed for both sets of samples.

4.4.3 Near Surface Chemical Structure

In this subsection, XES measurements are presented and used to assess the deposited buffer layer thicknesses and, more importantly, the chemical environment in the near-surface bulk. This is possible due to the greater ID of the photon-in photon-out spectroscopic techniques (see Sect. 3.2 for a more detailed explanation).

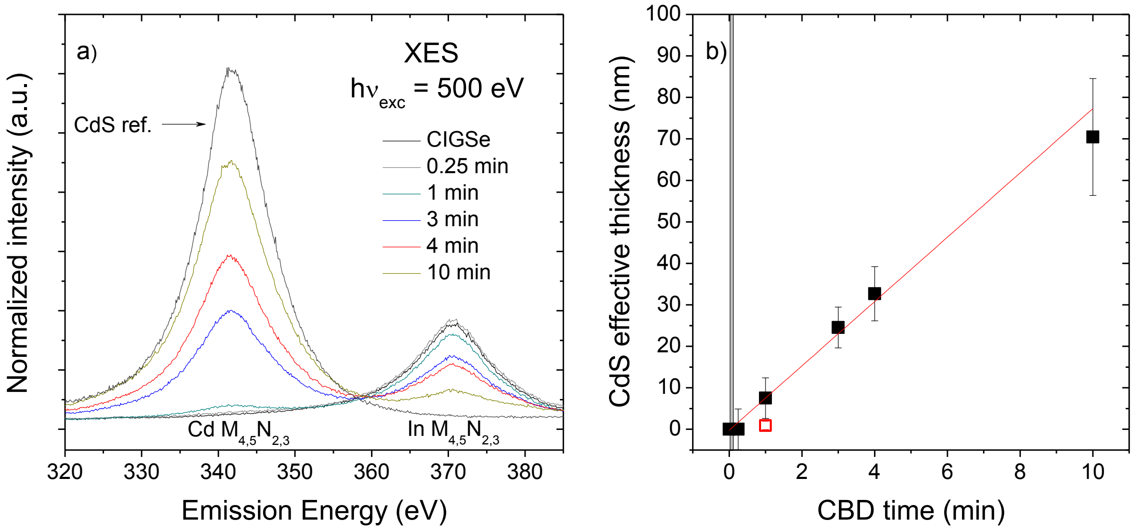

Figure 4.10 (a) Cd $M_{4,5}$ and In $M_{4,5}$ XES spectra of the investigated set of CdS/CIGSe samples, normalized according to measurement time. (b) Thickness of deposited CdS layer as a function of CBD time, determined from the attenuation of the substrate-derived In $M_{4,5}$ emission. The red hollow square represents the XPS-determined CdS effective thickness. The gray-shaded area indicates the delayed onset of the buffer deposition, as determined by the XPS analysis.

The XES spectra of the Cd $M_{4,5}$ and In $M_{4,5}$ emission regions for the CdS/CIGSe sample series are presented in Fig. 4.10 (a). The buffer-related Cd $M_{4,5}$ emission signal can be distinctly observed in the XES spectra of the 1-min CBD-CdS/CIGSe treated sample, and it continues to increase as a function of CBD time. Simultaneously, the intensity of the In $M_{4,5}$ emission signal, which is substrate-related, decreases with CBD time. This observation can be explained by the attenuation effect of the deposited buffer layer, analogous to the previously seen attenuation of photoelectrons in XPS (see Sect. 4.4.1). The fact that, in the present case, the substrate-related signal (i.e., In $M_{4,5}$ emission) is not completely attenuated even after 10 min of CBD treatment is accounted by the increased ID of the probed emission photons.

The XES spectra were interpreted as the sum of a CdS contribution and a CIGSe substrate contribution, as represented in equation (4.3) [99]:

$$sample = a \cdot CdS_{ref} + b \cdot CIGSe \qquad (4.3),$$

where a and b are appropriate weighting factors. To estimate the thickness of the deposited CdS buffer layer in the sample series, the following analysis was focused on the attenuation of the In $M_{4,5}$ emission signal. If the substrate emission is attenuated by a homogenous layer of thickness *d*, the resulting attenuated substrate emission intensity, $I^{sub}(d)$, can be described by the following formula:

$$I^{sub}(d) = I^{sub}_{ref} \cdot e^{-d/\lambda^*} \qquad (4.4),$$

where I^{sub}_{ref} is the intensity of the bare substrate, and λ^* is the effective attenuation length of the investigated emission signal in the cover layer. Moreover, λ^* is related to the separate attenuation lengths in the cover layer of the photons involved in the excitation step (λ_{exc}) and the emission step (λ_{emi}), as follows:

$$\frac{1}{\lambda^*} = \left(\frac{1}{\lambda_{exc} \cdot \sin\alpha}\right) + \left(\frac{1}{\lambda_{emi} \cdot \sin\beta}\right) \qquad (4.5),$$

where α and β stand for the angles of excitation and emission relative to the sample surface, respectively (for the present measurements $\alpha = \beta = 45$ °).

Taking into account the excitation ($h\nu_{exc}$ = 500.0 eV) and In $M_{4,5}$ emission (370.4 eV) energies, the λ_{exc} and λ_{emi} in CdS, as obtained from ref. [70], are 215 nm and 109 nm, respectively. Introducing these values into eqn. (4.5) yields a λ^* of 51 nm. In order to derive the CdS layer thicknesses, the obtained weighing factor *b* of eqn. (4.3) was set as the $I^{sub}(x)$:I^{sub}_{ref} ratio of the In $M_{4,5}$ emission. The determined CdS layer thickness as a function of CBD-treatment time is presented in Fig. 4.10 (b). Based on the linear regression fit conducted on the CdS effective thickness values as a function of CBD time, a deposition rate of 7.75 ± 0.53 nm/min was estimated. (As explained in Sect. 4.4.1, an XPS-determined CdS deposition rate could not be computed because only the CdS-effective-thickness of the 1 min CBD-CdS/CIGSe sample could be determined. However, the XPS- and XES-derived effective thicknesses of the 1 min CBD-CdS/CIGSe sample are, within the margin of error, comparable.) The 10 min CBD-CdS/CIGSe sample was assessed to have a CdS layer thickness of 70 ± 15 nm, in agreement with the reported ZSW CdS thickness (i.e., 80 nm for 10 min of CBD-CdS treatment) [100].

Next, the chemical environment near the heterointerface was studied. Fig. 4.11 shows the changes of the overlapping Se $M_{2,3}$ and S $L_{2,3}$ XES range as a function of CBD time for the CdS/CIGSe sample series (after normalization to the spectrum area). The overlapping of the XES signals is caused by the similar energetic positions of the states involved in the Se $M_{2,3}$

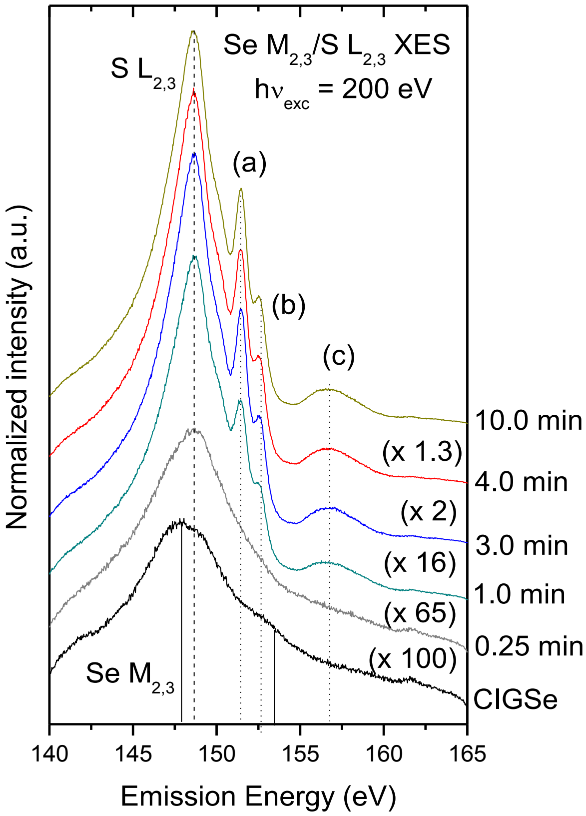

Figure 4.11 Se $M_{2,3}$/S $L_{2,3}$ XES spectra of the CdS/CIGSe sample series, normalized to spectrum area. Solid and dashed lines indicate Se- and S-related transitions, respectively. These transitions are identified in the text. Vertical offsets added for clarity.

and S $L_{2,3}$ transitions (i.e., Se 4s → Se 3p and S 3s → S 2p, respectively). Literature values for the photoionization cross sections of the S 2p and Se 3p subshells at $h\nu_{exc} = 200$ eV are 3.799 Mbarns and 0.643 Mbarns, respectively [101]. Furthermore, fluorescence yields of the S $L_{2,3}$ and Se $M_{2,3}$ transitions are reported to be 9.30E-4 and 2.51E-4, respectively [102]. Based on these values only, the present experimental settings favor S $L_{2,3}$ emission by a factor of at least 22 over Se $M_{2,3}$ emission. This fact helps to account for the greater normalization factors (shown in parentheses for each spectrum of Fig. 4.11) in samples with no or lower sulfur content (i.e., without or shorter CBD times). Moreover, it is noted that the Se $M_{2,3}$ natural linewidth (~ 2 eV) is much larger than the S $L_{2,3}$ natural linewidth (~ 0.08 eV) [74]. This fact explains the reason behind the lower peak-height-to-background for spectra with greater Se $M_{2,3}$ contributions (i.e., samples with shorter CBD times).

The spectrum of the bare CIGSe absorber sample is produced entirely by Se $M_{2,3}$ emission. It features a main peak and a shoulder (indicated by solid lines), with an approximate 5.7 eV separation from each other, which is in agreement with the 5.8 eV spin-orbit doublet separation of Se 3p states [53]. On the other hand, spectra of CBD-CdS/CIGSe samples show a combination of Se $M_{2,3}$ and S $L_{2,3}$ emission. After 0.25 min of CBD-CdS treatment, the main peak broadens and shifts towards a higher emission energy. Furthermore, the Se $M_{2,3}$ doublet features become less evident, as the S $L_{2,3}$ emission contribution originating from the sulfur atoms deposited by the CBD treatment increases. With longer CBD times, the spectral shapes converge, making the following features more pronounced: the main peak, positioned ~ 148 eV, becomes sharper and three new spectral features, located approximately at (a) 151.4, (b) 152.6, and (c) 157 eV, emerge. The spectral shape is characteristic of CdS [92,103,104]. Features (a) and (b) correspond to Cd 4d-related transitions (i.e., Cd 4d → S $2p_{3/2}$, and Cd 4d → S $2p_{1/2}$ transitions, respectively), directly indicating the presence of S-Cd bonds. Feature (c) arises from upper valence band electrons relaxing into S 2p core holes.

4.4.4 Principal Component Analysis

The Se $M_{2,3}$/S $L_{2,3}$ XES spectra of the 0.25 – 4 min CBD-CdS/CIGSe samples were evaluated using principal component analysis (PCA) in order to ascertain the number of different spectral contributions needed to reproduce the spectra set by a linear combination of reference spectra [71-73]. The number of potential components used in the PCA can be used to identify changes in the chemical structure of the studied heterointerface. The two-component PCA reconstruction can be considered to model a relatively inert heterointerface (i.e., no secondary phases or strong layer interactions at the interface). For this to be so, all measured XES spectra should be reproduced by a linear combination of the bare CIGSe substrate and the CdS buffer material spectra, with varying weighing factors. On the other hand, a PCA reconstruction with >2 components would model a reactive heterointerface, in which new interfacial chemical species are formed and have detectable contributions to the analyzed spectra. In such a scenario, a superposition of the bare CIGSe substrate and the CdS buffer material reference spectra would not satisfactorily describe the shape of all investigated XES spectra.

Fig. 4.12 (a) shows the measured XES spectra along with two-component and three-component PCA reconstructions. The energy range of the analysis was 145 - 160 eV. This shortened energy range is presented in order to concentrate on the range with the greater

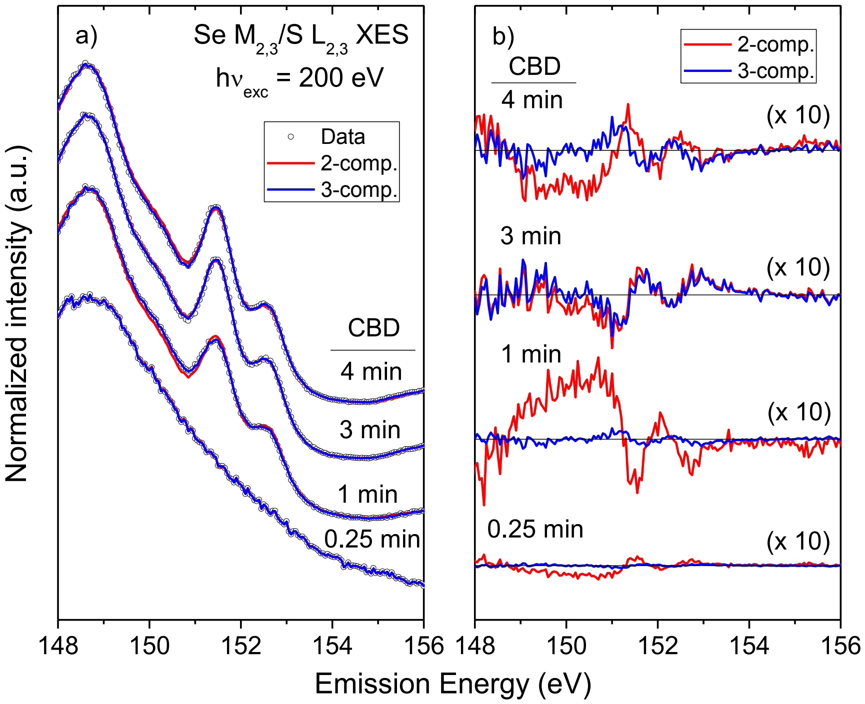

Figure 4.12 (a) Reconstruction of the Se $M_{2,3}$/S $L_{2,3}$ XES spectra of the 0.25 - 4 min CBD-CdS/CIGSe samples using two and three PCA components. (b) Magnified difference between the measured Se $M_{2,3}$/S $L_{2,3}$ XES spectra and the respective PCA reconstructions.

variability. The magnified difference between the measured XES spectra and the PCA reconstructions is displayed in Fig. 4.12 (b). Both two- and three-component reconstructions reasonably reproduce the XES measurements; nonetheless, better agreement is always found when three principal components are used in the analysis. The two-component simulation of the XES spectrum of the 1 min CBD-CdS/CIGSe sample yields the biggest mismatch shown in Fig. 4.12 (b), in which case the structure of the difference line cannot be considered statistical noise. The 1 min CBD-CdS/CIGSe sample will inherently have the highest relative contribution from near the interface, and so the results suggest that a new interfacial chemical species may be present in the investigated heterointerface. Furthermore, the fact that the improved agreement of the three-component reconstructions to the measured spectra is rather subtle, compared to the agreement of two-component reconstructions, is consistent with only a small quantity of the interface chemical species being formed.

In order to identify the interfacial chemical species, the Se $M_{2,3}$/S $L_{2,3}$ XES spectra of selenium- and sulfur-containing reference compounds were assessed via target transformation. This mathematical treatment attempts to reproduce a reference spectrum using

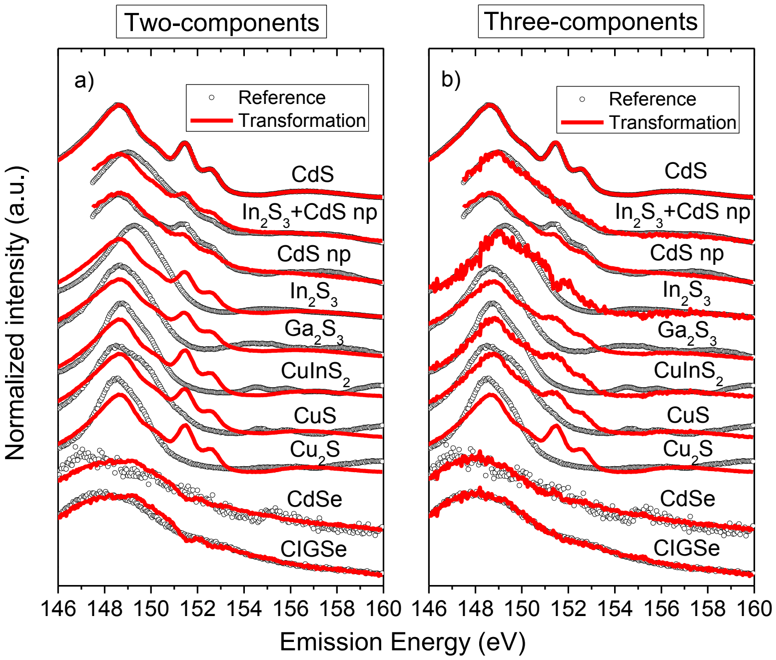

Figure 4.13 Target transformations of Se $M_{2,3}$/S $L_{2,3}$ XES spectra of several selenium- and sulfur-containing reference compounds calculated by linear combinations of the eigenvectors of the (a) two-component and (b) three-component PCAs. Vertical offsets added for clarity.

the set of eigenvectors determined from the PCA reconstructions [71,72]. Target transformation produces a best-fit line (i.e., transformation) from a linear combination of the eigenvectors to test whether a candidate spectrum is a fundamental component of the investigated spectra set. Confirmation is based on the quality of the match between the tested reference spectrum and its respective transformation. It must be noted that if, in a mixture of chemical species present in an investigated sample series, there are species having a constant ratio to each other, the target transformation matches the combined signal contribution of the mixture more closely than that of the components of the mixture.

Fig. 4.13 (a) and (b) show the reference spectra and the resulting target transformations using the two-component and three-component PCA reconstruction eigenvectors, respectively. Before discussing these results, it must be mentioned that the following two spectra were not directly measured (as labeled in Fig. 4.13): “CdS np” (nanoparticle CdS, as digitized from ref. [105]) and “In_2S_3 + CdS np” (the combination of the measured In_2S_3 spectrum and the digitized “CdS np” spectrum). Grounds for including “CdS np” in the set of references will be discussed in the following paragraphs. Moreover, the “In_2S_3 + CdS np” spectrum is intended to serve as a model for a mixture of interfacial chemical species. The validity of this assumption will be fully explained when results of least-squares fits on spectra of the investigated sample series are considered in the following subsection.

An interfacial species would have the highest relative contribution in spectra of thin samples representing the investigated near-interface region (i.e., samples with shorter CBD times). In these samples, the crystalline structure of the deposited CdS layers is found to be less perfect than the ones with longer CBD times [105]. The crystallinity of CdS has been reported to influence its spectral shape, with spectra of samples closer to a bulk CdS environment exhibiting higher intensities of the Cd 4d-related emission [105].

PES studies have reported “CdS np” to be sulfur-terminated, rendering a Cd-poor composition [106-109]. Such an off-stoichiometry may explain the relative lower intensity of the Cd 4d-related emission peaks [i.e., features (a) and (b) of Fig. 4.11]. Based on the results of the Cd α* evaluation in Sect. 4.4.2, the deposited Cd also forms CdSe during the initial stages of the CBD process. Because the deposited Cd does not fully contribute to emission related to S-Cd bonding, the CdS spectral contribution of the S $L_{2,3}$ XES spectra of low CBD times exhibit a “Cd-poor” CdS character. The “CdS np” spectrum was chosen to more appropriately render the spectral contribution of CdS during the initial stages of the CBD treatment.

Comparison of the reference and transformation spectra of the selection of reference compounds in Fig. 4.13 gives additional support to determine the minimum number of relevant spectral components in the investigated set of sample spectra. An inert heterointerface would lead to only two compounds with matching reference and transformation spectra: CIGSe and CdS. Indeed, in Fig. 4.13 (a), the agreement between the CdS spectrum and its transformation is excellent. For CIGSe, the quality of the match between reference and transformation spectra is much better than the ones for the other remaining compounds in the set of references, however, the agreement is not as good as was observed for CdS.

If the target transformation analysis is carried out with the eigenvectors of the three-component PCA, a similar agreement is maintained between the CdS spectrum and its transformation, as seen in Fig. 4.13 (b). The quality of the match between the CIGSe spectrum and its transformation significantly improves with this setup. This finding further confirms that the minimum number of spectral components in the investigated set of sample spectra is >2. Although in Sect. 4.4.2 CdSe was found to be an interface species, and a reasonable agreement is found between the CdSe spectrum and its transformation, the rather featureless shape and low-intensity of the CdSe reference spectrum, as well as the similarity between the CIGSe and CdSe transformation spectra, prevent an unambiguous confirmation about the CdSe spectrum being a principal spectral component. Regarding the rest of the monocompound references, "CdS np" shows the least disagreement between reference and transformation spectra. However, the low quality of the match rules it out as being the sole additional spectral contributor. The match between the "In_2S_3 + CdS np" reference "spectrum" and its transformation is very good, and, notably, improves significantly when the third component is added to the target transformation. In contrast, there is little or no improvement in the other tested references. This finding raises the possibility of having a mixture of interfacial chemical species in the heterointerface.

4.4.5 Least-squares Fitting Analysis

To complete the identification of the interfacial species, the measured Se $M_{2,3}$/S $L_{2,3}$ XES spectra of the investigated sample series were submitted to a least-squares fitting analysis. Fig. 4.14 (top panels) shows the fits of the 0.25 – 3 min CBD-CdS/CIGSe sample spectra using only the spectra of the two confirmed compounds: CIGSe and CdS. It is clear from the residua of the fits that the spectra of samples with shorter CBD treatment periods cannot be satisfactorily simulated by the spectra of these two reference compounds, as predicted by the PCA and target transformation results. Next, the least-squares fitting procedure was carried out using sets of three spectra: CIGSe, CdS and each of the unconfirmed reference compounds in turn. According to the target transformation analysis, CdSe was the interface species showing the highest correspondence to the measured reference spectra. Although not shown in the following figures, linear-squares fits of the spectra conducted using the CIGSe, CdSe and CdS spectra set were the same as the ones obtained for the two-component fit [i.e., Fig. 4.14 (top panels)]. After CdSe, the measured spectra of candidate interfacial species that produce the best matches were the Ga_2S_3 and In_2S_3 spectra; however, the quality of the match between these reference spectra and their respective target transformations does not suggest either of them as being suitable interfacial species candidates. Fig. 4.14 (middle panels) show the respective fits using the CIGSe, Ga_2S_3 and CdS spectra, whereas Fig. 4.14 (bottom panels) show the fits using the CIGSe, In_2S_3 and CdS spectra. If the Ga_2S_3 spectrum is used as the third component, the residua of the fits do not improve significantly compared to the two-component fits. In contrast, there is a close agreement found between all measured sample spectra and their respective fits when In_2S_3 is used.

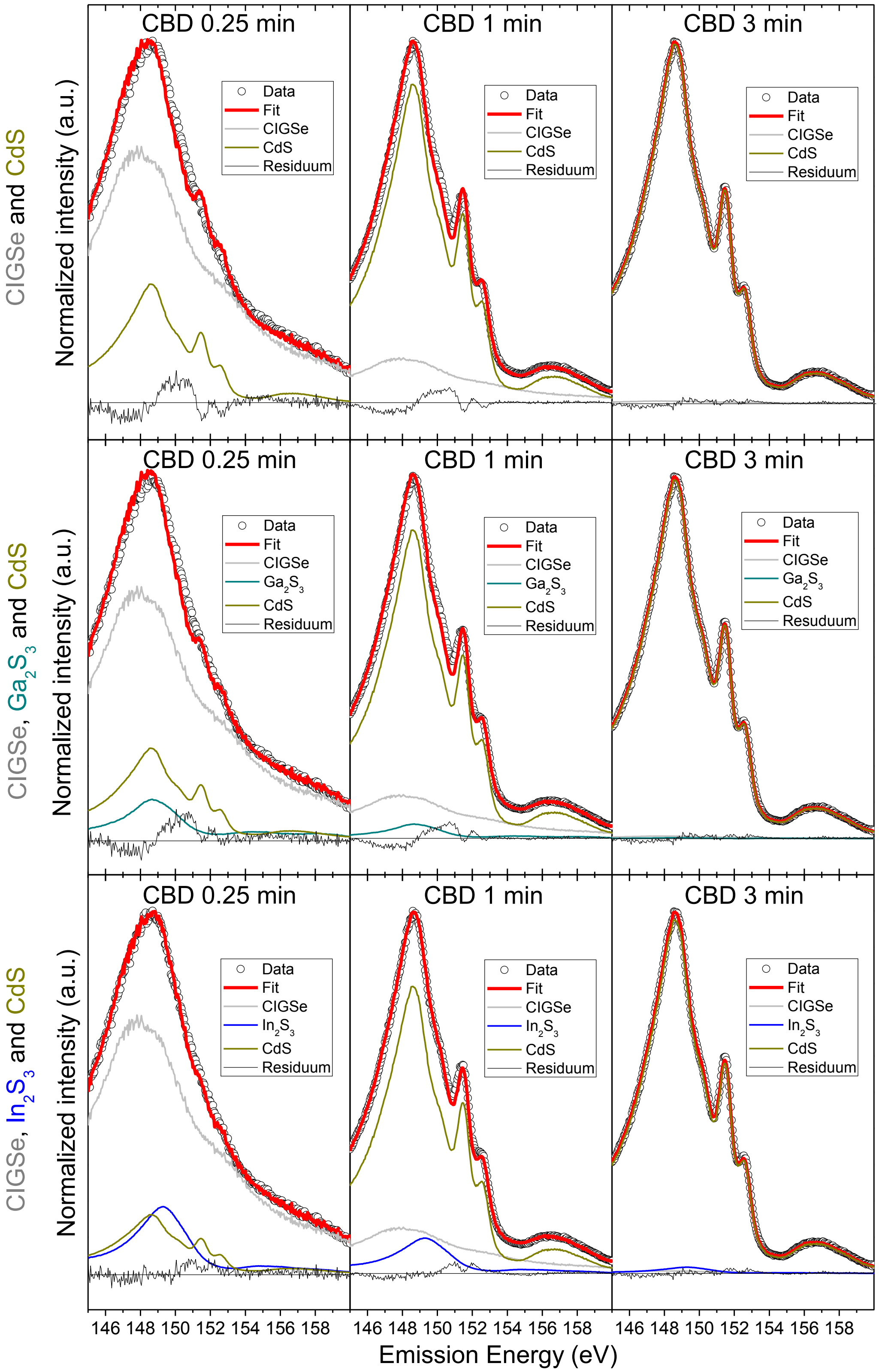

Figure 4.14 (previous page) Least-squares fits of the Se $M_{2,3}$/S $L_{2,3}$ XES spectra of the 0.25 - 3 min (left – right) CBD-treated samples using the following sets of reference spectra as spectral contributions (top panels): CIGSe and CdS; (middle panels): CIGSe, Ga_2S_3 and CdS; and (bottom panels): CIGSe, In_2S_3 and CdS, respectively.

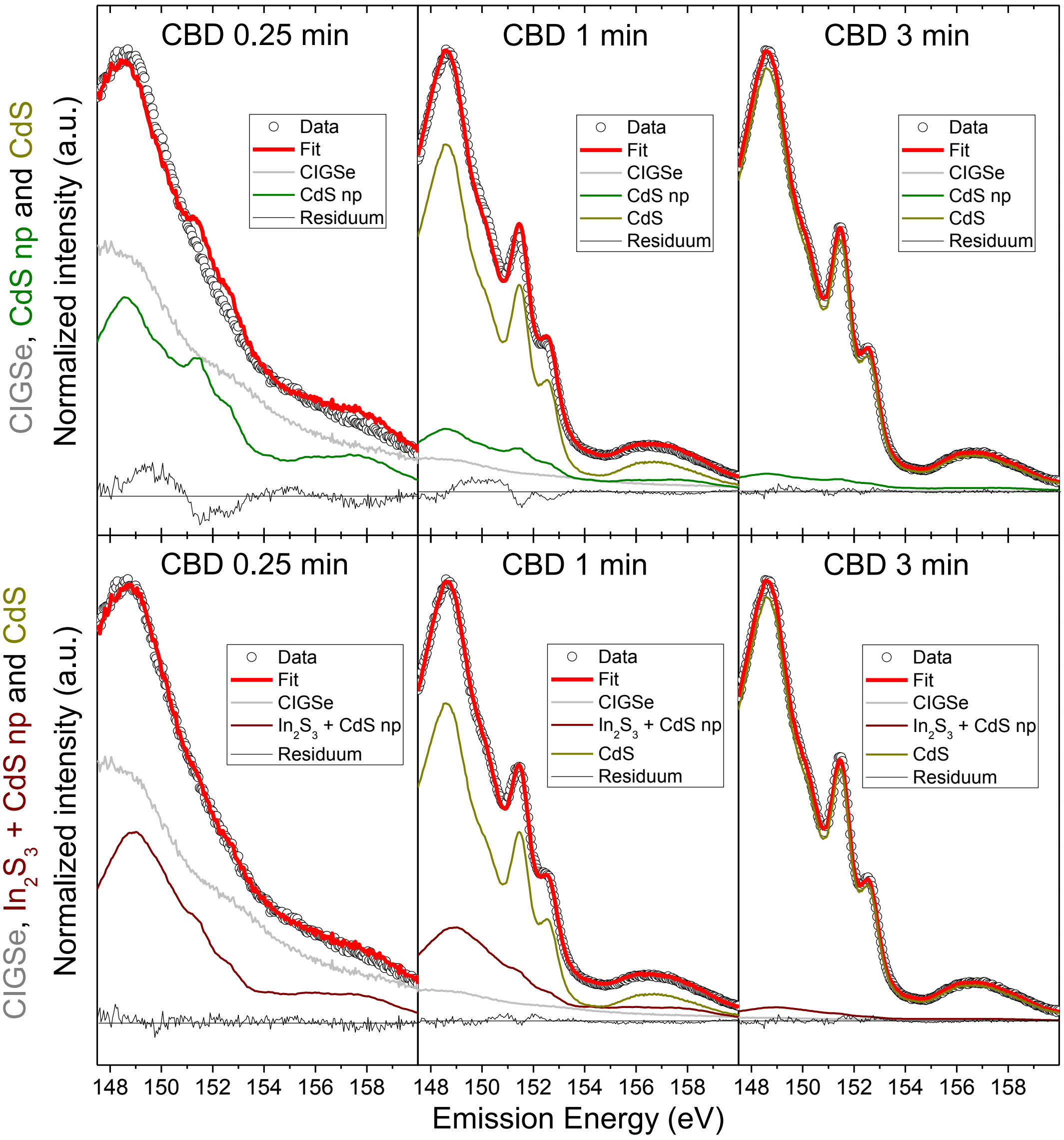

Figure 4.15 Least-squares fits of the Se $M_{2,3}$/S $L_{2,3}$ XES spectra of the 0.25 - 3 min CBD-CdS/CIGSe samples using the following sets of reference spectra as spectral contributions (top panels): CIGSe, CdS np and CdS; and (bottom panels): CIGSe, "In_2S_3 + CdS np" and CdS, respectively.

The residua of the fits in Fig. 4.14 (bottom panels) have a double-peak adjacent to the Cd 4d-related doublet positions (i.e., transitions characteristic of S-Cd bonding), which are more prominent in the spectra of the 0.25 min (left) and 1 min (center) CBD-CdS/CIGSe samples. As previously discussed, the crystallinity of the deposited CdS layers in these samples is less perfect than the CdS reference sample (i.e., 10 min CBD-CdS/CIGSe sample). Consequently, the CdS spectrum used in the linear-squares fits features a higher Cd 4d-related emission intensity than that found in the CdS spectral contributions of these samples [105]. The observed residuum feature is caused by this Cd 4d-related peak overestimation in the analysis of samples with thinner CdS layers. As the thickness of the deposited CdS layer increases and, concomittantly, its crystallinity, the Cd 4d-related emission intensity better resembles that of bulk CdS, and the residuum feature disappears.

In order to minimize the effects of this overestimation, "CdS np" was included as a reference spectrum for CdS deposited during the initial stages of the CBD treatment. However, the PCA target transformation of the "CdS np" spectrum does not clearly identify it as the interfacial spectral component. Accordingly, the least-squares fitting of the 0.25 – 3 min CBD-CdS/CIGSe sample spectra using the CIGSe, CdS np and CdS spectra, as seen in Fig. 4.15 (top panels), does not satisfactorily reproduce the measured spectra. Despite "CdS np" producing a transformation closer matching its reference spectrum than the one produced by the In_2S_3 spectrum, it is the latter spectrum that yields better results in the linear-squares fit analysis. These apparently contradicting results, along with the observed residuum feature in Fig. 4.14 (bottom panels), lead us to envision the interface as consisting of a mixture of chemical species in a constant ratio to each other (i.e., In_2S_3 + CdS np).

Fig. 4.15 (bottom panels) displays the least-squares fits of the 0.25 – 3 min (left – right) CBD-CdS/CIGSe sample spectra using the CIGSe, "In_2S_3 + CdS np" and CdS spectra set. In this case, a better agreement is found between all measured sample spectra and their respective fits than in any of the previous sets of spectra used for linear-squares fitting. Moreover, this spectral analysis results further support the target transformation testing of the "In_2S_3 + CdS np" spectrum as indicative of the presence of a mixture of interface chemical species at the heterointerface.

Based solely on reported values for the heat of formation of In_2S_3 and Ga_2S_3 (i.e, -346 kJ/mol [110] and -513 kJ/mol [111], respectively), Ga_2S_3 would be more energetically favored to form part of the interface chemical mixture. The formation of In_2S_3 rather than Ga_2S_3 further supports the finding of a Ga-depleted surface [i.e., lower Ga/(In+Ga)] discussed in Sect. 4.3.2.

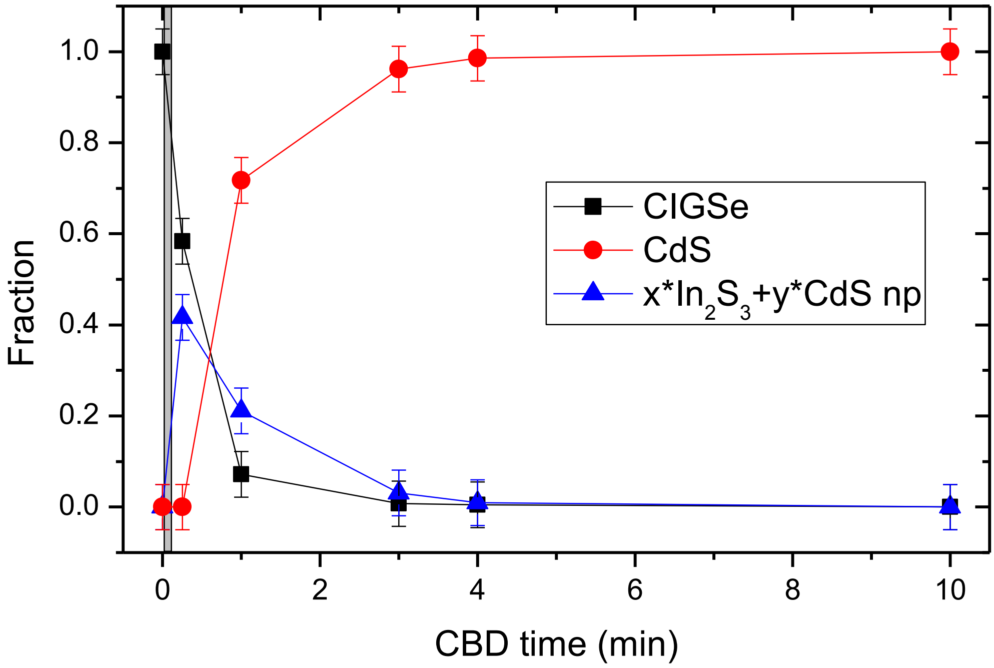

Figure 4.16 Calculated fractions of the CIGSe, CdS, and interface species contributions to the Se $M_{2,3}$/S $L_{2,3}$ XES spectra of the CBD-CdS/CIGSe sample series, as a function of CBD time. The gray-shaded area indicates the delayed onset of the buffer deposition, as determined by the XPS analysis.

The spectral fractions of the CIGSe, the interface species and the CdS components in the spectra of the sample series are plotted in Fig. 4.16 as a function of CBD time. In this case, the spectral contribution of CdS np is included in the interface species spectral fraction. As expected, the CIGSe spectral contribution decreases as a function of CBD time, whereas that of CdS increases. The interface species (i.e., In_2S_3 + CdS np) contribution grows, at first, but then diminishes as the deposited buffer thickness increases. The reason behind the detection of an interface species spectral contribution even in the spectrum of the 4.0 min CBD-CdS/CIGSe sample is due to the ID of the S $L_{2,3}$ XES. Considering the excitation and the S $L_{2,3}$ emission energies (i.e., 200 and ~ 151 eV, repectively), the λ_{exc} and λ_{em} in CdS, as obtained from ref. [70], are 106 and 375 nm, respectively. Introducing these values into eqn. (4.5) yields a λ^* of 59 nm, close to the thickness of the sample with the thickest buffer layer (i.e., 10 min CBD-CdS/CIGSe sample). The trend of the interface species spectral fraction as a function of CBD time is consistent with species confined to the vicinity of the CdS/CIGSe interface.

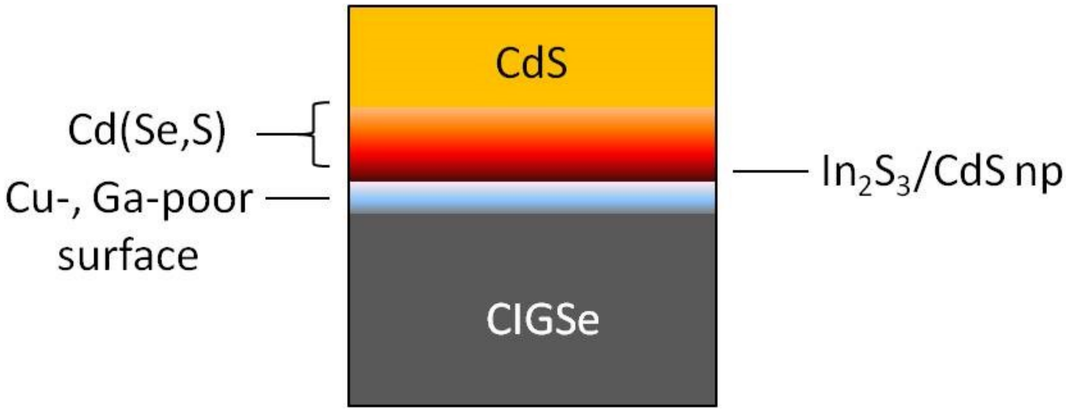

Figure 4.17 Schematic of the chemical structure of the investigated CdS/CIGSe heterointerface.

The complexity of the chemical properties of CdS/CI(G)Se heterointerfaces, allowing for the presence of interface structures beneficial to the performance of solar devices, has been for some time reported in literature. It has been suggested that S-Se intermixing, also detected in the investigated heterointerface, spreads unfavorable band alignment discontinuities over a distance, thus minimizing the detrimental effect of interface recombination paths [41]. More recently, the discovery of a S-containing interfacial compound in a different high-performing buffer/CIGSe heterointerface has been reported; although the identity of the compound in question could not be clearly established [112]. By using a more rigorous data analysis approach (i.e., the combination of PCA and least-squares fitting analysis), the presence of CdS np and In_2S_3 as interfacial chemical species was revealed in the present study. The formation of these interfacial compounds are deemed to widen the E_g of the absorber in the vicinity of the interface, providing an optimal heterointerface band gap grading that can extend to the bulk of the absorber (as will be discussed in the next subsection). Furthermore, the formation of these interfacial species potentially can be controlled by the length of the induction period of the CBD treatment, potentially opening a new optimization route for buffer/absorber heterointerfaces. A schematic of the chemical structure of the investigated CdS/CIGSe heterointerface is presented in Fig. 4.17.

4.4.6 Interface Band Alignment

The electronic properties of the CdS/CIGSe heterointerface are obtained by combining XPS, UPS and IPES: UPS and IPES are employed to determine the positions of the VBM and CBM, respectively, and XPS was used to monitor the interface-induced band bending (IIBB) resulting from the buffer deposition. The electronic structure of the CIGSe absorber has already been discussed in Sect. 4.3.3. For visual comparison purposes, Fig. 4.5 is again presented in Fig. 4.18 (a).

In Fig. 4.18 (b), the UPS and IPES spectra of the 10 min CBD-CdS/CIGSe sample are presented after various Ar^+ ion treatment steps. After three steps of Ar^+ ion treatment [Fig. 4.18 (b), top], the VBM and CBM positions are determined to be -1.57 ± 0.1 eV and 0.85 ± 0.15 eV, respectively. From these results, the surface E_g of the examined sample with the thickest CdS layer is assessed to be 2.42 ± 0.2 eV, which is in good agreement with the reported bulk E_g for CdS (e.g., ~ 2.5 eV) [32].

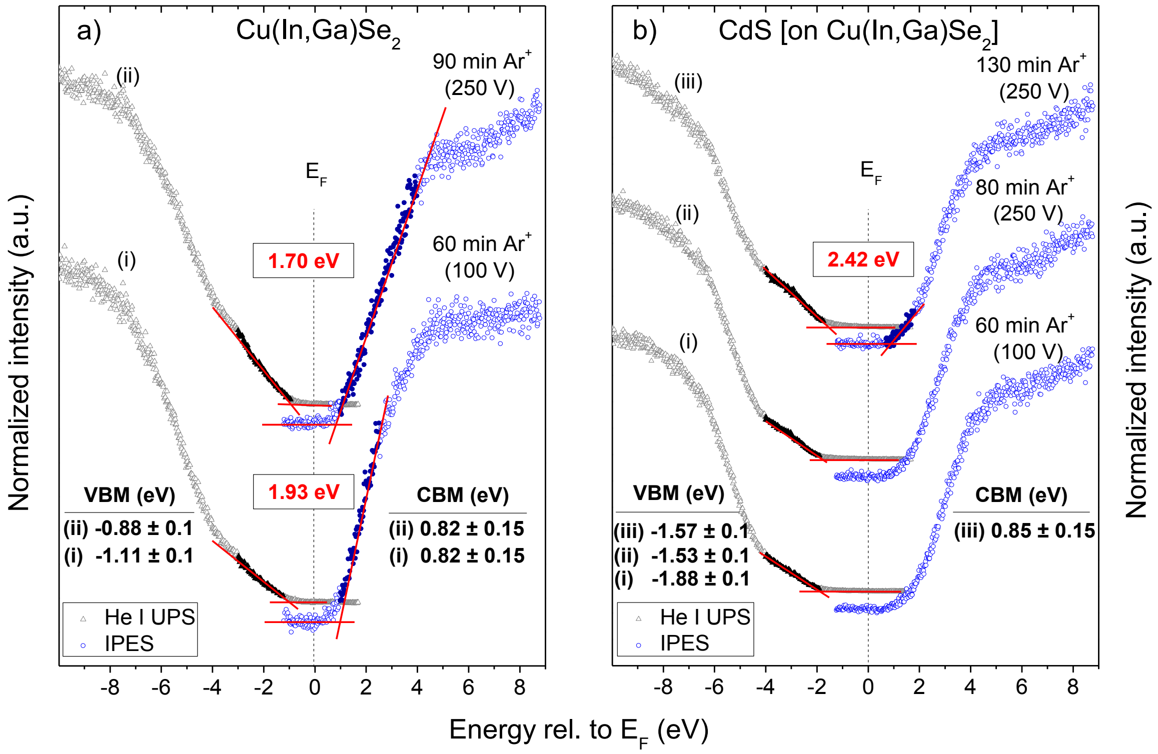

Figure 4.18 He I UPS and IPES spectra of (a) CIGSe, and (b) 10 min CBD-CdS/CIGSe sample after the indicated mild Ar^+ ion treatments. Linear extrapolations of the respective edges are shown in red lines. Measured E_g^{surf} values are shown in the rectangular insets. The experimental uncertainty of the assessed E_g^{surf} values is ± 0.2 eV. Note that the bottom and middle IPES spectra in (b) do not show a sufficiently-resolved leading edge and an extrapolation of the background line would result in an overestimation of the CdS E_g^{surf} value.

By comparing the CBM of the bare CIGSe absorber with that of the thick CdS on CIGSe sample, a rough approximation of the heterointerface band alignment can be made: a flat +0.03-eV CBO is found at the heterointerface. In order to complete the band alignment determination, the band bending that occurs at the heterointerface due to the deposition of the CdS layer (i.e., IIBB) must be taken into account [113]. In order to factor in this effect, the VBO and CBO are calculated by the following expressions:

$$\mathrm{VBO} = \mathrm{VBM}_{\mathrm{CdS}} - \mathrm{VBM}_{\mathrm{CIGSe}} + \mathrm{IIBB}, \text{ and} \qquad (4.6)$$

$$\mathrm{CBO} = \mathrm{CBM}_{\mathrm{CdS}} - \mathrm{CBM}_{\mathrm{CIGSe}} + \mathrm{IIBB}. \qquad (4.7)$$

The changes in the heterointerface IIBB are monitored via detected shifts in the BE-position of absorber-related XPS lines (i.e., Cu $2p_{3/2}$, In $3d_{3/2}$ and Ga $2p_{3/2}$) and the CdS buffer layer (i.e., Cd $3d_{3/2}$ and S $2p_{3/2}$) in samples with intermediate buffer thicknesses (e.g., samples with 0.25 and 1 min CBD-CdS-treatment times). In these samples, core level lines from both the absorber and the buffer layer can still be detected. A Se XPS line is not used due to the earlier detected Se diffusion into the buffer layer. In this case, chemical shifts in Se lines cannot be excluded; therefore, shifts in BE directly associated to band bending changes cannot be satisfactorily ascertained. By employing the selected XPS core levels, the impact of non-IIBB-related mechanisms (i.e., chemical shifts and/or chemical intermixing between the layers) influencing the energies of the PES lines is minimized. Determination of core level peak centers was carried out via the curve fit analysis explained in the beginning of this section.

The IIBB was calculated using the following expression:

$$\mathrm{IIBB} = [E^{0}_{a,i} - E^{t}_{a,i}] + [E^{t}_{b,j} - E^{f}_{b,j}] \qquad (4.8),$$

where $E^{0}_{a,i}$ is the BE-position of an absorber-related PES line *i* in the bare absorber; $E^{t}_{a,i}$ is the BE-position of an absorber-related PES line *i* after a CBD time *t*; $E^{t}_{b,j}$ is the BE-position of a buffer-related PES line *j* after a CBD time *t*; and $E^{f}_{b,j}$ is the BE-position of a buffer-related PES line *j* after a 10 min CBD-CdS/CIGSe. In total, 9 values of IIBB were computed by using combinations of the selected CIGSe and CdS lines and are displayed in Fig. 4.19. The average IIBB-value of the analysis is 0.08 ± 0.08 eV (as denoted by the dashed line in Fig. 4.19).

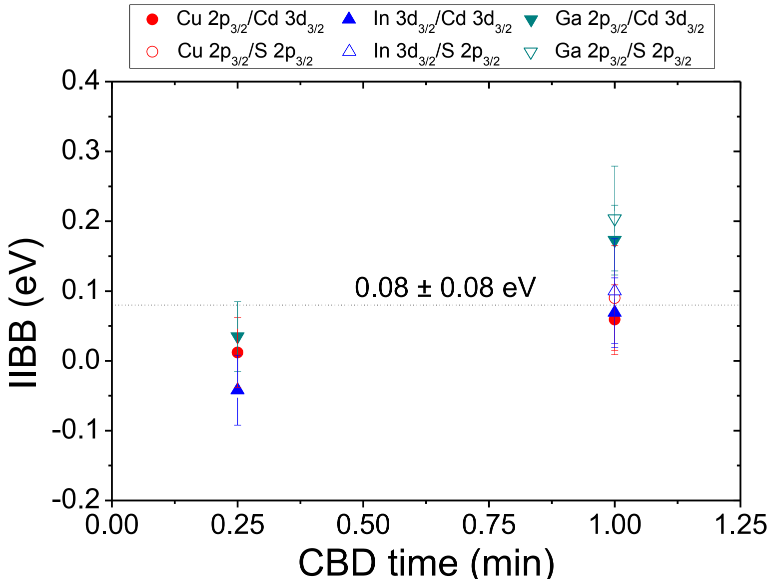

Figure 4.19 Interface-induced band bending (i.e., IIBB) as determined by combining core level positions of the absorber sample, the sample with the thickest CdS layer, and three samples with intermediate CdS layer thicknesses.

Consequently, the VBO and CBO for the heterointerface are ascertained to be -0.61 ± 0.15 and +0.11 ± 0.25 eV, respectively. The determined VBO (i.e., -0.61 ± 0.25 eV) is in strong agreement with density functional theory VBO calculations of CdS on a Cu-poor CIGSe surface (i.e., -0.65 eV) [114]. The conduction band alignment at the heterointerface reveals a slight spike CBO (i.e., +0.11 ± 0.25 eV). This is an almost ideal band alignment at the CdS/CIGSe interface, as seen in reported electronic band alignments of previously studied

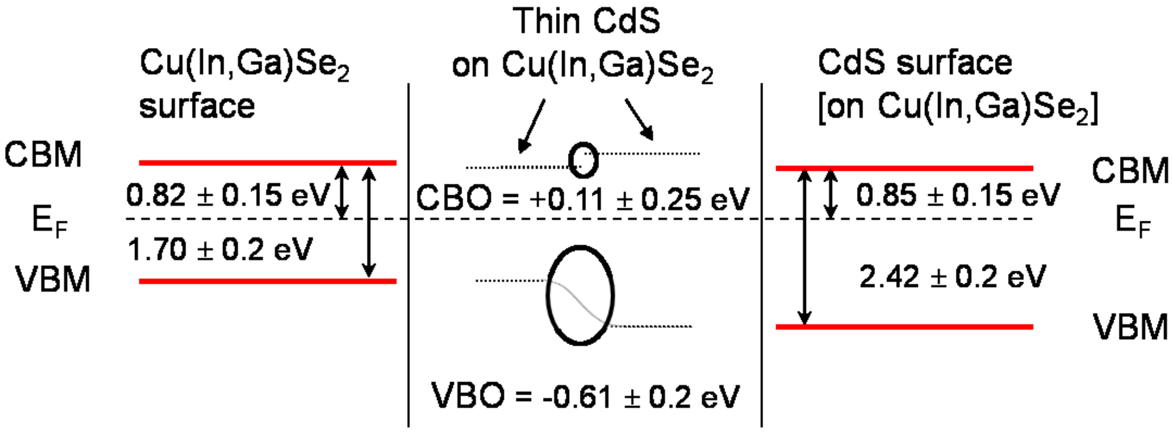

Figure 4.20 Schematic diagram of the ZSW CdS/CIGSe heterointerface electronic band alignment. The left and right sides of the diagram display the electronic E_g^{surf} (as derived by UPS and IPES) for the bare CIS absorber and the CdS buffer, respectively. The middle portion of the diagram shows the electronic band alignment at the heterointerface after considering interface-induced band bending effects.

high-efficiency CIGSe solar cells [15,83]. A schematic diagram of the complete electronic band alignment of the ZSW CdS/CIGSe heterointerface is shown in Fig. 4.20.

4.5 ZnS/Cu(In,Ga)Se_2 Heterointerface

In the following section, the characterization of the chemical and electronic structure of the ZnS/CIGSe heterointerface is presented. Although in this discussion the buffer layer is nominally ZnS, a Zn(O,OH) content is expected due to the CBD process [100]. However, the Zn chemical environment of the buffer is predominantly ZnS (at least away from the interface), as will be discussed in Sect. 4.5.2. Overall, results are discussed in an order similar to that of Sect. 4.4. First, surface-sensitive XPS and XAES experimental results give indication of surface composition, diffusion and layer thicknesses. These results are then complemented by XES measurements that provide chemical information about the heterointerface. In the final part of this section, the electronic band alignment of the ZnS/CIGSe heterointerface is determined.

4.5.1 Surface Chemical Structure and Buffer Growth

In this subsection, surface-sensitive PES and XAES measurements are used to monitor the surface composition of the ZnS/CIGSe heterointerface as a function of CBD time (i.e., ZnS layer thickness).

The XPS survey spectra of the ZnS thickness series on CIGSe, along with respective peak identification, are shown in Fig. 4.21. The XPS survey spectrum of the bare CIGSe absorber shows the photoemission lines of the absorber elements (i.e., Cu, In, Ga, and Se). Na-related lines are also present, as a result of Na-diffusion from the soda-lime glass substrate, as discussed in Sect. 4.3.1 [20,21]. Furthermore, Zn- and S-related photoemission lines are observed in the XPS survey spectra of samples submitted to the various CBD-ZnS-treatment times. As an expected effect of the deposition of a top (cover) layer, the intensity of the buffer-related XPS lines increases with CBD time, whereas the intensities of the absorber-related XPS lines decreases. This effect is more clearly distinguished in the detail XPS spectra of selected absorber- and buffer-derived XPS core levels, as shown in Fig. 4.22 along with curve fits. For the present sample series, the shortest chemical bath treatment step did not lead to an increase in the absorber-related line intensities, in contrast to the effect of the chemical

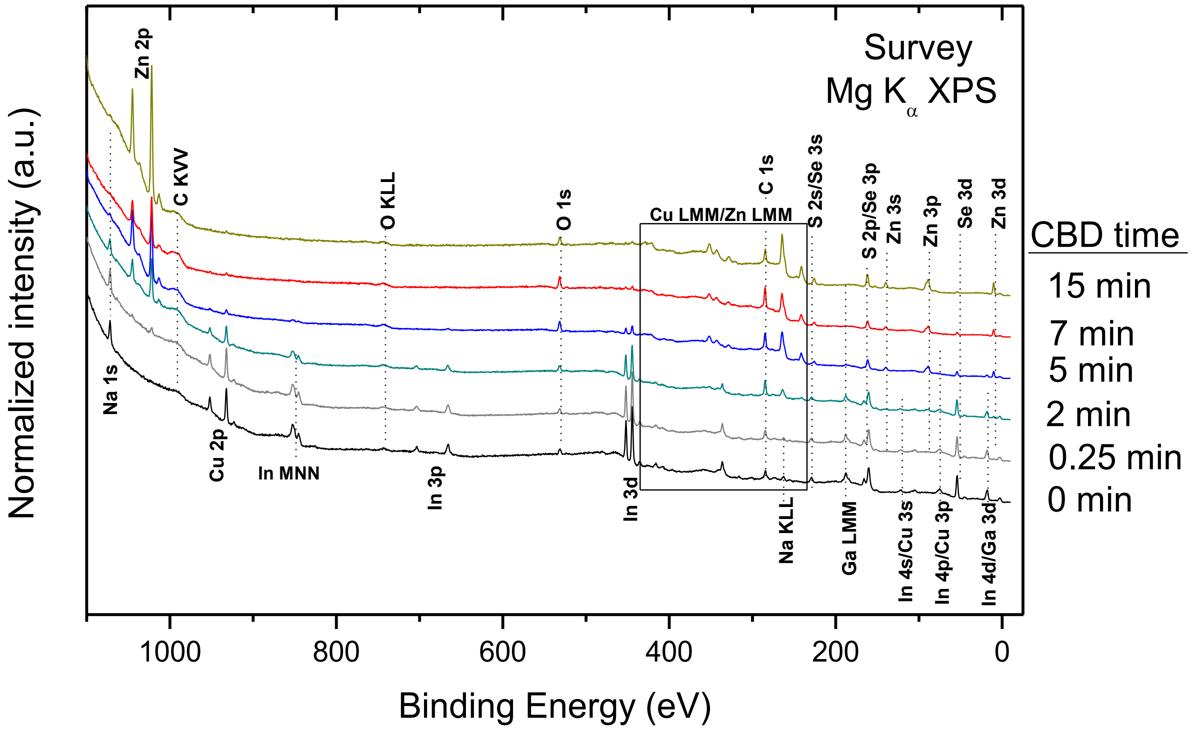

Figure 4.21 XPS Survey spectra of the CIGSe samples after different CBD-ZnS-treatment times. Vertical offsets are added for clarity.

bath in the CBD-CdS/CIGSe sample series (Sect. 4.4.1). This outcome may be due to an initially cleaner bare absorber surface for the present set of samples. Nevertheless, the availability of a greater number of samples with buffer layers of intermediate thickness potentially allows for a more detailed analysis of the ZnS layer deposition rate. Table 4.3 shows the relative intensities of selected XPS lines as a function of CBD-ZnS treatment time. As in Sect. 4.4.1, variances in the relative intensities with respect to time of treatment are ascribed to differences in λ. The effective thickness of the deposited buffer layers was calculated using eqns. (4.1) and (4.2). Based on these results, the XPS-determined ZnS deposition rate is 0.3 ± 0.1 nm/min. However, there are reasons to suspect that the actual ZnS deposition rate is higher, as will be now discussed. Despite the range of ID available due to the selection of the XPS lines analyzed, the obtained estimate of thickness for the sample with the thickest buffer layer (i.e., the 15 min CBD-ZnS/CIGSe sample) heavily depends on the ID of the XPS line in question. These results are not in agreement with the expected outcome of a layer-by-layer deposition model. For example, based on the calculated effective thicknesses of the In 3d$_{3/2}$ and Se 3d$_{5/2}$ XPS lines (i.e., $d_{\text{In 3d}}$ and $d_{\text{Se 3d}}$, respectively), the Ga 2p$_{3/2}$ and Cu 2p$_{3/2}$ XPS lines (with respective IDs of ~ 1.8 and ~ 3 nm [50,51]) should become complete attenuated after 5 min of CBD-ZnS treatment. Because this is not observed to happen,

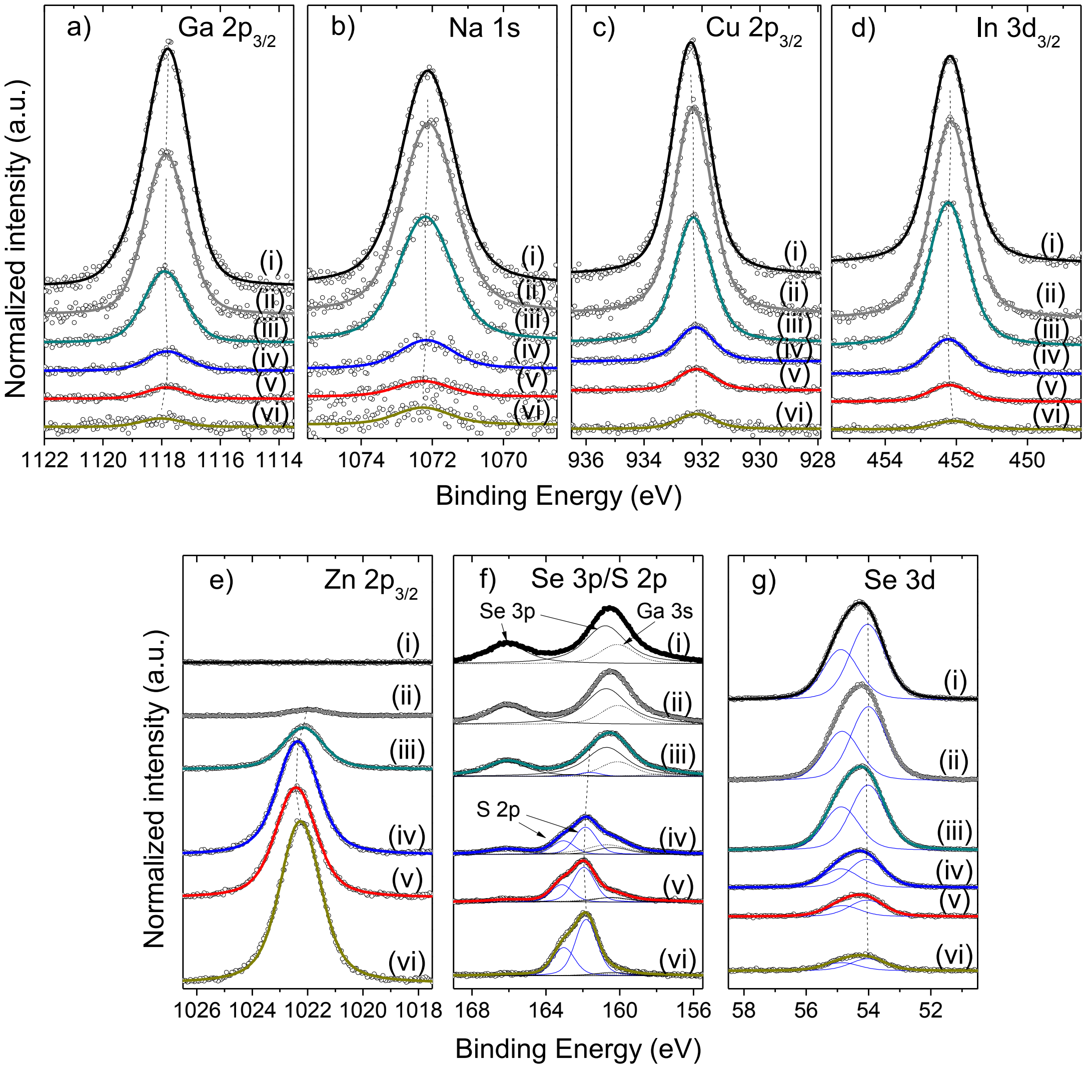

Figure 4.22 XPS detail spectra of the (a) Ga 2p$_{3/2}$, (b) Cu 2p$_{3/2}$, (c) In 3d$_{3/2}$, (d) Se 3d, (e) Na 1s, (f) Zn 2p$_{3/2}$ and (g) Se 3p/S 2p regions of the ZnS/CIGSe sample series, as normalized to background intensity. The following CBD-ZnS treatment times were used: (i) 0, (ii) 0.25, (iii) 2, (iv) 5, (v) 7, and (vi) 15 min. All spectra were measured using Mg K$_\alpha$ excitation. Vertical offsets are added for clarity.

detection of the lower-KE photoelectron signals strongly suggest that portions of the absorber surface do not become (sufficiently) covered by the deposited buffer layers. In such a scenario, the effective thickness values of the XPS lines producing higher-KE photoelectrons would be the lower limit of the buffer layer thicknesses, with their average thicknesses expected to be higher than the calculated values.

Table 4.3 Effective buffer thicknesses, d (in nm), of the CBD-ZnS/CIGSe sample series. λ values are also reported in nm and were obtained from refs. [50,51]).

CBD (min)	Ga 2p (I/I$_0$)	$d_{Ga\ 2p}$ ($\lambda = 0.61$)	Cu 2p (I/I$_0$)	$d_{Cu\ 2p}$ ($\lambda = 0.96$)	In 3d (I/I$_0$)	$d_{In\ 3d}$ ($\lambda = 1.80$)	Se 3d (I/I$_0$)	$d_{Se\ 3d}$ ($\lambda = 2.45$)	Zn 2p (I/I$_0$)	$d_{Zn\ 2p}$ ($\lambda = 0.79$)	S 2p (I/I$_0$)	$d_{S\ 2p}$ ($\lambda = 2.28$)
0	1	-	1	-	1	-	1	-	0	-	1	-
0.25	0.64	0.3 ± 0.1	0.78	0.2 ± 0.1	0.83	0.3 ± 0.1	0.87	0.4 ± 0.1	0.07	0.1 ± 0.1	0.36	-
2	0.32	0.7 ± 0.2	0.54	0.6 ± 0.1	0.75	0.5 ± 0.1	0.82	0.5 ± 0.1	0.48	0.5 ± 0.1	0.09	0.2 ± 0.1
5	0.07	1.6 ± 0.3	0.12	2.1 ± 0.4	0.17	3.2 ± 0.6	0.19	4.1 ± 0.8	0.90	1.9 ± 0.4	0.38	1.1 ± 0.2
7	0.04	1.9 ± 0.4	0.08	2.5 ± 0.5	0.10	4.2 ± 0.8	0.12	5.2 ± 1.0	1.11	-	0.50	1.6 ± 0.3
15	0.03	2.2 ± 0.4	0.04	3.0 ± 0.6	0.05	5.3 ± 1.0	.07	6.6 ± 1.3	1	-	0.90	5.3 ± 1.3

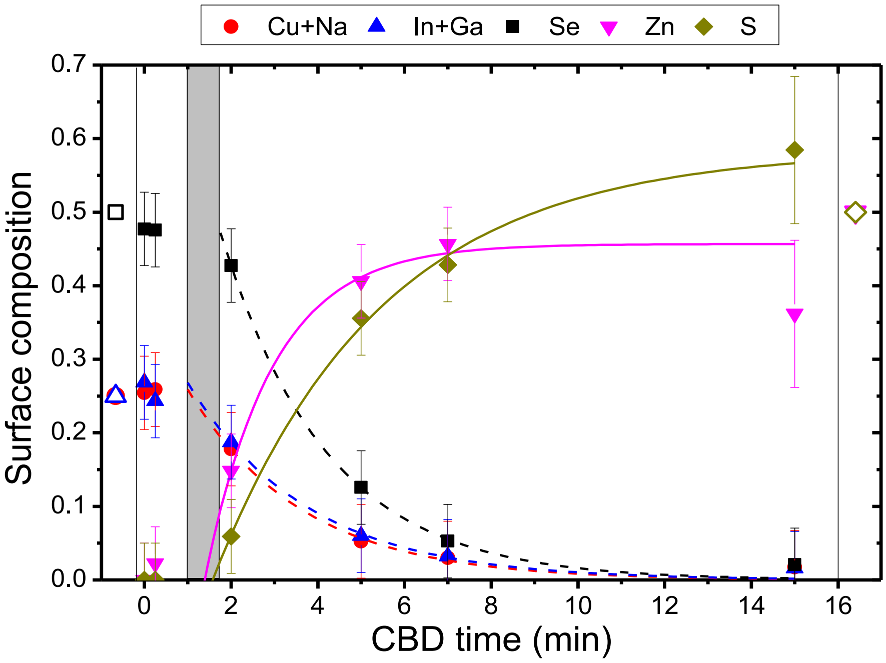

Figure 4.23 Relative surface composition of the investigated sample series as a function of CBD-ZnS-treatment time. The gray-shaded area indicates the onset of the buffer deposition, as determined by the XPS analysis. The hollow icons at the left and right extremities of the figure represent stoichiometric 1:1:2 and 1:1 compositions expected for the absorber and 15 min CBD-ZnS/CIGSe samples, respectively.

The present results differ from those obtained from the CdS/CIGSe heterointerface study, in which complete coverage of the absorber surface was attained after 3 min of CBD-CdS-treatment, indicating different buffer growth model in the two buffer CBD processes. The

XPS of the CBD-ZnS/CIGSe sample series suggests a buffer layer growth mode involving island formation (i.e., either Volmer-Weber mode or Stranski-Krastanov mode) [115].

The elemental surface composition was quantified as a function of CBD-ZnS-treatment time. In addition to the addressed corrections in λ [50,51], the intensity of the fitted XPS core level peaks was also analyzed accounting for respective differences in σ [46,47], and the transmission function of the electron analyzer [48]. The results of this evaluation are shown in Fig. 4.23.

As shown in Fig. 4.23, the surface element composition of the samples does not significantly change up to 2 min of CBD-ZnS treatment. After longer CBD times, changes in surface composition occur, suggesting a more delayed start of the ZnS deposition compared to the CBD-CdS. After 2 min of CBD-ZnS treatment, the fractions of surface composition of the absorber-related elements decrease exponentially with CBD time, as shown by the line fits of the respective element surface fractions. (Nevertheless, it is observed that, even in samples with prolonged CBD-ZnS-treatment times, a small fraction of the probed sample surface is derived from elements of the CIGSe substrate.) Likewise, the fractions for the buffer-related elements show an asypmtotic growth trend at around the same CBD time. The onset of the ZnS buffer deposition was estimated by using the functions of the line fits, as described in Sect. 4.4.1 for the CBD-CdS/CIGSe sample series. Table 4.4 presents the results of the analysis. The average onset of buffer deposition was determined to be 1.35 ± 0.32 min (81 ± 19 s), indicating a longer activation period than the one estimated for the CBD-CdS process [i.e., 0.07 ± 0.05 min (4 ± 3 s)]. Differences in the growth kinetics of the two buffer CBD processes have been reported, including a larger induction period for the CBD-ZnS process than for the CBD-CdS process [100]. The impact of this longer exposure of the absorber to the chemical bath prior to the formation of the heterointerface on the chemical and electronic structure of the interface will be the point of interest for the remainder of this section.

Table 4.4 Estimation of the onset of ZnS deposition

Elements	Surface composition (at CBD = 0 min)	Fit line formula (x stands for CBD time)	Buffer deposition onset (min)
Cu + Na	0.25 ± 0.05	$0.38*e^{-x/2.63}$	1.05 ± 0.3
In + Ga	0.27 ± 0.05	$0.39*e^{-x/2.76}$	0.99 ± 0.3
Se	0.48 ± 0.05	$0.97*e^{-x/2.44}$	1.73 ± 0.3
Zn	0	$0.46-(1.11*e^{-x/1.56})$	1.39 ± 0.3
S	0	$0.58-(0.88*e^{-x/3.85})$	1.58 ± 0.3

4.5.2 Zn Modified Auger Parameter Analysis

The chemical environment of the deposited Zn atoms is examined based on changes in the Zn $L_3M_{45}M_{45}$ (LMM)/Na $KL_{23}L_{23}$ (KLL) XAES line region as a function of CBD-ZnS treatment time. The modified Zn α* of the investigated sample series are then calculated using the Zn $2p_{3/2}$ XPS core level and the Zn LMM XAES line of the respective samples.

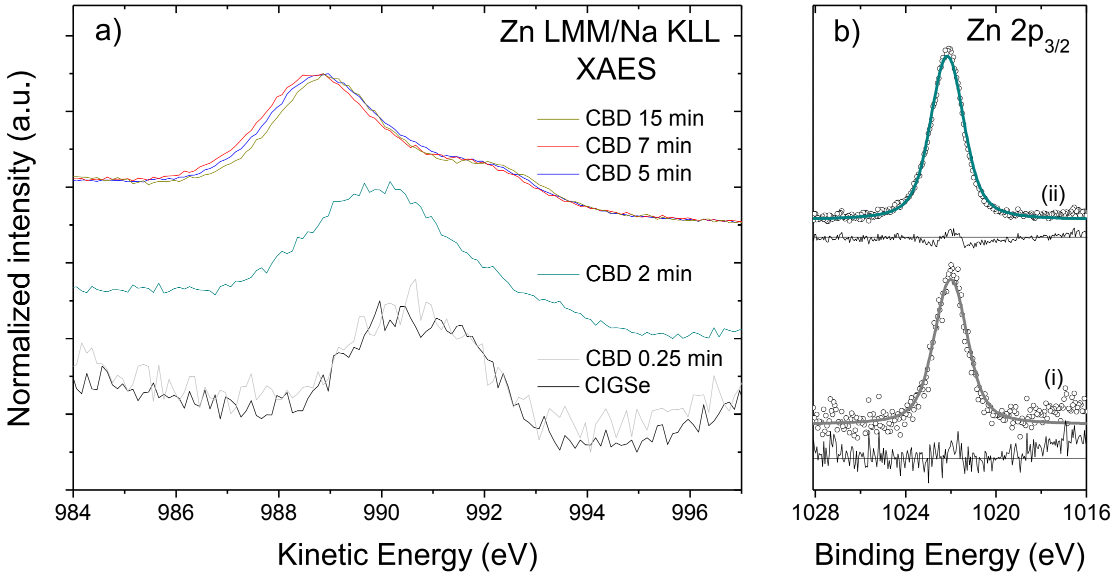

Figure 4.24 (a) Zn $L_3M_{45}M_{45}$/Na $KL_{23}L_{23}$ XAES lines of CBD-treated samples in the investigated ZnS/CIGSe sample series, normalized to maximum intensity. (b) Zn $2p_{3/2}$ XPS detail spectra of the (i) 0.5 min and (ii) 1.0 min CBD-treated samples. All spectra were measured using Mg K_α excitation. Vertical offsets are added for clarity.

Fig. 4.24 (a) displays the Zn LMM/Na KLL XAES lines of all samples in the investigated series, normalized to the maximum intensity value of each spectrum. The spectra of the bare CIGSe and the 0.25 min CBD-ZnS/CIGSe sample consist of only the Na XAES line, and spectra of samples submitted to CBD-treatment periods of at least 5 min are composed of mainly the Zn XAES line. The λ for the Na KLL electrons (KE ~ 990 eV) is 2.1 nm [50,51]. The average buffer thickness of the 5 min CBD-ZnS/CIGSe sample is 2.32 ± 1.11 nm, leaving the possibility that a small fraction of the spectrum of this sample could derive from the Na KLL. The 2 min CBD-treated sample spectrum shows a broader shape than the the two XAES lines found for the other samples. Furthermore, the spectrum of the 2 min CBD-treated sample is located in the energy range between the other two XAES lines. These observations are in line with overlapping of at least two XAES lines, as seen in Sect. 4.4.2 in the analysis of the Cd XAES lines. In order to ascertain whether this is true in the present case, appropriately weighted fractions of the Zn LMM line of 15 min CBD-ZnS/CIGSe sample (i.e., the sample with the thickest ZnS layer) and of the Na KLL line of the bare CIGSe were subtracted from the spectrum in question, while not allowing the difference to fall into a negative intensity. This method yields a difference "line" with a "Zn LMM line"-like shape, as illustrated in Fig. 4.25 (left). [An energetically-shifted Zn LMM line (red line) is superimposed over the obtained difference "line" (hollow dots) to serve as a guide to the eye when examining its shape.] Thus, at least two Zn species are formed during the early stages of the heterointerface formation.

The modified Zn Auger parameters (α^*) of the sample series are presented in Fig. 4.25 (right), along with reported ranges Zn α^* values for ZnSe, ZnS, ZnO, $Zn(OH)_2$ and $ZnIn_2Se_4$ references [45,52,53,116-118]. The samples treated with CBD times of at least 5 min show Zn α^* values within the range reported for ZnSe/ZnS references; a clear distinction could not be made between the Zn α^* values for ZnSe and ZnS based on the literature search. In the case of the 2 min CBD-ZnS/CIGSe sample, its calculated α^* lies above the reported range of values for ZnSe/ZnS [45,52,53,116-118] but in the vicinity of reported values $ZnIn_2Se_4$ [118]. Although no reference Zn α^* values were found for $ZnIn_2S_4$, the wide overlap found for ZnSe/ZnS may indicate a similar trend for $ZnIn_2Se_4$/$ZnIn_2S_4$. If α^* values are computed from the two Zn XAES lines derived from the curve analysis of the 2 min CBD-ZnS/CIGSe sample spectra [as denoted by the circled triangles in Fig. 4.25 (right)], the lower KE-shifted line yields a α^* within the range of ZnS/ZnSe, whereas the higher KE-shifted line again results in

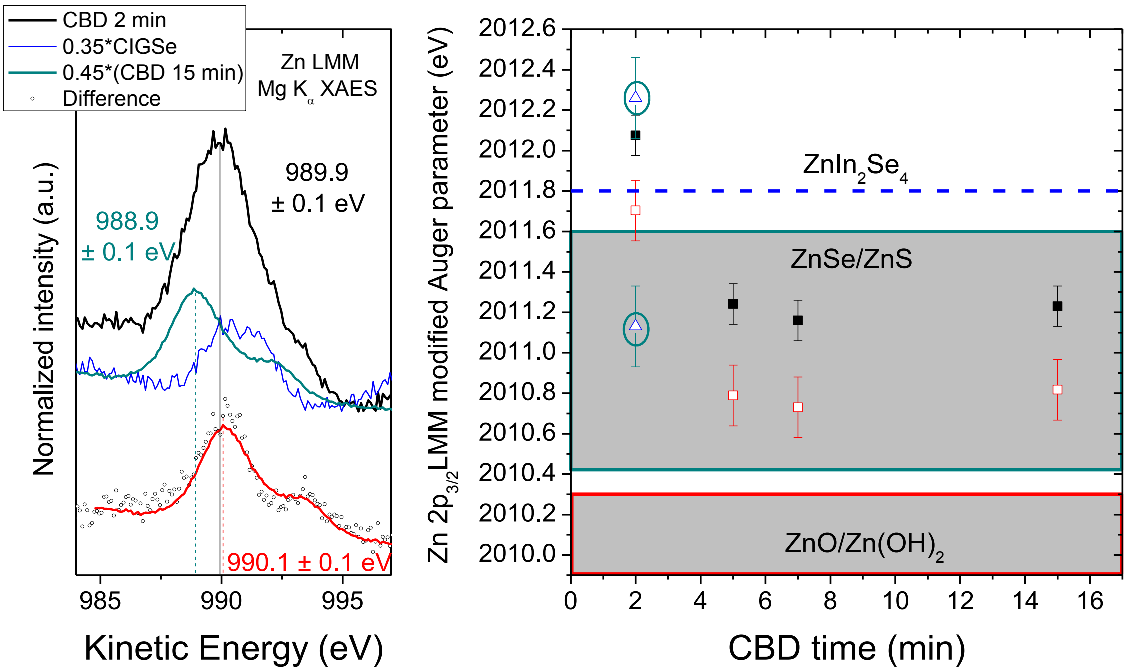

Figure 4.25 (left) Zn $L_3M_{45}M_{45}$/Na $KL_{23}L_{23}$ XAES line of the 2 min CBD-ZnS/CIGSe sample together with weighted spectra of the CIGSe absorber and the 15 min CBD-ZnS/CIGSe sample, and the corresponding difference (2 min – 0.65 * 15 min – 0.35 * CIGSe). (Right) Zn modified Auger parameter (α*) of CBD-treated samples in the ZnS/CIGSe sample series shown as a function of CBD time. The encircled triangles indicate the α*-values obtained by using the KEs of the two Zn LMM contributions into which the 2 min CBD-ZnS/CIGSe sample spectrum was decomposed. The red hollow squares are Zn α*-values of another set of independently-measured CBD-ZnS/CIGSe sample series produced by the same ZSW production line (more details can be found in the text).

a α* reported for $ZnIn_2Se_4$. [Note that no indication of a second contribution was observed in the curve fit of the Zn $2p_{3/2}$ XPS line of the 2 min CBD-ZnS/CIGSe sample, as shown in Fig. 4.24 (b)]. The formation of this (these) compound(s) during the early stages of the investigated ZnS/CIGSe heterointerface formation may involve the incorporation of Zn into the surface of the absorber, a well-documented phenomenon [116-119]. The red hollow square in Fig. 4.25 (right) are also data points of a different CBD-ZnS/CIGSe sample series produced by the same ZSW production line using the same CBD times employed for the currently investigated sample series. The samples were independently measured (and the spectra were provided) by the group of Prof. Andreas Klein of the Surface Science Division of the Institute of Materials Science of the Technische Universität Darmstadt. Differences in Zn α* values for the two sets may be associated with variances in sample handling, experimental measurement setups and/or electron analyzer calibration methods. However, the general trend in the Zn-α*-value evolution as a function of CBD time is observed for both sets of samples.

4.5.3 Near Surface Chemical Structure

In this subsection, XES measurements conducted on the ZnS/CIGSe sample series are used to estimate the thickness of the deposited buffer layers and gain a better understanding of its chemical environment at the near-surface bulk.

The XES spectra of the Zn $L_{2,3}^{III}$ and In $M_{4,5}$ emission regions for the ZnS/CIGSe sample series are presented in Fig. 4.26 (a). To estimate the thickness of the deposited ZnS layers on the sample series, the analysis was focused on the attenuation of the In $M_{4,5}$ emission, as described in Sect. 4.4.3. The XES spectra were interpreted as the sum of a bare CIGSe contribution and a ZnS contribution, as described by eqn. (4.3). In this case, the weighing factor b of eqn. (4.3) was set as the $I^{sub}(x):I^{sub}_{ref}$ ratio of the In $M_{4,5}$ emission. The λ_{exc} and λ_{em} attenuation lengths of In $M_{4,5}$ emission (370.4 eV) energies in ZnS for the employed excitation energy (i.e., $h\nu_{exc}$ = 550.0 eV) are 311 nm and 130 nm, respectively, as retrieved from ref. [70]. Knowledge of these values allows for the use of eqn. (4.5), which yields a λ^* of 65 nm. The estimated ZnS thicknesses of the investigated sample series as a function of CBD time is presented in Fig. 4.26 (b). Based on a linear regression fit of the calculated ZnS effective values, a deposition rate of 2.54 ± 0.56 nm/min is obtained. The XES-determined

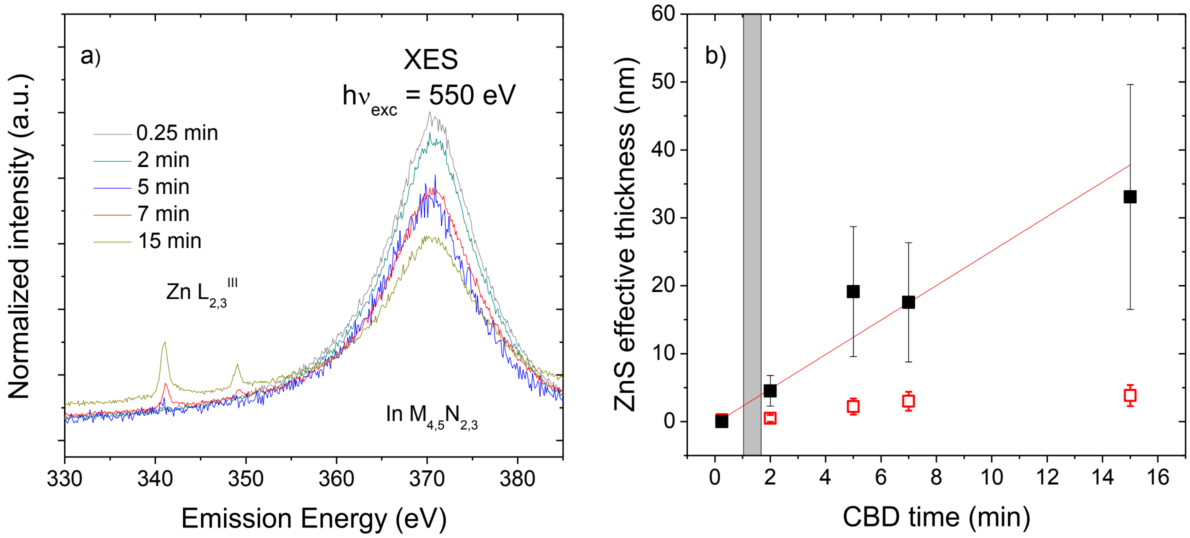

Figure 4.26 (a) Zn $L_{2,3}^{III}$ and In $M_{4,5}$ XES spectra of the ZnS/CIGSe samples, normalized according to measurement time. (b) Thickness of deposited ZnS layer as a function of CBD-treatment time, determined from the attenuation of the In $M_{4,5}$ substrate-derived emission. The red hollow squares represents the XPS-determined ZnS effective thicknesses. The gray-shaded area indicates the onset of the buffer deposition, as determined by the XPS analysis.

CBD-ZnS deposition rate is significantly higher than the XPS-determined one (i.e., 0.3 ± 0.1 nm/min). As discussed in Sect. 4.5.1, this variance arises due to the incomplete coverage of the ZnS layer on the absorber surface, causing a considerable underestimation of the XPS-determined buffer deposition rate. Because of the higher ID of the XES technique, the XES-determined value does not become significantly altered by the morphological effect of the buffer layer. The 15 min CBD-ZnS/CIGSe sample was assessed to have a ZnS layer thickness of 33 ± 17 nm, in agreement with the reported ZSW ZnS thickness [100]. The buffer thickness evaluation also confirms that the buffer deposition rate of the CBD-ZnS treatement is lower than the CBD-CdS treatment [100].

XES experiments probing the chemical environment near the heterointerface were conducted. Fig. 4.27 shows the changes of the Se $M_{2,3}$/S $L_{2,3}$ XES region as a function of CBD treatment time (after normalization to the spectrum area) for the ZnS/CIGSe sample series. As explained in Sect. 4.4.3, the overlapping of the XES signals originates from the similar energetic positions of the states involved in the Se $M_{2,3}$ and S $L_{2,3}$ transitions (i.e., Se 4s → Se 3p and S 3s → S 2p, respectively). The Se $M_{2,3}$ emission is considerably weaker than the S $L_{2,3}$ emission, as highlighted by the magnification factors of samples with lower sulfur content in the sample series (i.e., shorter CBD-ZnS treatment times).

The spectrum of the bare CIGSe absorber sample (Fig. 4.27, bottom) is completely ascribed to Se $M_{2,3}$ emission. A combination of Se $M_{2,3}$ and S $L_{2,3}$ emissions is, however, expected for the spectra of all CBD-ZnS/CIGSe samples. After 0.25 min of CBD-ZnS treatment, the main peak broadens and shifts to higher emission energy. In contrast to the spectrum of the equivalent CBD-CdS/CIGSe sample series, the Se $M_{2,3}$ doublet features are still visible in the present spectrum, an indication of slower S deposition on the sample. Longer CBD-ZnS periods result in the following spectral changes: the main peak becomes sharper, while its energy position shifts to ~ 148 eV, and three new spectral features [e.g., located approximately at (a) 152.1, (b) 153.2, and (c) 157 eV] appear. The observed changes are consistent with a CIGSe-to-ZnS spectral shape evolution. Features (a) and (b) correspond to Zn 3d-related transitions (i.e., Zn 3d → S $2p_{3/2}$, and Zn 3d → S $2p_{1/2}$ transitions, respectively), indicative of S-Zn bonding. Feature (c) arises from the relaxation of upper valence band electrons into S 2p core holes.

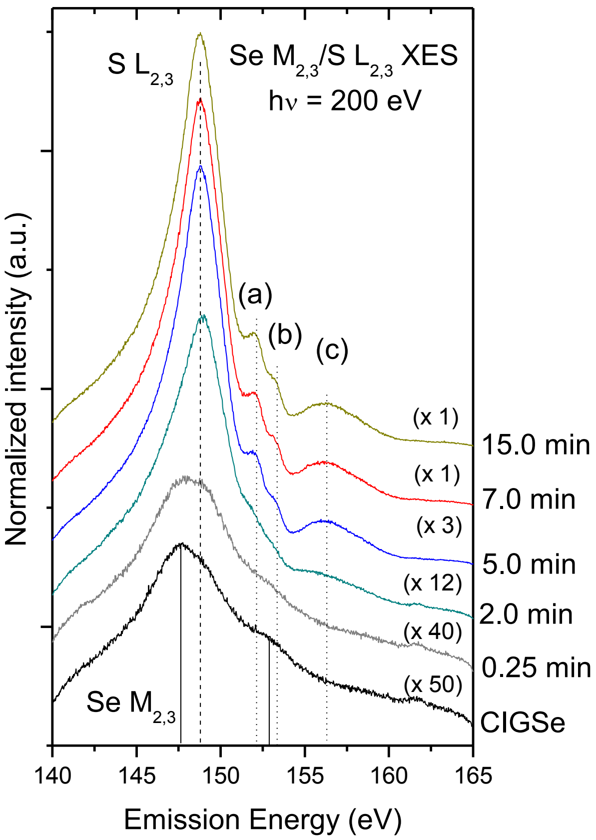

Figure 4.27 Se $M_{2,3}$/S $L_{2,3}$ XES spectra of the ZnS/CIGSe samples, normalized to spectrum area. Solid and dashed lines serve as guides for spectral features pertaining to Se- and S-related transitions, respectively. These transitions are identified in the text.

4.5.4 Principal Component Analysis

In order to determine the minimum number of spectral contributions comprising the set of sample spectra, the Se $M_{2,3}$/S $L_{2,3}$ XES spectra of the 0.25 – 7 min CBD-ZnS/CIGSe samples were evaluated using principal component analysis (PCA). As explained in Sect. 4.4.4, the spectra set of an inert heterointerface may be satisfactorily reconstructed by two spectral components. Requiring more than 2 components to do so would suggest the presence of interface species in the heterointerface. The measured XES spectra along with respective two-component and three-component PCA reconstructions are presented in Fig. 4.28 (a). The magnified residua of the reconstruction are shown in Fig. 4.28 (b). Clearly, the three-component reconstructions yield a better agreement for all evaluated spectra, especially for lower CBD times. The effect of the third component on the quality of the match between the measured and reconstructed spectra is more evident for the ZnS/CIGSe samples than for the CdS/CIGSe samples. Furthermore, the shape of the residua for the two-component reconstruction of the 2 min CBD-ZnS/CIGSe sample spectra is very similar to that of the 1 min CBD-CdS/CIGSe sample [see Fig. 4.12 (b)]. It was established that a mixture of In_2S_3 and CdS nanoparticles is present in the CdS/CIGSe heterointerface. Comparable PCA results of the spectra of the ZnS/CIGSe samples would also suggest the presence of interface species in this heterointerface.

Target transformation analysis of the Se $M_{2,3}$/S $L_{2,3}$ XES spectra of selenium- and sulfur-containing references was carried out to reveal the identity of the interface species. Fig. 4.29 (a) and (b) show the reference spectra and resulting target transformation using the eigenvectors of the two- and three-component PCA reconstructions (see Fig. 4.28), respectively. In an inert heterointerface scenario, only the measured CIGSe and ZnS spectra would be expected to be revealed as components by the target transformation analysis. As shown in Fig. 4.29 (a), the quality of the match between the measured spectra and the two-component transformation is good for ZnS and CIGSe; although a slight deviation is found at

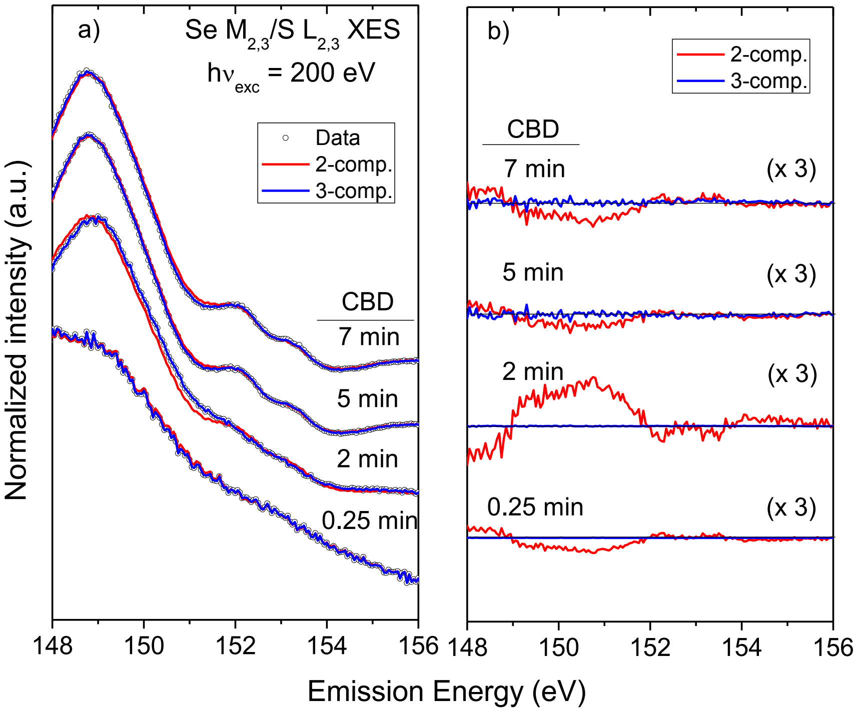

Figure 4.28 (a) Reconstruction of the Se $M_{2,3}$/S $L_{2,3}$ XES spectra of the 0.25 - 7 min CBD-ZnS/CIGSe samples using two and three eigenvectors determined from principal component analysis (PCA). (b) Magnified difference between the measured Se $M_{2,3}$/S $L_{2,3}$ XES spectra and the respective PCA reconstructions.

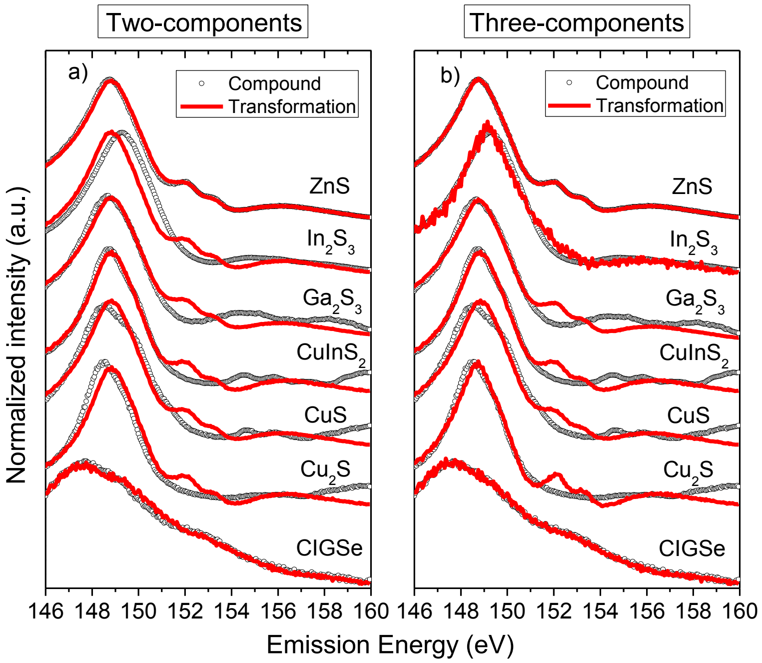

Figure 4.29 Target transformations of Se $M_{2,3}$/S $L_{2,3}$ XES spectra of several selenium- and sulfur-containing reference compounds calculated by linear combinations of the eigenvectors of the (a) two-component and (b) three-component PCAs. Vertical offsets added for clarity.

149-152 eV, the same energy range at which deviations occurred in the two-component PCA reconstruction of CdS. The good agreement is not surprising because, even if an interface species is present in the investigated heterointerface, ZnS and CIGSe are expected to be the two main components. Fig. 4.29 (b) shows the target transformation when a third component is included in the analysis. A drastic improvement is found for the In_2S_3 fit, whereas no significant improvements occur in the fits of the other reference spectra (except minor improvements in the ZnS and CIGSe fits). This clear result is a strong indication that In-S bonds are formed. Additionally, the three-component target transformation yields better matches for the ZnS and CIGSe spectra, further backing a reactive heterointerface scenario for the present samples series.

4.5.5 Least-squares Fitting Analysis

Next, the Se $M_{2,3}$/S $L_{2,3}$ XES spectra of the ZnS/CIGSe sample series were analyzed through least-squares fitting. Fig. 4.30 (top panels) presents the fits of the 0.25 – 5 min (left - right) CBD-ZnS/CIGSe sample spectra using only the CIGSe and ZnS reference spectra. The residua of the fits, particularly those of the lower CBD times, confirm that the analyzed spectra cannot be modeled as only a linear combination of these two reference spectra, as

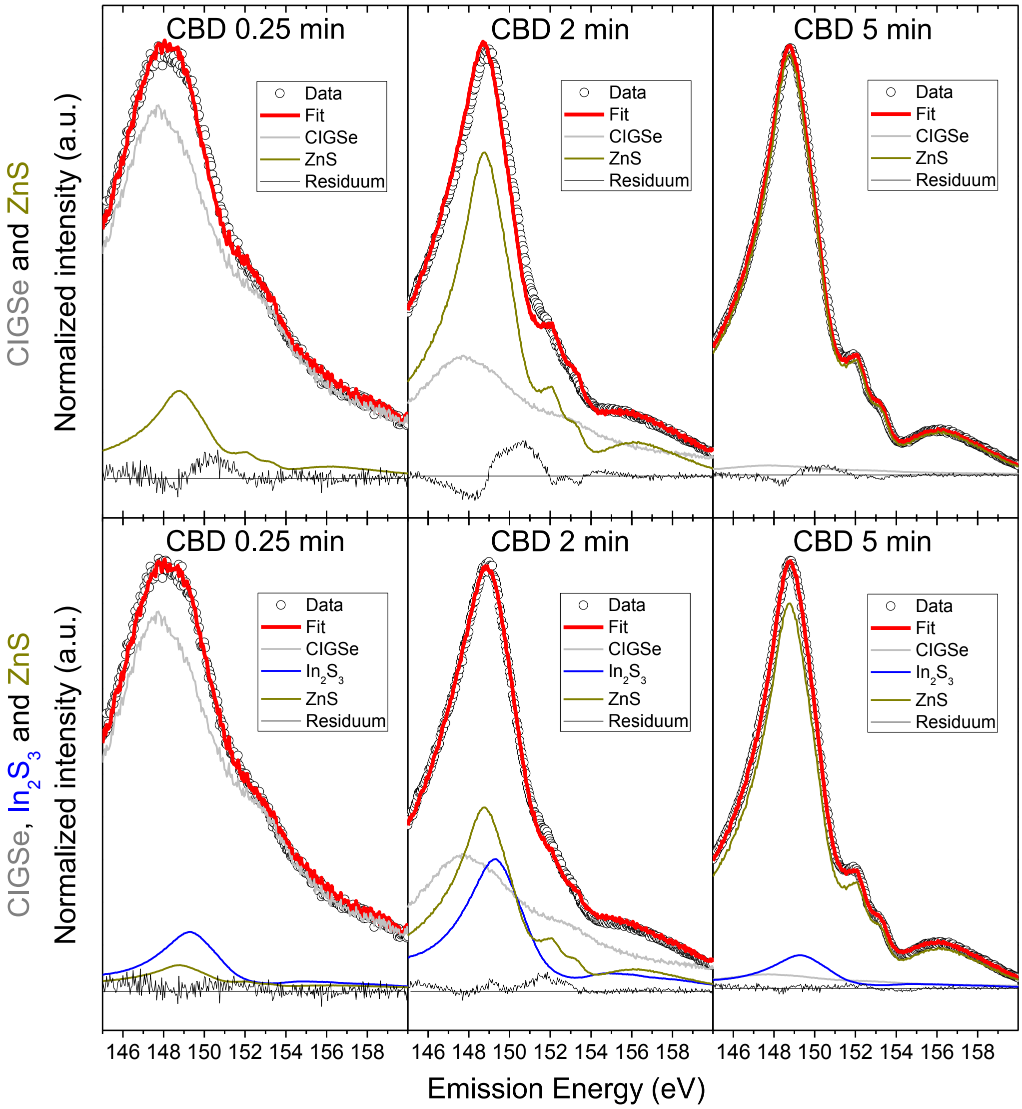

Figure 4.30 Least-squares fits of the Se $M_{2,3}$/S $L_{2,3}$ XES spectra of the 0.25 - 5 min CBD-ZnS/CIGSe samples using the following sets of reference spectra as spectral contributions (top panels): CIGSe and ZnS; and (bottom panels): CIGSe, In_2S_3 and ZnS, respectively.

predicted by the PCA and target transformation results. Fig. 4.30 (bottom panels) shows the linear-squares fits of the measured spectra using CIGSe, In_2S_3 and ZnS spectra. When this set of reference spectra is used, a better agreement is found between the measured sample spectra and their respective fits. The residuum of the 2 min CBD-ZnS/CIGSe sample spectrum fit in Fig. 4.30 (bottom panels, center) exhibits a double-peak adjacent to the Zn 3d-related doublet positions (i.e., transitions characteristic of S-Zn bonding), similar to what was seen in the least-squares fit analysis of spectra of CBD-CdS/CIGSe samples (see Fig. 4.14). The origin of this feature was ascribed to a change in shape of the Cd 4d-related peaks, and a spectrum of

CdS nanoparticles was used to represent the spectral contribution of CdS layers deposited on samples with shorter CBD periods. For the present sample series, a suitable spectrum of ZnS nanoparticles was not found to carry out a similar correction. However, due to the fact that the residuum feature occurs for the sample of the series with the most diverse Zn surface chemical environment (i.e., as demonstrated by the Zn XAES experiments in Sect. 4.5.2) and at a CBD-ZnS time just above the threshold of the buffer deposition latency period (i.e., 1.35 ± 0.32 min), it seems safe to assume that the residuum feature is based on the crystalline structure of the ZnS layer. As the thickness of the deposited ZnS layer increases and its crystallinity improves, the Zn 3d-related intensity better resembles that of bulk ZnS, and the residuum spectral feature disappears. The least-squares fit of the 5 min CBD-ZnS/CIGSe sample spectrum supports this argument.

In Fig. 4.31, the evolution of the spectral fractions of the CIGSe, In_2S_3, ZnS components is presented as a function of CBD-ZnS time, as ascertained by analysis shown in Fig. 4.30. As expected, the CIGSe spectral contribution decreases as a function of CBD time, whereas that of ZnS increases. The In_2S_3 contribution grows quickly, at first; the sample with the highest In_2S_3 spectral fraction is the one with the 2 min CBD-ZnS treatment, a CBD time close to the

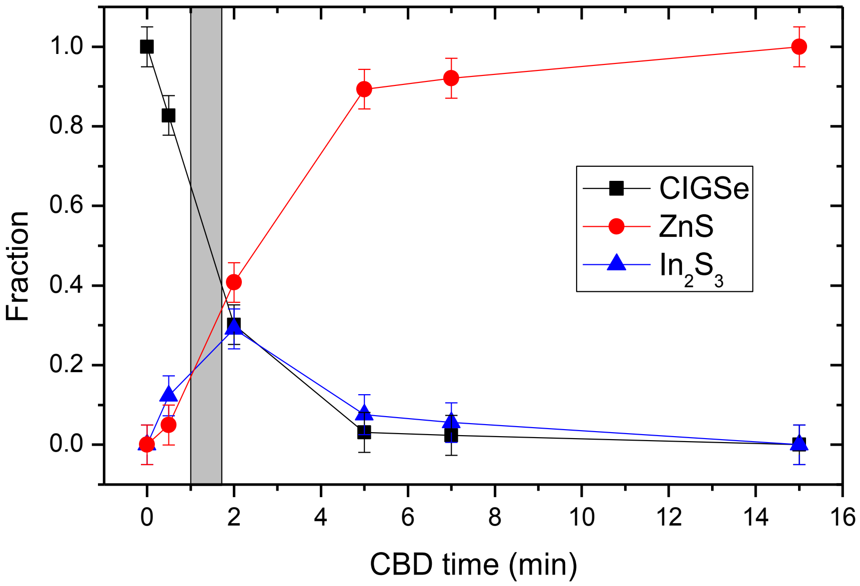

Figure 4.31 Calculated fractions of the CIGSe, ZnS, and In_2S_3 components in the Se $M_{2,3}$/S $L_{2,3}$ XES spectra of the investigated sample series as a function of CBD-ZnS time. The gray-shaded area indicates the onset of the buffer deposition, as determined by the XPS analysis.

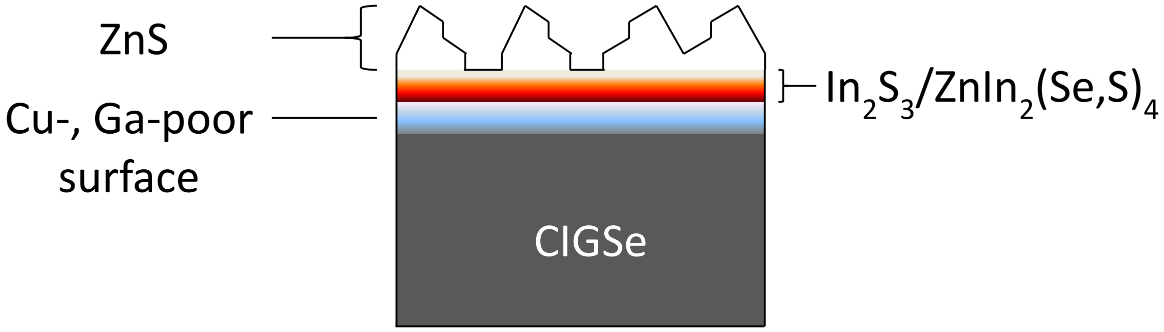

Figure 4.32 Schematic of the chemical structure of the investigated ZnS/CIGSe heterointerface.

(XPS analysis) estimated onset of the buffer deposition. In contrast, the In_2S_3 spectral fraction decreases with CBD times longer than 2 min. Under the present experimental settings [i.e., the excitation (hν = 200 eV) and S $L_{2,3}$ emission (~ 151 eV) energies, $\alpha = \beta = 45$ °], the λ_{exc} and λ_{emi} in ZnS, as obtained from ref. [70], are 48 nm and 60 nm, respectively. Making use of eqn. (4.5), the calculated λ^* is 19 nm. Such value is in agreement with the observed drop in the In_2S_3 spectral fraction of the 5 and 7 min CBD-ZnS/CIGSe samples when the respective XES-determined effective buffer thicknesses are considered. These results indicate that the In_2S_3 is confined to the vicinity of the ZnS and CIGSe interface. The growth period of the In_2S_3 contribution in the present heterointerface sample series is longer than that of the CdS/CIGSe heterointerface; likewise, the fraction of the In_2S_3 contribution in the ZnS/CIGSe surpasses that which was reached in the CdS/CIGSe. These events are correlated to the period of exposure of the bare absorber surface to the chemical bath environment (i.e., the induction period). A schematic of the chemical structure of the investigated ZnS/CIGSe heterointerface is presented in Fig. 4.32.

4.5.6 Interface Band Alignment

In this section, the electronic band alignment of the ZnS/CIGSe heterointerface, experimentally obtained by combining XPS, UPS and IPES, is discussed. UPS and IPES was employed to determine the positions of the VBM and CBM, respectively, and XPS was applied to monitor the IIBB resulting from the buffer deposition. The electronic structure of the CIGSe absorber has already been discussed in Sect. 4.3.3. For visual comparison purposes, Fig. 4.5 is again presented in Fig. 4.33 (a).

In Fig. 4.33 (b), the UPS and IPES spectra of the 15 min CBD-ZnS/CIGSe sample are shown in the course of two Ar^+ ion treatment steps. Once more, the E_g^{surf} of the sample becomes

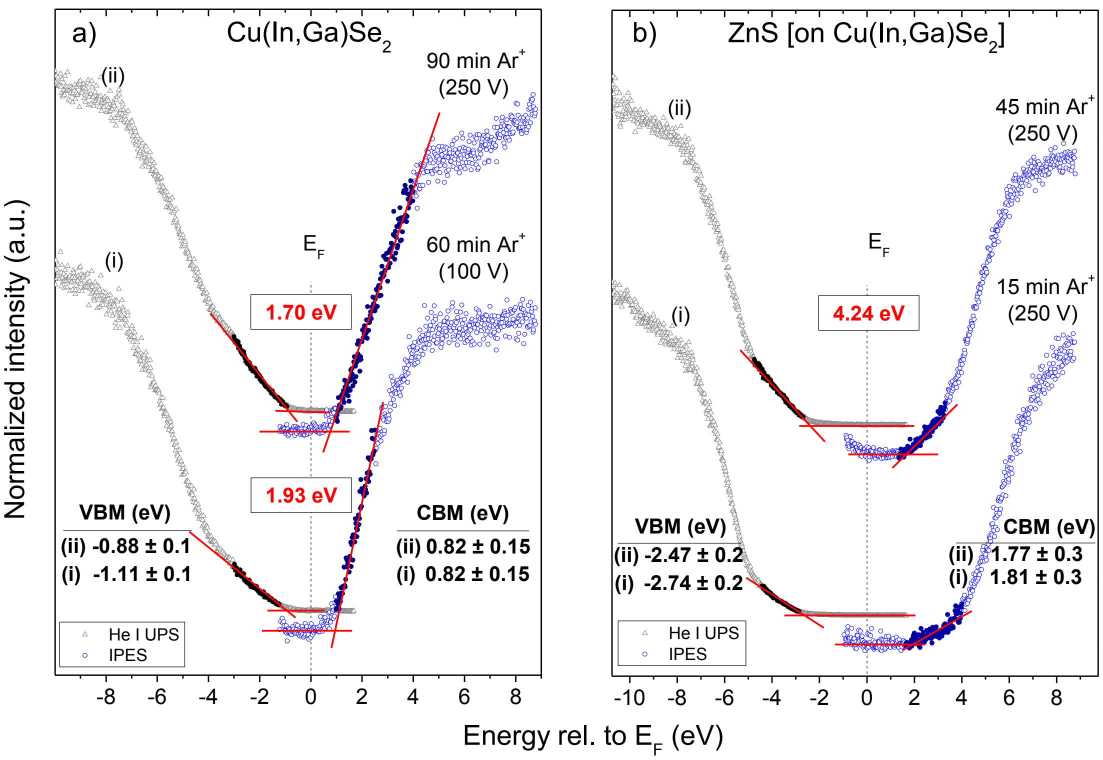

Figure 4.33 He I UPS and IPES spectra of (a) CIGSe, and (b) 15 min CBD-ZnS/CIGSe sample after the indicated mild Ar$^+$ ion treatments. Linear extrapolations of the respective edges are shown in red lines. Measured E_g^{surf} values are shown in the rectangular insets. The experimental uncertainties of the assessed E_g^{surf} values for (a) and (b) are ± 0.2 eV and ± 0.4 eV, respectively.

clearly reduced by the cleaning process, and the leading edges become more pronounced. By linear extrapolation of the sample's VB and CB edges, the VBM and CBM are determined to be -2.47 ± 0.2 eV and 1.77 ± 0.3 eV, respectively. Combining these values yields a E_g^{surf} of 4.24 ± 0.4 eV for the sample with the thickest ZnS layer of the sample series. This E_g^{surf} value is larger than the reported E_g^{bulk} of ZnS (e.g., ~ 3.6 eV) [120].

Changes in band bending at the heterointerface result from deposition of ZnS on top of the CIGSe absorber (i.e., IIBB) [113]. Because the XPS analysis revealed a delayed onset of the buffer deposition, only data of samples that underwent at least 2 min of CBD-ZnS times were used. Furthermore, the only suitable absorber-related lines were the Cu $2p_{3/2}$ and Ga $2p_{3/2}$, as a result of the discovered formation of interface species involving In and Se. Using this combination of XPS core levels (at the selected CBD times) the effects of non-IIBB-related mechanisms (i.e., chemical shifts and/or chemical intermixing between the layers) on the

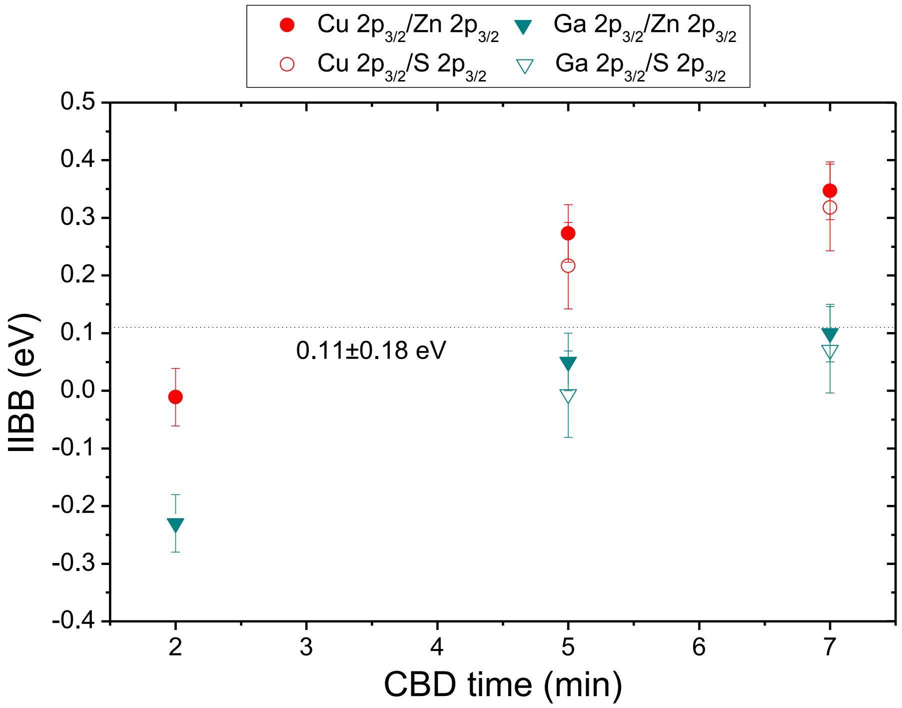

Figure 4.34 Interface-induced band bending (i.e., IIBB) as determined by combining core level positions of the absorber sample, the sample with the thickest ZnS layer, and three samples with intermediate ZnS layer thicknesses. The gray-shaded area indicates the onset of the buffer deposition, as determined by the XPS analysis.

energetic position of evaluated XPS lines are reduced.

The IIBB was calculated using eqn. (4.8). In total, 12 values of IIBB were computed by using combinations of the selected CIGSe and CdS lines. The complete set of IIBB values are displayed in Fig. 4.34. The average IIBB-value of the analysis is 0.11 ± 0.18 eV (as denoted by the dashed line in Fig. 4.34).

Consequently, the VBO and CBO for the heterointerface are ascertained to be -1.48 ± 0.15 and +1.06 ± 0.4 eV, respectively. A schematic diagram of the complete electronic band alignment of the ZSW ZnS/CIGSe heterointerface is shown in Fig. 4.35.

In contrast to the CB alignment found for the CdS/CIGSe heterointerface, a pronounced spike-like CBO (i.e., +1.06 ± 0.4 eV) is observed at the ZnS/CIGSe interface. This is a rather surprising finding, considering the high-performance character of the resulting solar cell devices. In fact, device simulations set a CBO of +0.4 eV as the upper limit band misalignment, at which solar cell performance does not become adversely affected by a reduction in current transport through the absorber/buffer heterointerface. Two plausible mechanisms which may mitigate the (expected) detrimental impact of the misaligned CBO on the perfomance of solar cells are discussed below.

The first plausible mechanism to be discussed is a band gap grading in the heterointerface (and even extending into the bulk of the absorber). A significant intermixing was observed to occur near the heterointerface, along with the formation of chemically similar new interface species (i.e., In_2S_3, $ZnIn_2Se_4$, $ZnIn_2S_4$ with reported E_g values of 2.0-2.3 eV, 2.1-2.2 eV and 2.8 eV, respectively [120-123]). In addition to the beneficial effects the formation of these compounds may exert by widening the E_g near the interface (to be discussed in more detail in Ch. 7), they may also produce better intermediate CBO alignments than the one above ascertained. For example, the CBO of an In_2S_3/CIGSe heterointerface was recently determined to be +0.4 ± 0.26 eV [124]. Such an intermediate step in the CBO configuration could reduce the energetic barrier for carrier transport across the present heterointerface.

A second point of consideration pertains to the changing buffer layer topography, as observed by the uncovered areas of the absorber surface. This scenario opens the possibility for the formation of transport-point contacts between the absorber surface and the ZnO window layer of the solar cell in the portions left uncovered by the buffer, in which case the deposited ZnS acts a passivation layer [125]. This point contact setup would also lower the energetic barrier

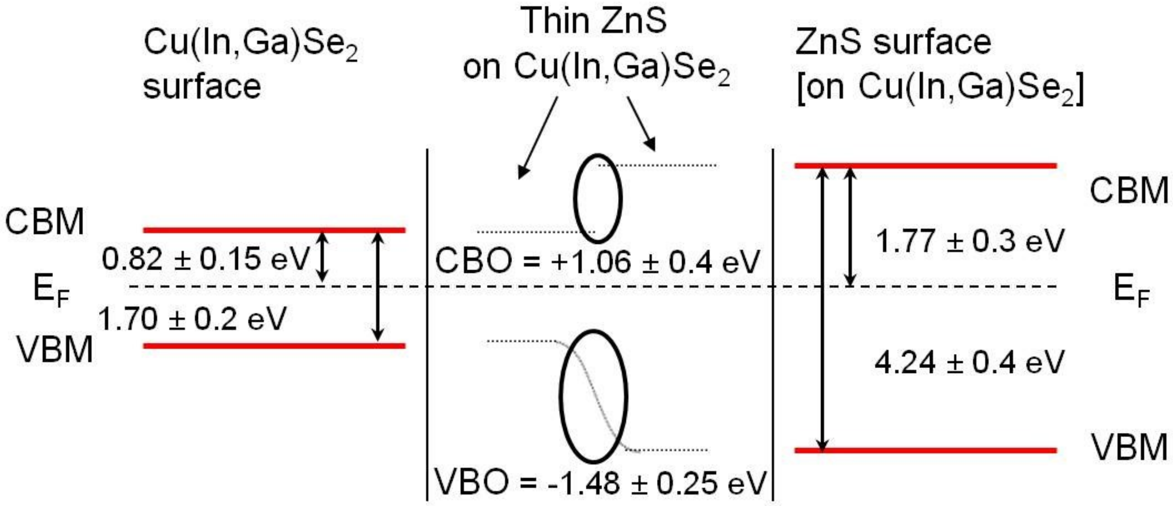

Figure 4.35 Schematic diagram of the ZSW ZnS/CIGSe heterointerface electronic band alignment. The left and right sides of the diagram display the electronic E_g^{surf} (as derived by UPS and IPES) for the bare CIGSe absorber and the ZnS buffer, respectively. The middle portion of the diagram shows the electronic band alignment at the heterointerface after considering interface-induced band bending effects.

to current transport expected of a +1.06 eV CBO alignment. A similar model has been reported for other CIGSe absorber-based solar devices [125].

4.6 Solar Cells

A comparison of the parameters of the best solar cells based on the CdS- and ZnS/CIGSe heterointerfaces produced by the ZSW production line (reported in ref. [126]) is made to associate the electronic structure with the performance of the solar devices. Table 4.5 shows the parameters of the best-perfoming solar cell devices based on the investigated buffer/absorber heterointerfaces [126].

Table 4.5 Parameters of best-perfoming solar cell devices based on the CdS- and ZnS/CIGSe heterointerfaces produced by the ZSW production line, taken from ref. [126].

Heterointerface	η (%)	j_{SC} (mA/cm^2)	V_{OC} (V)	FF
CdS/CIGSe	18.3	34.1	0.695	0.77
ZnS/CIGSe	17.3	35.1	0.661	0.75

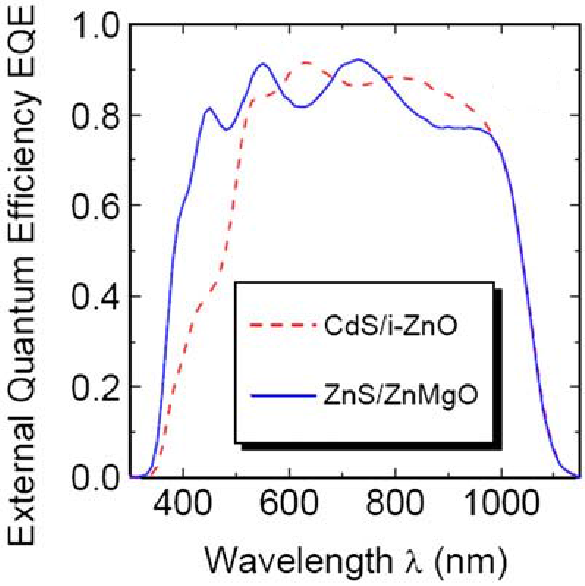

Figure 4.36 External quantum efficiency spectra of solar cell devices based on the CdS- and ZnS/CIGSe heterointerfaces produced by the ZSW production line, taken from ref. [126].

An improvement in J_{SC} is observed for the ZnS/CIGSe-based solar cell, which is ascribed to lower light absorption losses in the ZnS buffer layer compared to the CdS buffer layer. This effect is better perceived in the EQE spectra of the discussed solar cell devices, shown in Fig. 4.36. Losses in the ~ 500 nm region (i.e., ~ 2.5 eV) are evident in the external quantum efficiency (EQE) spectrum of the CdS/CIGSe-based solar cell device, which match the E_g of the CdS layer. This characteristic has made ZnS a potential buffer material substitute of CdS. However, the better electronic structure of the CdS/CIGSe heterointerface, as experimentally determined earlier, explains the better V_{OC} and FF results of the CdS/CIGSe-based solar cell device, which overcome lower obtained j_{SC} values.

4.7 Summary

The characterization of the chemical and electronic structures of the CdS/CIGSe and ZnS/CIGSe heterointerfaces of a ZSW high-efficiency small-area solar cell production line was presented. The starting bare CIGSe absorber was found to exhibit a strong Cu-poor surface, with Na acting as an occupier of Cu-site vacancies. Experimental results of a depth-profile analysis suggest a Ga-depletion at the very surface of the bare CIGSe absorber. The direct measurement of the absorber E_g^{surf} reveals a significant widening with respect to the E_g^{bulk}. Different growth modes and kinetics were observed for the two buffer CBD processes. In both sets of sample series, evidence of significant intermixing across the heterointerfaces was found, as well as the formation of new interface chemical species. Direct measurements of the electronic band alignments of the studied heterointerfaces showed an ideal band alignment configuration for the CdS/CIGSe heterointerface, whereas, a pronounced "spike-like" band configuration was found for the ZnS/CIGSe heterointerface. Plausible mechanisms that may counteract the non-optimal band configuration impact on the perfomance of solar cells were discussed. The here presented results provide an exhaustive analysis of the formation of the CdS/- and ZnS/CIGSe heterointerfaces. The knowledge gained from these investigations should be useful for the development of new optimization routes of chalcopyrite-based solar cell devices.

5 Characterization of the $CdS/CuInS_2$ Heterointerface

5.1 Introduction

As mentioned in Sect. 1.1, one of the features of the CIGSSe alloy system is that by changing the chemical of the absorber, its optical E_g can be tuned between 1.04 eV (for CISe) and 2.53 eV (for CGS) [9]. This property allows the synthesis of chalcopyrite absorber materials with E_g^{bulk} values that match the optimum E_g for solar energy conversion (i.e., ~ 1.4 eV for AM 1.5 [8]). To date, the best-performing chalcopyrite-based thin film solar cells (over 20% on lab-scale [7,10]) are based on $Cu(In_{1-x}Ga_x)Se_2$ (CIGSe) absorbers with a Ga/(In+Ga) = x ratio of around 0.3, resulting in a E_g of approximately 1.2 eV. Despite having an E_g which is better matched to the terrestrial solar spectrum, the performance of "wide-gap" chalcopyrite-based thin film solar cells (i.e., chalcopyrite absorbers with $E_g > 1.25$ eV), are considerably lower than their "low-gap" counterparts {i.e., solar devices based on CIS ($E_g = 1.54$ eV) and CGSe ($E_g = 1.68$ eV) absorbers are currently limited to around 12% and 10% [11,12], respectively}. These comparatively low power conversion efficiencies inhibit development of monolithically connected tandem solar cells (based on a low-gap chalcopyrite solar cell bottom and a wide-gap chalcopyrite solar cell top configuration), which are expected to achieve efficiency maxima in the vicinity of 45% [127].

It has been found that one reason for the lower efficiency of devices based on "wide-gap" chalcopyrite absorber materials is an unfavorable CBO at the buffer/absorber heterojunction [16]. In contrast to the favorable flat conduction band alignments reported for "low-gap" chalcopyrite-based solar cells [15] (and confirmed for the CdS/CIGSe hetrointerface in Ch. 4), the conduction bands of wide-gap absorbers are expected [36,37] (and in one case reported [16]) to be higher than the conduction band of the buffer material. The resulting "cliff"-like (i.e., negative) CBO would decrease the energetic barrier for electron-hole recombination at the heterointerface, opening a recombination path at the interface that leads to a reduced V_{OC} [36,37,41].

In order to establish whether the buffer/absorber heterojunction is indeed responsible for the deficiencies of "wide-gap" absorber-based solar devices, the chemical and electronic properties of the CdS/CIS heterointerface are here addressed. Special attention is given to directly measure the electronic band alignment of the investigated heterointerface. If the CBO is found to be non-optimal, deliberate surface modifications of "wide-gap" CIGSSe absorbers, two of which will be carried out in Ch. 6 and 8, could be used to improve the performance of corresponding thin film solar cell devices. As demonstrated in the previous chapter, it is possible to mitigate the expected deteriorating effect of an unfavorably aligned heterointerface CB on the perfomance of resulting solar cells.

5.2 Experimental Details

A series of CIS substrates with varying CdS buffer thicknesses was prepared. The CIS samples were prepared by collaborators in the HZB Institute of Technology via co-deposition of Cu and In (1.6 μm) on 0.5-μm Mo layers sputtered onto glass substrates, followed by sulfurization using RTP [30]. Prior to the sulfurization step, the deposited precursors are strongly copper rich. Sulfurization produces a uniform CIS layer, with excess Cu contained in a Cu_xS capping phase, which is subsequently removed via a KCN etching process [31]. CdS layers were deposited by immersion in a mixture of cadmium ammonia and thiourea solutions, as described in ref. [33]. Deposition times ranged from 0.5 - 7.0 min. to vary the CdS thickness of the samples. When samples were transported for experimental campaigns outside the HZB, they were sealed in an inert atmosphere (in order to minimize their exposure to air). For the bulk-sensitive XES characterization conducted at the ALS, samples were briefly exposed to air prior to their introduction into the UHV-based beamline.

The surface-sensitive XPS and XAES characterizations of the CdS/CIS sample series were carried out at the HZB employing Mg K_α excitation energies and a SPECS PHOIBOS 150MCD electron analyzer. UPS measurements were conducted with a He discharge lamp using the He I excitation source. IPES experiments were carried out in the laboratory facilities of the group of Prof. Clemens Heske at the University of Nevada, Las Vegas, with the same IPES setup used in Ch. 4 [57-59]. Sputter-cleaned Au foil was probed by both UPS and IPES, and its measured E_F was used as the energy scale calibration reference for subsequent UPS and IPES measurements. To remove adsorbates from sample surfaces, the investigated sample series were submitted to mild Ar^+ ion treatment (kinetic energy upto 250 eV) for short time periods. XES experiments were performed at ALS Beamline 8.0.1 using the Soft X-ray Fluorescence (SXF) endstation [62-64]. Cd $M_{4,5}$ and In $M_{4,5}$ XES measurements were performed on the CdS/CIGSe sample series using an excitation energy of 500 eV. S $L_{2,3}$ XES spectra were measured with an excitation energy of 169.2 eV. All excitation energies were chosen to avoid resonant excitation effects.

5.3 $CdS/CuInS_2$ Heterointerface

In the following section, the characterization of the chemical and electronic structures of the CdS/CIS heterointerface is presented. Surface-sensitive XPS and XAES experimental results are first considered. XES measurements are then presented to complement the heterointerface chemical structure characterization. Finally, the results of a direct investigation of the electronic band alignment of the CdS/CIS heterointerface are discussed.

5.3.1 Surface Chemical Structure

Fig. 5.1 shows the XPS survey spectra of the investigated sample series. The survey spectrum of the bare absorber displays the expected photoemission lines of the absorber elements (i.e., Cu, In, S). In contrast to the ZSW CIGSe absorber studied in Ch. 4, there is no evidence for the presence of Na on the surface of the bare CIS absorber. In general, the Na concentration in Cu-rich prepared CIS films are reported to be significantly lower (i.e., at least by an order of magnitude) than that found in films of selenium-containing chalcopyrites [128-131]. Moreover, the etching process used to remove Cu_xS binary phases from the CIS surface, prior to CdS deposition, is performed in a KCN aqueous solution, followed by extensive washing of the sample with deionized water (to remove KCN traces); it is hence likely that these treatments remove the (small) Na content from the CIS samples. CBD-CdS-treated samples show additional Cd- related photoemission lines in their respective XPS survey spectra, which increase in intensity with longer CBD-CdS treatment periods. At the same time, the signal of absorber-related XPS lines decreases. These events are better observed in the detail XPS spectra of selected absorber- and buffer-related core levels, shown in Fig. 5.2. As in Ch. 4, these changes are attributed to the growth of the CdS layer on top of the CIS substrates. The signals of Cu and In core levels become completely attenuated for samples with CBD-CdS times greater than 2 min, indicating a complete coverage of the absorber surface by the buffer. [The low intensity signal of the Cu $2p_{3/2}$ and In $3d_{3/2}$ lines detected for sample (vi) are attributed to scratches produced during sample mounting, leaving some of the absorber surface exposed.]

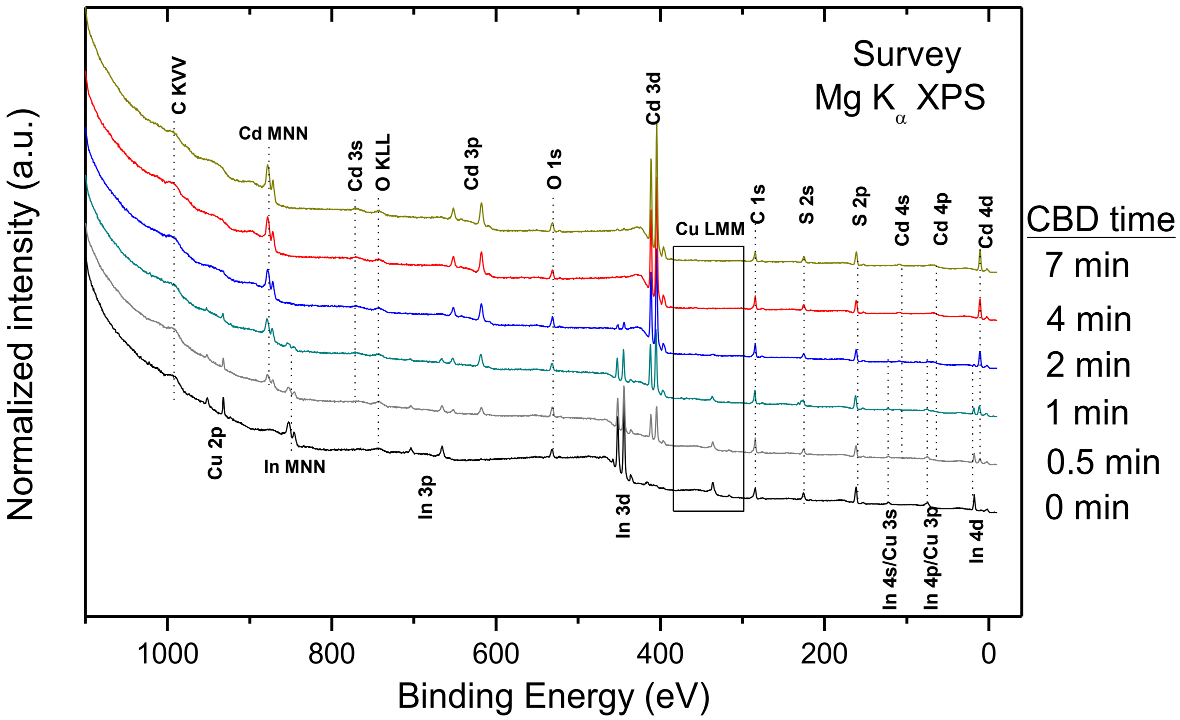

Figure 5.1 XPS Survey spectra of the CdS/CIS sample series. Labels indicate duration of CBD-CdS treatment of respective samples. Vertical offsets are added for clarity. Note that all samples (including the "0 min" sample) have been KCN-etched prior to CBD-CdS treatment.

Because S is found in both the absorber and the buffer, its intensity remains relatively constant. The sample with the longest CBD-CdS time (i.e., 7 min) shows minimal signs of surface S-O$_x$ bonds, as observed by the (magnified) peak at a BE ~ 168 eV. Considering that signs of sulfur oxidation are only found on the sample with the thickest CdS buffer layer, it is not probable that it exerts a considerable impact on the chemical environment near the interface (i.e., constitutes an interface species). Moreover, the removal of surface CdSO$_x$ has been reported to result from the conventional deposition of the ZnO window on top (i.e., by rf-sputtering) of the CdS buffer layer [132].

An estimation of the effective thickness of the CdS layers was performed by evaluating the resulting attenuation and increase of the absorber- and buffer-related XPS core level lines, respectively. The effective thickness of the deposited buffer layers was calculated using eqns. (4.1) and (4.2). Table 5.1 shows the results of this evaluation. The calculated values are fairly

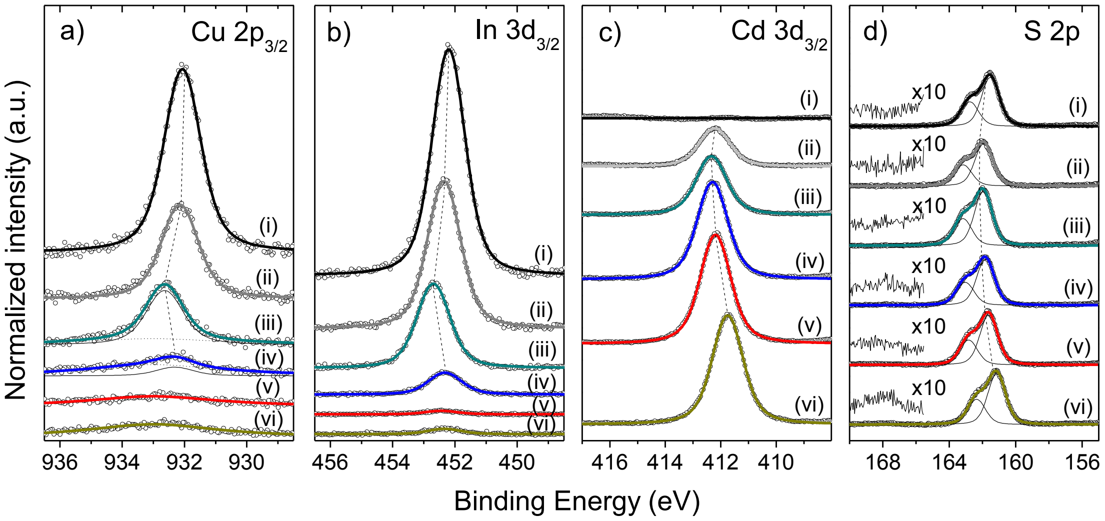

Figure 5.2 XPS detail spectra of the (a) Cu $2p_{3/2}$, (b) In $3d_{3/2}$, (c) Cd $3d_{3/2}$ and (d) S 2p regions of the CdS/CIS sample series, normalized to background intensity. The following CBD-CdS treatment times were used: (i) 0, (ii) 0.5, (iii) 1, (iv) 2, (v) 4, and (vi) 7 min. Dashed lines indicate peak centers, as determined by curve fit analysis. All spectra were measured using Mg K_α excitation. Vertical offsets are added for clarity. The origin of the low intensity detected in (a) and (b) for sample (vi) is discussed in the text.

consistent for the three used photoemission lines. Any variance in the obtained values is attributed to differences in λ. (This is especially the case for the 2.0 min CBD-CdS/CIS sample, in which the signal of the Cu $2p_{3/2}$ is within the XPS detection limit range of 0.1-1.0 at% [45,52].) The absorber-related lines are completely attenuated after 4.0 min of CBD-CdS treatment. Similar results were obtained in the CdS/CIGSe heterointerface study (i.e., Sect. 4.3.1), in which complete coverage was attained after 3 min of CBD-CdS treatment (i.e., of a thickness greater than the ID of the analyzed XPS core levels). The elemental composition of the samples was quantified from the XPS spectra as a function of CBD-CdS time. Once intensities of the fitted core levels were assessed, corrections were made to account for differences in inelastic mean free path [50,51], photoionization cross section [46,47], and the transmission function of the electron analyzer [48]. The resulting compositions are shown in Fig. 5.3.

The surface composition of the CIS absorber without CBD-CdS treatment, as determined by the peak fits, is approximately Cu:In:S = 1:3:5. Although the bulk of the absorber is Cu-rich (due to the CIS growth process), the surface stoichiometry reveals a Cu-poor surface content. Furthermore, the Cu and In surface concentrations decrease exponentially as a function of

CBD-CdS treatment time, as demonstrated by the line fits of the element composition fractions. At the same time, the surface concentration of Cd manifests an asymptotic growth

Table 5.1 Effective buffer thicknesses, d (in nm), of the CBD-CdS/CIS sample series. IMFP (λ) values are also reported in nm and were obtained from refs. [50,51].

CBD (min)	Cu 2p (I/I_0)	$d_{Cu\ 2p}$ ($\lambda = 0.89$)	In 3d (I/I_0)	$d_{In\ 3d}$ ($\lambda = 1.67$)	Cd 3d (I/I_0)	$d_{Cd\ 3d}$ ($\lambda = 1.74$)
0	1	-	1	-	0	-
0.5	0.46	0.7 ± 0.2	0.56	1.0 ± 0.2	0.26	0.5 ± 0.2
1	0.28	1.1 ± 0.2	0.35	1.8 ± 0.8	0.58	1.5 ± 0.3
2	0.05	2.7 ± 0.5	0.09	4.0 ± 0.8	0.95	5.2 ± 1.0
4	0	-	0	-	1.07	-
7	0	-	0	-	1	-

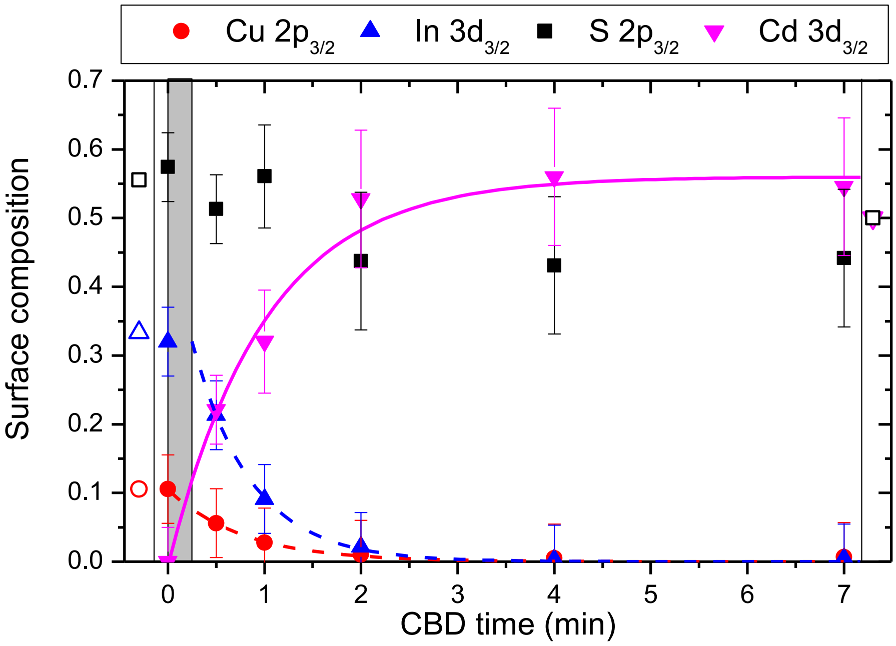

Figure 5.3 Relative surface composition of the CDB-CdS/CIS sample series as a function of CBD-CdS treatment time. The hollow icons at the left and right extremities of the figure represent 1:3:5 and 1:2 stoichiometries, respectively. The gray-shaded area indicates the onset of the buffer deposition, as determined by the XPS analysis.

trend. These findings are in agreement with a uniform layer-by-layer buffer (i.e., Frank-van der Merwe) growth mode [94,95] and are predicted by eqns. (4.1) and (4.2). Likewise, no significant change in surface composition is perceived past 4 min of CBD-CdS treatment, confirming earlier assumptions of a complete coverage of the absorber surface by the buffer layer (i.e., of a thickness greater than the ID of the analyzed XPS core levels). The Cd:S surface composition of samples treated with these CBD times was observed to be slightly Cd-rich (i.e., deviating from the expected Cd:S = 1:1 stoichiometry). To estimate the length of CBD-CdS latency period, the functions of the line fits of the element composition fractions were used to compute the CBD-CdS treatment time at which the element composition remains equal to that of the bare absorber. Table 5.2 presents the results of this evaluation. The average latency period value is 0.11 ± 0.12 min (i.e. 7 ± 7 s), simlar to the mean latency period for the CdS/CIGSe sample series in Sect. 4.4.1 (i.e., 0.07 ± 0.05 min).

Table 5.2 Estimation of the onset of CdS deposition

Elements	Surface composition (at CBD = 0 min)	Fit line formula (x stands for CBD time)	Buffer deposition onset (min)
Cu	0.11 ± 0.05	$0.10*e^{-x/0.784}$	0.00 ± 0.1
In	0.32 ± 0.05	$0.48*e^{-x/0.608}$	0.24 ± 0.1
Cd	0	$0.56-(0.57*e^{-x/1.01})$	0.01 ± 0.1

5.3.2 Cd Modified Auger Parameter Analysis

In order to assess the chemical environment of the deposited Cd atoms, an evaluation of the modified Cd Auger parameter (Cd α^*) is studied as a function of CBD-CdS treatment time.

Fig. 5.4 displays the Cd $M_{45}N_{45}N_{45}$ (MNN) XAES lines of all CBD-CdS/CIS samples in the series (spectra are normalized to the maximum intensity value). The spectra shown at the bottom part of the figure correspond to samples in which absorber-related XPS core levels are still detected (i.e., thin CdS layers). The top spectra are of samples in which absorber-related XPS lines are no longer detected (i.e., thick CdS layers). Spectra comparison shows overall similar Cd MNN lines with respect to spectral shape and KE position, with the two following exceptions: (i) the broader shape of the 0.5 min CBD-CdS/CIS sample spectrum and (ii) an energetic shift of the 7 min CBD-CdS/CIS sample spectrum. Exception (i) suggests an overlapping of two Cd XAES lines, hinting at the presence of two Cd species. In order to test such a prospect, an appropriately weighted fraction of the 7 min CBD-CdS/CIS sample XAES

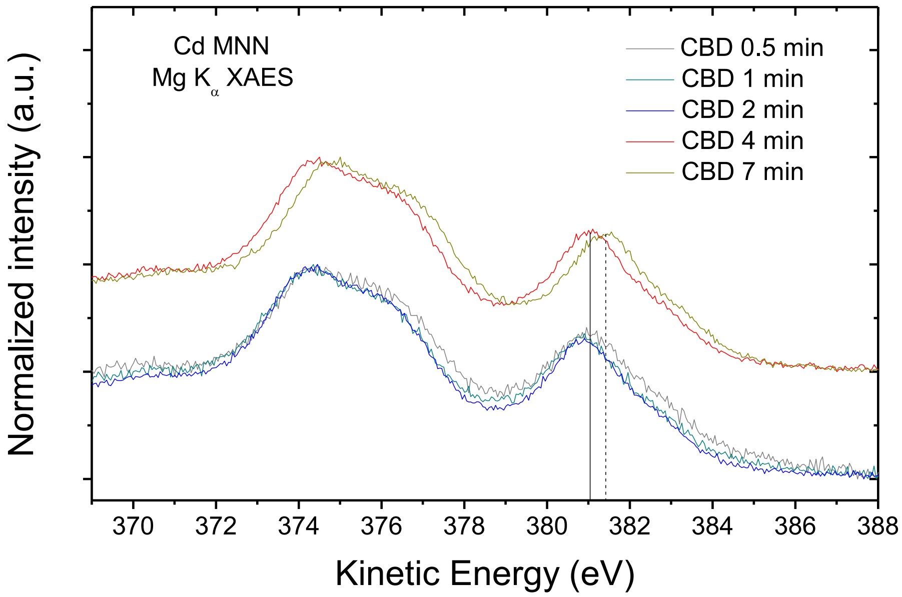

Figure 5.4 Cd $M_{45}N_{45}N_{45}$ XAES lines of CBD-CdS-treated samples in the investigated CdS/CIS sample series. Vertical offsets are added for clarity

line was subtracted from the spectrum in question, while not allowing the difference to fall into a negative intensity. The results of this evaluation are shown in Fig. 5.5 (left). The difference spectrum resembles the non-linear background of the CIS absorber in the same energy range (red line). Based on the effective thickness calculations of the deposited CdS layers in Sect. 5.3.1, the average CdS thickness value for the 0.5 min CBD-CdS/CIS sample is 0.73 ± 0.23 nm. The λ of the Cd MNN line (KE ~ 382 eV) in CdS is 0.99 nm [50,51]. Therefore, the CIS-derived background line is not completely attenuated by the deposited CdS layer and causes the broadening of the 0.5 min CBD-CdS/CIS sample spectrum. In the case of exception (ii), the relative shift in KE position has no significant effect on the modified Cd Auger parameter (α*) for the 7.0 min CBD-CdS/CIS sample (as will be shown below), due to a similar shift in the BE position of the sample's Cd $3d_{3/2}$ core level peak core. Because the deposited CdS layer for the 4.0 min CBD-CdS/CIS sample is sufficiently thick to completely attenuate the intensity of the absorber-related XPS lines, such a significant shift in the XAES line of the 7.0 min CBD-CdS/CIS sample cannot be ascribed due to band bending. Instead, the observed shift in the XAES line arises due to sample surface charging because of the thicker CdS layer on the sample.

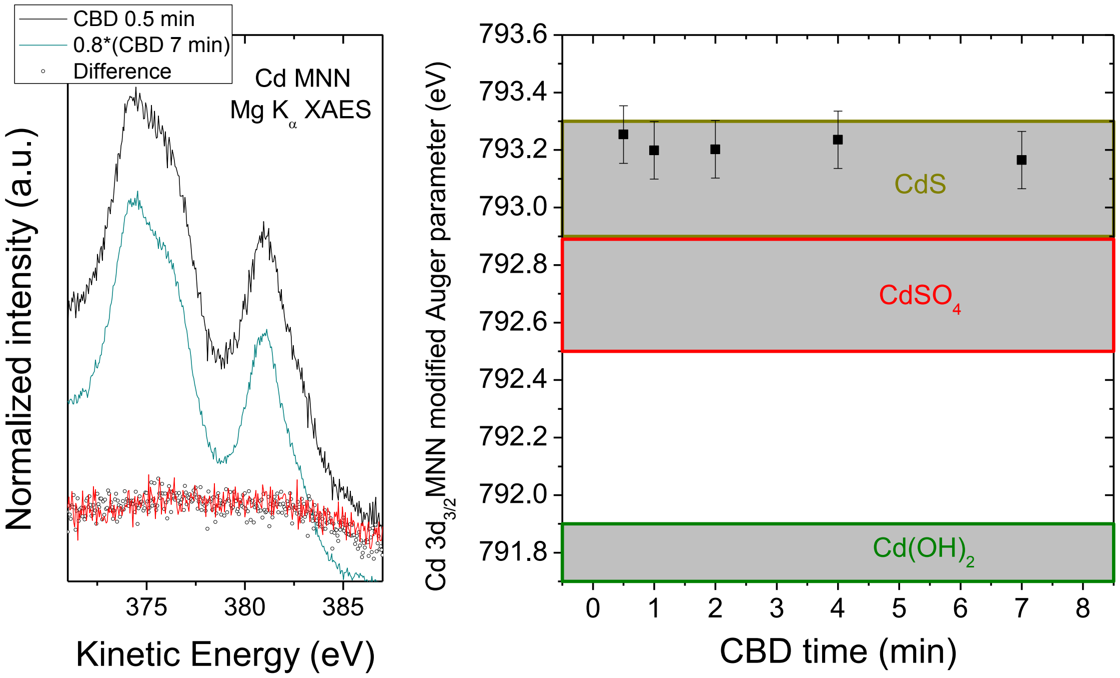

Figure 5.5 (left) Decomposition of the Cd $M_{45}N_{45}N_{45}$ XAES line of the 0.5 min CBD-CdS/CIS sample. (Right) Cd modified Auger parameter (α*) of CBD-CdS-treated samples in the CdS/CIS sample series shown as a function of CBD time.

The modified Cd Auger parameters of the samples were computed by adding the BE of the Cd $3d_{3/2}$ XPS core level and the KE of the Cd $M_4N_{45}N_{45}$ XAES lines. The modified Cd Auger parameters computed for the investigated sample series are presented in Fig. 5.5 (right), along with reported Cd α* value ranges for CdS, $CdSO_4$ and $Cd(OH)_2$ [45,52,53,133-135]. The Cd α* values only vary by approximately 0.1 eV among the sample set and fall within the reported range for CdS. Consequently, the modified Auger parameter analysis does not reveal the formation of new Cd species during the early stages of the CBD process. The fact that Cd atoms are deposited on a S-containing substrate (as is the case of the CIS absorber surface) appears to facilitate the formation of more defect-free CdS layers [93,99]. Based on these results, the CdS/CIS heterointerface appears to be chemically abrupt.

5.3.3 Near Surface Chemical Structure

In this subsection, XES measurements conducted on the CdS/CIS sample series are presented. The thickness of the deposited buffer layers can be evaluated and, more importantly, a better understanding of the chemical environment at the near-surface bulk can be assessed from these spectra.

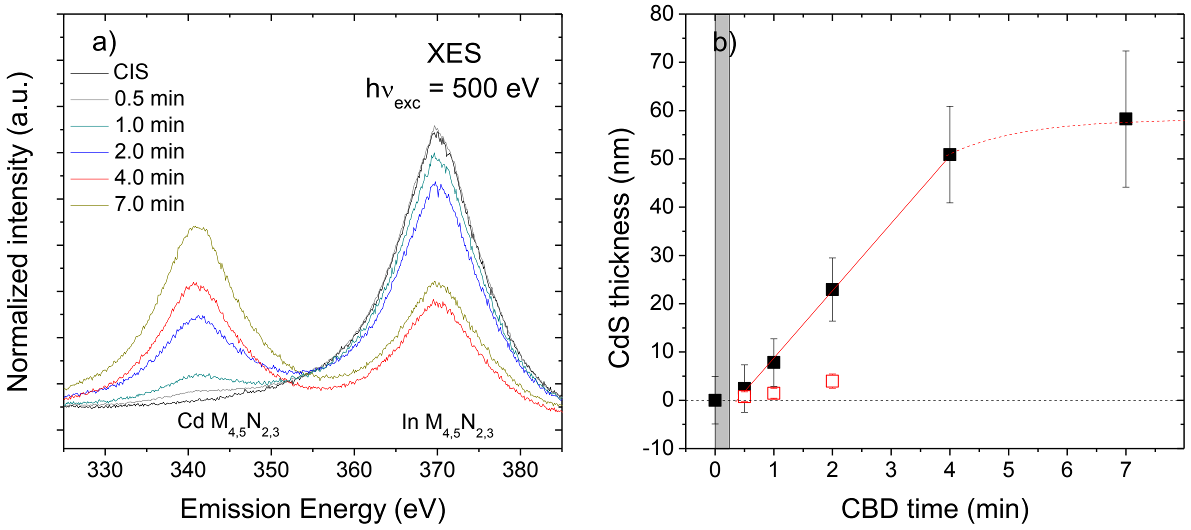

Figure 5.6 (a) Cd M$_{4,5}$ and In M$_{4,5}$ XES spectra of the investigated set of CdS/CIS samples. (b) Thickness of deposited CdS layer as a function of CBD-CdS treatment time, determined from the attenuation of the In M$_{4,5}$ substrate-derived emission. The hollow red squares represent the XPS-determined CdS effective thicknesses. The gray-shaded area indicates the onset of the buffer deposition, as determined by the XPS analysis.

The XES spectra of Cd M$_{4,5}$ and In M$_{4,5}$ emission regions for the CdS/CIS sample series are shown in Fig. 5.6 (a). To estimate the thickness of the deposited CdS layers on the sample series, the attenuation of the In M$_{4,5}$ emission was analyzed in the same manner as in Ch. 4. The XES spectra of the investigated sample series were interpreted as the sum of a bare CIS contribution and a CdS contribution, as described by eqn. (4.2). In this case, the weighing factor *b* of eqn. (4.2) was set as the $I^{sub}(x):I^{sub}_{ref}$ ratio of the In M$_{4,5}$ emission.

The required λ_{exc} and λ_{emi} attenuation lengths in CdS for the employed excitation energy, as retrieved from ref. [70], are 215 nm and 109 nm, respectively. Introducing these values into eqn. (4.4) yields a λ^* of 51 nm. (The same λ^* value was used in Sect. 4.3.5 in the analysis of the CdS/CIGSe heterointerface). The calculated CdS layer thicknesses of the investigated sample series is presented in Fig. 5.6 (b) as a function of CBD-CdS treatment time. The XPS-determined CdS effective thicknesses (from Sect. 5.3.1) are also shown for comparison. Because of the higher ID of the XES technique, the XES-determined values are significantly higher than the values estimated by XPS. The buffer layer growth is seen to plateau after 4 minutes of CBD-CdS treatment [as shown by the red-dashed line (---)], an observation that is consistent with the reported buffer growth trend for the current CBD-CdS treatment protocol [33]. Based on the linear regression fit conducted on the estimated CdS thickness values of

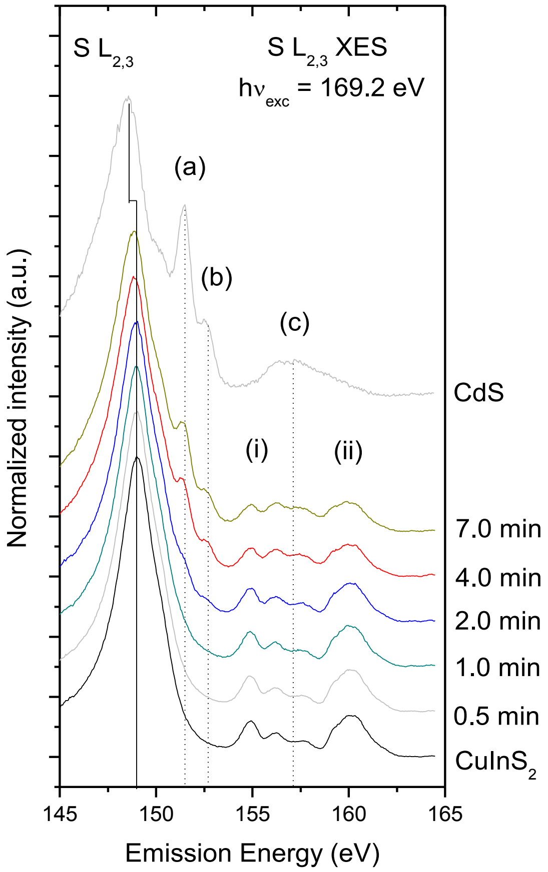

Figure 5.7 S $L_{2,3}$ XES spectra of the investigated set of CdS/CIS samples, normalized to spectrum area. Solid and dashed lines indicate various spectral features arising from S-related transitions. These transitions are identified in the text. Vertical offsets are added for clarity.

the set of samples with the 0.5 – 4.0 CBD-CdS treatment time range, a deposition rate of 10.3 ± 1.8 nm/min was found. The 7 min CBD-CdS/CIS sample is estimated to have a CdS thickness layer of 58 ± 15 nm.

Continuing with the near-surface bulk chemical environment analysis, Fig. 5.7 presents changes in the S $L_{2,3}$ XES as a function of CBD time for the investigated CBD-CdS/CIS sample series (normalized to spectral area). The spectrum of the bare CIS absorber sample (Fig. 5.7, bottom) is dominated by 3 spectral features. The main peak, located ~ 149 eV, is derived from S 3s → S 2p transitions. Feature (i) corresponds to In 5s → S 2p transitions, directly indicating the presence of S-In bonding. Feature (ii) is associated with Cu 3d → S 2p transitions. These spectral features continue to be observed in spectra of the CBD-CdS/CIS samples, although more slightly in samples with longer CBD times. As determined earlier, the thickest deposited CdS layer of the sample series is 58 ± 15 nm. This thickness is insufficient to completely attenuate the S $L_{2,3}$ XES signal stemming from the CIS substrate (i.e., at hν = 169.2 eV, the λ* is 54 nm). Other spectral changes associated with the CBD treatment are: a main peak position shift towards lower emission energies (~ 148 eV) and the emergence of three new spectral features [e.g., located approximately at (a) 151.4, (b) 152.6, and (c) 157 eV]. These spectral peaks are characteristic of CdS [103,104]. Features (a) and (b) correspond to Cd 4d-related transitions (i.e., Cd 4d → S $2p_{3/2}$, and Cd 4d → S $2p_{1/2}$ transitions, respectively), directly indicating the presence of S-Cd bonding. Feature (c) arises from upper valence band electrons relaxing into S 2p core holes.

5.3.4 Principal Component Analysis and Least-squares Fit Analysis

In order to detect the possible presence of interface species, the spectra of CBD-CdS/CIS samples were evaluated through principal component analysis. Fig. 5.8 (a) show the measured XES spectra along with two-component (representing an inert heterointerface scenario) and three-component (representing a reactive heterointerface scenario) reconstructions. The magnified difference between the measured spectra and the PCA reconstructions is displayed

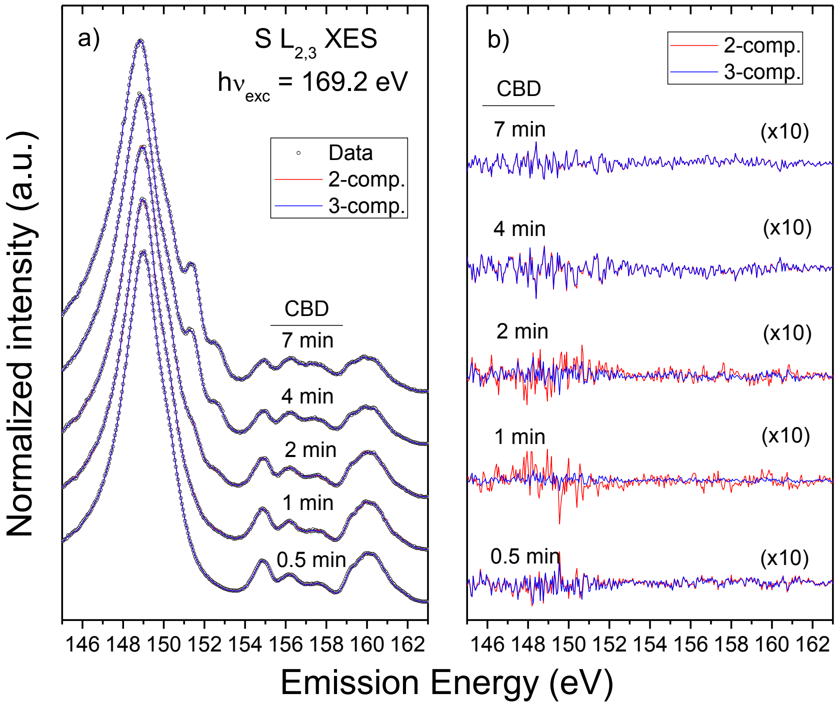

Figure 5.8 Reconstruction of the S $L_{2,3}$ XES spectra of the 0.5 - 7 min CBD-CdS-treated samples using two and three eigenvectors determined from principal component analysis (PCA). (b) Magnified difference between the measured S $L_{2,3}$ XES spectra and the respective PCA reconstructions. Vertical offsets are added for clarity.

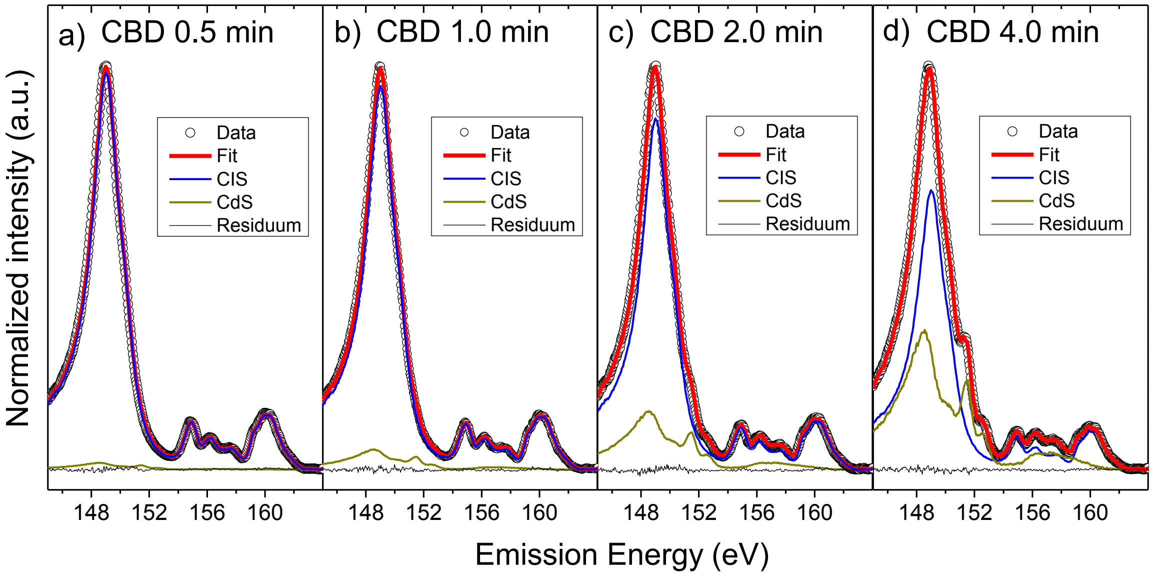

Figure 5.9 (a)-(d) Least-squares fits of the S $L_{2,3}$ XES spectra of samples treated with 0.5 min, 1 min, 2 min and 4 min CBD-CdS times, respectively. Appropriate weights of the CIS and CdS references are shown, along with the corresponding residuum lines.

in Fig. 5.8 (b). Both reconstructions are in excellent agreement with the measured spectra, meaning that adding a third component to the PCA does not result in significant improvement of the simulation. This fact is a strong indication for an abrupt CdS/CIS heterointerface.

The measured S $L_{2,3}$ XES spectra of the CBD-CdS/CIS samples were submitted to least-squares fitting analysis. The spectra of the bare CIS absorber and a thick CdS sample were used as reference spectra. Fig. 5.9 (a) – (d) show the fits of the spectra for samples with 0.5 – 4 min CBD-CdS treatment times. All spectra could be satisfactorily simulated with these two reference spectra, as expected by the PCA results. Consequently, there was no indication of any new interface chemical species being formed during the CBD process, which is in agreement with the earlier presented modified Auger parameter results (Sect. 5.3.2).

5.3.5 Interface Band Alignment

In order to determine whether the buffer/absorber heterojunction is indeed the limiting interface in “wide-gap” absorber-based solar devices, a firsthand experimental determination of the band alignment at the CdS/CIS interface is sought. A complete picture of the electronic interface properties was experimentally obtained by combining the XPS, UPS and IPES techniques, similar to what was presented in Sections 4.4.6 and 4.5.6.

Fig. 5.10 (a) shows UPS and IPES spectra of the bare CIS absorber prior to and after mild Ar$^+$ treatment cycles. As the sputtering time (and/or ion energy) increases, it is observed that the leading edges of the UPS and IPES spectra shift closer to E_F due to removal of surface contaminants. After a 15-min Ar$^+$ ion treatment at an ion energy of 250 eV, a VBM and CBM of -1.08 ± 0.1 eV and 0.80 ± 0.15 eV, respectively, can be determined via linear extrapolation. {Sputtering-induced metallic phases are detected after more prolonged sputtering treatments [15,136], as indicated by the appearance of states at the E_F level in the top UPS and IPES spectra of Fig. 5.11 (a).} From these obtained values, a E_g^{surf} of 1.88 ± 0.2 eV can be assigned to the investigated CIS absorber. Note that at the surface, E_F within the gap is located closer to the CBM than to the VBM, which would be expected for an n-type semiconductor. Furthermore, it can be observed that the determined CIS E_g^{surf} is significantly higher than the CIS E_g^{bulk}. This E_g widening seems to be a recurring feature of chalcopyrite absorbers, as it

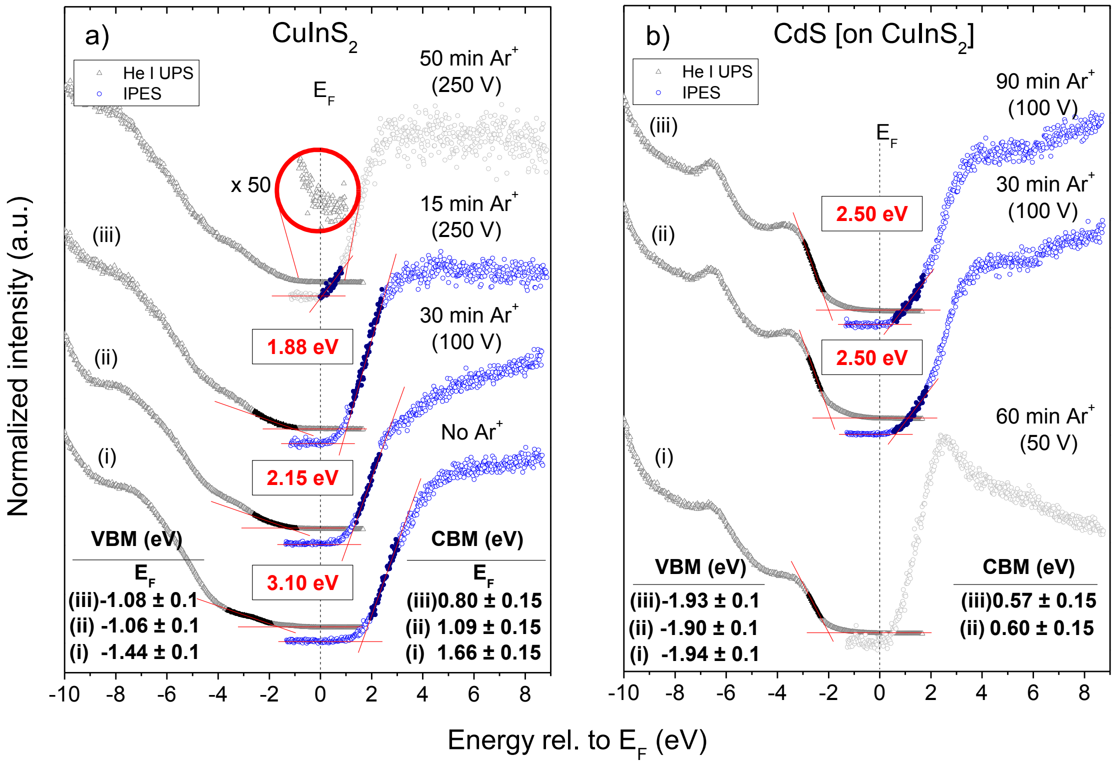

Figure 5.10: He I UPS and IPES spectra of (a) CIS, and (b) 7 min CBD-CdS/CIS samples. The ion energy used for the Ar$^+$ ion treatment is shown in parenthesis next to the Ar$^+$ ion treatment time. Linear extrapolations of the respective edges are shown in red lines. Measured E_g^{surf} values are shown in the rectangular insets. The experimental uncertainty of the assessed E_g^{surf} values is ± 0.2 eV. Vertical offsets are added for clarity.

was also observed for CIGSe in Ch. 4 and has been reported for other chalcopyrite absorbers [15,16,83,89]. The band gap widening is again ascribed to a Cu-poor absorber surface, discussed in the XPS results of Sect. 5.3.1. Note that the obtained E_g^{surf} (i.e., 1.88 ± 0.2 eV) is close to reported E_g values of In_2S_3 thin films (i.e., 2.0 - 2.3 eV) [121].

Fig. 5.10 (b) shows UPS and IPES spectra of the 7 min CBD-CdS/CIS sample before and after mild Ar^+ treatment cycles. As in the case of the CIS absorber, the leading edges of the UPS and IPES spectra shift closer to E_F as surface contaminants are removed. After a 15-min Ar^+ ion treatment using an ion energy of 250 eV, a VBM and CBM of 1.93 ± 0.1 eV and 0.57 ± 0.15 eV, respectively, can be determined via linear extrapolation. From these obtained values, a E_g^{surf} of 2.5 ± 0.2 eV can be assigned to the investigated 7 min CBD-CdS/CIS sample, which is the reported E_g^{bulk} of CdS [32].

By comparing the CBM of the bare CIGSe absorber to that of the thick CdS on CIGSe sample, a rough approximation of the heterointerface band alignment can be calculated. This coarse estimate indicates a CBO of -0.23 eV (i.e., a cliff configuration) at the heterointerface. For a correct band alignment determination, the IIBB must be taken into account, as described in Sect. 4.4.6 [113].

XPS results are used to monitor band bending changes at the heterointerface caused by the deposition of the CdS layer on top of the CIS absorber (i.e., IIBB) [113]. For this purpose, shifts in BE-position of the above-mentioned XPS lines from the absorber [i.e., Cu $2p_{3/2}$, In $3d_{3/2}$ and S $2p_{3/2}$ (for the 3 shortest CBD-CdS treatment times)] and the CdS buffer layer (i.e., Cd $3d_{3/2}$) were examined for samples with intermediate buffer thicknesses (e.g., samples with 0.5, 1, and 2 min CBD-CdS treatment periods). Core level lines from both the absorber and the buffer layer can still be detected in these samples. The impact of non-IIBB-related mechanisms (i.e., chemical shifts and/or chemical intermixing between the layers) influencing the energy of the evaluated XPS lines is minimized by this approach. Core level peak centers were determined by curve fit analysis, as discussed in the beginning of Sect. 5.3.

The IIBB was calculated by making use of eqn. (4.8). Due to the minor $CdSO_4$ formation on the surface of the 7.0 min CBD-CdS/CIS sample, which likely induces the surface charging detected for this sample, the BE of the Cd $3d_{3/2}$ line of the 4.0 min CBD-CdS/CIS sample is used as $E^f_{b,j}$ in eqn. (4.8). In total, 6 values of IIBB were computed by using combinations of the selected CIS and CdS lines. The complete set of IIBB values are displayed in Fig. 5.11.

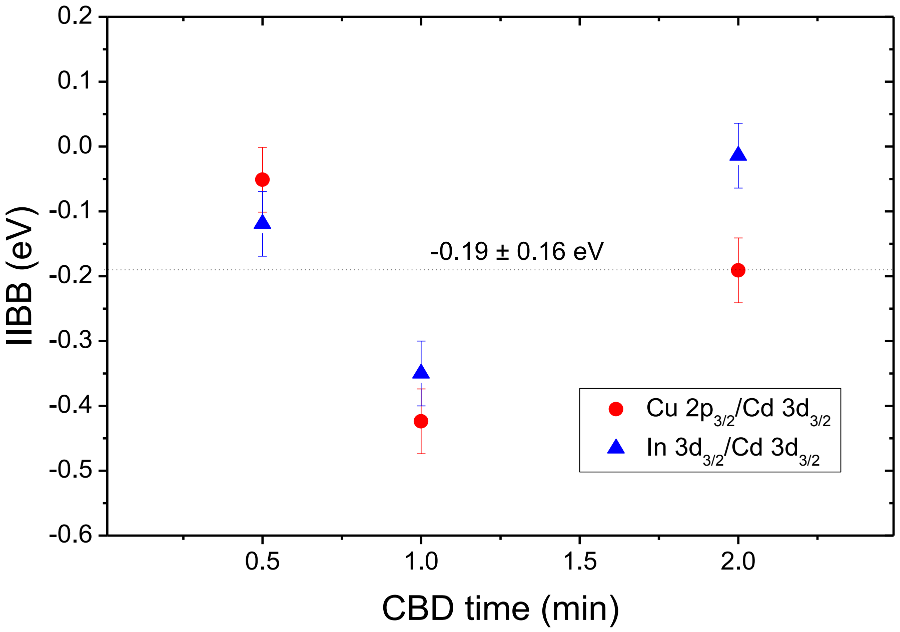

Figure 5.11 Interface-induced band bending (i.e., IIBB) as determined by combining core level positions of the absorber sample, the sample with the thickest CdS layer, and three samples with intermediate CdS layer thicknesses.

The average IIBB-value of the analysis is -0.19 ± 0.16 eV (as denoted by the dashed line in Fig. 5.11).

The VBO and CBO are calculated by using eqns. (4.6) and (4.7), which are ascertained for the heterointerface to be -1.04 ± 0.15 and -0.42 ± 0.25 eV, respectively. A schematic diagram of the complete electronic band alignment of the studied CdS/CIS heterointerface is shown in Fig. 5.12.

Hence, the conduction band alignment of the CdS/CIS is confirmed to have an unfavorable "cliff-like" configuration, with a CBO of -0.42 ± 0.25 eV. The here-determined CBO alignment is in complete agreement with the reported CBO of the CdS/Cu(In,Ga)S_2 heterointerface (e.g., -0.45 eV) [16], which shows that the electronic CdS/CIS interface structure is not well optimized. Moreover, even a small negative CBO configuration (i.e., -0.1 eV) has been postulated to significantly reduce the V_{OC} and FF of resulting solar cell devices [36]. This finding suggests that deliberate surface modifications of "wide-gap" CIGSSe absorbers could improve the performance of corresponding thin film solar cell devices.

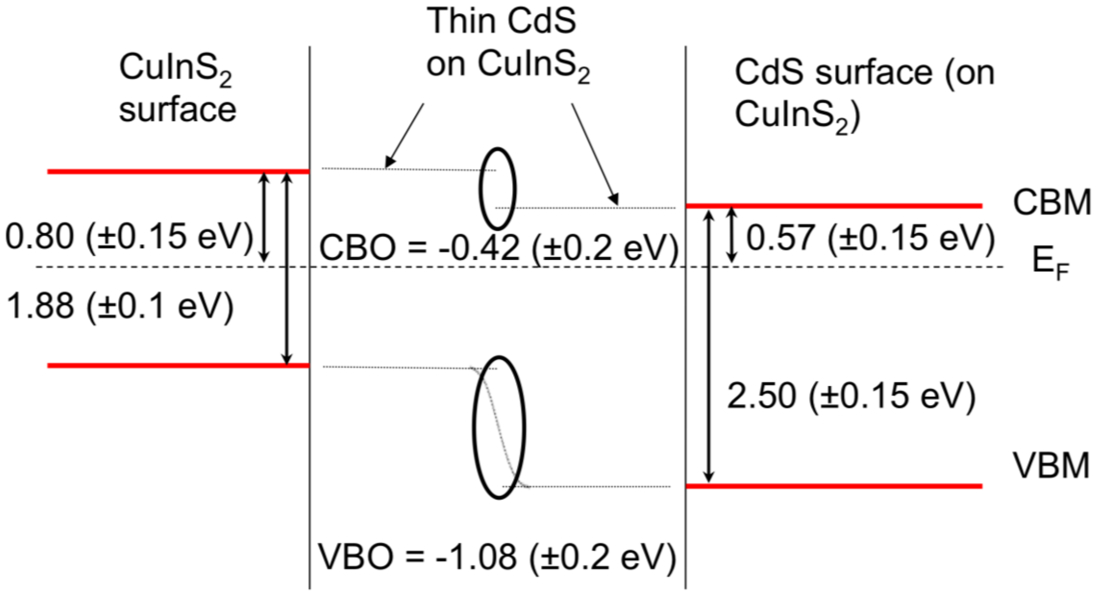

Figure 5.12 Schematic diagram of the CdS/CIS heterointerface electronic band alignment. The left and right sides of the diagram display the electronic E_g^{surf} (as derived by UPS and IPES) for the bare CIS absorber and the CdS buffer, respectively. The middle portion of the diagram shows the electronic band alignment at the heterointerface after considering interface-induced band bending effects.

5.4 Summary

In conclusion, the characterization of the chemical and electronic structures of the CdS/CIS was presented. Although the bulk of the CIS absorber is Cu-rich, the surface composition was revealed to be strongly Cu-poor. No evidence of intermixing across the heterointerface was found, nor the formation of interface chemical species. The direct measurement of the absorber E_g^{surf} showed, as has been found in other chalcopyrites, a significant widening with respect to the E_g^{bulk}. Direct measurement of the electronic band alignment of the CdS/CIS heterointerface showed a non-ideal, negative band alignment configuration. Optimization of the electronic band alignment may improve the performance of wide-gap chalcopyrite-based solar cell devices.

6 Tailoring of the CdS/$CuInS_2$ Heterointerface via Selenization of $CuInS_2$

6.1 Introduction

As observed in Ch. 4, selenium-containing (low-E_g) chalcopyrites are not only well-suited to form optimal heterointerface band alignments with the CdS buffer but also produce heterointerface mechanisms (i.e., intermixing across the heterointerface, interface E_g widening, E_g-grading toward the bulk of the absorber, etc.) that help improve the overall performance of resulting solar cell devices. In contrast, an absence (or significant reduction) of these beneficial features has been observed in heterointerfaces formed by wide-E_g chalcopyrite absorbers and the conventional CdS buffer, which are associated with solar cell devices with lower power conversion efficiencies [11,12].

In this chapter, a wide-E_g absorber surface is tailored with the goal of producing a surface with a more favorable band alignment with the CdS buffer, and, potentially, with the beneficial heterointerface attributes discussed above. The surface modification involves selenizing the surface of CIS absorbers by RTP in elemental Se vapor. A schematic of the targeted surface modification is illustrated in Fig. 6.1. To maintain the high V_{OC} of the CIS absorber [in comparison to CI(S)Se absorbers], the selenization should be limited to the very surface of the treated samples. The influence of RTP process parameters (such as RTP temperature, RTP duration, and Se amount) on surface and bulk properties was determined by a non-destructive depth-resolved chemical and electronic structure analysis, using a suite of complementary spectroscopic techniques.

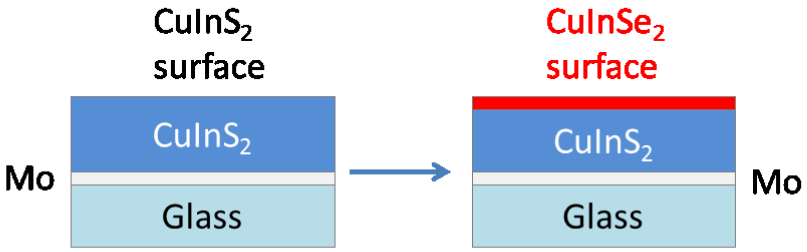

Figure 6.1 Targeted surface modification of CIS absorber via RTP selenization treatment.

6.2 Experimental Details

The CIS absorbers (the same as those used in Ch. 5 and 8) were prepared by HZB collaborators, by co-deposition of Cu and In on Mo-covered SLG back contacts followed by sulfurization using RTP [30]. Prior to the selenization treatment, the CIS samples were treated with a KCN etching process to remove Cu_xS binary phases from the absorber surface [31]. The selenization was conducted in elemental Se vapor. Table 6.1 labels the treated absorbers in the sample series and summarizes the parameters used in the RTP treatments. The baseline pressure of the RTP-chamber was ~$5x10^{-4}$ mbar. During the one-minute heating ramp step, the temperature inside the graphite box reaches the desired RTP-temperature. The RTP-temperature is then maintained for the duration of the treatment.

Table 6.1 List of samples and RTP treatment parameters

Sample	Duration (min)	Temp. (°C)	Se amount (mg)
CIS	–	–	–
i	30	500	–
ii	5	300	5
iii	5	400	5
iv	5	500	5
v	30	470	5
vi	30	500	5
vii	30	530	5

The surface chemical and electronic structures of the treated CIS absorbers were studied using XPS, XAES and UPS. The XPS and XAES measurements were carried out employing a SPECS PHOIBOS 150MCD electron analyzer using Mg and Al K_α excitation energies. UPS measurements were conducted with a He discharge lamp using the He I excitation source. When samples were transported for measurement purposes outside the HZB, they were sealed in N_2 (in order to minimize their exposure to air). During bulk-sensitive characterizations (i.e., XRF and UV-Vis), samples were exposed to ambient conditions. Therefore, these spectroscopic techniques were conducted only after the more surface-sensitive spectroscopic techniques.

Bulk elemental analysis was conducted via XRF. A wavelength-dispersive XRF spectrometer (Rigaku WD-XRF ZSX Primus II [75]) with an end-window-type Rh-target x-ray source used for the XRF measurements. A LiF(200) crystal setup was used for wavelength dispersion of the emitted fluorescent x-ray lines, along with a P10-gas flow proportional counter (PC) and a scintillation counter (SC) detector systems. The Cu K_α, In K_α, S K_α and Se K_α lines of the samples were analyzed.

The optical E_g values of the samples were obtained by means of UV-Vis spectroscopy. Reflectance spectra were measured on a Perkin-Elmer Lambda 950 UV/Vis/NIR spectrophotometer [78]. Tungsten-halogen and deuterium lamps were used as excitation sources. The UV-Vis portions of the spectra were detected via a photomultiplier. The near-infrared (NIR) portions of the spectra were recorded through a Peltier-cooled PbS detector setup. The measured reflectance spectra were evaluated by the Kubelka-Munk transformation method [77], described in Sect. 3.4. Assessment of the optical E_g was carried out by linear extrapolation of the leading edge of the transformed $(Kh\nu)^2$ vs photon energy, $h\nu$, plots.

6.3 Rapid Thermal Processing Treatment

In the following section, the chemical, electronic and optical properties of the RTP-treated sample series are presented.

6.3.1 Surface Chemical Structure

In this subsection, the results of surface-sensitive XPS and XAES measurements are discussed as a study of changes in the surface chemistry of CIS arising due to the various selenization treatments.

Fig. 6.2 shows the XPS survey spectra of the investigated sample series. The XPS survey spectrum of the untreated KCN-etched CIS absorber displays the photoemission lines of the absorber elements (i.e., Cu, In and S). Additionally, Se photoemission core levels appear in the survey spectra of all RTP-treated samples, even when no Se is intentionally supplied for the RTP process. The deposited Se is ascribed to the background Se concentration in the RTP

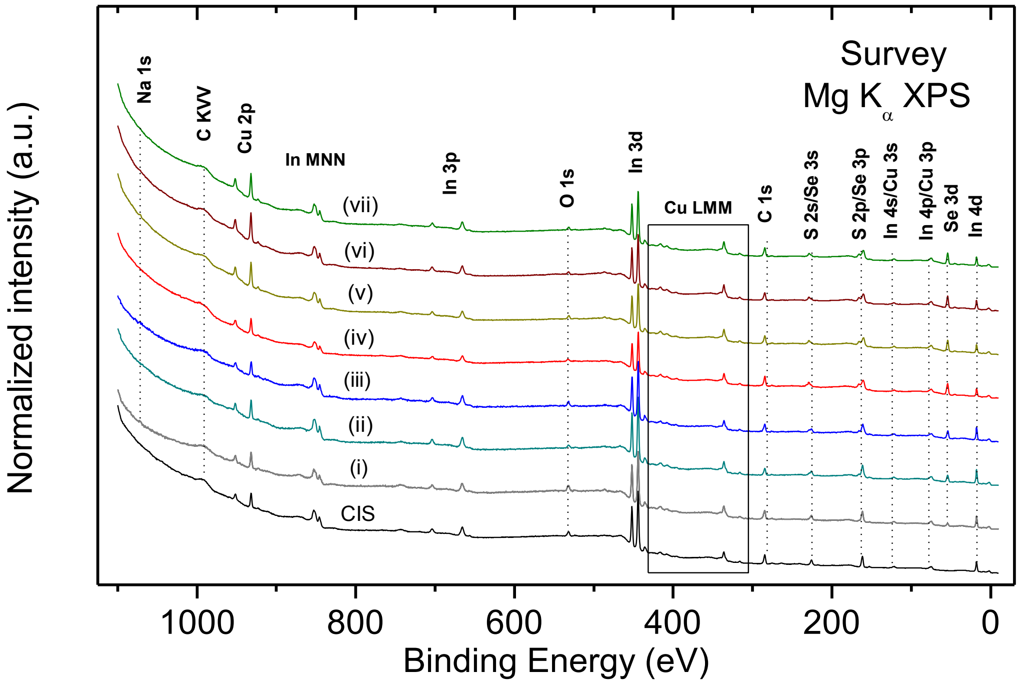

Figure 6.2 XPS Survey spectra of the investigated RTP-treated CIS sample series.

chamber. At the same time, a reduction in the intensity of S-related core levels occurs in the spectra of RTP-treated samples. Traces of Na are detected in all RTP-treated samples, which is ascribed to an enhancement of Na diffusion from the SLG back contact induced by the high-temperature treatments [20,21]. Furthermore, the intensity of Cu-related photoemission lines increases in samples treated using longer periods and higher temperature ranges in the presence of Se vapor [i.e., samples (v) – (vii)], suggesting an enrichment of surface Cu. These trends are better distinguished when examining detail XPS spectra in the Cu 2p, In $3d_{3/2}$ and S 2s/Se 3s regions, presented in Fig. 6.3 along with their curve fits.

The partially overlapping S 2s/Se 3s lines clearly show the impact of the RTP-treatment on the surface [Se]/[S + Se] of the samples. Because of the energetic proximity of these two peaks, signal changes associated with differences in λ and the electron analyzer's transmission function are negligible. After normalizing the intensity of the peaks by their respective photoionization cross section [18], the surface [Se]/[S + Se] ratios are presented in Fig. 6.4, in ascending order. The S 2s/Se 3s spectra indicate that a substitution of Se for S takes place as a result of all RTP treatments. Complementing these results, the XRF-probed bulk [Se]/[S + Se] ratios are also shown in Fig. 6.4. Changes in the bulk [Se]/[S + Se] composition are only notable in samples treated using higher RTP temperatures and when Se

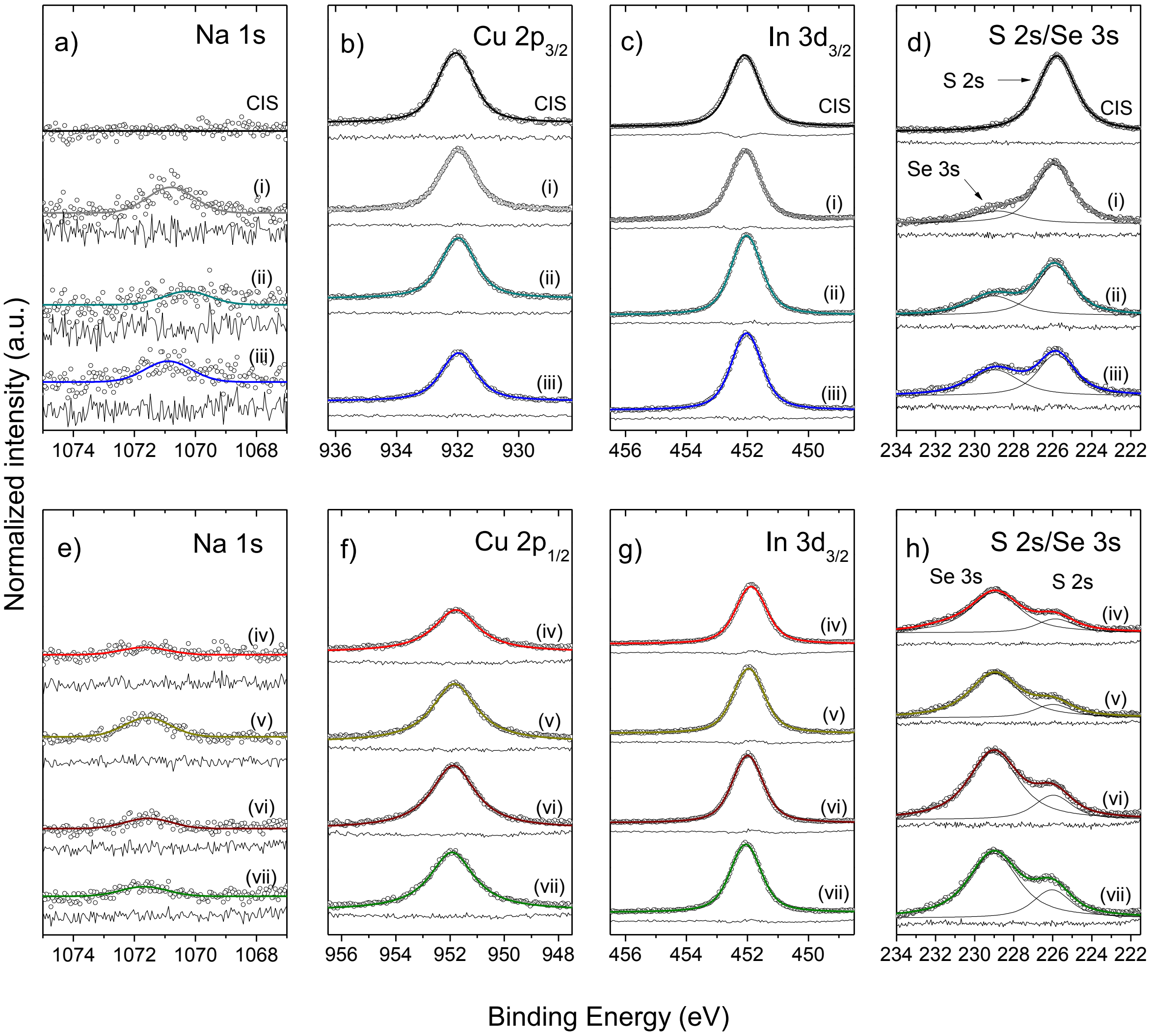

Figure 6.3 (a) - (d) XPS detail spectra of the Na 1s, Cu 2p$_{3/2}$, In 3d$_{3/2}$, and S 2s/Se 3s regions of the following samples in the series: CIS, (i), (ii) and (iii), normalized to background intensity. (e) - (h) XPS detail spectra of the Na 1s, Cu 2p$_{1/2}$, In 3d$_{3/2}$, and S 2s/Se 3s regions of the following samples in the series: (iv), (v), (vi) and (vii), normalized to background intensity. All spectra were measured using Mg K$_\alpha$ excitation. Vertical offsets are added for clarity.

is supplied [i.e., samples (iv) – (vii)]. Within the set of samples with RTP-induced bulk modifications, samples (vi) and (vii) show slightly lower degrees of (surface and bulk) selenization. These variations are ascribed to the sealing limits of the graphite box of the RTP system. With higher temperature treatments, the leaking rate of Se vapor from the graphite box increases. The surface properties of the RTP-treated samples will be discussed with respect to the measured surface [Se]/[S +Se] ratios in the following.

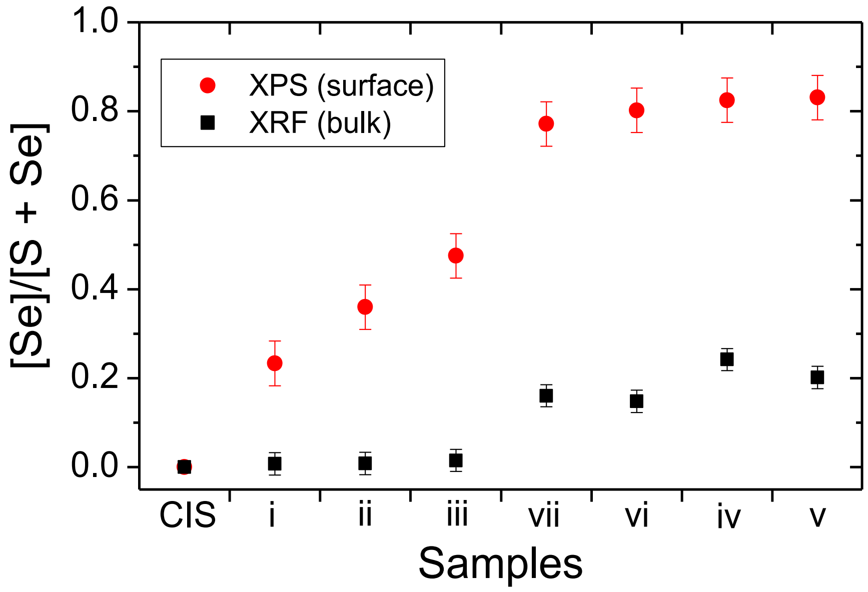

Figure 6.4 Surface and bulk [Se]/[S+Se] ratios obtained by XPS and XRF analysis, respectively.

The surface compositions of the treated samples were quantified by normalizing the intensities of the curve-fit-analyzed XPS core level peaks, shown in Fig. 6.3, by respective λ [50,51], σ [46,47] and transmission function values of the electron analyzer [48]. In contrast to CIGSe absorber discussed in Ch. 4, inclusion of surface Na in the quantification did not cause significant changes in the calculated surface compositions of the RTP-treated samples. Therefore, the surface compositions were not presented in a (Cu+Na):In:(S+Se) format. The obtained compositions are shown in Fig. 6.5.

The untreated CIS absorber shows a Cu-poor, In-rich surface. In contrast, XRF measurements of the untreated CIS absorber yield Cu and In elemental fractions of 0.25 and 0.28, respectively, thus indicating a Cu-rich and In-rich bulk. The surface composition of the CIS absorber deviates from the Cu:In:S = 1:3:5 stoichiometry observed for the CIS absorber in Ch. 5. An explanation for this deviation in surface composition (i.e., slightly Cu-richer and S-poorer than the composition detected for the CIS absorber in Ch. 5) may be an incomplete removal of the $Cu_{2-x}S$ cap by the KCN etching [137]. Further findings in the electronic structure of the CIS absorber, to be discussed in Sect. 6.3.3 seem to support this argument. As observed in Fig. 6.5, the effect that the RTP-treatments induce on the composition fractions of the chalcopyrite cations (i.e., Cu and In) is different for samples with different degrees of surface selenization. At first, deposition of Se (actual incorporation of Se into the chalcopyrite

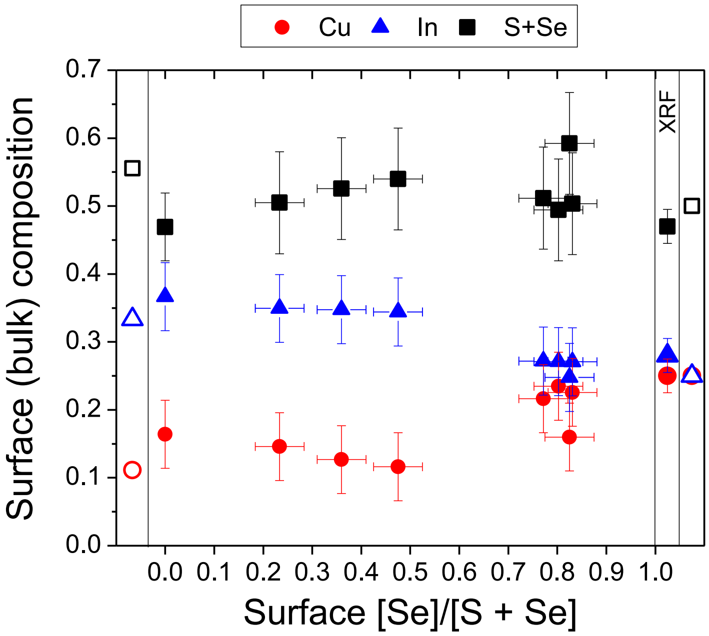

Figure 6.5 Surface compositions as a function of the surface [Se]/[S+Se] of the sample. Note that these surface compositions are revised later in the chapter. The hollow icons at the left and right extremities of the figure denote elemental fractions corresponding to 1:3:5 and 1:1:2 Cu:In:(S+Se) stoichiometries, respectively. Values labeled XRF represent the average bulk elemental fractions of the absorbers used in the sample series, as assessed by x-ray fluorescence analysis.

crystal lattice will be considered shortly) appears to decrease the surface concentration of Cu, while leaving the surface concentration of In relatively unchanged. This trend continues up to sample (iii) (i.e., the sample with a surface [Se]/[S+Se] ~ 0.48), which exhibits a surface that is in close agreement with a Cu:In:(S+Se) = 1:3:5 stoichiometry. Further increasing the degree of surface selenization induces a surface Cu-enrichment, along with a decrease in the initial In-rich character of the CIS absorber. Therefore, it is possible to change the initial Cu-poor surface of the CIS absorber through the RTP-selenization process into a surface with a Cu:In:(S+Se) = 1:1:2 stoichiometry. The mechanisms behind this observed evolution in chalcopyrite cation compositions is discussed in the end of Sect. 6.3.2.

6.3.2 Cu, In and Se Modified Auger Parameter Analysis

Changes in the chemical structure of the RTP-treated samples are discussed as a function of their degree of surface selenization. Changes in the modified Auger parameters (α*) of Cu-, In- and Se-related emission lines are examined for this purpose. In Sect. 6.3.1, the Se 3s XPS line was used, due to its energetic proximity to the S 2s XPS line, in the quantification of the surface [Se]/[S+Se] ratios of the samples. However, the Se 3d core level is chosen for purposes of chemical environment evaluation for the following reasons: (i) The FWHM value of the Se 3d peaks (1.2 eV), as determined by the curve fit analysis of the peaks, is significantly smaller than the FWHM value of the Se 3s peaks (3 eV). Therefore, the curve fit analysis of the Se 3d XPS line would more readily detect changes in peak shape associated with chemical speciation. (ii) The Se $3d_{5/2}L_3M_{45}M_{45}$ modified Auger parameter is the most prevalent modified Se α^* in literature.

Fig. 6.6 (a) shows the XPS Se 3d spectra and curve fits of the RTP-treated samples, along with respective curve fits. All spectra needed two sets of peaks in order to obtain satisfactory agreement between the curve fits and the measured data. The Se $3d_{5/2}$ peak of the two sets are located at the following BE: ~ 53.8 ± 0.1 eV (Se_I) and ~ 55.1 ± 0.4 eV (Se_{II}). These BE values are consistent for Se $3d_{5/2}$ XPS core levels of chalcopyrite selenides (Se_I) and elemental Se (Se_{II}), respectively [45]. Interestingly, the Se_{II} contribution is higher in the RTP control sample [i.e., sample (i)] and in samples produced by 5 min RTP treatments [samples (ii) – (iv)] than in samples produced by 30 min RTP treaments [samples (ii) – (iv)] . Corresponding Se_{II}/Se_{Tot} ratios, where $Se_{Tot} = Se_I + Se_{II}$, are shown in the inset above each Se 3d spectrum in Fig. 6.6 (a).

Fig. 6.6 (b) shows the measured Se $L_3M_{45}M_{45}$ (LMM) XAES line of all RTP-treated samples, together with a weighted spectrum of the Se LMM line of the ZSW CIGSe absorber of Ch. 4 (serving as a CISe reference) and (when necessary) the weighted background line of the KCN-etched CIS absorber in the same energy region. The magnified differences of the measured Se LMM lines and the fits produced by the sum of the weighted references are also shown in the Fig. 6.6 (c). The Se LMM lines of samples treated for periods of 30 min and supplied with Se [i.e., samples (v) – (vii)] are finely matched by the reference Se LMM line in Fig. 6.6 (b). The difference lines in Fig. 6.6 (c) corresponding to these samples can be ascribed to statistically distributed noise. This finding is expected, considering that Se is the overwhelming chalcopyrite anion at the surface of these samples. Morevover, only minor traces of the Se_{II} component are found in the curve fit analysis of the Se 3d line of these samples.

In contrast, the shape of the measured Se LMM line of the rest of the samples [i.e., (i) – (iv)] in the RTP-treatment series cannot be satisfactorily matched by the sum of the two weighted reference lines (i.e., the Se LMM and the CIS background lines), as seen in Fig. 6.6 (b). The difference between the measured spectra and the fit lines for these samples [i.e., (i) – (iv)],

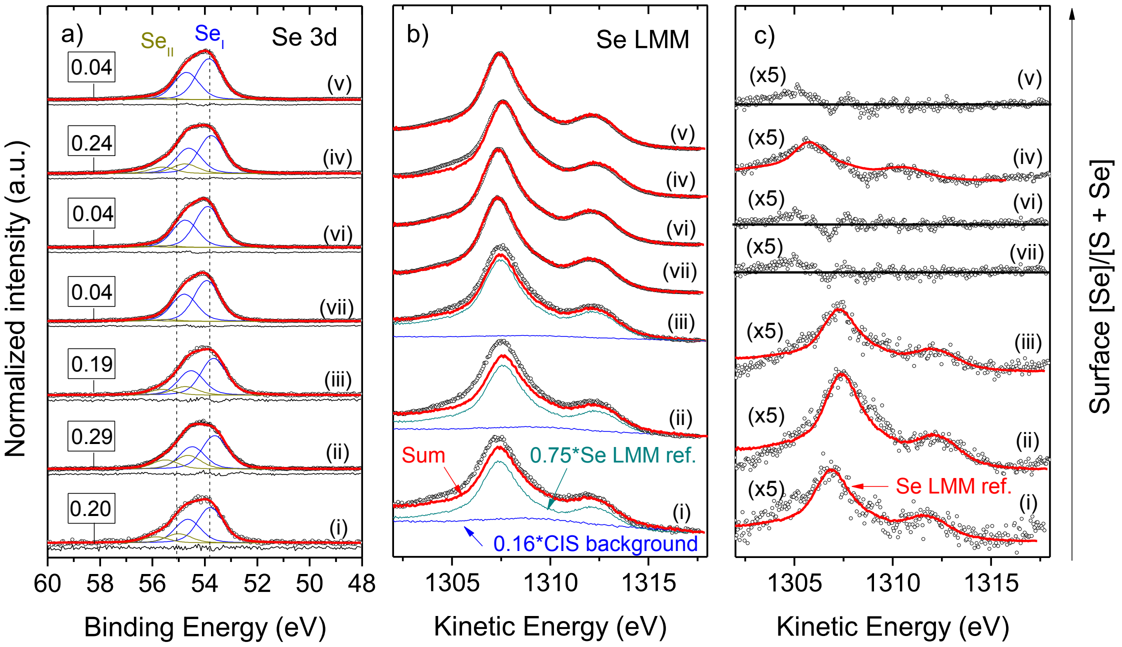

Figure 6.6 (a) Se 3d XPS detail spectra and (b) Se $L_3M_{45}M_{45}$ (LMM) XAES lines of all RTP-treated samples, including fits, normalized to maximum intensity. (c) Magnified difference of the measured Se LMM spectra from (b) and their corresponding fits. Spectra in (a) include curve fits and were measured using Mg K_α excitation. The inset in (a) shows the Se_{II}/Se_{Tot} ratio of the spectra. Spectra in (b) were measured using Al K_α excitation and are shown with fits consisting of the sum of a weighted Se LMM reference lines (—) and the weighted background line of the CIS absorber (—) in the same energy region. The red lines in (c) are energetically-shifted Se LMM reference lines aligned over difference lines. Vertical offsets are added for clarity.

in fact, resemble energetically shifted Se LMM line shapes. These results, as well as the two sets of Se 3d peaks, suggest that the surface Se exists in two different chemical environments in these RTP-treated samples. The identity of these Se chemical species will be addressed below.

The In $M_{45}N_{45}N_{45}$ (MNN) and Cu $L_3M_{45}M_{45}$ XAES lines of the selenized samples are displayed in Fig. 6.7 (a) and (b), respectively. Similar evaluations of these XAES lines did not unambiguously reveal the presence of multiple XAES lines, as in the case of the Se LMM lines. Neither was there any indication of a second component found in the curve fits of the Cu 2p and In 3d spectra shown in Fig. 6.3. However, a shift in the energy of the In MNN and Cu LMM lines is found for samples shown to possess a higher Se content at their surfaces, which is a plausible indication of changes in chemical environments of Cu and In.

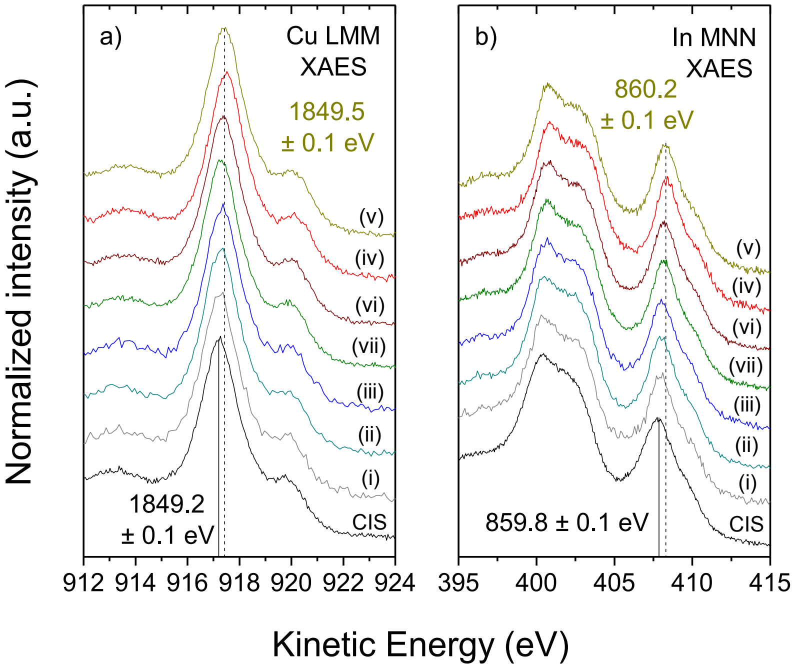

Figure 6.7 (a) Cu $L_3M_{45}M_{45}$ and (b) In $M_{45}N_{45}N_{45}$ XAES lines of the selenized CIS absorbers, normalized to maximum intensity. The solid and dashed lines are shown to help distinguish the energetic shifts in the XAES lines of the untreated CIS absorber and sample (v), respectively.

The calculated values of the modified Se α*, Cu α* and In α* (derived by using the Se $3d_{5/2}$ XPS core level and the Se $L_3M_{45}N_{45}$ XAES line, the Cu $2p_{3/2}$ XPS core level and the Cu $L_3M_{45}N_{45}$ XAES line, and the In $3d_{3/2}$ XPS core level and the In $M_4N_{45}N_{45}$ XAES line, respectively) are shown in Fig. 6.8 (a) – (c), as a function of surface [Se]/[S+Se]. Included in the figure are reported α* ranges of values for reference compounds [45,52,138-141].

All RTP-treated samples show Se α* values in the range reported for $CuInSe_2$ [within the margin of error for sample (iii), the sample with a surface [Se]/[S+Se] ~ 0.48], as seen (black hollow squares) in Fig. 6.8 (a). This fact indicates that Se incorporates into the chalcopyrite crystal lattice at the surface. However, a secondary Se α* can also be calculated for samples manifesting additional Se-related emissions [i.e., the red hollow circles in Fig. 6.8 (a) are calculated by adding the BE of the Se $3d_{5/2}$ peak of the Se_{II} component and the KE of the Se LMM-like line]. In these cases, the secondary Se α* values fall within the range of values reported for elemental Se. (The secondary Se α* sample (iv), the sample with a surface [Se]/[S+Se] ~ 0.82, is located close to the range of values reported for SeO_2; however, no signal is found near the BE ~ 59 eV region of its Se 3d XPS core level, expected for SeO_x bonding.)

These findings suggest that the reaction conditions provided by the RTP-treatment parameters of samples in which elemental Se is detected are insufficient for the full incorporation of reactant Se into the chalcopyrite alloy. Another possibility may be that the elemental Se is deposited during the cool down period of the RTP process, at which time the Se vapor may not be energetically capable of incorporating into the chalcopyrite crystal lattice.

Fig. 6.8 (b) shows the evolution of the Cu α* of the sample series. A direct relation is found between the Cu α* values of the samples and their surface [Se]/[S+Se]. Although the Cu α* values of the samples (i) and (ii) (i.e., samples with surface [Se]/[S+Se] ratios of 0.23 and 0.36, respectively) are still within the range of values reported for $CuInS_2$, these values are close to the lower limit of the range of values reported for $CuInSe_2$. Samples with higher surface Se contents show Cu α* values well within the range of values for $CuInSe_2$. Formation of $CuSe_2$ could not be excluded by this analysis due to overlapping Cu α* values reported for $CuSe_2$ and $CuInSe_2$.

As shown in Fig. 6.8 (c), the change in In α* values of the samples as a function of surface [Se]/[S+Se] is similar to that observed for the Cu α* values. The In α* has also been reported to be an effective indicator of the degree of surface Cu-deficiency in CIS absorbers, with Cu-richer CIS surfaces producing higher In α* values compared to those obtained from Cu-poorer CIS surfaces [141]. In the present case, the In α* seems to be more influenced by the surface

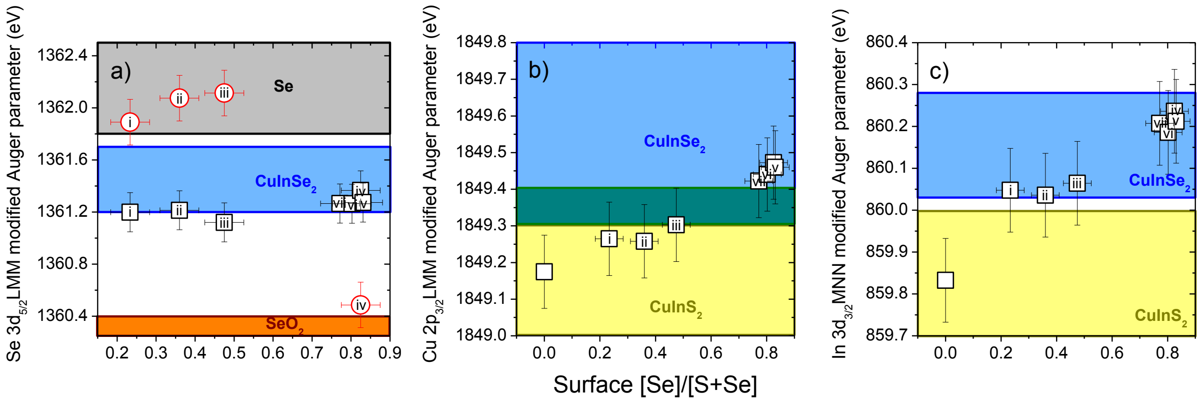

Figure 6.8 (a) Se, (b) Cu and (c) In modified Auger parameters (α*) of CIS and RTP-treated CIS absorbers shown as a function of surface [Se]/[S+Se]. More details on the attribution of the icons for (a) are found in the text.

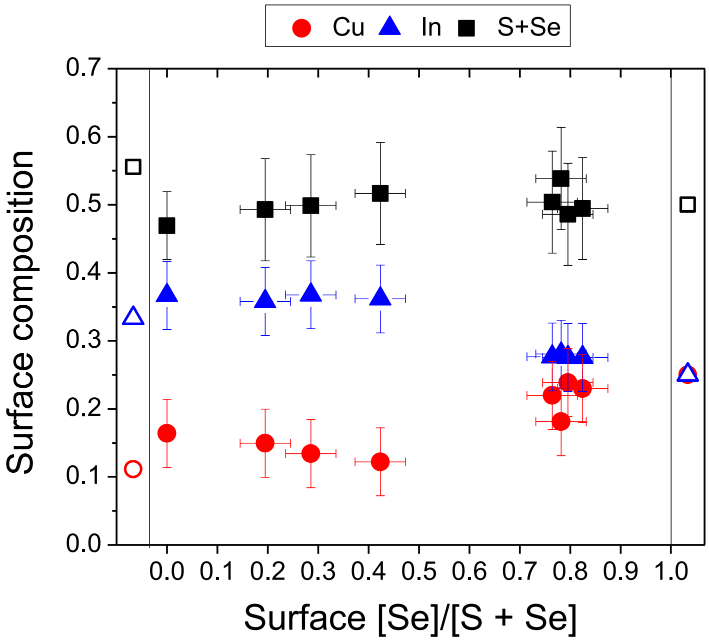

Figure 6.9 Revised surface compositions as a function of the surface [Se]/[S+Se] of the sample. The hollow icons at the left and right extremities of the figure represent 1:3:5 and 1:1:2 Cu:In:(S+Se) stoichiometries, respectively.

[Se]/[S+Se] than by the surface Cu content. This observation is based on the In α* value obtained for sample (iv), the sample with a surface [Se]/[S+Se] ~ 0.82. Although it shows a Cu-poorer surface than samples (v) – (vii), these four samples show comparable In α* values.

Based on the evidence of the presence of elemental Se, from the XAES analysis, on the surface of the RTP-treated samples, the surface composition of the samples was revised in order to obtain the actual chalcopyrite Cu:In:(S+Se) surface composition (i.e., the elemental Se contribution removed). For this purpose, a factor equivalent to the Se_{ii}/Se_{Total} was subtracted from the Se 3s intensity used for the quantification of the surface composition (i.e., Fig. 6.5). After this modification, the surface compositions of the samples were recalculated. The revised surface chalcopyrite composition is presented in Fig. 6.9.

Even after the revision in surface composition, samples with a lower Se surface content continue to show Cu-poor, In-rich surface compositions. Theoretical works propose that the presence of electrically neutral defect pairs is possible in chalcopyrite surfaces of similar compositions due to relatively low formation energies for Cu vacancies [26]. [More specifically, two Cu vacancy sites (acceptor states), V_{Cu}^{-}, couple with a In atom occupying a copper site (donor states), In_{Cu}^{++} (i.e., 2 V_{Cu}^{-} + In_{Cu}^{++}).]

In the present case, however, the chalcopyrite anion content is lower than expected for a surface Cu:In:(S+Se) = 1:3:5 composition, which suggests vacancies in S sites, V_{S}^{++}. The effect of the initial deposition of Se seems to be to fill these V_{S}^{++}, as no apparent change in Cu and In composition is noticed for the RTP control sample {i.e., sample (i) with a surface chalcopyrite [Se]/[S+Se] ~ 0.2}. With further incorporation of Se into the absorber surface, the Cu surface concentration decreases, as seen for samples (ii) and (iii) (i.e., samples with a surface chalcopyrite [Se]/[S+Se] ~ 0.3 and 0.4, respectively), suggesting a greater formation of V_{Cu}^{-} sites. Although a proportional formation of In_{Cu}^{++} would be expected to compensate for the new V_{Cu}^{-}, the In surface concentration remains unchanged for these samples, indicating no increase in In_{Cu}^{++}. This missing compensation in charged defect pairing can be explained by higher energies of formation of In_{Cu}^{++} antisites compared to V_{Cu}^{-} sites in Cu-poor, In-rich chalcopyrite lattices, as predicted by theoretical models [26]. An alternative charge pairing mechanism driven by the deposited Se and the conversion of V_{Cu}^{-} to V_{Cu}^{0} is proposed. Incorporation of Se into the chalcopyrite matrix entails a reduction process of the deposited elemental Se (Se^{0}) into a chalcopyrite Se anion (Se^{--}) (i.e., $Se^{0} + 2e^{-} \rightarrow Se^{--}$). Moreover, low formation energies for single neutral defects (more specifically, V_{Cu}^{0}) are also reported in Cu-poor $CuInSe_2$ surfaces [26]. The Cu depletion (i.e., increased formation of V_{Cu} sites) observed in samples (ii) and (iii) stands out as a potential source of electrons for the reduction of Se^{0} (i.e., $Se^{0} + 2V_{Cu}^{-} \rightarrow Se^{0} + 2V_{Cu}^{0} + 2e^{-} \rightarrow Se^{--} + 2V_{Cu}^{0}$).

The energy requirements for the formation of both V_{Cu}^{-} and V_{Cu}^{0} increase as the VBM of the chalcopyrite (more specifically, $CuInSe_2$) shifts closer to the E_F level. Because the substitution of S by Se moves the E_F level and the VBM of the RTP-treated samples closer together (a finding which is discussed in Sect. 6.3.3), V_{Cu}^{-} and V_{Cu}^{0} sites in samples with higher surface Se content [i.e., samples (iv) - (vi)] become energetically unfavorable [26,142]. As presented in Fig. 6.9, these samples undergo a surface Cu-enrichment, which leads to a surface composition transition from a Cu:In:(S+Se) ~ 1:3:5 stoichiometry to a Cu:In:(S+Se) = 1:1:2. Although thermally-mediated Cu diffusion mechanisms have been reported for heterointerfaces with elemental compositions similar to the RTP-treated CIS samples (i.e., In_2S_3/CIGSe [143,144]), the Cu-enrichment observed for the set of RTP-treated CIS samples with higher surface Se content [i.e., samples (iv) – (vi)] is not induced by the heat of the process. Otherwise, all RTP-treated samples should show signs of surface Cu-enrichment. {The 300 - 550 °C temperature range used in the RTP treatments is significantly above the 200 °C annealing temperature reported to induce Cu-diffusion across the In_2S_3/CIGSe heterointerface [143,144]. Moreover, the treatment of the RTP control sample [i.e., sample (i), which shows no signs of surface Cu-enrichment] uses the same treatment temperature and duration as the treatment for sample (vi), which shows a surface Cu-enrichment.} A threshold for the Se composition, which controls the energetic distance of the VBM to the E_F level, seems to activate the observed Cu-diffusion from the bulk to the surface of the samples.

6.3.3 Surface Electronic Structure

UPS was used to monitor the position of the VBM with respect to the E_F level of the samples. Fig. 6.10 (a) shows the UPS spectra of the samples along with linear fits of the VB leading edges, presented in ascending order of surface [Se]/[S+Se]. The VBM of all RTP-treated samples shifts closer to the E_F level [from -0.88 ± 0.08 eV for CIS → -0.51 ± 0.08 eV for sample (vii)] due to incorporation of Se in the surface of the samples. Based on the results of Sect. 6.3.2, V_{Cu} sites are expected to form in samples with a VBM lower boundary down to ~ -0.7 eV [i.e., sample (iii), with a surface chalcopyrite [Se]/[S+Se] ~ 0.42]. This lower limit in the distance between the VBM and the E_F level is slightly lower (by ~ 0.1 eV) than the ones reported in previous works [142]. Nonetheless, the measured VBM levels of samples undergoing surface Cu-enrichments (i.e., ~ -0.55 eV) are consistent with the E_F-level dependence of the formation of Cu-related defects in chalcopyrite absorbers [26,142].

Based on the obtained VBM values, an assessment (though partial) of changes in surface E_g of the samples is attempted. (Direct measurement of the CBM of the samples, as carried out for absorbers in Ch. 4 and 5, could not be performed for the present sample series.) For the present CIS absorber, its VBM is closer to the E_F level than the VBM of the CIS absorber analyzed in Ch. 5 (i.e., -1.08 eV). As mentioned in Sect. 6.3.1, the surface composition of the present CIS absorber shows signs consistent with the presence of $Cu_{2-x}S_x$. A reduced surface E_g^{surf} is expected for the present case, in comparison to the one determined for the CIS absorber in Ch. 5 [137]. Assuming that the CBM values of both CIS absorbers are the same (i.e., ~ 0.8 eV), the E_g^{surf} of the present CIS absorber is estimated to be ~ 1.7 eV. For the RTP-treated samples, a reduction in the E_g^{surf} of all samples is expected if changes in VBM level are considered. For example, based solely on the VBM level of sample (iii) (i.e., ~ -0.68 eV) and again assuming a CBM of ~ 0.8 eV, the E_g^{surf} of this sample is expected to be ~ 1.5 eV.

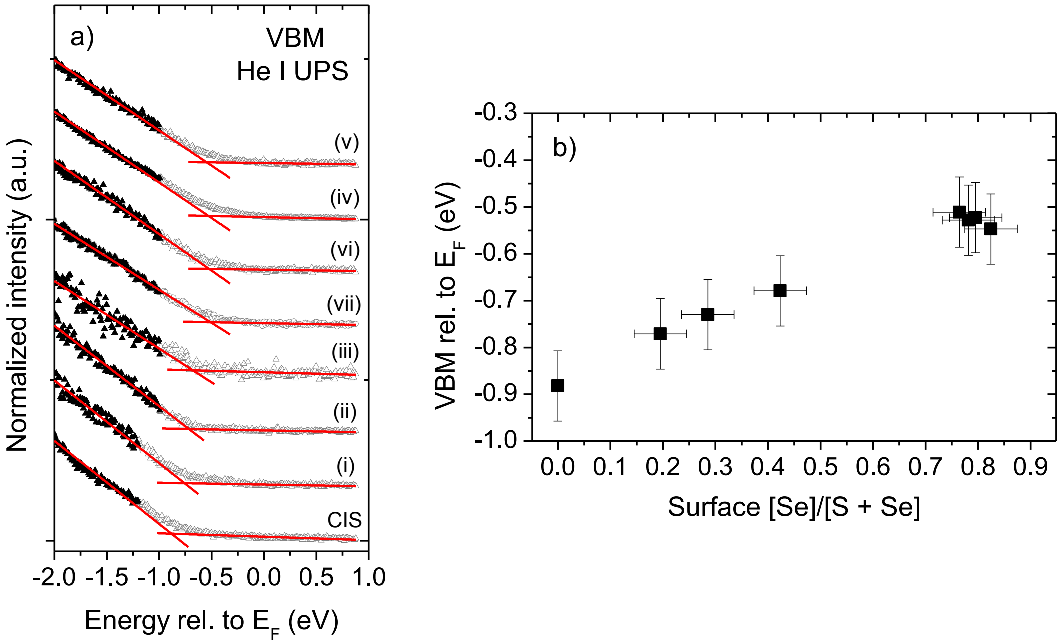

Figure 6.10 (a) He I UPS spectra of the investigated sample series. Linear extrapolations of the respective leading edge are shown in red lines. (b) VBM positions of the investigated sample series as determined from (a).

The E_g^{surf} values of CISSe absorbers of similar surface composition detected for sample (iii) have been reported to be 1.4 ± 0.15 eV [145]. If this E_g^{surf} value were assumed for sample (iii) instead of the computed 1.5 eV value, a minor shift in the CBM position (i.e., 0.8 eV → 0.7 eV) could be expected to be induced by the RTP-treatment. Although such a hypothetical shift in CBM could potentially improve the heterointerface CB of this RTP-treated absorber and the CdS buffer, it would not justify the larger reduction in eV_{bb} produced by the observed shift in the VBM level (i.e., -0.88 ± 0.08 eV → -0.68 ± 0.08 eV)

The VBM level of samples in the series with higher surface Se contents shifts to ~ -0.5 eV. If CBM values of ~ 0.8 eV are assumed for these samples, the resulting E_g^{surf} are estimated to range ~ 1.3 – 1.4 eV, comparable to E_g^{surf} values reported for CISSe absorbers [145]. However, because the surface of these samples undergo a Cu-enrichment, the CBM positions of these samples are expected to shift closer to the E_F level, bringing the E_g^{surf} closer to the reported E_g^{bulk} value reported for $CuInSe_2$ (i.e., 1.0 eV [146]).

Based on these findings, changes in the electronic structure of the samples induced by the selenization RTP-treatments seem to exert a greater impact on the position of the VBM level than on the position of the CBM level. Such an effect is not expected to bode well for the performance of resulting solar cell devices.

6.3.4 Bulk Optical Properties

The purpose of the RTP-selenization treatments is to tailor only the surface; in order to monitor any changes to the bulk properties, the optical E_g values of the samples were measured via UV-Vis spectroscopy.

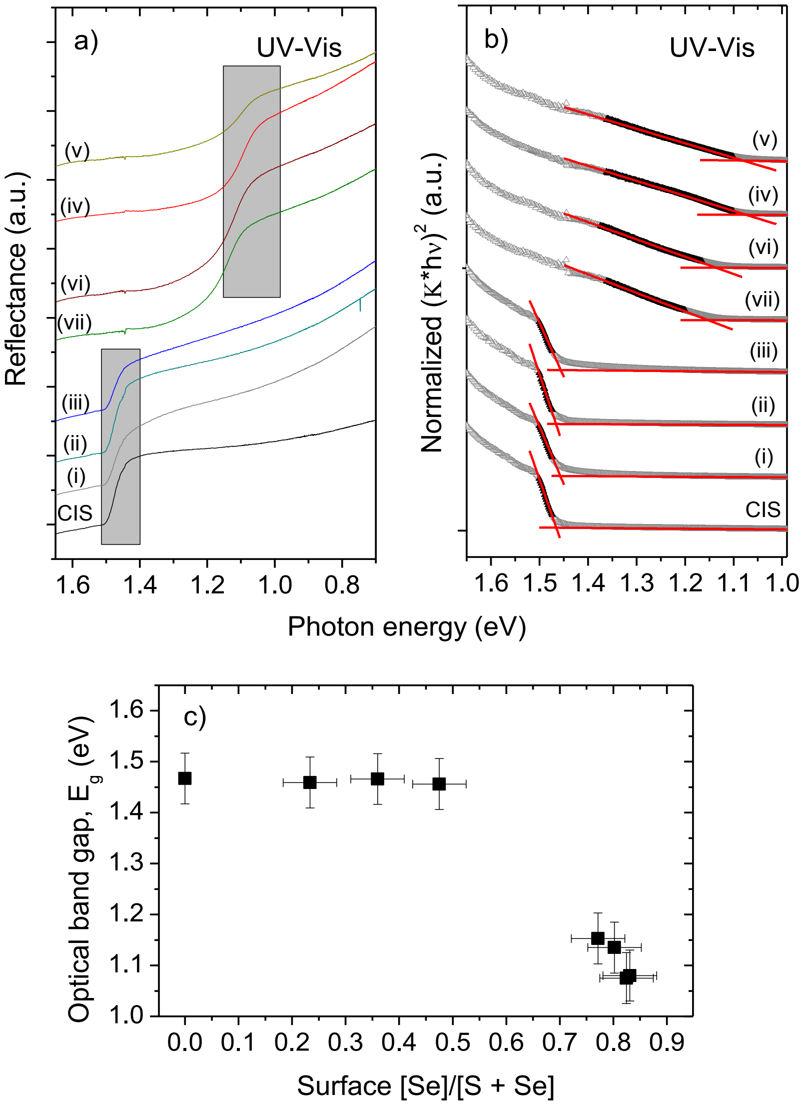

Figure 6.11 (a) UV-Vis reflectance spectra and (b) normalized Kubelka-Munk transformed reflectance spectra of the investigated sample series. Linear extrapolations of the respective leading edges are shown in red lines. (c) Optical E_g values of the investigated sample series as determined from (b).

Fig. 6.11 (a) shows UV-Vis reflectance spectra of the samples series as a function of photon excitation energy. Fig. 6.11 (b) shows the reflectance spectra after conducting a Kubelka-Munk transformation (K) analysis [77]. Linear approximations of the leading edges are also included in the figure. Fig. 6.11 (c) shows the extrapolated optical E_g values as a function of the surface chalcopyrite [Se]/[S+Se] ratios of the absorbers. Optical E_g values of ~ 1.47 eV are found for the CIS absorber and for RTP-treated samples with low surface Se contents, indicating the selenization is limited to the near-surface region of the absorbers. The observed optical E_g values are slightly lower than the E_g^{bulk} value of CIS (i.e., 1.54 eV [146]). Similar slightly reduced optical E_g values of CIS absorbers have been reported and are ascribed to absorption/reflectance losses due to surface roughness and/or deviations of stoichiometric compositions [147]. Because the CIS absorbers were produced by RTP, a rough absorber morphology can be expected [30]. Moreover, the XRF measurements of the CIS absorber showed a Cu-rich (0.25) and S-poor (0.47) bulk composition; both of which have been shown to reduce the optical E_g to the observed values [147].

For samples with a higher degree of selenization, the measured optical E_g is lower (i.e., 1.06 – 1.14 eV), which is a range of optical E_g values close to the optical E_g of CISe [146]. These findings suggest that the RTP-parameters used for the treatments of samples with higher surface chalcopyrite [Se]/[S+Se] ratios have an increased effective depth, to such an extent as to alter the electronic, chemical and optical properties inside the bulk of the samples. These observations are in agreement with the formation of a CISSe phase on top of the treated CIS substrate. However, this CIS → CISSe conversion strongly depends on the RTP process parameters.

Fig. 6.12 combines the observed changes in electronic and optical properties of the sample series. The black squares show the surface VBM position of the samples in the series as a function of surface [Se]/[S+Se], as determined in Sect. 6.3.3. By adding the optical (bulk) E_g value to the VBM value of the corresponding sample, the CBM of each sample (i.e., calc. CBM = VBM + E_g^{bulk}, hollow red circles) could be estimated, provided that the elemental compositions of the bulk and the surface of the sample are uniform. However, the surface elemental compositions of CIS absorbers and the RTP-treated samples (i) – (iii) (i.e., samples with [Se]/[S+Se] > 0.5) were found to be Cu-poor. An enlarged E_g can be expected at the surface compared to the bulk in these samples. This effect is illustrated by the red-shaded area

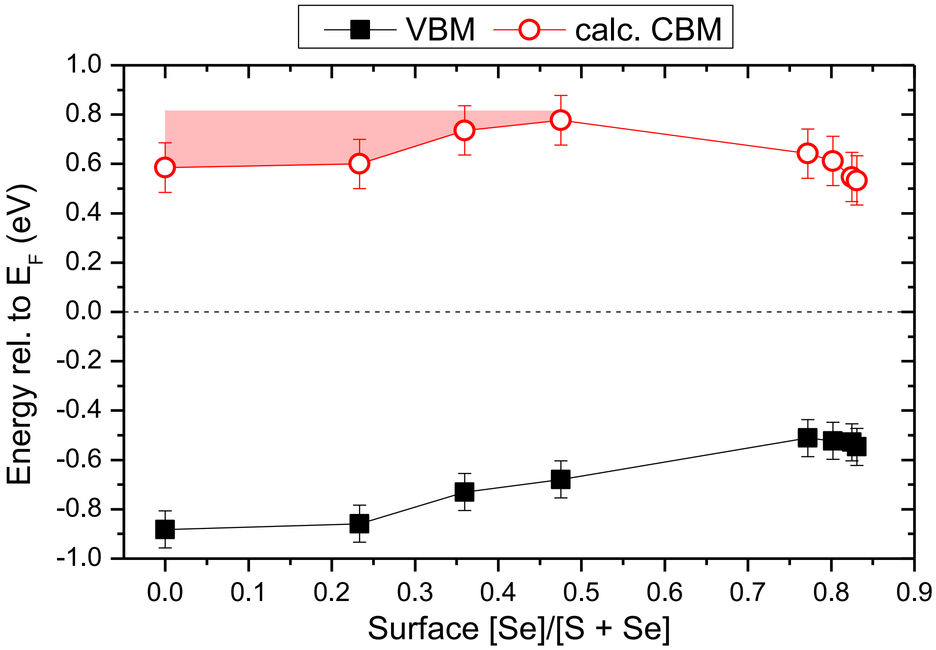

Figure 6.12 Comparison of changes in VBM positions and estimated CBM values (i.e., calc. CBM = VBM + E_g^{bulk}) of the investigated RTP-treated sample series as a function of the surface chalcopyrite [Se]/[S+Se]. The red-shaded area represents the expected E_g^{surf} enlargement.

in Fig. 6.12, where the measured CBM value of the CIS absorber (from Sect. 5.3.5) is assumed to be the upper limit of the CBM of the Cu-poor samples of the series. Because IPES measurements could not be conducted on the RTP-treated samples, it is not possible to conclude whether the shifting of the VBM values closer to the E_F level is ascribed solely to a reduction of the E_g^{surf} (due to a higher Se surface content) or whether a shifting of both, the CBM and the VBM, takes place due to changes in doping level as a function of surface [Se]/[S+Se]. In the latter case, CBM values of the RTP-treated samples could be greater than the assumed 0.8-eV upper boundary, which would not be expected to act favorably on band alignment of the modified buffer/absorber heterointerface.

Samples with surface [Se]/[S+Se] > 0.5 eV [i.e., samples (iv) – (vii)] exhibit more uniform elemental compositions at the surface and bulk due to the surface Cu-enrichment resulting from the RTP treatments. Therefore, the approach taken to estimate the CBM value of these samples (i.e., adding the optical E_g value to the VBM value of the sample) is more valid. The lower CBM values calculated for these samples suggest that the modified absorber surfaces may be better suited for the formation of potentially optimized buffer/absorber band alignments with CdS; however, the reduction in eV_{bb} of these modified absorbers (due to the

VBM shift toward the E_F level) is expected to degrade the performance of produced solar cell devices.

6.4 Solar Cells

Solar cells were prepared with the following thin film stacking configuration (from top to bottom): n-type ZnO window layer/CdS/(RTP treated) CIS absorber/Mo contact. RTP-treated CIS absorbers were produced using the same parameters of sample (ii) (i.e., 300 °C RTP-temperature for 5 min). This treatment in particular was selected because sample (ii) showed a surface Cu:In:(S+Se) composition close to 1:3:5, while attempting to minimize the reduction in VBM resulting from the incorporation of Se (which would in turn decrease the eV_{bb} of resulting solar cell devices). Reference solar cells were produced from untreated CIS stripes (except for KCN etching) from the same batch as the stripes that were subjected to RTP-treatment.

Fig. 6.13 shows the IV-curves of the best performing solar cells based on RTP-selenized CIS stripes and from the reference solar cells. A reduction in j_{SC}, V_{OC} and FF is observed for the solar cell based on the surface modified absorbers in comparison to the reference solar cell,

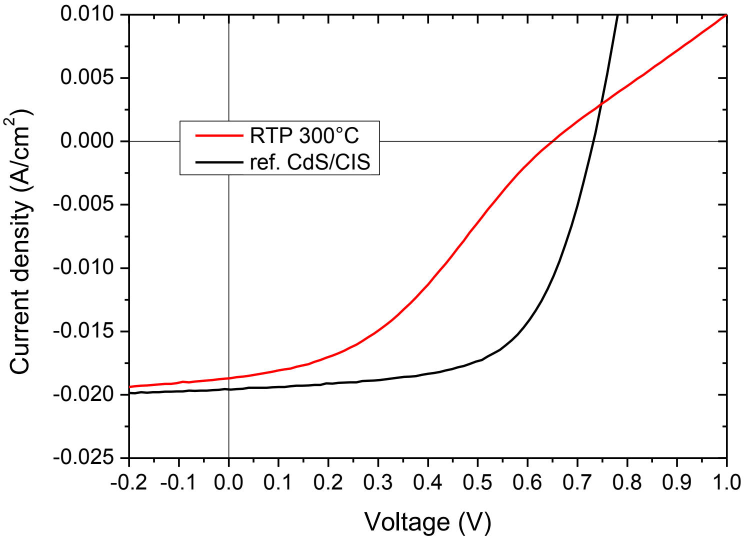

Figure 6.13 *j*-V curves of best performing solar cell based on surface modified (RTP 300 ºC) and reference (ref. CdS/CIS) CIS absorbers.

indicating an increase in power loss related to parasitic resistance. Table 6.2 summarizes the mean solar cell parameters obtained for both types of solar cell devices.

Table 6.2 Mean solar cell parameters of devices based on surface modified and reference CIS absorbers

Absorber	η (%)	V_{OC} (V)	FF
CIS	8.43 ± 0.51	0.722 ± 0.030	0.62 ± 0.02
RTP-treated	3.26 ± 0.63	0.630 ± 0.037	0.30± 0.06

A great reduction in the FF of the solar cells based on the modified absorbers is observed. As considered in Sect. 2.5, such an effect would be expected from both major forms of parasitic resistance: large series and low shunt resistance (R_s and R_{sh}, respectively). However, a significant reduction in V_{OC} is seen for solar cells based on the RTP-treated CIS absorbers. Such a loss in V_{OC} cannot be ascribed to the surface modification (i.e., change in V_{OC} due to a reduction in absorber E_g) because no reduction in optical E_g was found for the absorber resulting from the selected RTP-process, as shown in Sect. 6.3.4. Loss of V_{OC} is not an effect associated with parasitic R_s; however, it is consistent with a reduction in R_{sh} [148-151]. Power losses due to a reduction in R_{sh} (thus, providing alternative paths for the light-generated current) are generally ascribed to unforeseeable manufacturing defects, rather than poor solar cell design [149-151].

For the present modified solar cells, it is possible that the unreacted elemental Se plays a role in the observed R_{sh} reduction. Furthermore, works on directly measured E_g^{surf} of CISSe absorbers have reported strong n-type surfaces [145]. The estimation of the E_g^{surf} values of the samples in the series, carried out in Sect. 6.3.3, gives no indication of such an electronic structure character for any of the RTP-treated samples. Again, it is possible that a lowering in band alignment relative to the E_F level is induced by the presence of elemental Se (i.e., e^- capture by the elemental Se may simulate p-type doping). Based on these conjectures, the elemental Se detected on the surface of the RTP-treated absorbers appears to be a limiting factor in the performance of the modified solar cell devices. In future work, post-treatment annealing to evaporate surface Se should be conducted [152]. Another potential limiting factor will be discussed in greater detail in Ch. 7.

6.5 Summary

In conclusion, an RTP-based treatment to incorporate Se into the surface of CIS absorbers was presented. A substitution of Se for S takes place as a result of all RTP treatments. The VBM shifts towards E_F and a reduction of the optical E_g can be observed. Both observations are in agreement with the formation of a CISSe phase *on top* of the treated CIS substrate. However, this CIS → CISSe conversion (i.e., its [Se]/[S+Se] ratio) and the effective depth of the treatment depend strongly on the RTP process parameters. In samples with higher selenization, the initially Cu-poor CIS surface changes to a surface with a stoichiometric 1:1:2 = Cu:In:(S+Se) composition. The selenization treatment appears to exert a greater impact on the position of the VBM level than on the position of the CBM level. The presence of elemental Se is also detected in all treated samples, which may act as a limiting factor in the performance of solar cell devices based on RTP-treated CIS absorbers.

7 Electronic Structures of CdS/Cu(In,Ga)(S,Se)$_2$ Heterointerfaces: A Conclusion

As observed in Ch. 4 and 5, a characteristic feature of chalcopyrite thin films is a widening of the E_g^{surf} with respect to the E_g^{bulk}. Such relative band gap widenings ($\Delta E_g = E_g^{surf} - E_g^{bulk}$) have been hypothesized to be linked to the formation of ordered defect compounds (ODC) (i.e., changes in element stoichiometry) at the surface of chalcopyrite absorbers or a surface reconstruction that involves the complete Cu-depletion of the uppermost layers of the chalcopyrite materials [26, 153]. In principle, a symmetric increase in the E_g^{surf} should also increase the eV_{bb} of the resulting solar cell device, which in turn increases its performance [142]. [As discussed in Sect. 2.4, eV_{bb} is the energetic difference between the E_F level and the VBM outside the SCR of the solar cell p-n junction (i.e., it is safe to assume that the bulk of the absorber is outside the SCR) and the E_F level and VBM at the absorber's surface]. However, this expected beneficial effect is not as apparent for absorbers with larger E_g^{bulk} values. In fact, the V_{OC} of chalcopyrite-based solar cell devices begins to saturate in absorbers with $E_g^{bulk} > 1.25$ eV, instead of increasing linearly as a function of E_g^{bulk}. This effect is well-illustrated in Fig. 7.1 (as taken from ref. [154]) and has been explained by a pinning of the VBM of the formed surface ODCs to a maximum distance relative to the E_F level [142]. Further increases in absorber E_g^{surf} cause only a shift in the CBM away from the E_F level. Consequently, chalcopyrite absorbers with larger E_g^{bulk} produce heterointerface CBO with CdS with greater discontinuities, which can potentially open recombination paths across the interface.

The activation energy for current saturation at the heterointerface of a p-n junction has been shown to equal the interface band gap, $E_g^{interf} = E_g^{surf} + \text{CBO}$, for heterointerface band alignments with $\text{CBO} \leq 0$ (i.e., cliff to flat band configurations) and to equal the absorber's E_g^{surf} for heterointerface band alignments with $\text{CBO} > 0$ (i.e., spike configurations) [155]. The E_g^{interf}-concept has been used to interpret the effect of heterointerface band alignments on the performance of resulting solar cell devices [156]. However, recent findings of CIS absorbers with electronic structure properties (i.e., VBM and CBM positions) comparable to those found for high-performance CIGSe absorbers (which are, thus, expected to possess comparable heterointerface band alignments with CdS, meaning similar E_g^{interf} values) but still lagging in solar cell performance suggest that a misaligned CB absorber/buffer heterointerface is not the only factor limiting the efficiency of these solar cell devices [157].

In order to better address this issue, the results presented in this dissertation are put into perspective with respect to available literature values of directly measured heterointerface electronic structures [16,89,145,158-161]. The heterointerfaces consisted of chalcopyrite and (related) kesterite absorbers of various E_g^{bulk} values onto which CdS had been deposited. Findings presented in Ch. 4 and 5 were also included in this analysis. Close consideration is given to the influence of various electronic structure parameters on the performance of the resulting solar cell devices. These electronic structure parameters range from absorber-related properties (i.e., ΔE_g values), to heterointerface-related properties (i.e., CBO and E_g^{interf} values), and to a combination of both (i.e., $\Delta E_g^{interf} \equiv E_g^{interf} - E_g^{bulk}$).

The E_g^{bulk} of the absorbers in the reviewed works were determined using UV-Vis or EQE. The absorber E_g^{surf} values were all directly measured using a combination of XPS, UPS and IPES, as described in Ch. 4 and 5. The values are compiled in Table 7.1 for an absorber E_g^{bulk} range of 1.06 – 1.65 eV. (More detailed lists of CBM, VBM and IIBB values for the absorber and buffer components of each heterointerface are provided in Appendix B). For CIGSSe and

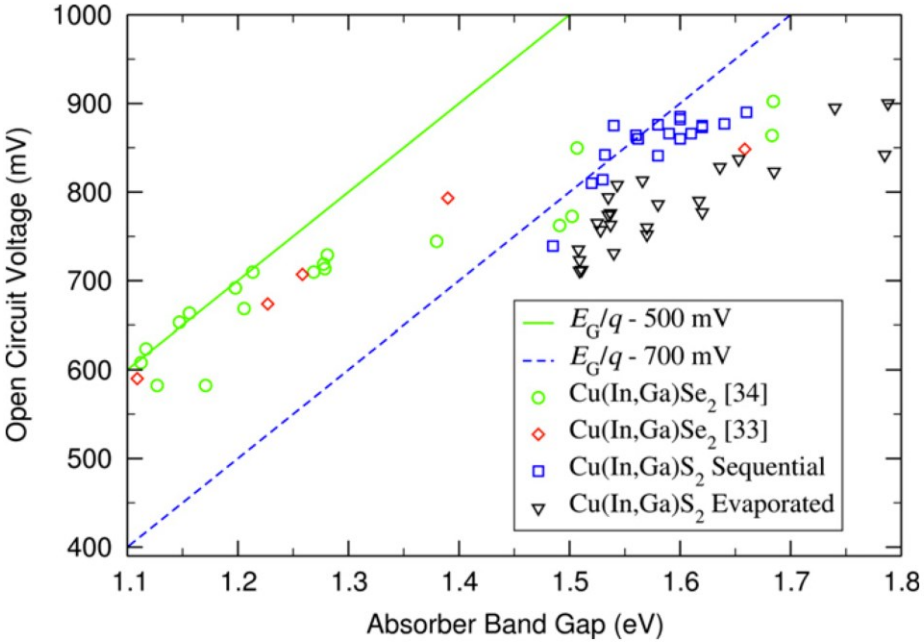

Figure 7.1 V_{OC} values of chalcopyrite-based solar cell devices as a function of absorber E_g^{bulk} (taken from ref. [154]).

CGSe, measurements were found for the absorbers but not for the complete heterointerfaces. Estimates of the CBO of these heterointerfaces were calculated by using the average CBM position of CdS buffers on the other selenium-containing chalcopyrite absorbers in the compilation (i.e., 0.57 ± 0.17 eV). Because respective IIBB values could not be determined, the CBO estimates were assigned significantly larger margins of error than the other CBO values.

Table 7.1 Electronic structure properties of various absorbers, of respective heterointerfaces formed with CdS, and efficiencies of resulting solar cell devices.

Absorber	E_g^{bulk} (eV)	E_g^{surf} (eV)	ΔE_g (eV)	CBO (eV)	E_g^{interf} (eV)	ΔE_g^{interf} (eV)	Eff. (%)	E_g^{bulk} method	Ref.
CISSe	1.06±0.05	1.4 ± 0.15	0.34±0.15	0 ± 0.15	1.4 ± 0.18	0.34±0.2	14.1	UV-Vis	[145,158]
CIGSe	1.23±0.05	1.68±0.15	0.45±0.15	-0.16 ± 0.15	1.52±0.18	0.29±0.2	17.8	UV-Vis	[159]
CIGSe	1.17±0.05	1.63±0.15	0.46±0.1	-0.03 ± 0.15	1.60±0.18	0.43±0.2	20	UV-Vis	[160]
CIGSe	1.21±0.05	1.70 ± 0.2	0.49± 0.2	0.11 ± 0.25	1.70±0.25	0.49±0.25	18.3	EQE	Ch. 4,[29]
CIS	1.47±0.05	1.88 ± 0.2	0.41± 0.2	-0.42 ± 0.2	1.46±0.2	-0.01±0.2	9	UV-Vis	Ch. 5,6,8
CIGS	1.5±0.05	1.76±0.15	0.26±0.15	-0.45 ± 0.15	1.31±0.18	-0.19±0.2	7	EQE	[16,162]
CIGSSe	1.38±0.05	1.92±0.15	0.54±0.15	-0.52 ± 0.3*	1.40±0.3*	0.02±0.3*	9	UV-Vis	[161]
CGSe	1.65±0.05	2.2 ± 0.15	0.55±0.15	-1.03 ± 0.3*	1.17±0.3*	-0.48±0.3*	6	UV-Vis	[89]
CZTS	1.5±0.05	1.53±0.15	0.03±0.15	-0.33 ± 0.15	1.20±0.18	-0.3±0.2	6.8	UV-Vis	[156]
CZTS	1.5±0.05	1.92±0.15	0.42±0.15	-0.34 ± 0.15	1.58±0.18	0.08±0.2	10.1	UV-Vis	[156]

Abbreviations of spectroscopic methods used for determination of E_g are defined in text. Values followed by an asterisk (*) are estimates; more details found in text. These electronic properties are shown in future figures along with error margins.

Fig. 7.2 (a) – (c) show plots of the tabulated ΔE_g, CBO and ΔE_g^{interf} values (i.e., electronic properties linked to the absorbers, to the formed heterointerfaces, and to a combination of both, respectively) as a function of the absorber E_g^{bulk}. A widening of the E_g^{surf} with respect to the E_g^{bulk} is found for all absorbers, except for one of the kesterite absorbers. Moreover, except for the outlier value of the kesterite absorber, the obtained ΔE_g values are within the margin of error for all absorbers. Based on these results, increases in eV_{bb} are expected to be comparable in all samples. In contrast, pronounced changes in CBO are seen throughout the analyzed range of absorber E_g^{bulk} values. Strong cliff heterointerface alignments are produced for absorbers with $E_g^{bulk} > 1.25$ eV (denoted by the red line), which correlates to the start of

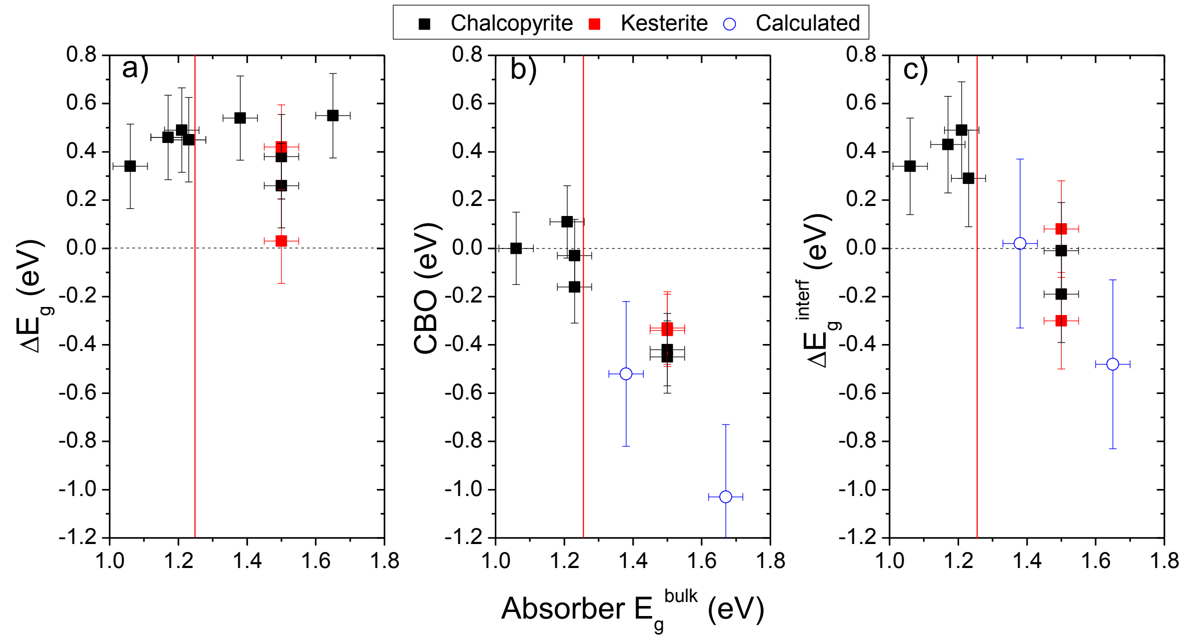

Figure 7.2 Changes in (a) ΔE_g, (b) CBO and (c) ΔE_g^{interf} of the reported (analyzed) heterointerfaces as a function of absorber E_g. The blue hollow circles represent calculated values for which the estimated CBO values of the CdS/CIGSSe and CdS/CGSe heterointerfaces were used. The red line denotes the 1.25 eV E_g value, at which the V_{OC} of solar cell devices start to deviate from acting as a linear function of the absorber E_g.

the non-linear V_{OC} deviation of solar cell devices shown in Fig. 7.1. Furthermore, by combining the ΔE_g and CBO values, the ΔE_g^{interf} values are obtained, which are shown in Fig. 7.2 (c) as a function of absorber E_g^{bulk}. The figure suggests that heterointerfaces formed with absorbers of E_g^{bulk} < 1.25 eV retain all the benefits derived by an improved eV_{bb}, due to not encountering significant interface recombination. On the other hand, the ΔE_g^{interf} of absorbers with E_g^{bulk} > 1.25 eV suggest that their gains in eV_{bb} cannot compensate for the decrease in activation energy of interface recombination loss mechanisms.

Four of the evaluated absorbers possess the same E_g value (i.e., the CIS, CIGS and the two CZTS absorbers), while at the same time showing two slightly different CBO values and completely different E_g^{interf} (and therefore ΔE_g^{interf}) values, presenting an ideal case to determine whether the performance of solar cell devices are predominantly related to heterointerface limitations or to a combination of factors. For this purpose, the reported conversion factors, η, of solar cell devices resulting from the analyzed heterointerfaces are presented in Fig. 7.3 (a) and (b) as a function of CBO and ΔE_g^{interf}, respectively. Although a

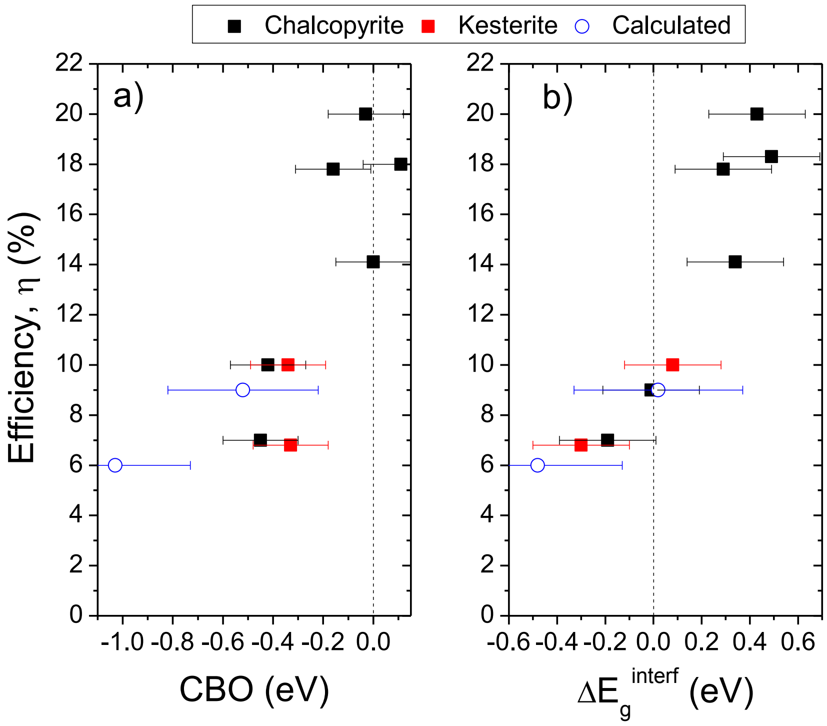

Figure 7.3 Conversion factor of solar cell devices resulting from the reported (analyzed) heterointerfaces as a function of the determined (a) CBO and (b) ΔE_g^{interf}, respectively. ($\Delta E_g^{interf} = E_g^{interf} - E_g^{bulk}$) The blue hollow circles represent calculated values for which the estimated CBO values of the CdS/CIGSSe and CdS/CGSe heterointerfaces were used. Dashed lines are shown at the 0 x-value.

similar trend is observed in both plots, a better agreement is found in Fig. 7.3 (b), especially for the above-noted absorbers of equal E_g value.

These findings are consistent with reported models of recombination loss mechanisms of low- and wide-gap absorber-based solar cell devices (see Sect. 2.5) [13,14]. A positive ΔE_g^{interf} value, found for all high-performance chalcopyrite-based solar cells, signals for enhanced carrier transport through the buffer/absorber heterointerface. The absence of significant recombination loss at the buffer/absorber heterointerface leads to predominant carrier recombination at the bulk of the absorber. Moreover, a negative ΔE_g^{interf} value, found for wide-gap chalcopyrite-based solar devices, translates into poor carrier transport across the buffer/absorber heterointerface due to significant interface recombination loss.

Furthermore, these findings strengthen the claim that even though a misaligned CB absorber/buffer heterointerface is a powerful factor that limits the efficiency of solar cell devices based on wide-gap CIGSSe absorbers, it should not be the only point of consideration. An effective strategy for the deliberate surface modifications of wide-gap CIGSSe absorber should target increasing the ΔE_g of the absorber (or at least, not decreasing it), while minimizing the CB misalignment of the buffer/absorber heterointerface; thus, effectively increasing the ΔE_g^{interf}.

In retrospect, the optimization method presented in Ch. 6 seems to not have been an ideal route, as was evidenced by the performance of solar cell devices based on RTP-treated CIS absorbers. Although the goal was to produce an absorber surface with a more favorable band alignment with the CdS buffer, substituting Se for S appears to have reduced the E_g^{surf} of the absorber (see Sect. 6.3.3), which decreases the ΔE_g of the absorber. This effect and the seemingly insufficient lowering of the CB level induced by the selenization treatments suggest that the heterointerface formed by the RTP-treated CIS would have a lower ΔE_g^{interf} value than the heterointerface formed by untreated CIS absorbers. The observed decline in performance of solar cell devices based on RTP-treated CIS absorbers is consistent with a reduction in ΔE_g^{interf}.

In Ch. 8, a surface treatment aiming at optimizing the misaligned electronic structure of the CdS/CIS heterointerface, while not unfavorably altering the ΔE_g of the CIS absorber, is presented.

8 Electronic Structure Tuning of the CdS/CuInS₂ Heterointerface via SAMs

8.1 Introduction

The use of dipole-charge-inducing self-assembled monolayers (SAM) has proven to be a suitable means to control energy levels in electronic devices [163-168]. For example, the modulation of the Schottky electron (hole) barriers of various metal/polymer heterointerfaces (i.e., the difference between the metal's Φ and the χ of the polymer) has been achieved by insertion of monolayers of polar molecules between the investigated heterointerfaces [163,164]. This kind of tailoring is illustrated in Fig. 8.1. The introduction of dipole charges between semiconductor-based heterointerfaces have shown similar effects of electronic band re-alignment [35]. Building upon this premise, it can be surmised that the insertion of suitable SAMs between the buffer/absorber heterointerface in wide-gap chalcopyrite solar cell structures could be employed to correct unfavorable CBO configurations.

The major goal of this chapter is to demonstrate that the electronic properties of the CdS/CIS heterojunction can be tailored by employing dipole-charge-inducing SAMs. In order to be able to tune the electronic buffer/absorber interface structure in general, a "library" of potential dipole interlayers was produced using a variety of SAMs of alkanethiols and benzoic acid derivatives.

Based on the finding in Ch. 5 of an unfavorable cliff-like CBO at the CdS/CIS heterointerface, an optimization of the heterointerface CBO would entail raising the CBM of the CdS interface with respect to the E_F level. A SAM inducing a negative dipole could be used for this purpose [163,164], as shown in Fig. 8.1 (b). In contrast to the heterointerface tailoring approach presented in Ch. 6, the use of SAMs would not reduce the treated (modified) heterointerface's ΔE_g^{interf} and, in turn, deter the efficiency of resulting solar cell devices, as discovered in Ch. 7.

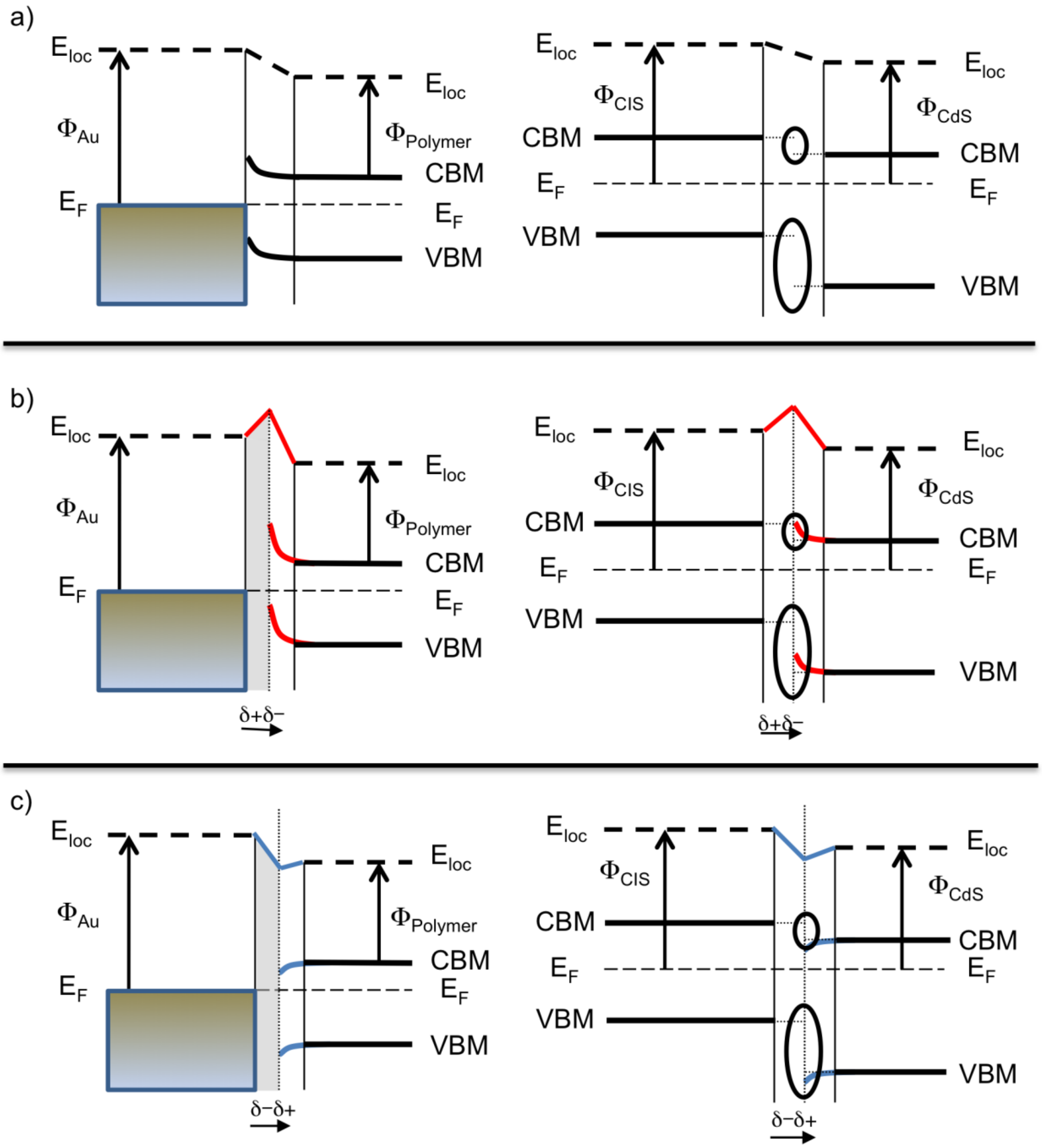

Figure 8.1 (a) Schematic displaying the electronic structure of: (left half) a metal/polymer heterointerface and (right half) a CdS/CIS heterointerface. (b) The effect on (a) by inserting a negative dipole charge (directed away from the metal or CIS absorber surface, respectively) between the heterointerfaces. (c) The effect on (a) by inserting a positive dipole charge (directed away from the metal or CIS absorber surface, respectively) between the heterointerfaces.

8.2 Experimental Details

Au-coated Si wafers (denoted Au ref. henceforth) and CIS samples were treated with millimolar concentration solutions (i.e., 1, 5, 10 and 20 mM) of selected benzoic acid derivative and alkanethiol SAMs (using acetonitrile and ethanol as solvents, respectively).

The CIS absorbers were prepared in the same way as those used in Ch. 5 and 6 [30]. The selected benzoic acid derivatives (and their abbreviations) were benzoic acid (bz), 4-methoxybenzoic acid (OCH_3-bz), 4-fluorobenzoic acid (F-bz), and 4-nitrobenzoic acid (NO_2-bz). The two alkanethiol SAMs (and their abbreviations) used were 1-dodecanethiol (H-th) and 1H,1H,2H,2H-perfluorodecanethiol (F-th). The molecular structures of these compounds are displayed in Fig. 8.2. All Au ref. samples were submitted to Ar^+ treatments to remove absorbates prior to a SAM or a stage (control) treatment. CIS samples were KCN etched to remove Cu_xS binary phases from the absorber surface before SAM treatments. The wet chemistry procedure involved in the deposition of the SAM organic dipole layers (i.e., sample immersion into SAM solution, treatment duration, washing off residue with solvent, etc.) and sample mounting were performed inside a N_2-filled glovebox (gb) directly attached to the surface analysis system. Treatment of samples in SAM solutions lasted 12 hours.

The surface chemical and electronic structures of the SAM-treated samples were studied using XPS and UPS. The XPS measurements used Mg K_α excitation energies and a SPECS PHOIBOS 150MCD electron analyzer. UPS measurements were conducted with a He discharge lamp using the He I line. The magnitude and polarity of the deposited surface dipoles were determined by monitoring changes in Φ of the treated samples, derived from their He I UPS secondary electron cut-off spectra. The E_F level of a sputter-cleaned Au foil was used as the energy scale.

Solar cells were prepared with the same stacking configuration used in Sect. 6.4. KCN-etched CIS stripes were treated for 12 hours with 20 mM solutions of selected SAMs inside the N_2-

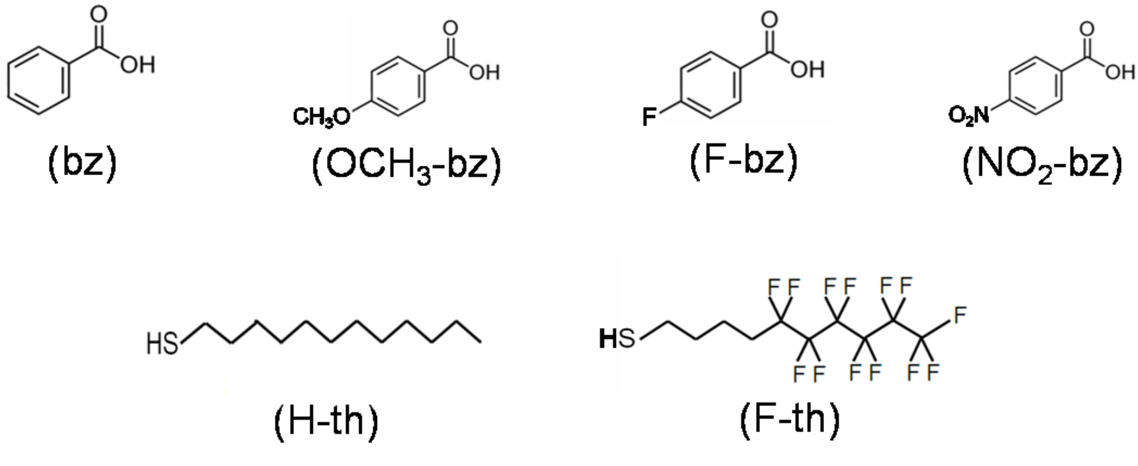

(bz) (OCH_3-bz) (F-bz) (NO_2-bz)

(H-th) (F-th)

Figure 8.2 Molecular structure of the SAMs used for surface tailoring treatments in this chapter.

filled glovebox directly attached to the surface analysis system. Reference solar cells were produced from untreated (except for KCN etching) CIS stripes from the same batch as the stripes treated with SAM solutions.

8.3 SAM Adsorption on Au

In the following section, the characterization of the chemical and electronic structure of the SAM-treated Au ref. samples is presented. First, surface-sensitive XPS measurements yield a better understanding of the composition and thickness of the deposited SAMs layers. These results are then complemented by UPS secondary electron cut-off measurements, which allow us to link changes in the Φ of the samples to the deposited organic dipole layers and establish a “library” of potential dipole interlayers to later deliberately tune the electronic structure of the CdS/CIS heterointerface.

8.3.1 Chemical Structure

Fig. 8.3 presents the XPS survey spectra of a sputter-cleaned Au ref. sample prior to and after various stages of the wet chemical process and SAM solutions, along with corresponding peak identification. In addition to Au-related photoemission lines, the survey spectra of the sputter-cleaned Au ref. sample shows low signals of C-related photoemission lines; however, O-related photoemission lines are not detected. Because the SAM treatments are expected to deposit organic films in the monolayer range (i.e., not sufficiently thick to completely attenuate the photoemission signal of the Au substrate), it is not surprising that the survey spectra of the other samples consist predominantly of Au-related photoemission lines. However, a reduction in the intensity of Au-related core levels is observed when comparing the spectra of the treated (exposed) samples to that of the sputter-cleaned Au ref. sample (i.e., sp. Au ref.). This effect is more clearly discernable in Fig. 8.4, which features the detail XPS spectra in the Au 4f region of the discussed samples, and will be adressed in greater depth below. C- and O-related photoemission lines of higher intensities compared to the sputter-cleaned Au ref. samples are found in all treated (exposed) samples. (An exception is the absence of O-related photoemission lines for H-th treated samples.) Additionally, photoemission lines related to elements comprising the moiety of the used SAM compounds

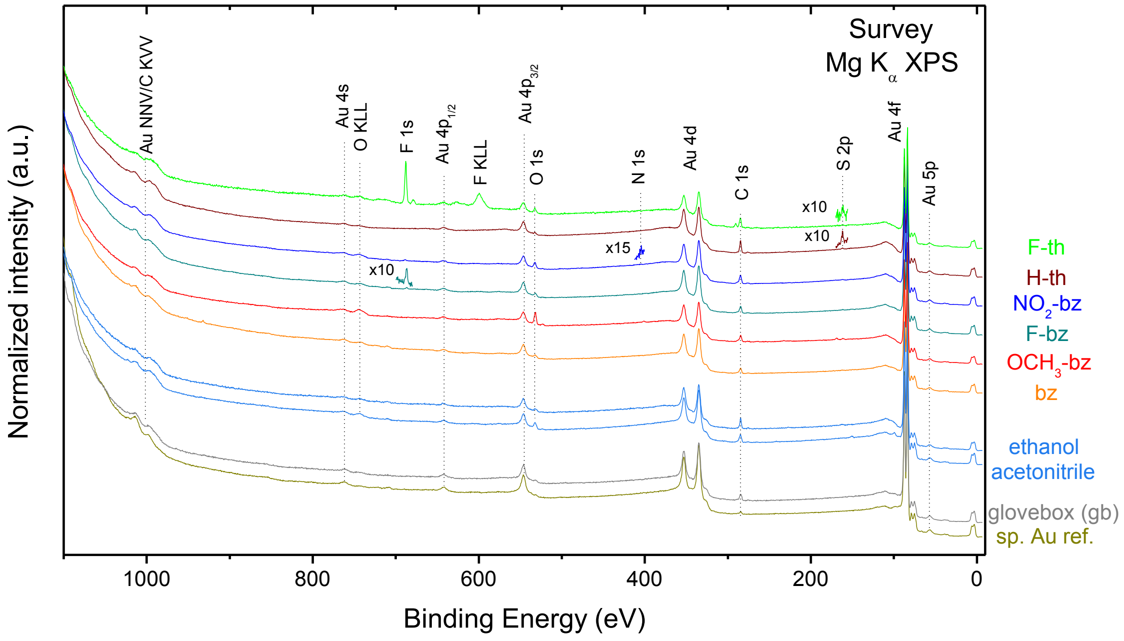

Figure 8.3 XPS survey spectra of sputter-cleaned Au ref. samples prior to and after exposure to various stages of SAM solution treatments [10 mM]. Vertical offsets are added for clarity.

are also found in the spectra of samples submitted to SAM treatments (shown magnified). All these changes in surface chemical structure are expected and in agreement with the adsorption of the selected organic compounds to the surface of Au ref. samples.

To estimate the degree of SAM adsorption on the Au ref. substrates, the attenuation of the photoemission of the Au ref. substrate, as monitored by the Au 4f lines (shown in Fig. 8.4) resulting from the various SAM treatments, was evaluated. First, the following qualitative observations can be made regarding the effects of these treatments (treatment stages) on the Au ref. samples. A slight reduction in Au 4f intensity results from a 30 min. exposure of a sputter-cleaned Au ref. sample to the N_2 ambient inside the glovebox (i.e., gb, the approximate amount of time needed for sample mounting and introduction to the surface analysis system). Immersion of a sputter-cleaned Au ref. sample in acetonitrile (i.e., the solvent of the benzoic acid derivative SAM solutions) for a time period equal to the SAM treatment duration does not appear to significantly alter the Au 4f intensity. On the other hand, a reduction in Au 4f intensity is observed after immersion of a Au ref. sample in ethanol (i.e., the solvent of the thiol SAM solutions) for the same period of time, suggesting the adsorption

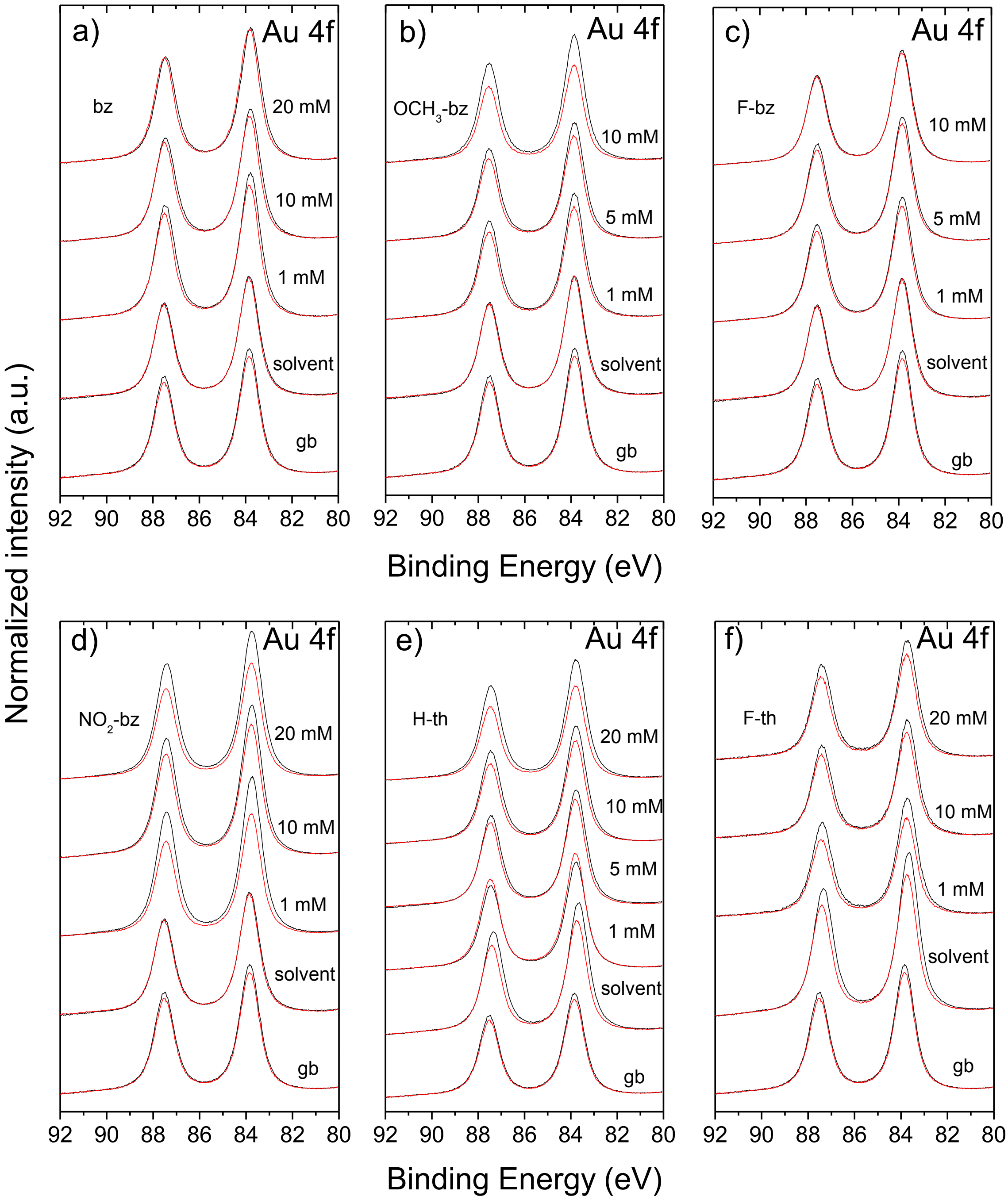

Figure 8.4 XPS detail spectra of the Au 4f region of sputter-cleaned Au ref. samples prior to (black) and after (red) exposure to various stages of the following SAM solution treatments: (a) bz, (b) OCH_3-bz, (c) F-bz, (d) NO_2-bz, (e) H-th and (f) F-th. For (a) – (d), acetonitrile was used as a solvent. For (e) and (f), ethanol was used as a solvent. All spectra were measured using Mg K_α excitation. Vertical offsets are added for clarity.

of ethanol-related molecules to the surface of the substrate. The chemical nature of these adsorbates will be discussed below. Treating the Au ref. samples with SAM solutions of increasingly high concentrations also correspondingly reduces the signal of the Au 4f lines. In the case of the benzoic acid derivative SAMs, the adsorption-related attenuation increases with higher moiety sizes.

The intensities of the Au 4f lines of the discussed Au ref. samples were determined through curve fit analysis. The respective fits are not shown in Fig. 8.4 to allow for an easier visual comparison of the Au 4f lines prior to and after treatments (the intensities of which are labeled I_0 and I, respectively). Table 8.1 shows the quantified changes in Au 4f intensity (i.e., I/I_0) and the effective thickness of the SAM layers (d_{SAM}), as calculated by using eqn. (4.1).

The cleanliness (i.e., absence of surface contaminants) of the substrate has been demonstrated to be an important factor in the adsorption of SAM compounds, with a delay in the onset of SAM adsorption in contaminated surfaces [169,170]. Although all Au ref. samples were submitted to the same Ar^+ ion treatments for adsorbate removal prior to SAM treatment, the time lapses for a given Au ref. sample between (i) its Ar^+ ion treatment and its immersion in the SAM solution and (ii) its retrieval from the SAM solution and its actual measurement were not the same for all samples. The reason for this is that all samples of a given SAM series were treated simultaneously. These interval variations alter the extent to which extraneous adsorbates, which even under UHV conditions cannot be entirely prevented, may affect the attenuation of the analyzed Au 4f lines. Considering that the calculated d_{SAM} values are in the Å (monolayer) range, the distortive impact of extraneous adsorbates on the d_{SAM} estimates cannot be ignored.

Table 8.1 Effective thicknesses, d_{SAM} (in Å), of the adsorbed SAM layers. λ_{SAM} values are also reported in Å and were obtained from refs. [50,51].

	bz		OCH_3-bz		F-bz		NO_2-bz		H-th		F-th	
SAM [mM]	Au 4f (I/I_0)	d_{bz} (λ= 31.3)	Au 4f (I/I_0)	$d_{OCH3\text{-}bz}$ (λ= 31.5)	Au 4f (I/I_0)	$d_{F\text{-}bz}$ (λ= 31.3)	Au 4f (I/I_0)	$d_{NO2\text{-}bz}$ (λ= 31.4)	Au 4f (I/I_0)	$d_{H\text{-}th}$ (λ= 31.6)	Au 4f (I/I_0)	$d_{F\text{-}th}$ (λ= 30.8)
1	0.91	3.1 ± 0.6	0.88	4.2 ± 0.8	0.92	2.7 ± 0.5	0.75	8.9 ± 1.8	1.07	-	0.82	6.3 ± 1.3
5	-	-	0.87	4.2 ± 0.8	0.93	2.3 ± 0.5	-	-	0.89	3.8 ± 0.8	-	-
10	0.93	2.3 ± 0.5	0.75	9.0 ± 1.8	0.97	1.0 ± 0.2	0.86	4.7 ± 0.9	0.87	4.2 ± 0.8	0.89	3.7 ± 0.7
20	0.98	0.7 ± 0.2	-	-	-	-	0.77	8.1 ± 1.6	0.77	8.4 ± 1.7	0.86	4.6 ± 0.9

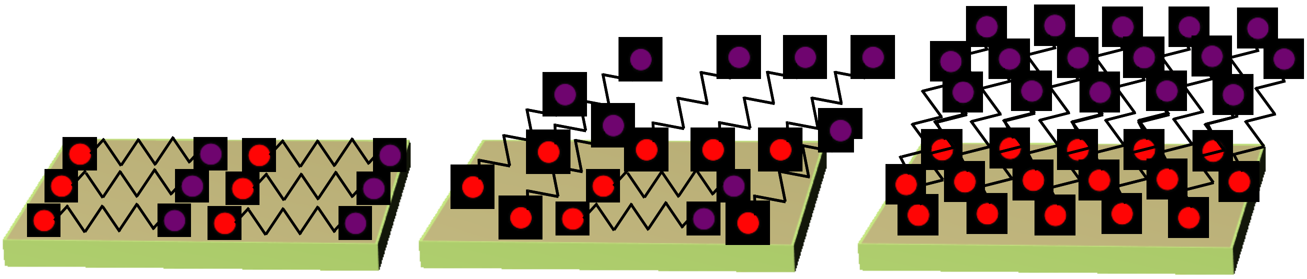

Figure 8.5 Changes in orientation of a thiol-based SAM as a result of different surface densities (coverages), adapted from ref. [169].

A second point of consideration is the density-dependence of the SAM, with flatter or more upright orientations leading to lower and higher SAM surface densities, respectively [169,171]. This effect is illustrated in Fig. 8.5 and implies that changes in λ_{SAM} values will arise due to different SAM orientations. Based on these factors, the evaluation of the Au 4f line attenuation may not provide the best estimate of the d_{SAM} on the Au ref. samples treated with SAM solutions. Instead, changes in surface chemistry ascribed to adsorption of SAMs (i.e., expected for C, O and moiety-related photoemission lines) will be monitored as an alternative guide to SAM layer growth.

Fig. 8.6 shows the detail XPS C 1s spectra of the Au ref. samples prior to and after various stages of SAM treatments, along with respective curve fits. As expected, a significant increase in C 1s intensity is observed for all samples submitted to a SAM treatment or one of its stages. Changes in the lineshape and the energy position of the C 1s line of treated Au ref. samples also suggest changes in carbon speciation. Satisfactory fits of the measured C 1s spectra for samples of the benzoic acid derivative SAM treatment series can be attained by using three peaks (with equal FWHM values), here referred to as C_I, C_{II} and C_{III} (in order of increasing BE). For the fitting of C 1s spectra of F-th-treated Au ref. samples, an additional peak (i.e., C_{IV}) is need. The C 1s spectra of H-th-treated Au ref. samples can be fitted using two peaks. An explanation for these variances will be discussed below. The BE of the fitted peaks of the C 1s spectra of samples treated with benzoic acid derivative SAMs and thiol SAMs (and their control samples) are shown in Fig. 8.7 (a) and (b), respectively, as the mean BE value of all the concentration treatments, along with literature BE value ranges (gray-filled boxes) for various carbon-based bonds taken from ref. [45].

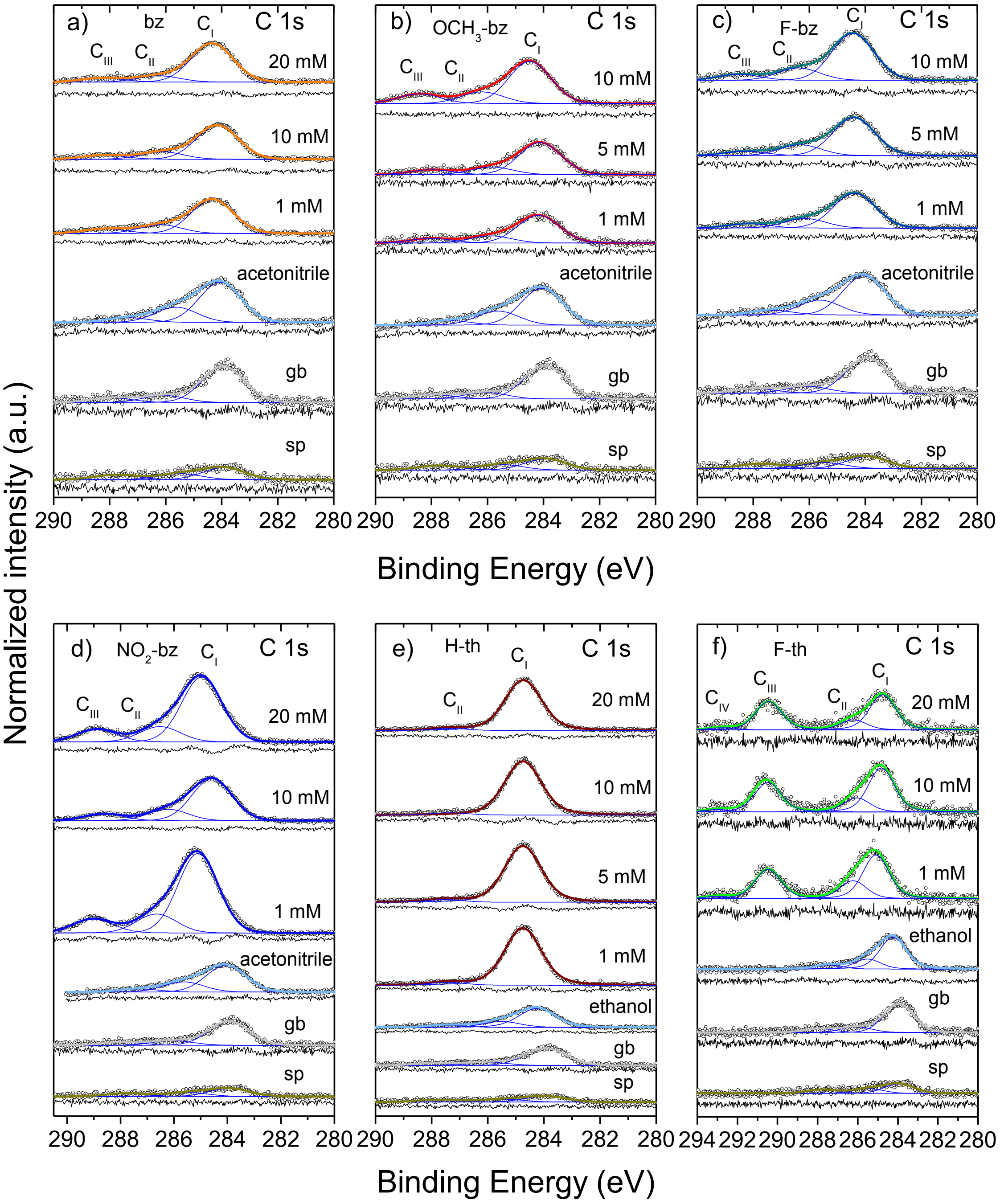

Figure 8.6 Curve fit analysis of the C 1s spectra of sputter-cleaned Au ref. samples prior to and after exposure to various stages of the following SAM solution treatments: (a) bz, (b) OCH_3-bz, (c) F-bz, (d) NO_2-bz, (e) H-th and (f) F-th. For benzoic acid derivative SAMs [i.e., (a) – (d)], acetonitrile was used as a solvent. For thiol SAMs [i.e., (e) and (f)], ethanol was used as a solvent. All spectra were measured using Mg K_α excitation. Vertical offsets are added for clarity.

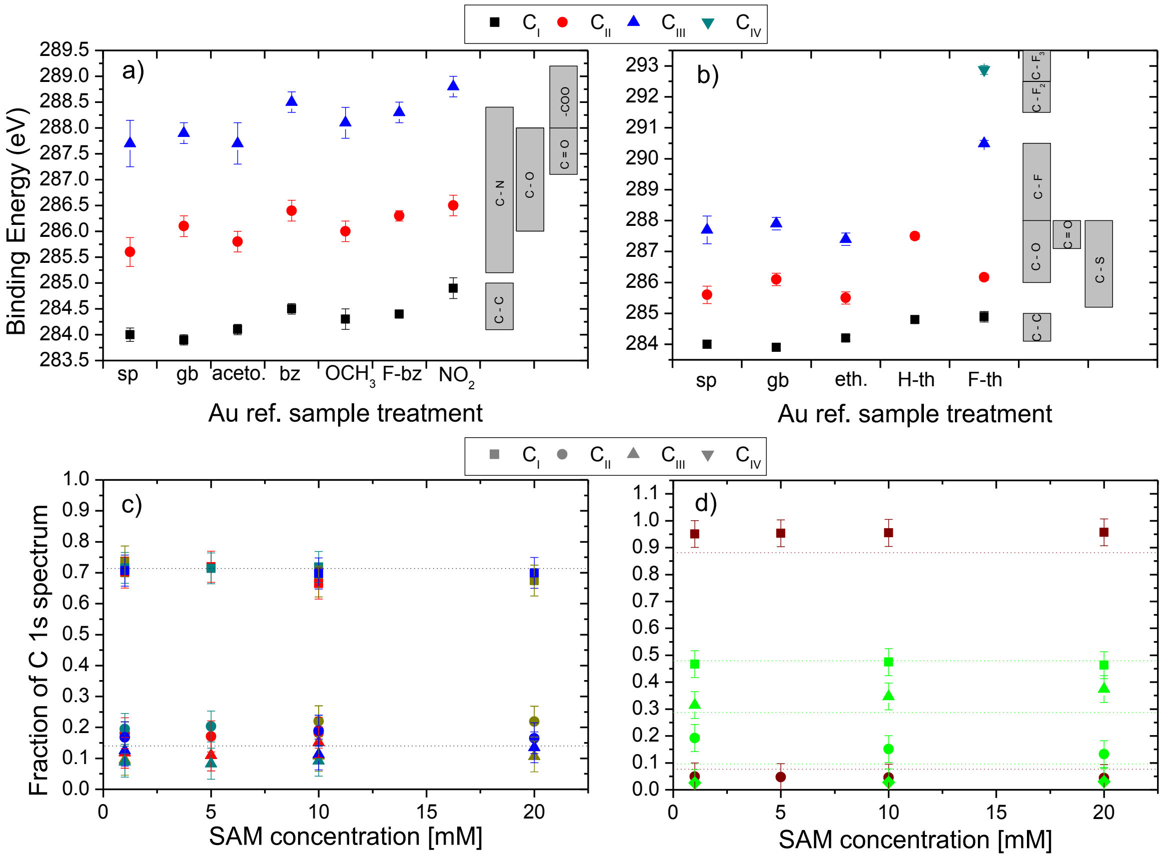

Figure 8.7 Top row: Mean BE of the curve-fit peaks of the C 1s region of sputter-cleaned Au ref. samples prior to and after exposure to various stages of (a) benzoic acid derivative and (b) thiol SAM treatments, along with reference BE ranges for different carbon species. The aceto., OCH_3, NO_2 and eth. treatment abbreviations refer to acetonitrile, OCH_3-bz, NO_2-bz and ethanol, respectively. Bottom row: Fraction comprised by each of the curve-fit peaks of the total area of C 1s spectra of Au ref. samples treated with (c) bz, OCH_3-bz, F-bz, NO_2-bz, (d) H-th and F-th SAMs (as color-coded). The gray legend icons above (c) and (d) shows the shape that each C 1s curve-fit peak represents. The dashed lines (---) in (c) denote the spectral fractions expected of C_I:C_{II}:C_{III} = 5:1:1 ratios. The wine- (---) and green-colored (---) dashed lines in (d) denote the spectral fractions expected of C_I:C_{II} = 11:1 and C_I:C_{II}:C_{III}:C_{IV} = 3:1:5:1, respectively.

The C_I and C_{III} peaks of the fitted C 1s spectra of sputter-cleaned and control Au ref. samples for the benzoic acid derivative SAM series (i.e., Au ref. samples exposed to the glovebox ambient or immersed in acetonitrile) are located at 284.0 ± 0.1 and 287.8 ± 0.4 eV, respectively. These peaks are ascribed to sp^2-hybridized carbon and to carbonyl carbon. These assumptions are consistent with the fact that even carbon nanoparticles and amorphous carbon clusters contain different carbon hybridizations and that Au has been shown to act as a catalyzer for the synthesis of carbonyl groups in the presence of oxygen [172,173]. Moreover, the intensity of the C_{III} peak is low for the control samples, also consistent with their low O 1s intensities (to be covered below). The BE of the C_{II} peak of the sputter-cleaned Au ref. sample (i.e., 285.6 ± 0.3) is close to reported values of sp^3-hybridized carbon. For the other two control samples, their C_{II} peaks are located at a significantly higher BE, in the C-N (i.e., 285.8 ± 0.2 eV for the acetonitrile-immersed Au ref. sample) and C-O (i.e., 286.1 ± 0.2 eV for the glovebox-exposed Au ref. samples) regions. C-N bonds are consistent with reports of acetonitrile-adsorption to Au surfaces [174]. As already considered, C-O bonds can result also from Au acting as a catalyzer of oxygen-containing functional groups in the presence of oxygen [173,174].

Regarding the C 1s spectra of Au ref. samples treated with benzoic acid derivative SAM solutions, the C_I, C_{II} and C_{III} peaks are ascribed to five of the benzyl ring carbons, the benzyl ring carbon bonding the moiety group, and the carboxylic carbon. When the fractions comprised by each of the fit peaks with respect to the total C 1s intensity are compared for the various benzoic acid derivative SAMs, a C_I:C_{II}:C_{III} = 5:1:1 ratios are obtained, as shown in Fig. 8.7 (c).

As shown in Fig. 8.7 (b), the C_I, C_{II} and C_{III} peaks of the fitted C 1s spectrum of a sputter-cleaned Au ref. sample immersed in ethanol are located at similar BEs to those of a sputter-cleaned Au ref. sample. The C 1s spectra of Au ref. samples treated with H-th SAM solutions are fitted with two peaks. In this case, C_I is positioned at a BE (i.e., 284.8 ± 0.1 eV) close to reported values of sp^3-hybridized carbon, corresponding to hydrated carbon [175-177]. The C_{II} peak is located at a BE similar to the C_{III} peak of the control samples (ascribed to carbonyl carbon). However, considering that the O 1s lines of H-th treated Au ref. samples [Fig. 8.8 (e)] are practically absent (in contrast to the ethanol-immersed Au ref. sample), the C_{II} of the H-th treated Au ref. samples is ascribed to C-S bonding. This designation is further strengthened by comparing the fraction each peak comprises with respect to the total C 1s intensity. As shown in Fig. 8.7 (d), the C_I:C_{II} ratio is, within the margin of error, 11:1, consistent with the eleven completely hydrated carbons of the H-th molecule and the one carbon bonding to the thiol group.

Regarding the Au ref. samples treated with F-th solutions, the C_I (at 284.9 ± 0.2 eV) and C_{II} (at 286.2 ± 0.1 eV) peaks are ascribed to hydrated sp^3-hybridized carbon and C-S bonding (i.e., carbon bonding to the thiol), respectively. The C_{III} (at 290.5 ± 0.1 eV) and C_{IV} (at 292.9 ± 0.1 eV) peaks, located at significantly higher BEs than the C_I and C_{II} peaks, are ascribed to the two types of fluorinated carbon found in the F-th molecule. The fraction of the total C 1s intensity that each peak fit comprises is also shown in Fig. 8.7 (d). In this case, the average C_I:C_{II}:C_{III}:C_{IV} = 3:1:2:0.2 deviates from the expected 3:1:5:1 ratio. This deviation appears to be caused by ethanol molecules H-bonding to the adsorbed F-th SAMs, which would contribute to the intensity in the C_I and C_{II} BE regions. The shift becomes less pronounced with higher F-th concentration.

Changes in oxygen speciation are also detected in samples treated with SAM solutions. Fig. 8.8 shows the O 1s spectra of Au ref. samples prior to and after various SAM treatments, along with corresponding curve fits. Similar results to the corresponding C 1s spectra are found: Changes in the lineshape and the energy position of the O 1s line of treated Au ref. samples also suggest changes in oxygen speciation. Exposure of sputter-cleaned Au ref. samples to the glovebox ambient did not lead to a significant increase in O 1s intensity. (In the corresponding C 1s spectra in Fig. 8.6, exposure of sputter-cleaned Au ref. samples to the glovebox ambient did increase the intensity of its C 1s line; however, the effect was significantly lower than sample immersion in the solvents.) Sample immersion in the employed solvents, however, did increase the surface oxygen content; sometimes comparably to increases seen in samples treated with solutions of SAMs not containing oxygen in their moiety groups. For example, the O 1s intensity of the acetonitrile-immersed sample is comparable to that detected for the bz- and F-bz-treated samples. Likewise, the O 1s intensity of the ethanol-immersed sample is similar to that of the F-th-treated samples. In comparison, the OCH_3-bz- and NO_2-bz-treated samples (i.e., SAM with oxygen-containing moieties) show significantly higher O 1s intensities.

No significant O 1s signal was detected for samples treated with H-th solutions. In this case, the hydrophobic hydrocarbon chains of the H-th molecules seem to replace oxygen-containing functional groups remaining at the surface of the Au ref. samples prior to treatment. Moreover, they also appear to prevent any ethanol from dispersing into the SAMs. This finding is consistent with the two-peak curve fit of the C 1s spectra of the H-th-treated samples, in which the C_{III} peak is associated with carbonyl/carboxylic carbon.

Unlike the benzoic acid derivative SAMs, the F-th molecule does not contain an oxygen site, which means that the oxygen signal has another source. Considering that the electronegative fluorine atoms can attract the hydrogen of the ethanol's alcohol group, it is likely that the O 1s signals arise from non-covalently bonded (i.e., H-bonding) ethanol molecules on the F-th

SAMs. This configuration is consistent with the detected fractions of the fit peaks used for the curve fit analysis of the C 1s spectra of the F-th-treated samples [Fig. 8.7 (d)].

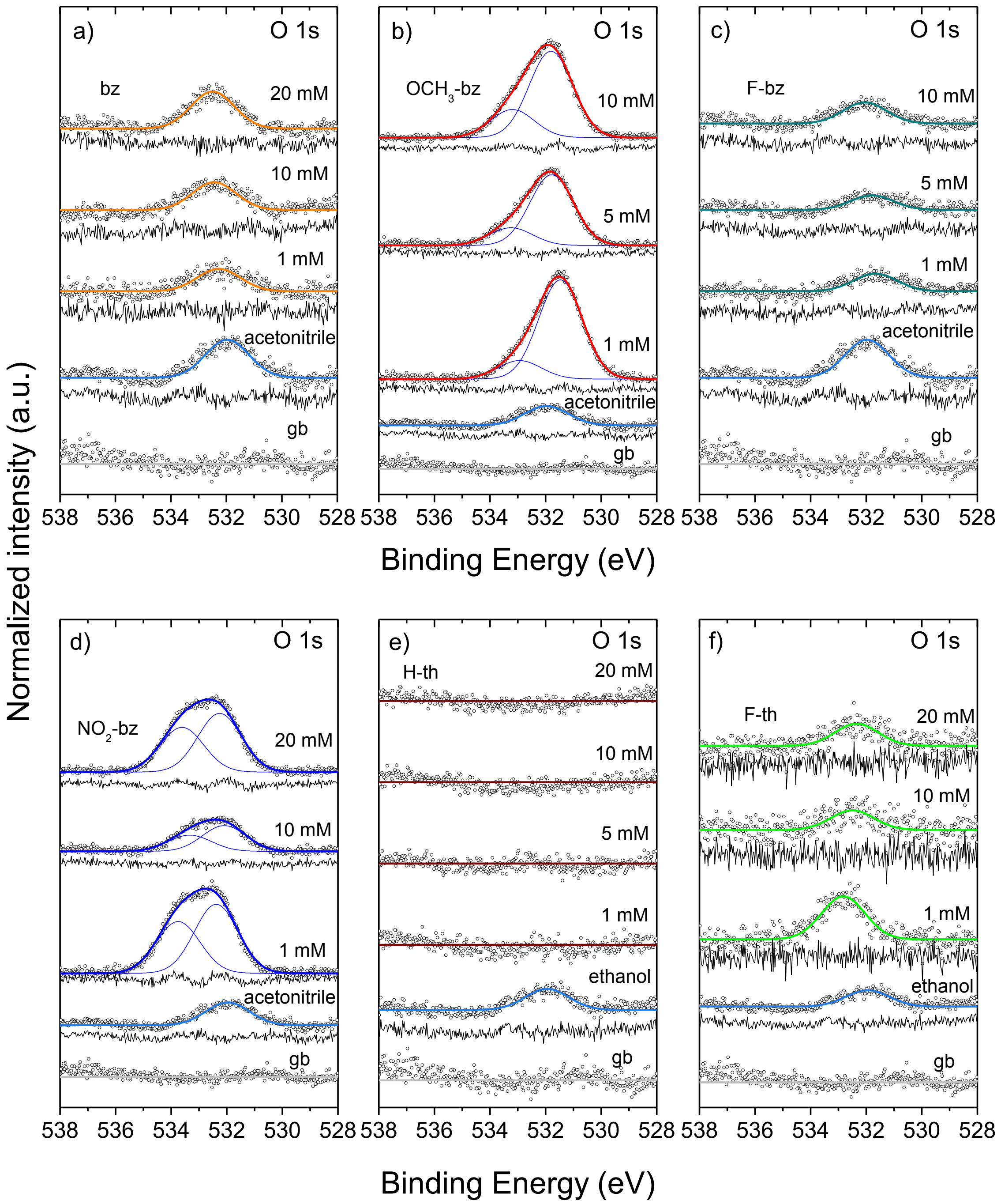

Figure 8.8 Curve fit analysis of the O 1s spectra of sputter-cleaned Au ref. samples prior to and after exposure to various stages of the following SAM solution treatments: (a) bz, (b) OCH_3-bz, (c) F-bz, (d) NO_2-bz, (e) H-th and (f) F-th. All spectra were measured using Mg K_α excitation. Vertical offsets are added for clarity.

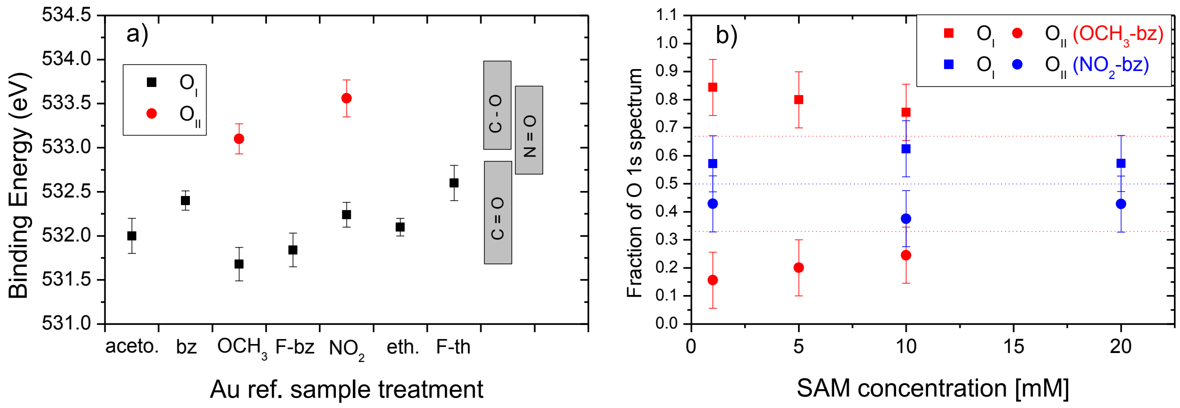

Figure 8.9 (a) Mean BE of the curve-fit peaks of the O 1s region of sputter-cleaned Au ref. samples prior to and after exposure to various stages of SAM treatments, along with reference BE ranges for different oxygen-based bonds. The abbreviations aceto., OCH_3, NO_2 and eth. refer to acetonitrile, OCH_3-bz, NO_2-bz and ethanol treatments, respectively. (b) Fraction comprised by each of the curve-fit peaks of the total area of C 1s spectra of Au ref. samples treated with OCH_3-bz and NO_2-bz. The red- (---) and blue-colored (---) dashed lines in (b) denote the spectral fractions expected of C_I:C_{II} = 2:1 and C_I:C_{II} = 1:1 ratios, respectively.

As shown in Fig. 8.8, O 1s spectra of samples treated with solutions of SAMs not containing oxygen in their moiety groups can be satisfactorily fitted using only one peak (i.e., O_I). In the case of samples treated with SAMs with oxygen-containing moieties, satisfactory fits of O 1s spectra were obtained only if a second peak (i.e., O_{II}) was used. The BE position of the fitted peaks of the O 1s spectra of SAM-treated (as the mean BE value of all the concentration treatments) and control samples are shown in Fig. 8.9 (a), along with literature BE value ranges (gray boxes) for various oxygen-based bonds taken from refs. [45]. O_I peaks are located in the vicinity of carbonyl and carboxylic oxygen BE ranges. O_{II} peaks are located within BE ranges reported for alcohol/ether-oxygen and nitrogen-oxygen bonding. Moreover, the derived O_I:O_{II} ratios are, for the OCH_3- and NO_2-bz SAMs, close to the 2:1 and 1:1 expected ratios, as shown in Fig. 8.9 (b).

Fig. 8.10 (a) - (f) show the detail XPS spectra, along with curve fits, of photoemission lines related to the SAM molecules: a magnified view of the C 1s spectra in the BE range ascribed to carboxylic carbon for the bz and OCH_3-bz treated samples, F 1s for F-bz and F-th treated samples, N 1s for NO_2-bz treated samples, and S 2p for H-th treated samples. To highlight changes in intensity of the BE region of interest with the used SAM treatments in Fig. 8.10 (a) and (b), the measured spectra had their respective background line and C_{II} fit curve peak subtracted [from the curve fit analysis shown in Fig. 8.6 (a) and (b)]. Differences are shown as

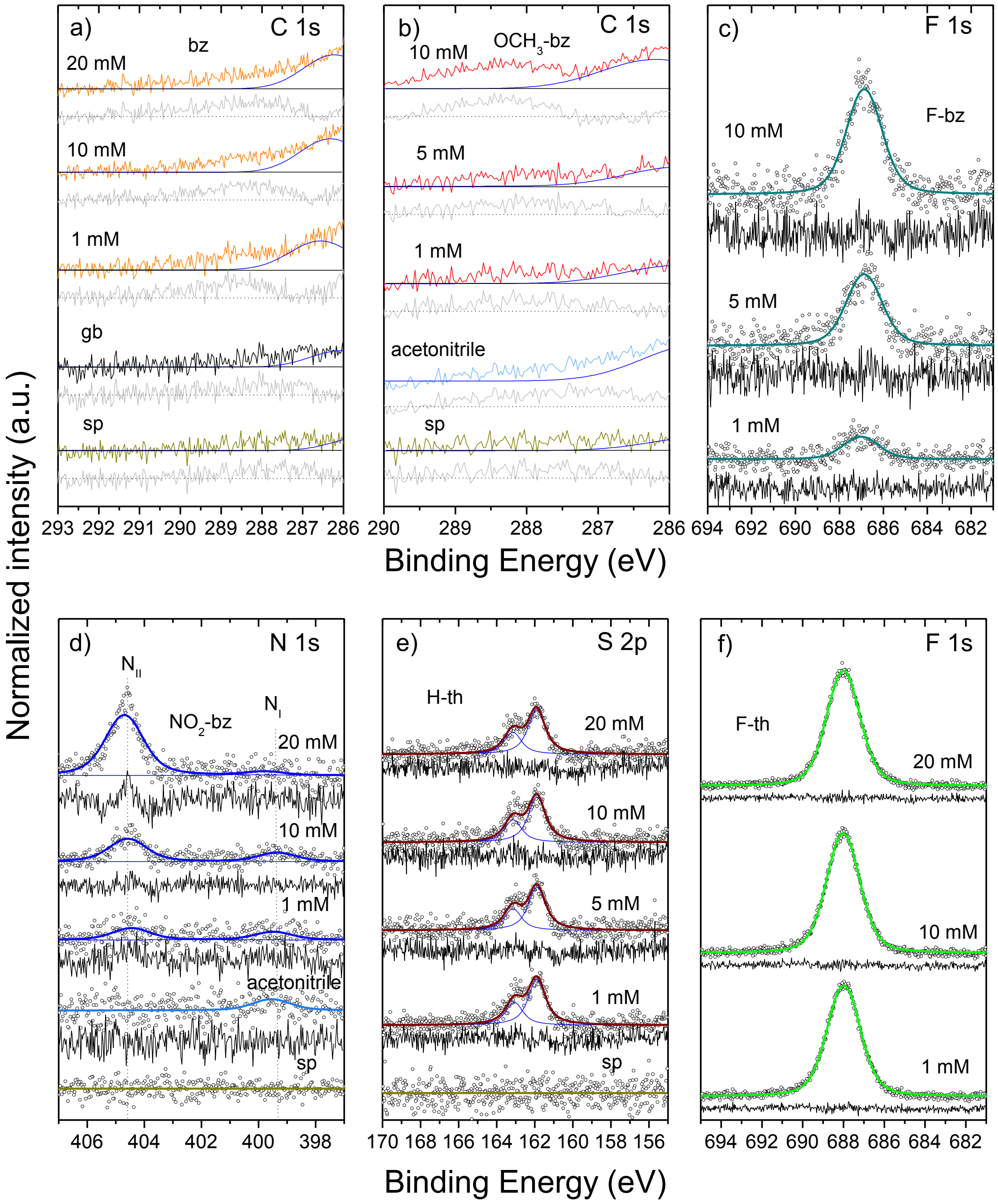

Figure 8.10 Curve fit analysis of photoemission lines of elements linked to SAM molecules: (a) and (b) magnified higher-BE portion of C 1s (bz and OCH$_3$-bz); (c) and (f) F 1s (F-bz and F-th); (d) N 1s (NO$_2$-bz); and (e) S 2p (H-th). All spectra were measured using Mg K$_\alpha$ excitation. Vertical offsets are added for clarity.

gray lines. For the N 1s detail spectra in Fig. 8.10 (d), satisfactory curve fits are attained by using two fit peaks. N$_I$ is located at a BE of approximately 400 eV and is ascribed to the nitrile group of adsorbed acetonitrile. N$_{II}$, which is located at a BE of approximately 405 eV, is ascribed to the nitro group of the NO_2-bz SAM molecules [45,178]. In Fig. 8.11, changes in intensity of these new photoemission lines are presented relative to the intensity of the 1 mM treated sample (i.e., $I_{[1\ mM]}$) of each SAM series (i.e., I/ $I_{[1\ mM]}$). In contrast to the Au 4f attenuation evaluation (discussed above, Fig. 8.4), a direct relation is found between the intensity of the SAM-associated photoemission lines and the concentration of the SAM solution treatments. Judging by the changes in intensity, samples treated with bz, H-th and F-th solutions seem to reach layer saturations with all employed solution concentrations. For samples treated with F-bz, OCH_3-bz and NO_2-bz solutions, the point of saturation is not detected for the used solution concentration range, as the intensity of the SAM-associated photoemission lines continue to increase with higher solution concentration treatments.

In this subsection, changes in the chemical structure of SAM-treated Au ref. samples were presented. The attenuation of Au photoemission lines, the appearance (or increase) of new (or existing) C and O surface chemical species, and the appearance of new SAM-related photoemission lines indicate the adsorption of SAMs on the surface of the treated Au ref. samples. Next, the surface dipole charges induced by the adsorbed SAMs are studied.

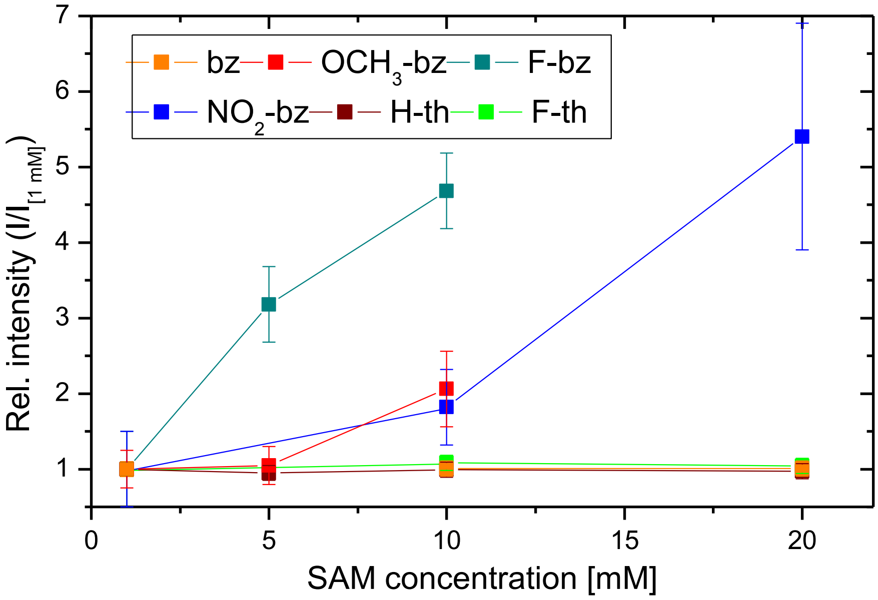

Figure 8.11 Change in intensity of SAM-related photoemission lines, relative to the intensity of the 1-mM treated samples (i.e., I/$I_{[1\ mM]}$), as a function of SAM solution concentration.

8.3.2 Work Function Modulation

UPS was used to measure the secondary electron cut-off of the Au ref. samples prior to and after SAM treatment, as shown in Fig. 8.12. Linear extrapolation of the secondary electron cut-off allows us to determine the lowest KE of electrons escaping from the system; thus yielding the Φ value of the measured sample. The UPS cut-off spectra shown in the lower half of the figures are those of control samples, whereas the spectra shown in the upper half are those of the SAM-treated samples. The mean Φ value of Au ref. samples without Ar^+ ion treatment was 4.8 ± 0.4 eV. Surface cleaning of the Au ref. samples slightly increases their Φ, which is consistent with removal of lower-Φ elements from the surface, such as carbon (Φ ~ 4.4 eV) [177]; however, the mean value Φ of sputter-cleaned Au ref. samples (i.e., 4.9 ± 0.3 eV) falls short of reported Φ values of pristine-ordered Au in literature (i.e., 5.0 – 5.3 eV) [179,180]. This variance in Φ is ascribed to the remaining surface carbon detected on the Au ref. samples and/or Φ–losses due to an increase in surface roughness, resulting from the Ar^+ ion treatments [181,182]. Exposing a sputter-cleaned Au ref. sample to the N_2 glovebox environment for 30 minutes results in a reduction of Φ (ΔΦ = -0.3 ± 0.1 eV), which is consistent with XPS results showing a greater surface carbon content in samples after glovebox exposure. Immersion of a sputter-cleaned Au ref. sample into acetonitrile slightly increases the Φ of the sample (ΔΦ = +0.2 ± 0.1 eV). The reason behind this increase in Φ is unclear. Adsorption of acetonitrile to Au surfaces, by the N-end of the nitrile group, has been reported [174]. Moreover, the C 1s curve fit and the weak N 1s signal of the acetonitrile-immersed Au ref. sample [see Fig. 8.6 and 8.10 (d), respectively] seem to support this case. However, the adsorbed acetonitrile is expected to reduce the Φ of Au because the exposed methyl-end-groups produce a positive surface dipole. A plausible scenario entails that the acetonitrile adsorption to Au removes extraneous surface adsorbates. Such a surface cleaning could provide a Φ-increase sufficiently large to offset the expected Φ-reduction directly linked to the positive surface dipole of the adsorbed acetonitrile molecules. However, the surface of the acetonitrile-immersed sample does not seem to become cleaner, judging from its O 1s intensity. A conclusion regarding whether the observed increase in oxygen is the result of acetonitrile reacting with oxygen (prior to or after adsorption) cannot be made with the present data. Immersion of a sputter-cleaned Au ref. sample into ethanol decreases the Φ of the sample from (ΔΦ = -0.5 ± 0.1 eV), consistent with an increase in surface carbon.

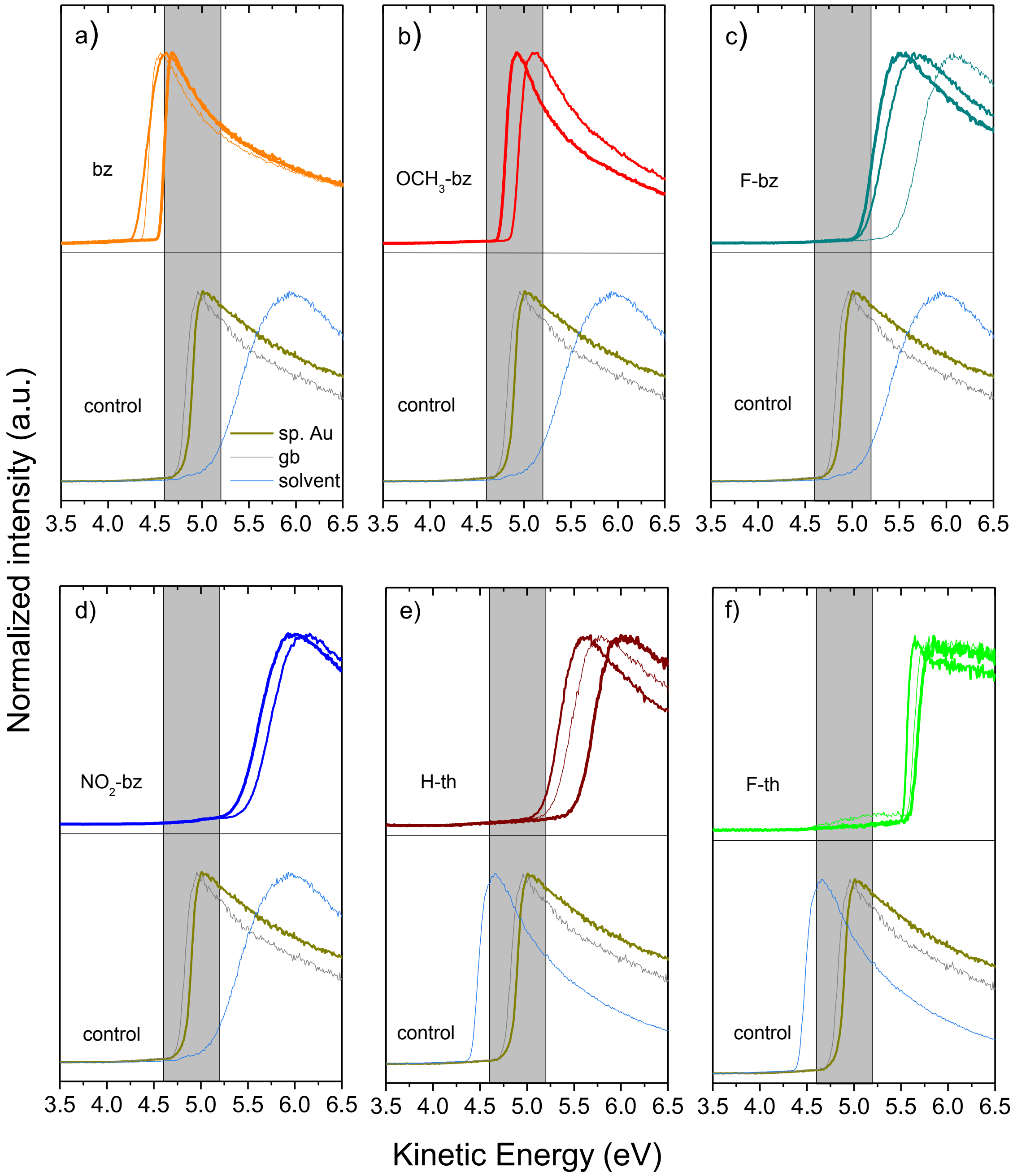

Figure 8.12 He I UPS cut-off spectra of sputter-cleaned Au ref. samples (i.e., sp. Au) prior to and after exposure to various stages of the following SAM solution treatments (cut-off spectra are shown thicker with increasing SAM solution concentration): (a) bz, (b) OCH$_3$-bz, (c) F-bz, (d) NO$_2$-bz, (e) H-th and (f) F-th. The cut-off spectra of the control samples are shown at the lower half, whereas the spectra of the SAM-treated samples are shown in the upper half. Gray rectangles indicate the Φ range of sputter-cleaned Au ref. samples measured.

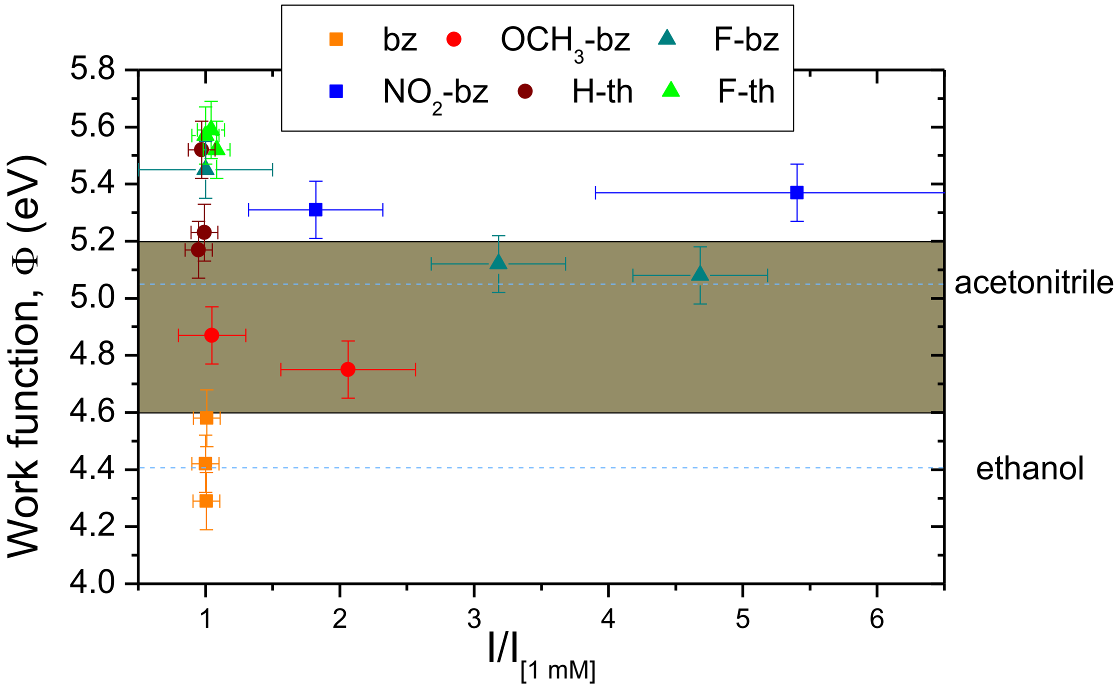

Figure 8.13 Work function (Φ) of SAM-treated Au ref. samples as a function of I/I$_{[1\ mM]}$. The shaded-area (—) shows the mean Φ-values of sputter-cleaned Au ref. samples. Dashed lines (---) show the Φ of Au ref. samples immersed in the solvents used for the SAM solutions.

The Φ-values of the SAM-treated samples are presented in Fig. 8.13 as a function of the intensity of the SAM-associated photoemission lines relative to the intensity of the 1 mM treated sample (i.e., I$_{[1\ mM]}$) of each SAM series (i.e., I/ I$_{[1\ mM]}$, see Fig. 8.11 for more details).

The Φ of F-bz-treated Au ref. samples stabilizes to 5.1 ± 0.1 eV as a function of SAM coverage, representing a ΔΦ = +0.2 ± 0.1 eV. The Φ of NO_2-bz-treated Au ref. samples plateaus to 5.3 ± 0.1 eV, producing a ΔΦ = +0.4 ± 0.1 eV. Treatment of F-th increase the Φ of Au ref. samples to 5.6 ± 0.1 eV, inducing a ΔΦ = +0.7 ± 0.1 eV.

Treatment of samples with SAMs containing moieties expected to induce positive surface dipole charges (i.e., OCH_3-bz, and H-th) did not significantly reduce the Φ of the treated samples. The Au ref. samples with the highest detected coverage of OCH_3-bz shows a ΔΦ = -0.1 ± 0.1 eV, a work function change within the measurement error bar. The Φ value of H-th treated Au ref. samples actually increases (ΔΦ = +0.5 ± 0.1 eV). Based on the C 1s and O 1s XPS results of the H-th-treated Au ref. samples (see Fig. 8.6 and 8.10, repectively), a surface cleaning takes place during the H-th SAM treatment. The resulting Φ (i.e., to 5.4 ± 0.1 eV) is

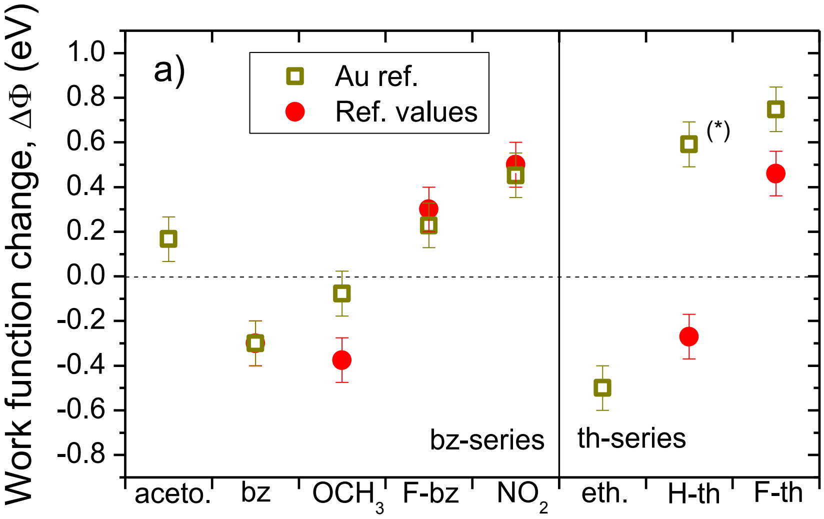

Figure 8.14 Summary of the detected work function changes of Au ref. samples resulting from SAM treatment. Reported work function changes of GaAs (treated with bz-derivatives SAMs) and Au (treated with thiol-based SAMs) are also presented, as taken from refs. [167,168]. The aceto., OCH_3, NO_2 and eth. treatment abbreviations refer to acetonitrile, OCH_3-bz, NO_2-bz and ethanol, respectively.

in the vicinity of the Φ-value range reported for pristine Au, consistent with such a surface cleaning effect.

Although the bz molecule does not have a dipole-inducing moiety, the adsorbed bz molecule may produce a surface dipole charge (i.e., the carboxylic and benzyl group ends can develop a negative and positive dipoles, respectively) [167]. Therefore, treatment of Au ref. sample treated with bz concentration solutions reduced their Φ values (ΔΦ = -0.3 ± 0.1 eV).

Fig. 8.14 summarizes the results of the Φ-tuning of Au via adsorption of dipole-inducing SAMs, along with reported ΔΦ of GaAs and Au samples induced by treatments of the currently employed SAMs [167,168]. Similar results are obtained. In the present case, a Φ-modulation range of 1.0 eV is achieved (i.e., from 4.6 ± 0.1 eV to 5.6 ± 0.1 eV). Findings in the current section will prove useful for SAM adsorption experiments on CIS absorbers discussed below.

8.4 SAM Adsorption on $CuInS_2$

This section presents the results of treating CIS absorbers with SAMs solutions. Findings are discussed in the same manner and sequence as the previous section, starting with changes in the chemical environment of the CIS absorbers, as determined by XPS measurements, followed by changes in work function derived by UPS cut-off measurements. The thickness of the deposited SAM layers will also be estimated by evaluating the attenuation of absorber-derived photoemission lines.

8.4.1 Chemical Structure

The XPS survey spectra of CIS substrates prior to and after various SAM treatments are displayed in Fig. 8.15. The spectrum of the CIS absorber shows the signature Cu, In and S photoemission lines. C- and O-related core level lines of weaker intensity are present and are ascribed to extraneous adsorbates. As discussed in Sect. 8.3.1, it was not possible to completely remove these surface species from sputter-cleaned Au ref. samples. Considering that Au, as a noble metal, is less reactive to these type of adsorbates than chalcopyrite semiconductors, the presence of the C- and O-related photoemission lines is not surprising. A quick inspection of the spectra of SAM-treated CIS samples also reveals the appearence of photoemission lines derived from elements associated to the treating SAMs. The most conspicuous of these are the F-related lines found in the survey spectrum of the F-th-treated CIS sample. Greater evidence of the appearance of SAM-linked photoemission lines in the other SAM-treated CIS samples will be shown later in this section.

An attenuation of the CIS signature lines is found for SAM-treated samples. This effect is better observed by comparing the XPS detail spectra of the principal Cu, In and S core level lines of the CIS samples prior to and after SAM treatment, as shown in Fig. 8.16 (a) – (c). Except for the spectra of F-bz-treated CIS samples, all other SAM treatements produce a reduction in the signal of these photoemission lines. The quantification of the intensity of these lines was carried out through curve fit analysis; however, the obtained fits are again omitted for purposes of visual comparison. Table 8.2 shows the quantified intensity changes and the effective thicknesses of the adsorbed SAMs, d_{SAM}, as calculated using eqn. (4.1). The mean d_{SAM} value derived from the attenuation of the three lines is ~ 3 Å for all SAMs, a value close to the 4-Å molecular size reported for benzoic acid [183]. (Because the thiol-based SAMs contain sulfur, the d_{SAM} value obtained from the S 2p line was not used to calculate the mean d_{SAM} value of thiol-treated CIS samples.)

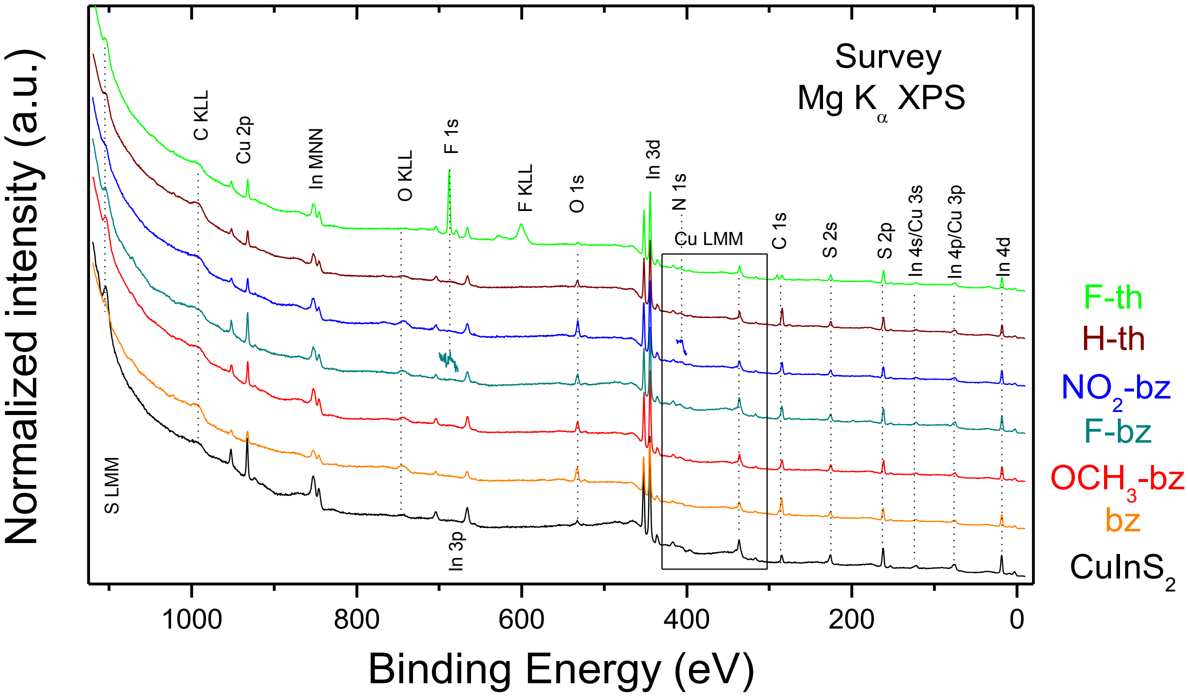

Figure 8.15 XPS survey spectra of CIS absorbers prior to and after treatment of the different SAM solutions [20 mM].

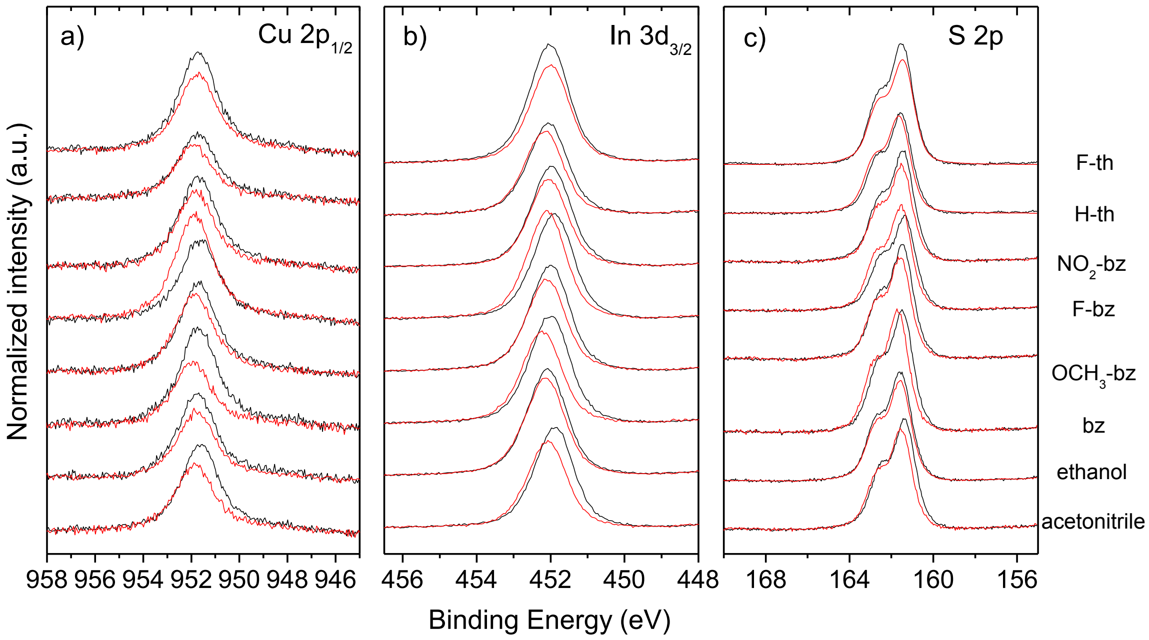

Figure 8.16 XPS detail spectra of the (a) Cu $2p_{1/2}$, (b) In $4d_{3/2}$, and (c) S 2p energy regions of CIS absorbers prior to (black) and after exposure (red) to various stages of the following SAM solution treatments [20 mM]. All spectra were measured using Mg Kα excitation. Vertical offsets are added for clarity.

Moreover, the photoemission lines shown in Fig. 8.16 shift to higher BE positions for SAM-treated CIS samples. The determined BE shifts are presented in Fig. 8.17 and suggest the formation of downward band bending with SAM adsorption. Such an effect was not observed for the SAM-treated Au ref. samples. The implications of the discovered band bending on the local vacuum level, E_{loc}, of SAM-treated CIS samples will be discussed in Sect. 8.4.2.

Table 8.2 Effective thicknesses, d_{SAM} (in Å), of the adsorbed SAM layers. λ_{SAM} values are also reported in Å and were obtained from refs. [50,51]).

SAM	Cu 2p (I/I$_0$)	d_{SAM} (λ~ 12)	In3d (I/I$_0$)	d_{SAM} (λ~ 23)	S 2p (I/I$_0$)	d_{SAM} (λ~ 30)	d_{SAM} (mean)
bz	0.66	4.8 ± 1.0	0.84	4.0 ± 0.8	0.98	0.6 ± 0.1	3.1 ± 2.2
OCH_3-bz	0.89	1.4 ± 0.3	0.87	3.4 ± 0.7	0.89	3.5 ± 0.7	2.8 ± 1.2
F-bz	1.30	-	1.10	-	1.09	-	-
NO_2-bz	0.84	2.1 ± 0.4	0.86	3.6 ± 0.7	0.85	4.7 ± 0.9	3.5 ± 1.3
H-th	0.84	2.0 ± 0.4	0.91	2.3 ± 0.5	1.01	-	2.2 ± 0.5
F-th	0.79	2.7 ± 0.5	0.82	4.5 ± 0.9	0.90	3.2 ± 0.6	3.5 ± 1.0

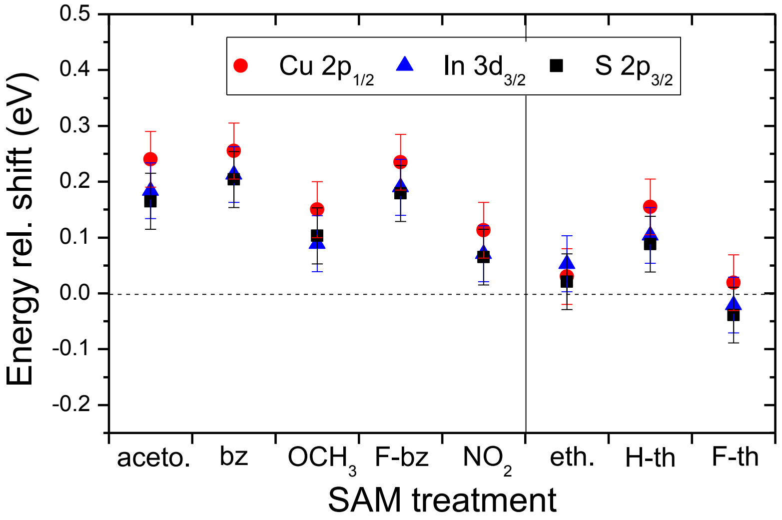

Figure 8.17 Change in BE of the Cu 2p$_{1/2}$, In 4d$_{3/2}$ and S 2p$_{3/2}$ photoemission lines of CIS absorbers after exposure to various stages of SAM treatments. The abbreviations aceto., OCH_3, NO_2 and eth. refer to acetonitrile, OCH_3-bz, NO_2-bz and ethanol treatments, respectively.

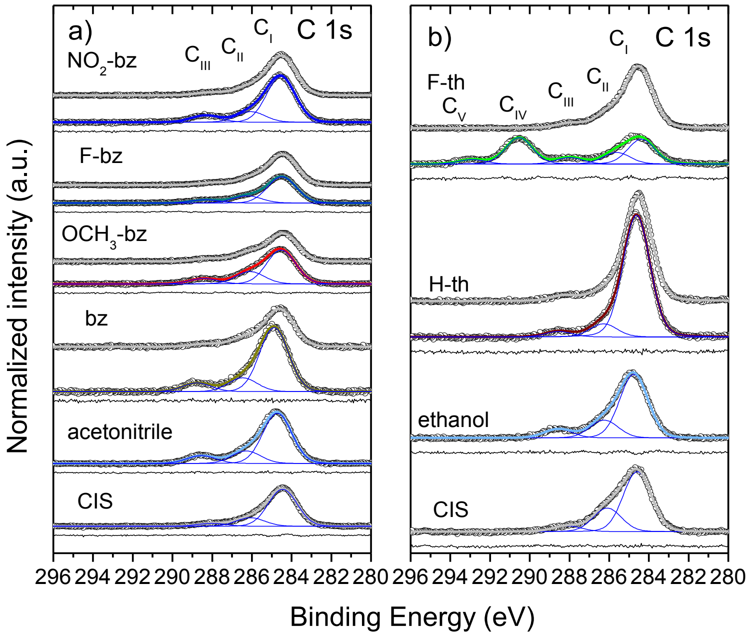

Figure 8.18 Curve fit analysis of the C 1s of CIS absorbers prior to and after treatment with (a) benzoic acid derivative and (b) thiol SAM 20 mM solutions. Spectra with gray fit lines correspond to CIS absorbers prior to SAM treatments. The component fit lines for these spectra are not displayed (except for the CIS absorbers used for the solvent control, labeled CIS) for visual clarity. All spectra were measured using Mg K$_\alpha$ excitation. Vertical offsets are added for clarity.

Changes in surface chemistry, expected of SAM adsorption, are detected in SAM-treated CIS samples. Fig. 8.18 shows XPS detail C 1s spectra, along with respective curve fits, of the CIS substrates prior to and after various SAM treatments. Satisfactory fits of the C 1s spectra of all measured CIS substrates, except for the F-th-treated CIS sample, are found using three fit peaks (i.e., C_I, C_{II} and C_{III}, with increasing BE). This result is mostly consistent with findings in Sect. 8.3.1 on Au ref. samples. (The curve fits of the H-th-treated Au ref. samples required only two fit peaks). A satisfactory curve fit of the C 1s spectrum of the F-th-treated CIS sample requires five fit peaks (only four are needed in the F-th-treated Au ref. samples) due to the appearance of new carbon species. The need for an extra peak for the curve fits of the C 1s spectra of CIS samples treated with thiol-based SAMs derives from the higher content of extraneous adsorbates in the surface of the CIS samples, as will be discussed below. Fig. 8.19 (a) shows BE values of the fit peaks of the C 1s spectra of CIS samples prior to and after various SAM treatments, along with reference BE value ranges (gray-filled boxes) for different carbon-based bonds taken from ref. [45]. Fig. 8.19 (b) shows the fraction that each fit peak comprises of the C 1s spectra of untreated, control and SAM-treated CIS samples.

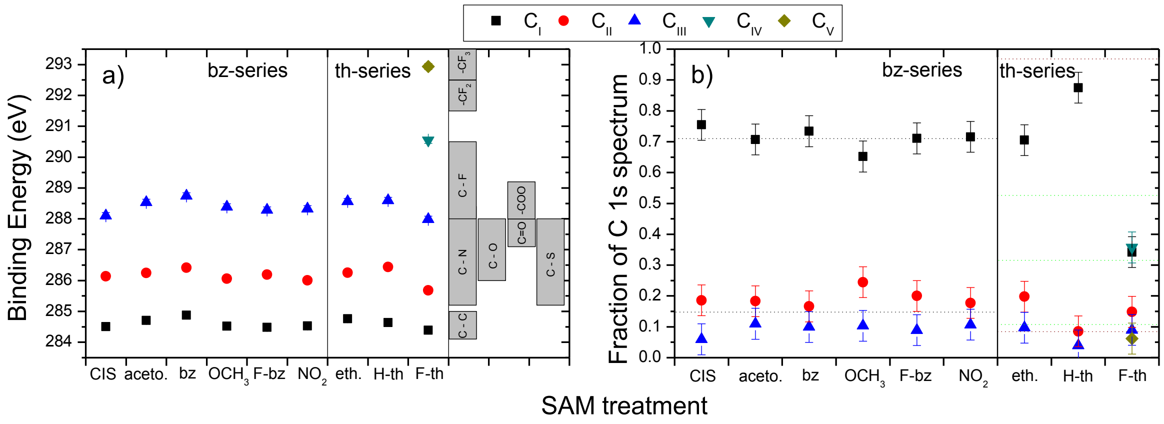

Figure 8.19 (a) BE of the curve-fit peaks of the C 1s region of CIS absorber prior to and after exposure to various stages of the SAM 20 mM solution treatments, along with reference BE ranges for different carbon species. (b) Fraction comprised by each of the curve-fit peaks of the total area of C 1s spectra of CIS absorbers treated with SAM solutions. The black- (---), wine- (---) and green-colored (---) dashed lines in (b) denote the spectral fractions expected of $C_I:C_{II}:C_{III}$ = 5:1:1, $C_I:C_{II}$ = 11:1 and $C_I:C_{II}:C_{III}:C_{IV}$ = 3:1:5:1, respectively. The abbreviations aceto., OCH_3, NO_2 and eth. refer to acetonitrile, OCH_3-bz, NO_2-bz and ethanol treatments, respectively.

The mean BE values of the fit peaks of the untreated CIS samples are 284.5 ± 0.1 (for C_I), 286.1 ± 0.1 (for C_{II}) and 288.1 ± 0.1 (for C_{III}) eV. These BE values are ascribed to sp^2-hybridized carbon, carbon single-bonded to oxygen (i.e., C-O), and carboxylic/carbonate carbon, respectively. The fit peaks of the C 1s spectrum of the acetonitrile-immersed CIS samples are located at 284.7 ± 0.1 (for C_I), 286.2 ± 0.1 (for C_{II}) and 288.1 ± 0.1 (for C_{III}) eV. The BE values of the fit peaks for the untreated and the acetonitrile-immersed CIS samples are very similar because the carbon chemical environment of both samples are composed of the same carbon species. In the acetonitrile-immersed sample, the increase in C 1s intensity could suggest acetonitrile adsorption to the CIS surface, as was observed for the acetonitrile-immersed Au ref. sample, in Sect. 8.3.1. The overlapping of the C-O and C-N reference BE ranges make ascribing the C_{II} peak of the spectrum of the acetonitrile-immersed sample difficult. Furthemore, Fig. 8.19 (b) shows that exposure to the solvent generates a higher carboxylic/carbonate surface content on the CIS sample, which could be caused by by-products adsorption of acetonitrile photolytic oxidation (i.e., CO_3^{2-}, $HCOO^-$, and CNO^- groups) [184,185].

The C_I, C_{II} and C_{III} fit peaks of the C 1s spectra of CIS samples treated with benzoic acid derivative SAM solutions were ascribed to the five carbon atoms in the benzyl ring, the carbon atom in the benzyl ring bonding to the moiety (i.e., the carbon in the *para*-position), and the carbon atom of the carboxylic group, respectively. Comparing the fraction of each fit peak to the total intensity of their C 1s spectrum shows a C_I:C_{II}:C_{III} ratio closer to 5:1:1 in the spectra of CIS samples treated with benzoic acid derivative SAMs than in the spectra of untreated CIS samples, as shown in Fig. 8.19 (b).

The BE of the fit peaks of the C 1s spectrum of the ethanol-immersed and H-th-treated CIS samples are close to those of the untreated CIS samples. Ethanol-immersion induces an increase in C 1s intensity, especially in the C_{II} and C_{III} regions, as demonstrated in Fig. 8.18 (b). The fit peaks of the C 1s spectrum of the H-th-treated CIS sample show a C_I:(C_{II}+C_{III}) ratio close to the C_I:C_{II} = 11:1 determined for the H-th-treated Au ref. samples in Sect. 8.3.1.

For the C 1s spectrum of the F-th-treated CIS sample, the fit peaks are located at 284.4 ± 0.1 (for C_I), 285.7 ± 0.1 (for C_{II}), 288.0 ± 0.1 (for C_{III}), 290.5 ± 0.1 (for C_{IV}) and 292.9 ± 0.1 (for C_V) eV. The C_I and C_{II} are ascribed to BE-shifted sp^3-hybridized carbon and carbon single-bonded to sulfur. The C_{III} peak, which was not detected in the C 1s spectra of the counterpart Au ref. samples, is ascribed to carboxylic/carbonate bonds. The relative BE shift in C_I and C_{II}, as well as the appearance of C_{III} seem to be caused by the carbon background signal of the untreated CIS sample. C_{IV} and C_V are ascribed to fluorinated carbon found in the F-th molecule.

Fig. 8.20 shows the O 1s spectra of CIS samples prior to and after being treated with (a) benzoic acid derivative and (b) thiol-based SAM solutions. An increase in the intensity along with changes in the shape of the O 1s line, similar to the C 1s line, are detected. For most of the O 1s spectra of untreated CIS samples, satisfactory fits were obtained using one peak (i.e., O_I). A second peak at a higher BE was required for the fitting of O 1s spectra of CIS samples to be immersed in solvents (i.e., control samples). However, the O_{II} intensities in these O 1s spectra were low. The O 1s spectrum of the acetonitrile-immersed CIS sample (i.e., the control samples for the benzoic acid derivative sample series) shows a significant increase in surface oxygen content. It is possible that this higher surface oxygen content in the CIS samples (compared to the Au ref. samples) facilitates an oxidative photolysis of acetonitrile. In Sect. 8.3.1, only the O 1s spectra of Au ref. samples treated with OCH_3-bz and NO_2-bz SAM solutions produced fits requiring two component peaks (see Fig. 8.8). In contrast, Fig. 8.20 (a) shows that in CIS substrates all benzoic acid derivative SAM treatments generate this oxygen speciation. This variation with different materials may be associated with the adsorption of oxygen-containing by-products of acetonitrile degradation.

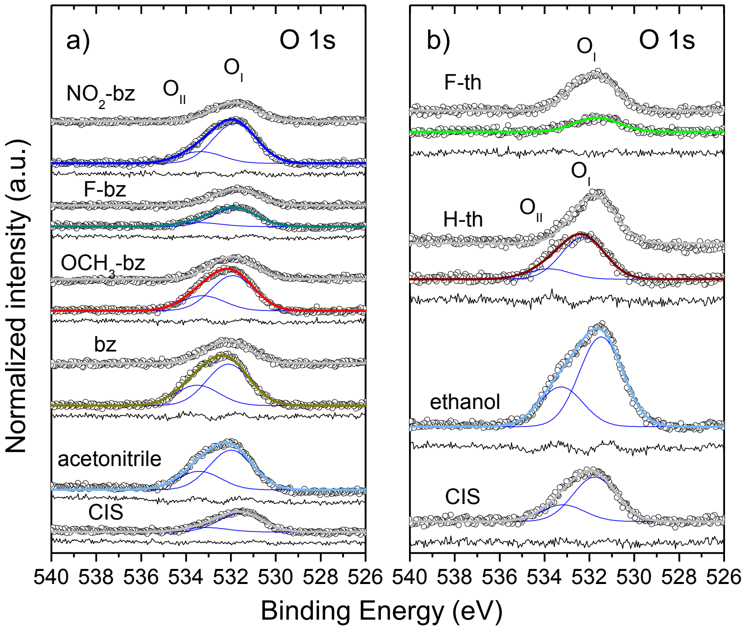

Figure 8.20 Curve fit analysis of the O 1s of CIS samples prior to and after treatment with (a) benzoic acid derivative and (b) thiol SAM 20 mM solutions. Spectra with gray fit lines correspond to CIS absorbers prior to SAM treatments. The component fit lines for these gray-fitted curve line spectra are not displayed (except for the CIS absorbers used for the solvent control, labeled CIS) for visual clarity. All spectra were measured using Mg K$_\alpha$ excitation. Vertical offsets are added for clarity.

As shown in Fig. 8.20 (b), the curve fits of the O 1s spectra of the ethanol-immersed and H-th-treated CIS samples are composed of two fit components. A pronounced increase in intensity is seen for the O 1s spectrum of the ethanol-immersed CIS sample (i.e., the control sample for the thiol SAMs). In the case of the H-th-treated CIS sample, the intensity of its spectrum does not increase significantly, as happens with the ethanol-immersed sample. However, the appearance of a second oxygen peak is in contrast to the O 1s spectra of the H-th-treated Au ref. samples. It appears that although the hydrophobic hydrocarbon tail of the H-th SAM limits the deposition (or formation) of new oxygen-containing adsorbates (i.e., ethanol molecules), the surface cleaning found in the H-th-treated Au ref. samples does not take place for the CIS sample. This occurence may be explained by a higher surface oxygen (and carbon) content in untreated CIS sample and/or a stronger binding (reactivity) of adsorbates to CIS compared to Au (a noble metal).

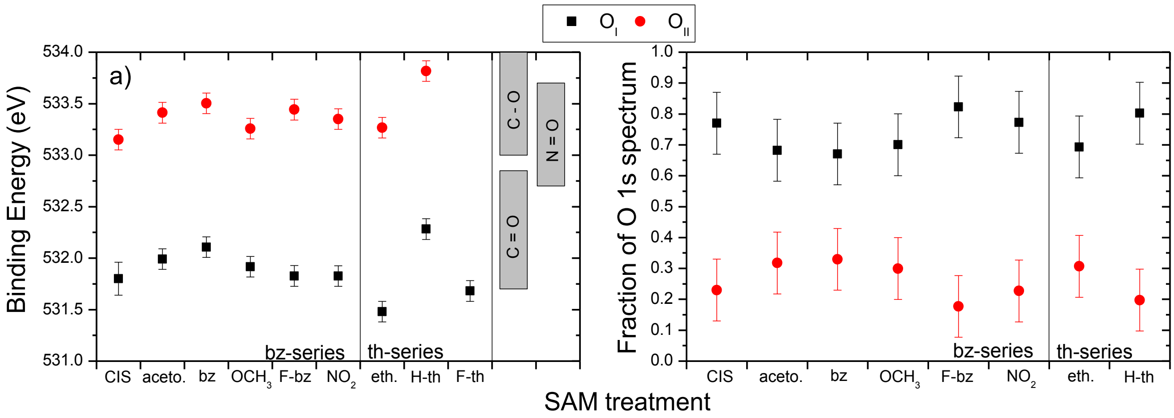

Figure 8.21 (a) BE of the curve-fit peaks of the O 1s region of CIS absorbers prior to and after exposure to various stages of SAM solution treatments [20 mM], along with reference BE ranges for different oxygen-based bonds. (b) Fraction comprised by each of the curve-fit peaks of the total area of O 1s spectra of CIS absorbers prior to and after exposure to various stages of SAM treatments. The abbreviations aceto., OCH_3, NO_2 and eth. refer to acetonitrile, OCH_3-bz, NO_2-bz and ethanol treatments, respectively.

Treatment with F-th induces a profound reduction of the initial surface oxygen content in the CIS substrate. The strong dipole charges produced by the highly fluorinated carbon tail of the F-th SAM repels the also negative-dipole-charged carbonate adsorbates present at the untreated CIS surface. The effect of this surface cleaning is greater than the potential increase in the O 1s signal related to hydrogen-bonding between the hydrogen atoms of the alcohol group of ethanol with the fluorine atoms of F-th.

The BE positions of the fit O_I and O_{II} peaks are shown in Fig. 8.21 (a) for untreated, control and SAM-treated CIS samples, along with reference BE value ranges (gray-filled boxes) for different oxygen-based bonds taken from ref. [45]. The O_I peaks are found within the BE value range for carboxylic/carbonate oxygen. The O_{II} peaks are located within the BE value ranges for alcohol/ether, and nitrogen-bonded oxygen. The fraction that each fit peak comprises of the O 1s spectra of untreated, control and SAM-treated CIS samples is shown in Fig. 8.21 (b). [Because the O 1s spectrum of the F-th-treated CIS sample yielded a satisfactory one-peak fit, the F-th SAM is not included in Fig. 8.21 (b).] Due to the more pronounced surface oxygen backgrounds of the untreated and control CIS samples, the measured O_I:O_{II} ratios of the O 1s spectra of the OCH_3- and NO_2-bz-treated CIS samples considerably deviate from the respective 2:1 and 1:1 expected ratios.

XPS detail spectra of SAM-related photoemission lines of CIS samples prior to and after SAM treatments, along with curve fits, are shown in Fig. 8.22. To highlight changes in intensity of the BE region of interest in Fig. 8.22 (a), all shown C 1s spectra are normalized at the maximum intensity. For a given treatment, the C 1s spectrum of the untreated CIS sample is then subtracted from the C 1s spectrum of the treated CIS sample. The difference is shown as a gray line. An increase in intensity is found in the BE region ascribed to carboxylic carbon in C 1s spectra of CIS samples treated with bz and OCH_3-bz solutions, as shown in Fig. 8.22 (a). A similar change is, however, found for the spectra of the acetonitrile-immersed CIS samples. It is not clear whether this occurence is also due to acetonitrile oxidative degradation, which would induce the formation of CO_3^{2-}, $HCOO^-$, NO_3^{2-} and CNO^- groups [184,185]. Fig. 8.22 (b) and (e) show the emergence of F 1s lines in CIS samples treated with F-bz and F-th SAM solutions, respectively. In Fig. 8.22 (c), an overlap in the N 1s core level and the (Mg K_α-excited) Cu $L_3M_{2,3}V$ XAES lines is found. This situation prevents the possibility of performing a curve fit analysis on the N 1s spectra of CIS samples treated with acetonitrile (i.e., control sample) and the NO_2-bz solution. [Using Al K_α excitation does not resolve this issue because measurements become less surface-sensitive and the cross section of N 1s electrons is reduced compared to Mg K_α excitation; as seen in Fig. 8.10 (d), the signal of the (Mg K_α-excited) N 1s line ascribed to acetonitrile adsorbed to Au ref. sample surfaces is already very low.] Subtracting the spectrum of the CIS sample prior to acetonitrile immersion from the spectrum of the CIS samples after acetonitrile immersion does not show any significant spectral features in the difference line. However, carrying out the same procedure with the spectra of the (to-be) NO_2-treated CIS sample reveals a peak located at a BE ~ 405 eV, consistent with the appearance of an N 1s peak at similar BE for NO_2-treated Au ref. samples [see Fig. 8.10 (d)]. Fig. 8.22 (d) shows the S 2p spectra (normalized to maximum intensity) of a CIS sample prior to and after H-th treatment. The spectrum of the H-th treated CIS samples shows a higher intensity in the BE region ~ 163 eV, which is more clear in the (H-th treated – untreated spectra) difference line. This finding suggests a sulfur speciation induced by the H-th treatement. The curve fit analysis of the S 2p spectrum of H-th-treated CIS sample, shown in Fig. 8.22 (e) confirms the presence of a second spectral line pair (i.e., sulfur species), ascribed to thiol sulfur. The appearance of this new S species is in agreement with H-th adsorption expectations. Changes in the surface chemical structure of SAM-treated CIS substrates are overall consistent with results observed in Sect. 8.3.1 for SAM-treated Au ref. samples. The attenuation of CIS-derived signal, the appearance (or increase) of new (or already present) C and O photoemission lines, and the emergence of SAM-related core level lines confirm SAM adsorption to the surface of CIS substrates. The

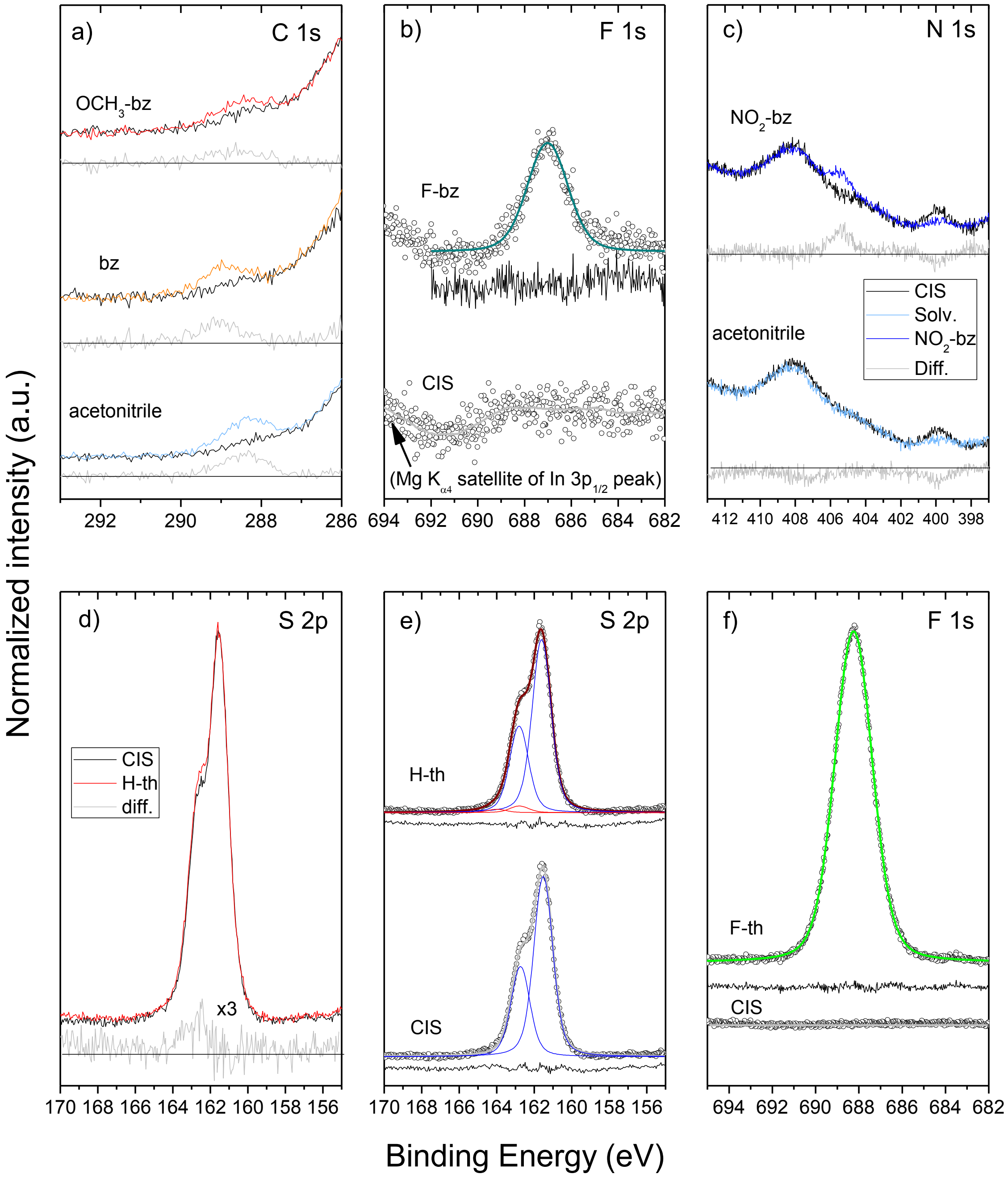

Figure 8.22 Analyses of photoemission line regions of elements linked to SAM molecules measured on CIS absorbers prior to and after exposure to various stages of SAM treatments (shown in parenthesis): (a) difference spectra analysis of the magnified higher-BE portion of C 1s (bz and OCH$_3$-bz); (b) and (f) curve fit analysis of the F 1s region (F-bz and F-th); (c) difference spectra analysis of the N 1s region (NO$_2$-bz); (d) difference spectra analysis of the S 2p region (H-th); and (e) curve fit analysis of the S 2p region (H-th). More details on the difference spectra analyses are given in the text. All spectra were measured using Mg K$_\alpha$ excitation. Vertical offsets are added for clarity.

next step, to investigate the effect of the inserted suface dipoles on the work function of CIS, is presented in the following subsection.

8.4.2 Work Function Modulation

The secondary electron cut-off spectra of CIS samples prior to and after SAM treatments, as well as the counterpart spectra for Au ref. samples are shown in Fig. 8.23 (top-half for CIS samples, bottom-half for Au ref. samples). The mean measured Φ-value of the untreated CIS samples is 4.5 ± 0.2 eV, a value within the range of Φ-values reported for chalcopyrite semiconductors with traces of surface carbon and oxygen in literature (i.e., 4.2-4.8 eV) [152,166,186]. Immersion of CIS in acetonitrile decreases the Φ of the sample ($\Delta\Phi = -0.2 \pm 0.1$ eV). As discussed in Sect. 8.3.2, adsorption of acetonitrile to various materials is reported to take place via the N-end of the nitrile group. This mode, which leaves the methyl-end group pointing away from the surface, is expected to produce a positive surface dipole charge due to the C-H bonds of the methyl group. As mentioned earlier, the XPS measurements do not provide definite evidence supporting acetonitrile adsorption to the CIS surface. However, the detected Φ reduction, along with observations of plausible acetonitrile by-product adsorbates, suggest that acetonitrile adsorption to CIS samples cannot, as of yet, be ruled out. Immersion of CIS in ethanol does not significantly change the Φ of the sample sample ($\Delta\Phi = -0.1 \pm 0.1$ eV). In Sect. 8.3.2, the relative decrease in Φ of the ethanol-immersed Au ref. sample is ascribed to an increase in surface carbon resulting from the solvent exposure. As demonstrated in Fig. 8.6 and 8.19 (b), the surface of the CIS sample prior to immersion in ethanol is not as pristine as its counterpart Au ref. sample. A change in Φ due to an increase in surface carbon is not expected to be as pronounced for the ethanol-immersed CIS sample as was the case for the ethanol-immersed Au ref. sample.

Treatment of CIS substrates with solutions of SAMs possessing negative-dipole-inducing moieties, as expected, increases the Φ of the treated samples (from the mean Φ value of 4.5 ± 0.1 eV), as follows: $\Delta\Phi = +0.5 \pm 0.1$ eV for F-bz, $\Delta\Phi = +0.2 \pm 0.1$ eV for NO_2-bz, and $\Delta\Phi = +0.8 \pm 0.1$ eV for F-th.

However, treatment of CIS substrates with solutions of SAMs possessing positive-dipole-inducing moieties do not significantly reduce the Φ of the treated samples: $\Delta\Phi = -0.1 \pm 0.1$ eV for OCH_3-bz and H-th. (For CIS, H-th treatment does not result in a cleaning of the surface. Finally, treatment of CIS with bz significantly reduces the Φ of the sample (ΔΦ = -0.5 ± 0.1 eV).

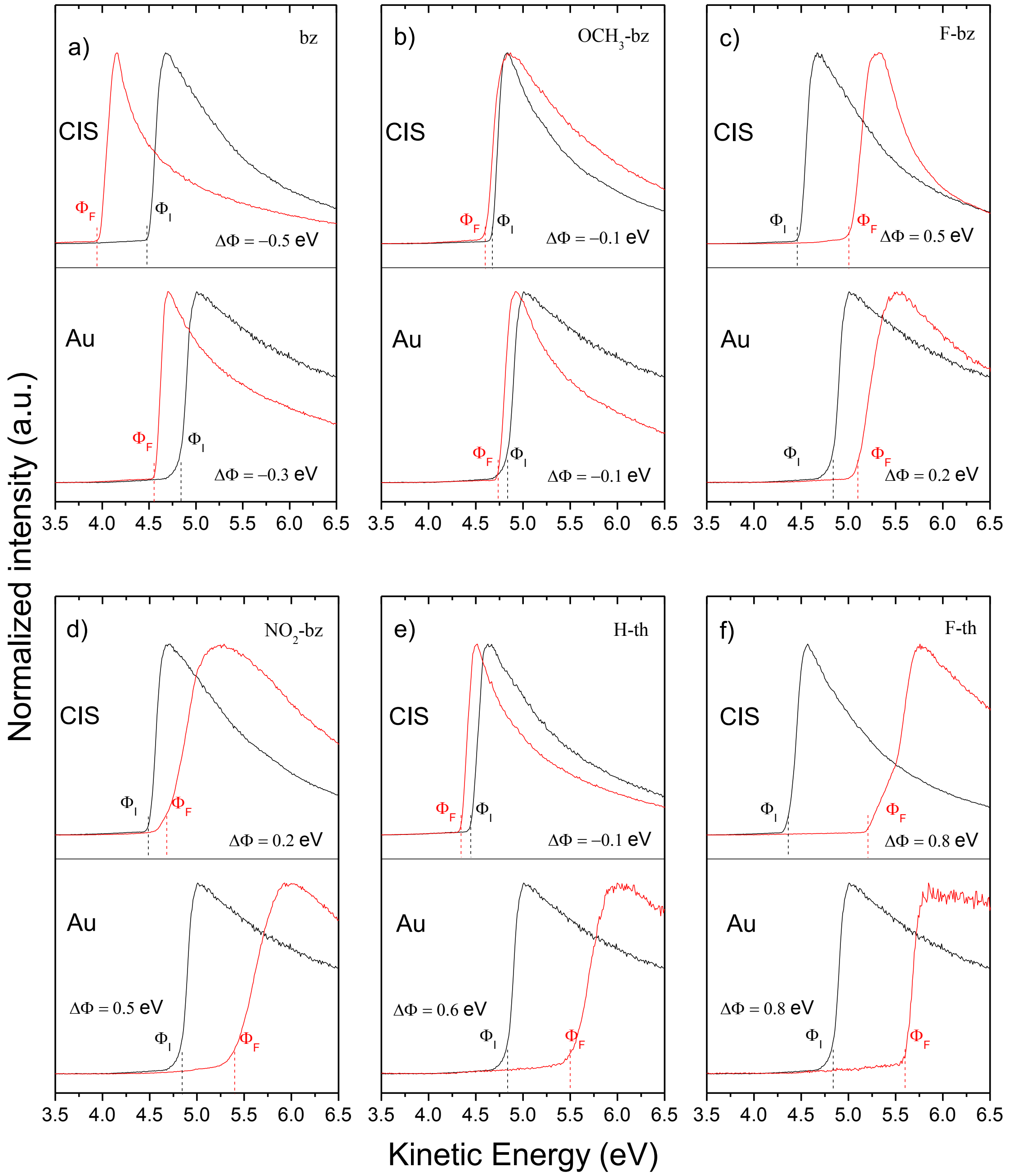

Figure 8.23 He I UPS cut-off spectra of CIS absorbers (top-halves) and Au (bottom-halves) prior to (black) and after (red) exposure to the following SAM solution treatments: (a) bz, (b) OCH_3-bz, (c) F-bz, (d) NO_2-bz, (e) H-th and (f) F-th.

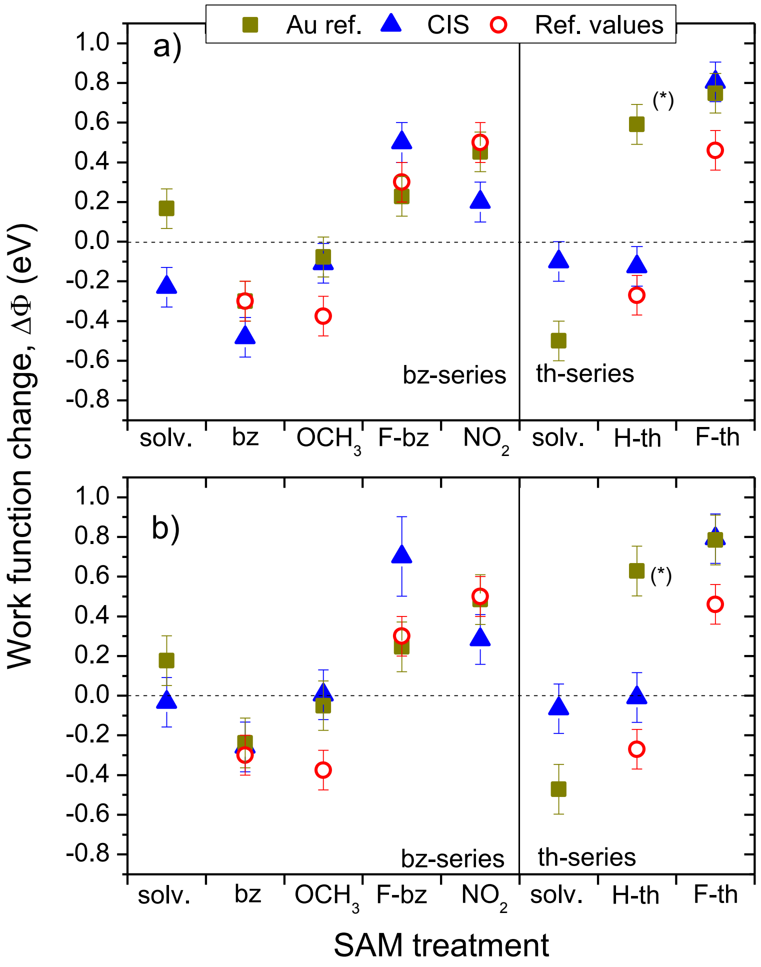

Figure 8.24 (a) Summary of the detected ΔΦ of Au ref. and CIS samples resulting from SAM treatment. (b) Values presented in (a) after correcting for band bending. Reported ΔΦ of GaAs (treated with bz-derivatives SAMs) and Au (treated with thiol-based SAMs) are also presented, as taken from refs. [167,168]. The aceto., OCH_3, NO_2 and eth. treatment abbreviations refer to acetonitrile, OCH_3-bz, NO_2-bz and ethanol, respectively.

Fig. 8.24 (a) presents a summary of the Φ-modulation of Au ref. and CIS samples via SAM treatments, along with reported SAM-induced Φ changes of GaAs and Au substrates from refs. [167,168]. Good agreement is found for results of all substrates, with exceptions having been already discussed in the previous paragraphs. Although the effect of band bending on the local vacuum level of the SAM/CIS interface has not yet been considered in these results, it cannot be neglected. Several of the SAM-treated CIS substrates showed a significant increase in the BE of their core levels (as shown in Fig. 8.15), indicating a downward band bend. To determine whether the measured Φ changes are caused by charge transfer between the SAM molecules and the CIS surface (i.e., expected to generate band bending, and expected to change with the deposition of the CdS layer) or by modulating the χ of the CIS sample by inserting surface dipole charges, the values shown in Fig. 8.24 (a) are corrected by including the mean BE shift of the Cu $2p_{1/2}$, In $3d_{3/2}$ and S $2p_{3/2}$ lines. The corrected values are shown in Fig. 8.24 (b). Judging by the fact that the general trend of the modified Φ values is conserved after the correction, it appears that the cause of E_{loc} variations is to a greater extent the surface dipole charges introduced by the deposition of SAMs.

As demonstrated by the results of this subsection, varying the moiety of the used SAM is an effective method for tuning the Φ of CIS surfaces (within a 4.4 ± 0.2 eV to 5.3 ± 0.2 eV span). As shown in Ch. 5, a rise of approximately 0.5 eV of the CBM of the CdS interface with respect to the E_F level could correct the unfavorable CBO of the CdS/CIS heterojunction. Based on Fig. 8.24 (b), insertion of NO_2-, F-bz, and F-th SAMs could improve the CBO of the CdS/CIS heterointerface (i.e., CBO of -0.42 ± 0.25 eV). In the next section, the performance of solar cells based on SAM-treated CIS absorbers is presented.

8.5 Solar Cells

Solar cells were produced from KCN-etched CIS stripes treated with 20 mM solutions of the following negative-dipole-inducing SAMs: NO_2-, F-bz, and F-th. As shown in Fig. 8.1, these SAM treatments were chosen to align (minimize) the unfavorable CBO configuration (i.e., CBO of -0.42 ± 0.25 eV) detected for the CdS/CIS heterointerface (see Sect. 5.3.5).

Fig. 8.25 presents calculated solar cell parameters of CIGSe-based solar cell devices as a function of the CBO of the window/absorber heterointerface for various electron and hole lifetimes, as taken from ref. [36]. The efficiency (η) of this type solar cell device greatly deteriorates with a negative CBO buffer/absorber configuration due to degradations in V_{OC} and FF. If these findings are applicable to CIS-based solar cells, these solar cell parameters (i.e., V_{OC} and FF) would be expected to show the greatest improvements in the event of a CBO optimization of the buffer/absorber heterointerface. As discussed in Sect. 8.4.2, the surface dipoles deposited on CIS by the adsorbed NO_2-, F-bz and F-th SAMs induced the following $\Delta\Phi$: +0.3 ± 0.1 eV, +0.7 ± 0.1 eV, and +0.8 ± 0.1 eV, respectively. If the SAM-induced surface dipoles deposited on CIS stripes are not removed in subsequent steps of the solar cell fabrication process (i.e., mainly during the CBD-CdS step) and the characteristics of

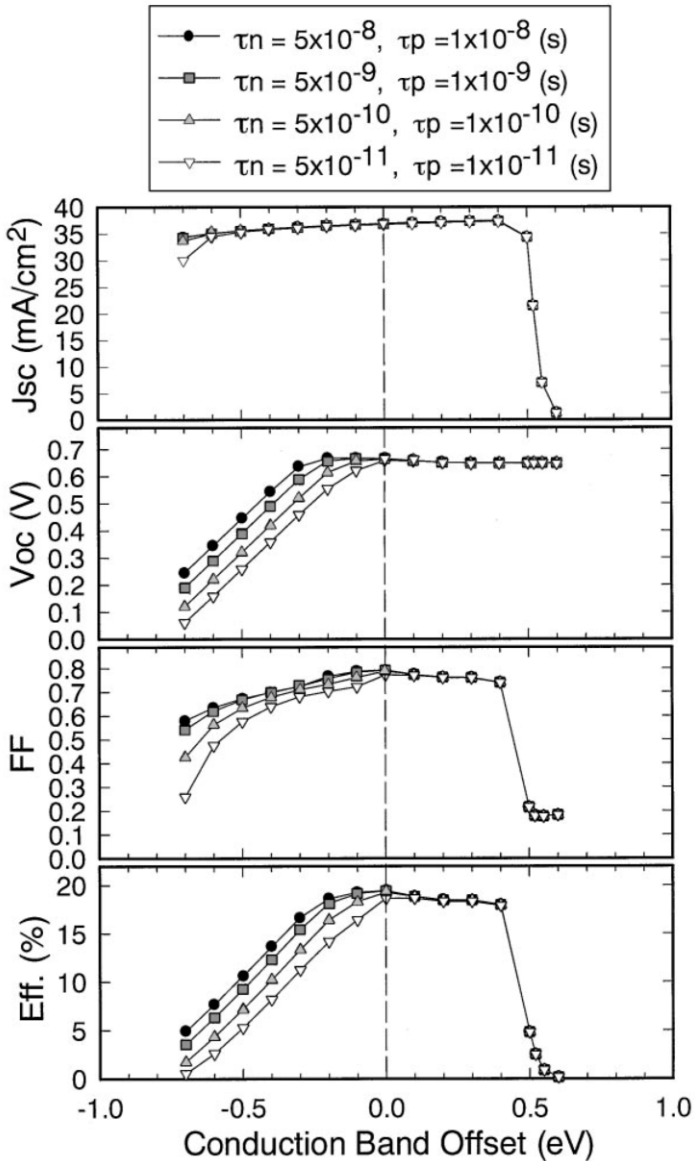

Figure 8.25 Calculated solar cell parameters of CIGSe-based solar cell devices as a function of the conduction band offset of the window/absorber heterointerface for various electron (τn) and proton (τp) lifetimes, taken from ref. [36].

the deposited CdS buffer layer do not drastically change as a result of the deposited SAMs, the following results would be expected: the NO_2-bz SAM treatment would significantly decrease the cliff CBO configuration of the treated CdS/CIS heterointerface, while the F-bz and F-th SAM treatments would change the cliff CBO configuration of the heterointerface into a spike CBO configuration of ~ +0.3 - 0.4 eV, which would not yet be too high to hinder current transport across the heterointerface [36].

Fig. 8.26 shows the *j*-V curves of the best performing solar cells based on the various SAM-treated CIS stripes and the reference solar cells. Modest improvements in j_{SC} and FF are found

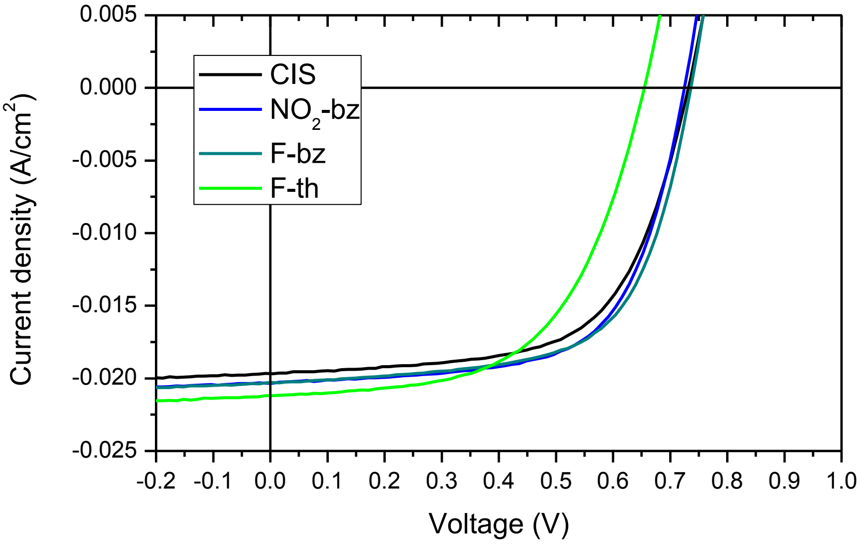

Figure 8.26 ***j*-V curves of best performing solar cell based on CIS absorbers treated with F-bz, NO_2-bz and F-th SAMs, and reference (ref. CdS/CIS) CIS absorbers.**

Table 8.3 Mean solar cell parameters of devices based on SAM-treated and reference CIS absorbers

Absorber	η (%)	V_{OC} (V)	FF
CIS	8.43 ± 0.51	0.722 ± 0.030	0.61 ± 0.02
F-bz-treated	8.82 ± 0.70	0.730 ± 0.013	0.62 ± 0.04
NO_2-bz-treated	8.77 ± 0.43	0.718 ± 0.016	0.62 ± 0.02
F-th-treated	7.43 ± 0.20	0.637 ± 0.013	0.57 ± 0.01

for the best performing solar cells based on F-, and NO_2-bz-treated CIS absorbers in comparison to the best performing reference solar cell. However, no significant changes in V_{OC} are detected. An unexpected increase in j_{SC} is found for the best performing solar cell based on F-th-treated CIS absorbers; however, this improvement is offset by a concomitant deterioration in V_{OC} and FF. Although the best-perfoming solar cells of the F- and NO_2-bz yield more favorable outputs than the ref. solar cells, the difference, which still appears to slightly favor the solar cells based on the SAM-modified absorbers, is reduced to within the margin of error, with a larger sampling number (i.e., 8 solar cells for the F-bz treatment, 14 solar cells for the NO_2-bz treatment, 14 solar cells for the F-th treatment and 17 solar cells for the ref. solar cells). Table 8.3 summarizes the mean solar cell parameters obtained for all sets of solar cell devices.

The presented solar cell results can be only taken as a proof of concept for the present surface tailoring approach. At present, it is not possible to conclude whether the effect of the SAM optimization treatments are overshadowed by the statistical variation of the limited sampling data of the modified solar cells. Furthermore, a complete characterization of the chemical and electronic structures of the CdS/(SAM-modified)CIS heterointerfaces, which is underway, is still needed to determine whether the deposited SAMs significantly alter the properties of the deposited CdS buffer layer. Preliminary measurements of F-bz-adsorbed CIS samples treated with varying CBD-CdS treatment times have been conducted. A F 1s line (i.e., a F-bz-derived photoemission line) signal is still detected for the F-bz/CIS sample treated with a 1-min CBD-CdS time, a treatment time past the induction period for CdS deposition in the CBD process (see Sect. 5.3.1). This result suggests that the adsorbed F-bz layer (if not all the benzoic acid derivative SAMs) withstands the caustic environment of the early CBD bath.

Similar CBD-CdS experiments on F-th-adsorbed CIS samples show that the CIS- and F-th-derived photoemission lines do not become completely attenuated even in samples treated for the entire CBD time. This finding suggests an incomplete surface coverage of the F-th-treated CIS sample by the buffer layer, which may explain the significant increase in j_{SC} for the solar cells of F-th-treated CIS absorbers while also sustaining reductions in V_{OC} and FF. XPS measurements of the discussed preliminary data are shown in Appendix C.

8.6 Summary

The energetic structure of CIS surface was modulated by depositing dipole-charge-inducing SAMs of different alkanethiols and benzoic acid derivatives. The magnitude and polarity of the induced dipoles were determined by observing the changes in the Φ of the SAM-treated CIS absorbers. By varying the polar moiety of the SAMs, the Φ of treated samples could be varied between a 4.2 - 5.3 eV range. By applying these dipole layers as interlayers in the CdS/$CuInS_2$ heterojunction, the electronic interface structure could deliberately be tailored, as suggested by the modest improvement in perfomance of solar cells produced from SAM-treated CIS absorbers.

9 Conclusion and Outlook

A depth-resolved photoemission spectroscopy (PES) characterization (by using a 150-5950 eV excitation energy range) revealed a Ga-depleted surface of a high-performance CIGSe absorber from the Zentrum für Sonnenenergie- und Wasserstoff- Forschung Baden-Württemberg (ZSW) (Sect. 4.3.2). A more conventional x-ray photoelectron spectroscopy (XPS) characterization of the same CIGSe absorber also showed a strongly Cu-poor surface, in which Na potentially acts as an occupier of Cu vacancy sites (Sect. 4.3.1). These elemental variations proved to affect the band gap at the surface of the CIGSe material. Combining ultraviolet photoelectron spectroscopy (UPS) and inverse photoemission spectroscopy (IPES) measurements, a surface band gap (E_g^{surf}) of 1.7 ± 0.2 eV was determined (Sect. 4.3.3), which represents a significant widening of the band gap at the surface (i.e., compared to the bulk optical band gap, E_g^{bulk}, ~ 1.2 eV). In CIGSe substrates submitted to buffer chemical bath deposition (CBD) treatments, evidence of strong intermixing across the buffer/absorber heterointerface was discovered, as determined by XPS measurements (Sect. 4.4.1 and 4.5.1) and Cd and Zn modified Auger analysis (Sect. 4.4.2 and 4.5.2) for CdS and ZnS buffer materials, respectively. It was demonstrated that the S $L_{2,3}$ x-ray emission spectra (XES) of these samples could not be satisfactorily described as a superposition of reference spectra of the absorber and the deposited buffer (Sect. 4.4.3 and 4.5.3). Principal component analysis of these XES spectra revealed the formation of interface chemical species. For CBD-CdS-treated CIGSe substrates, these newly formed chemical species (in addition to CdSe detected by Cd modified Auger analysis) could be modeled as a mixture of CdS nanoparticles and In_2S_3 (Sect. 4.4.4 and 4.4.5). For CBD-ZnS-treated CIGSe substrates, the interface chemical species consisted of a mixture of $(Zn,In)(S,Se)_2$ chemical analogs (Sect. 4.5.4 and 4.5.5). Direct measurement of the band alignment of these heterointerfaces revealed: an ideal conduction band offset (CBO) configuration for CdS/CIGSe [i.e., CBO: +0.11 ± 0.25 eV (Sect. 4.4.6)] and a spike CBO configuration for ZnS/CIGSe [i.e., CBO: +1.06 ± 0.4 eV (Sect. 4.5.6)].

The XPS elemental characterization of a (wide-gap) KCN-etched CIS absorber from the Helmholtz Zentrum Berlin für Materialien und Energie GmbH (HZB) also revealed a strongly Cu-poor surface; however, an absence of surface Na was in this case observed (Sect. 5.3.1), which was ascribed to the wet chemical steps involved in the KCN etching procedure. A significant band gap widening at the surface of the CIS absorber was found (i.e., E_g^{surf}: 1.88 ± 0.25 eV compared to E_g^{bulk} ~ 1.5 eV), which is also ascribed to the observed changes in elemental composition (Sect. 5.3.5). An analysis of the Cd modified Auger parameter of CIS samples treated by CBD-CdS did not reveal any significant change as a function of CBD treatment time (Sect. 5.3.2). The S $L_{2,3}$ XES spectra of these samples could be satisfactorily described as a superposition of CIS and CdS spectra (Sect. 5.3.3 and 5.3.4). These results suggest a much more abrupt character for this wide-gap chalcopyrite-based heterointerface (i.e., CdS/CIS) than the CdS/- and ZnS/CIGSe heterointerfaces. An evaluation of the band alignment at the CdS/CIS heterointerface showed a very unfavorable conduction band offset (CBO) configuration (i.e., CBO: -0.42 ± 0.25 eV), which is correlated to the poor performance of wide-gap chalcopyrite-based solar cell devices (Sect. 5.3.5).

Rapid thermal processing (RTP)-based treatments of KCN-etched (HZB) CIS substrates in Se vapor environments exchanged Se for S. X-ray fluorescence (XRF) analysis of the RTP-treated CIS substrates revealed that the effective depth of the Se incorporation (for the selected set of RTP parameters) could be limited to the surface of the treated samples, as gauged by the detected bulk [Se]/[S+Se] range [i.e., 0.01 ± 0.03 to 0.24 ± 0.03 (Sect. 6.3.1)]. XPS elemental characterization revealed that the surface [Se]/[S+Se] can be tuned from 0.23 ± 0.05 to 0.83 ± 0.05 (Sect. 6.3.1). The XRF and XPS results highlight the surface tailoring capabilities of the RTP selenization treatments. XPS elemental characterization also revealed the possibility of tuning the Cu:In:(S+Se) surface composition of the treated CIS samples from a 1:3:5 to a 1:1:2 stoichiometry, mainly as a result of a surface Cu-enrichment in samples with higher selenization. Changes in the Cu, In and Se modified Auger parameters were observed as a function of surface [Se]/[S+Se], confirming changes in Cu and Se content (Sect. 6.3.2). UPS measurements show a shift in the VBM of treated CIS samples towards the E_F level (i.e., -0.88 ± 0.1 to -0.51 ± 0.1 eV), which suggest a reduction in E_g^{surf} (Sect. 6.3.3). Ultraviolet-visible (UV-Vis) reflectance spectra show a reduction in the optical (bulk) band gap of samples with higher Se content [i.e., from 1.47 ± 0.05 to 1.08 ± 0.05 eV (Sect. 6.3.4)]. The optical (bulk) band gap of samples with [Se]/[S+Se] $\leq$ 0.48 ± 0.05 remain ~ 1.5 eV, which allows for a working window for optimization purposes. An improvement in solar cell performance was not achieved in trial solar cell devices produced from RTP-treated CIS absorbers (Sect. 6.4). It is possible that elemental selenium, which was found in all RTP-treated CIS samples in varying concentrations, may act as a performance limiting factor.

An overview of directly measured electronic structures of various chalcopyrite(kesterite)-based heterointerfaces reveals a direct relation between the widening of the heterointerface band gap (E_g^{interf}) with respect to the chalcopyrite (kesterite) E_g^{bulk} (i.e., ΔE_g^{interf}) and the conversion factor of the corresponding solar cell devices (Ch. 7). This finding broadens the focus of optimization efforts from the band alignment of the buffer/absorber interface to the bulk of the absorber.

The surface of Au reference samples and (HZB) CIS absorbers were functionalized with dipole-charge-inducing self-assembled monolayers (SAM) based on benzoic acid derivatives and thiol molecules, as confirmed by changes in surface chemistry detected by XPS measurements (Sect. 8.3.1 and 8.4.1). UPS measurements of the secondary electron cut-off region of SAM-treated samples showed a work function modulation of both substrates [i.e., Au ref. range: 4.6 ± 0.2 to 5.6 ± 0.2 eV (Sect. 8.3.2) and CIS range: 4.4 ± 0.2 to 5.2 ± 0.2 eV (Sect. 8.4.2)]. Solar cell devices produced from CIS absorbers treated with F-bz and NO_2-bz showed modest improvements in solar cell performance parameters (Sect. 8.5). As shown by the work function measurements, these SAMs orient negative dipole-charges away from the treated (adsorbed) surfaces, expected to shift the relative electronic bands of the components of the CdS/CIS heterointerface and reduce the detected negative CBO configuration. Observed improvements of solar cell parameters would be in agreement with better optimized CdS/CIS heterointerfaces.

Building upon these findings, one would in a next step more systematically investigate the observed relation between the ΔE_g^{interf} of a buffer/absorber heterointerface and the conversion factor of its corresponding solar cell device. The first steps in such an analysis could be an expansion of the two presented optimization approaches (i.e., RTP-selenization and SAM adsorption) to include characterizations of the chemical and electronic properties of the modified heterointerface instead of only the treated absorbers. In this respect, post-treatment annealing of the RTP-selenized CIS absorbers could be useful in the removal of the observed elemental Se residues. Concerning further SAM-related optimization efforts, a greater selection of negative dipole-charge-inducing molecules should be aimed. Vacuum-based SAM deposition methods (in contrast to the employed wet chemical treatments) should also be explored to minimize (compare) the effect of extraneous adsorbates (due to solvent and glovebox exposures) in the analysis. Further optimization of CIS-based solar devices could involve substituting Ga for In at the surface (similar to the RTP-selenization approach) to study the effect of E_g^{surf}-widening and E_g depth profiles. The study and optimization of heterointerfaces formed with wide-gap chalcopyrites and CdS-alternative buffer materials, especially with CBM values higher than CdS (i.e., ~ 0.5 eV), are other valuable goals. The pursuit and understanding of these topics would greatly further knowledge-based optimization efforts of wide-gap chalcopyrite-based thin film solar cell devices.

Appendix A: List of Symbols and Abbreviations

Symbol	**Explanation**
α	Absorption Coefficient of a Material
α^*	Modified Auger Parameter
A	Sample Area
ALS	Advanced Light Source
AM1.5	Air Mass 1.5 Times
B_0	Magnetic Density Flux
BE	Binding Energy
bz	Benzoic Acid
χ	Electron Affinity
c	Speed of Light in Vacuum
CB	Conduction Band
CBD	Chemical Bath Deposition
CBM	Conduction Band Maximum
CBO	Conduction Band Offset
CdS	Cadmium Sulfide
CdSe	Cadmium Selenide
CdTe	Cadmium Telluride
CGS	Copper Gallium Sulfide, $CuGaS_2$
CGSe	Copper Gallium Selenide, $CuGaSe_2$
CHA	Concentric Hemispherical Analyzer
CIGSe	Copper Indium Gallium Selenide, $Cu(In,Ga)Se_2$
CIGSSe	Copper Indium Gallium Sulfide Selenide, $Cu(In,Ga)(S,Se)_2$
CIS	Copper Indium Sulfide, $CuInS_2$
CISe	Copper Indium Selenide, $CuInSe_2$
CISSe	Copper Indium Sulfide Selenide, $CuIn(S,Se)_2$
c-Si	Crystalline Silicon

Cu_xS	Copper Sulfide
C_x	Elemental Composition Fraction
CZTS	Copper Zinc Tin Sulfide, Cu_2ZnSnS_4
CZTSSe	Copper Zinc Tin Sulfide Selenide, $Cu_2ZnSn(S,Se)_4$
ΔE_g	Band Gap Energy Widening at Surface with Respect to Bulk
ΔE_g^{interf}	Band Gap Energy Widening at Interface with Respect to Bulk
DCM	Double Crystal Monochromator
DOS	Density of States
ε	Electric Field
E_c	Critical Photon Energy of a Synchrotron Light Source
E_F	Fermi Energy Level
E_g	Band Gap Energy
E_g^{bulk}	Band Gap Energy at Bulk
E_g^{interf}	Band Gap Energy at Interface
E_g^{surf}	Band Gap Energy at Surface
$E_{k,F}$	Kinetic Energy of the Fermi Edge
$E_{k,min}$	Kinetic Energy of the Slowest Emitted Electrons
E_{loc}	Local Vacuum Level
E_{pass}	Pass Energy
EQE	External Quantum Efficiency
E_r	Specific Ring Energy of a Synchrotron Light Source
E_{Vac}	Vacuum Level
eV_{bb}	Maximum Band Bending
Φ	Work Function
F-bz	4-Fluorobenzoic Acid
FF	Fill Factor
$F(R_\infty)$	Kubelka-Munka Reflectance Transformation
F-th	1H,1H,2H,2H-Perfluorodecanethiol
FWHM	Full-Width at Half Maximum

γ	Lorentz Factor
G_u	Undulator Gap
η	Power Conversion Efficiency
h	Planck's Constant
HAXPES	Hard X-ray Photoemission Spectroscopy
H-th	1-Dodecanethiol
HZB	Helmholtz-Zentrum Berlin für Materialien und Energie GmbH
i-	Intrisincally-doped
ID	Information Depth
IIBB	Interface-Induced Band Bending
I_L (j_L)	Light-Generated Current (Density)
I_{MPP} (j_{MPP})	Current (Density) at the Maximum Power Point of a Solar Cell
In_{Cu}	Indium on Copper Antisite
In_2S_3	Indium Sulfide
IPES	Inverse Photoemission Spectroscopy
I_{SC} (j_{SC})	Short Circuit Current (Density)
j	Total Angular Momentum Quantum Number
j_{01}	Saturation Current Density
j-V	Current Density-Voltage
k	Boltzmann's Constant
K	Insertion Device Magnetic Strength Factor
KCN	Potassium Cyanide
KE	Kinetic Energy
λ	Inelastic Mean Free Path, IMFP
λ^*	Effective Attenuation Length of XES Signal
$\lambda_{e(p)}$	de-Broglie Wavelength of Electron (Proton)
λ_{emi}	Attenuation Length of XES Emission Step
λ_{exc}	Attenuation Length of XES Excitation Step
λ_u	Undulator Frequency

L	Angular Momentum Quantum Number
MCD	Multichanneltron Detector
mc-Si	Multicrystalline Silicon
ν	Frequency of Wave
n	Principal Quantum Number
NO_2-bz	4-Nitrobenzoic Acid
NIR	Near-Infrared
OCD	Ordered Defect Compound
OCH_3-bz	4-Methoxybenzoic Acid
PCA	Principal Component Analysis
PES	Photoemission Spectroscopy
P_{in}	Incoming Irradiative Power
P_{MPP}	Maximum Power Point of a Solar Cell
PV	Photovoltaics
q	Elementary Charge Unit
QNR	Quasi Neutral Region
ρ	Charge Density
R_∞	Reflectance on “Infinitely” Thick Material
rf-	Radiofrequency
R_s	Series Resistance
R_{sh}	Shunt Resistance
RSH	Shockley-Read-Hall Model
RTP	Rapid Thermal Processing
σ	Photoionization Cross Section
s	Spin Quantum Number
SALSA	Solid and Liquid Spectroscopic Analysis Endstation
SAM	Self-Assembled Monolayer
SCR	Space Charge Region
SGM	Spherical Grating Monochromator

SLG	Soda Lime Glass
SrF_2	Strontium Fluoride
SXF	Soft X-ray Fluorescence Spectrometer
T	Temperature
T	Transmission Function of Electron Analyzer
UHV	Ultra-High Vacuum
UPS	Ultraviolet Photoelectron Spectroscopy
UV-Vis	Ultraviolet Visible Spectrophotometry
v	Velocity of a Particle
V	Voltage
VB	Valence Band
V_{bi}	Built-In Voltage
VBM	Valence Band Maximum
VBO	Valence Band Offset
V_{Cu}	Copper Vacancy Site
V_{MPP}	Voltage at the Maximum Power Point of a Solar Cell
V_{OC}	Open Circuit Voltage
V_S	Sulfur Vacancy Site
XAES	X-ray Excited Auger Electron Spectroscopy
XES	X-ray Emission Spectroscopy
XPS	X-ray Photoemission Spectroscopy
XRF	X-ray Fluorescence Analysis
ZnO	Zinc Oxide
$Zn(OH)_2$	Zinc Hydroxide
ZnS	Zinc Sulfide
ZnSe	Zinc Selenide
ZSW	Zentrum für Sonnenenergie- und Wasserstoff- Forschung Baden-Württemberg

Appendix B: Electronic Structure Values of Buffer/Absorber Chalcopyrite-based Heterointerfaces

Table A.1 Electronic structure values of the absorber and buffer components of each of the heterointerfaces evaluated in Ch. 7, along with the efficiencies of the resulting solar cell devices.

	buffer		absorber					
Interface	CBM (eV)	VBM (eV)	CBM (eV)	VBM (eV)	IIBB (eV)	CBO (eV)	Eff. (%)	Ref.
CdS/CISSe	0.5 ± 0.1	-1.9 ± 0.1	0.5 ± 0.1	-0.9 ± 0.1	0.0 ± 0.15	0.0 ± 0.15	14.1	[145,158]
CdS/CIGSe	0.53 ± 0.1	-1.84 ± 0.1	0.96 ± 0.1	-0.72 ± 0.1	0.27 ±0.15	-0.16 ± 0.15	17.8	[159]
CdS/CIGSe	0.57 ± 0.1	-1.93 ± 0.1	0.78 ± 0.1	-0.85 ± 0.1	0.18 ± 0.07	-0.03 ± 0.15	20	[160]
CdS/CIGSe	0.85±0.15	-1.57 ± 0.1	0.82±0.15	-0.88 ± 0.15	0.08 ± 0.08	0.11 ± 0.25	18.3	Ch. 4, [29]
CdS/CIS	0.57±0.15	-1.93 ± 0.1	0.8 ± 0.15	-1.08 ± 0.1	-0.19 ± 0.16	-0.42 ± 0.2	9	Ch. 5,6,8
CdS/CIGS	0.46 ± 0.1	-2.01 ± 0.15	0.86 ± 0.1	-0.90 ± 0.15	-0.05 ± 0.1	-0.45 ± 0.15	7	[16,162]
CdS/CIGSSe	-	-	1.09 ± 0.1	-0.83 ± 0.1	-	-0.52 ± 0.3*	9	[161]
CdS/CGSe	-	-	1.6 ± 0.2	-0.6 ± 0.1	-	-1.03±0.3*	6	[89]
CdS/CZTS	0.74 ± 0.1	-1.65 ± 0.1	0.93 ± 0.1	-0.60 ± 0.1	0.14 ± 0.1	-0.33 ± 0.15	6.8	[156]
CdS/CZTS	0.74 ± 0.1	-1.75 ± 0.1	1.18 ± 0.1	-0.74 ± 0.1	-0.1 ± 0.1	-0.34 ± 0.15	10.1	[156]

Appendix C: Preliminary Results of the Characterization of the modified CdS/F-th:$CuInS_2$ Heterointerface

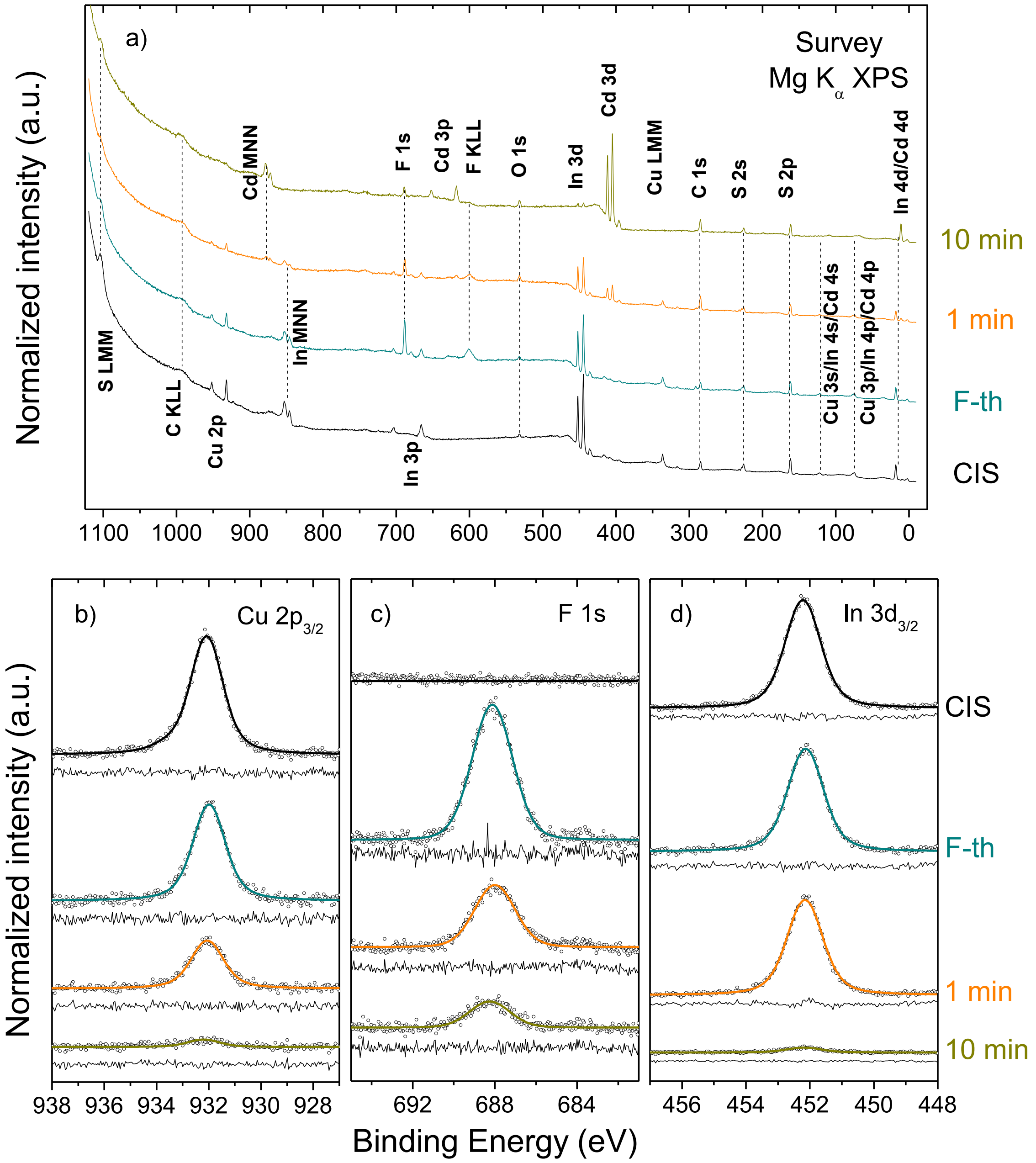

Figure A.1 (a) XPS Survey spectra of CIS absorber samples treated with a 20 mM F-th SAM solution (i.e., F-th), followed by CBD-CdS treatment times (i.e., 1 and 10 min). Labels indicate duration of the CBD-CdS treatment of respective samples. Note that all samples have been KCN-etched prior to F-th and CBD-CdS treatments. XPS detail spectra of the (b) Cu $2p_{3/2}$, (c) F 1s and (d) In $3d_{3/2}$ regions of the sample series, normalized to background intensity. Vertical offsets are added for clarity.

Fig. A.1 show XPS survey and detail spectra of CIS absorbers submitted, first, to a 20 mM SAM solution treatment and, subsequently, to CBD-CdS treatments. The intensity of photoemission lines related to the absorber (i.e., Cu $2p_{3/2}$ and In $3d_{3/2}$) and to the F-th SAM molecule (i.e., F 1s) in these samples are not attenuated by the deposited CdS buffer layer, even after 10 min of CBD-CdS treatment. In contrast, the absorber-related photoemission lines of the CBD-CdS-treated CIS absorber sample series analyzed in Sect. 5.3.1 are completely attenuated by 4.0 min CBD-CdS treatment. The here-presented measurements suggest significant changes in the properties of the deposited CdS layer (i.e., regions of the absorber surface remain uncovered by the deposited buffer layer) due to the adsorbed F-th on the CIS surface. Furthemore, the lower attenuation of the F 1s intensity compared to the two absorber-related photoemission lines also suggest a diffusion of F-th molecules through the buffer layer.

Bibliography

[1] O. Morton, “Solar energy: A new day dawning?: Silicon Valley sunrise,” *Nature*, vol. 443, p. 19, 2006.

[2] E. Becquerel, “Mémoire sur les effets électriques produits sous l’influence des rayons solaires,” *Comptes rendus de l’Académie des Sciences*, vol. 9, p. 561, 2011.

[3] H. Hertz, “Über einen Einfluss des ultravioletten Lichtes auf die elektrische Entladung,” *Ann. Physik*, vol. 31, p. 983, 1887.

[4] D.M. Chapin, C.S. Fuller, and G.L. Pearson, “A New Silicon p-n Junction Photocell for Converting Solar Radiation into Electrical Power,” *Journal of Applied Physics*, vol. 25, p. 676, 1954.

[5] M.A. Green, K. Emery, Y. Hishikawa, W. Warta, and E.D. Dunlop, “Solar cell efficiency tables (version 43),” *Progress in Photovoltaics: Research and Applications*, vol. 22, p. 1, 2014.

[6] A. Luque and S. Hegedus, *Handbook of Photovoltaic Science and Engineering*, 2nd ed., John Wiley & Sons, Ltd., 2011.

[7] Press release 09/2014, “Manz AG: New efficiency world record from exclusive research partner ZSW substantiates the tecnhological advantage of CIGS thin film. ”

[8] L.L. Kazmerski, *Technical Digest of the 12th International Photovoltaic Science and Engineering Conference (PVSEC-12), Cheju, South-Korea*, p. 1102, 2001.

[9] M. Bär, W. Bohne, J. Röhrich, E. Strub, S. Lindner, M.C. Lux-Steiner, C.-H. Fischer, T.P. Niesen, and F. Karg, “Determination of the band gap depth profile of the penternary $Cu(In_{(1-X)}Ga_X)(S_YSe_{(1-Y)})_2$ chalcopyrite from its composition gradient,” *Journal of Applied Physics*, vol. 96, p. 3857, 2004.

[10] P. Jackson, D. Hariskos, R. Wuerz, W. Wischmann, and M. Powalla, “Compositional investigation of potassium doped $Cu(in,Ga)Se_2$ solar cells with efficiencies up to 20.8%,” *Physica Status Solidi*, vol. 8, p. 219, 2014.

[11] J. Klaer, J. Bruns, R. Henninger, K. Siemer, R. Klenk, K. Ellmer, and D. Bräunig, “Efficient thin-film solar cells prepared by a sequential process,” *Semiconductor Science and Technology*, vol. 13, p. 1456, 1998.

[12] D.L. Young, J. Keane, A. Duda, J.A.M. AbuShama, C.L. Perkins, M. Romero, and R. Noufi, “Improved Performance in $ZnO/CdS/CuGaSe_2$ Thin-Film Solar Cells,” *Progress in Photovoltaics: Research and Applications*, vol. 11, p. 535, 2003.

[13] M. Turcu, O. Pakma, and U. Rau, “Interdependence of absorber composition and recombination mechanism in $Cu(In,Ga)(Se,S)_2$ heterojunction solar cells,” *Applied Physics Letters*, vol. 80, p. 2598, 2002.

[14] J. Reiß, J. Malström, A. Werner, I. Henge, R. Klenk, and M.C. Lux-Steiner, "Current Transport in $CuInS_2$ Solar Cells Depending on Absorber Preparation," *Materials Research Society Symposium Proceedings,* vol. 668, H. 9.4.1, 2001.

[15] M. Morkel, L. Weinhardt, B. Lohmüller, C. Heske, E. Umbach, W. Riedl, S. Zweigart, and F. Karg, "Flat conduction-band alignment at the CdS/$CuInSe_2$ thin-film solar-cell heterojunction," *Applied Physics Letters*, vol. 79, no. 27, p. 4482, 2001.

[16] L. Weinhardt, O. Fuchs, D. Groß, G. Storch, E. Umbach, N.G. Dhere, A.A. Kadam, S.S. Kulkarni, and C. Heske, "Band alignment at the CdS/Cu(In,Ga)S_2 interface in thin-film solar cells," *Applied Physics Letters*, vol. 86, p. 062109, 2005.

[17] W. Schottky, "Vereinfachte und erweiterte Theorie der Randschichtgleichrichter," *Zeitschrift für Physik*, vol. 118, p. 539, 1942.

[18] H.-J. Lewerenz and H. Jungblut, *Photovoltaik: Grundlagen und Anwendung*, Springer-Verlag, Berlin, 1995.

[19] W. Shockley, "The Theory of p-n Junctions in Semiconductors and p-n Junction Transistors," *Bell System Technical Journal*, vol. 28, p. 435, 1949.

[20] D. Schmid, M. Ruckh, F. Grunwald, and H.-W. Schock, "Chalcopyrite/defect chalcopyrite heterojunctions on the basis of $CuInSe_2$," *Journal of Applied Physics*, vol. 73, p. 2902, 1993.

[21] D. Schmid, M. Ruckh, and H.-W. Schock, "A comprehensive characterization of the interfaces in Mo/CIS/CdS/ZnO solar cell structures," *Solar Energy Materials and Solar Cells*, vol. 41–42, p. 281, 1996.

[22] C.A. Kaufmann, A. Neisser, R. Klenk, and R. Scheer, "Transfer of Cu(In,Ga)Se_2 thin film solar cells to flexible substrates using an in situ process control," *Thin Solid Films*, vol. 480–481, p. 515, 2005.

[23] R. Caballero, C.A. Kaufmann, T. Eisenbarth, T. Unold, R. Klenk, and H.-W. Schock, "High efficiency low temperature grown Cu(In,Ga)Se_2 thin film solar cells on flexible substrates using NaF precursor layers," *Progress in Photovoltaics: Research and Applications*, vol. 19, p. 547, 2011.

[24] H.G. Grimm and A. Sommerfeld, "Über den Zusammenhang des Abschlusses der Elektronengruppen im Atom mit den chemischen Valenzzahlen," *Zeitschrift für Physik*, vol. 36, p. 36, 1926.

[25] J.E. Jaffe and A. Zunger, "Theory of the band-gap anomaly in ABC_2 chalcopyritesemiconductors," *Physical Review B*, vol. 29, p. 1882, 1984.

[26] S.B. Zhang, S.-H. Wei, A. Zunger, and H. Katayama-Yoshida, "Defect physics of the $CuInSe_2$ chalcopyrite semiconductor," *Physical Review B*, vol. 57, p. 9642, 1998.

[27] S.-H. Wei, S.B. Zhang, and A. Zunger, "Effects of Na on the electrical and structural properties of $CuInSe_2$," *Journal of Applied Physics*, vol. 85, p. 7214, 1999.

[28] X. Song, R. Caballero, R. Félix, D. Gerlach, C. A. Kaufmann, H.-W. Schock, R. G. Wilks, and M. Bär, “Na incorporation into Cu(In,Ga)Se_2 thin-film solar cell absorbers deposited on polyimide: Impact on the chemical and electronic surface structure,” *Journal of Applied Physics*, vol. 111, p. 034903, 2012.

[29] G. Voorwinden, R. Kniese, P. Jackson, and M. Powalla, “IN-LINE Cu(In,Ga)Se_2 CO-EVAPORATION PROCESS ON 30 cm x 30 cm SUBSTRATES WITH MULTIPLE DEPOSITION STAGES,” *Proceedings of the 22nd European Photovoltaic Solar Energy Conference*, 3-7 September 2007, Milan, Italy.

[30] K. Siemer, J. Klaer, I. Luck, J. Bruns, R. Klenk, and D. Bräunig, “Efficient $CuInS_2$ solar cells from a rapid thermal process (RTP),” *Solar Energy Materials and Solar Cells*, vol. 67, p. 159, 2001.

[31] M. Weber, R. Scheer, H.-J. Lewerenz, U. Störkel, H. Jungblut, *Proceedings of the Spring Meeting E-MRS*, Strausbourg, France (1999).

[32] O. de Melo, L. Hernández, O. Zelaya-Angel, R. Lozada-Morales, M. Becerril, and E. Vasco, “Low resistivity cubic phase CdS films by chemical bath deposition technique,” *Applied Physics Letters*, vol. 65, p. 1278, 1994.

[33] V. Nadenau, D. Hariskos, H.-W. Schock, M. Krejci, F.-J. Haug, A. N. Tiwari, H. Zogg, and G. Kostorz, “Microstructural study of the CdS/$CuGaSe_2$ interfacial region in $CuGaSe_2$ thin film solar cells,” *Journal of Applied Physics*, vol. 85, p. 534, 1999.

[34] A. Mang, K. Reimann, and St. Rübenacke, “Band Gaps, Crystal-field Splitting, Spin-orbit Coupling, and Exciton Binding Energies in ZnO under Hydrostatic Pressure,” *Solid State Communications*, vol. 94, p. 251, 1995.

[35] L. Kronik and Y. Shapira, “Surface photovoltage phenoma: theory, experiment and applications,” *Surface Science Reports*, vol. 37, p. 1, 1999.

[36] T. Minemoto, T. Matsui, H. Takakura, Y. Hamakawa, T. Negami, Y. Hashimoto, T. Uenoyama, and M. Kitagawa, “Theoretical analysis of the effect of conduction band offset of window/CIS layers on performance of CIS solar cells using device simulation,” *Solar Energy Materials and Solar Cells*, vol. 67, p. 83, 2001.

[37] I. Hengel, A. Neisser, R. Klenk, and M.C. Lux-Steiner, “Current transport in $CuInS_2$:Ga/CdS/ZnO – solar cells,” *Thin Solid Films*, vol. 361–362, p. 458, 2000.

[38] P. Würfel, *Physik der Solarzellen*, Spektrum AkademischerVerlag, Heidelberg/Berlin, 2000.

[39] D. Fuertes-Marrón, “Structural and electronic characterization of thin film solar cells based on CVD-grown $CuGaSe_2$,” PhD thesis, Freie Universität Berlin, 2003.

[40] W. Shockley and W.T. Read, “Statistics of the Recombinations of Holes and Electrons,” *Physical Review*, vol. 87, p. 835, 1952.

[41] R. Klenk, “Characterisation and modelling of chalcopyrite solar cells,” *Thin Solid Films*, vol. 387, p. 135, 2001.

[42] A. Einstein, “Über einen die Erzeugung und Verwandlung des Lichtes betreffenden heuritischen Gesichtspunkt,” *Annalen der Physik*, vol. 17, p. 132, 1905.

[43] S. Hüfner, *Photoelectron Spectroscopy: Principles and Applications*, Springer, Berlin, 2003.

[44] H. Lüth, *Solid Surfaces, Interfaces and Thin Films*, Springer, 2001.

[45] J.F. Moulder, W.F. Stickle, and P.E. Sobol, *Handbook of X-ray Photoelectron Spectroscopy*, 1992nd ed. Perkin-Elmer, Physical Electronics Division, 1992.

[46] J.H. Scofield, “Hartree-Slater subshell photoionization cross-sections at 1254 and 1487 eV,” *Journal of Electron Spectroscopy and Related Phenomena*, vol. 8, p. 129, 1976.

[47] M.B. Trzhaskovskaya, V.I. Nefedov, and V.G. Yarzhemsky, “Photoelectron angular distribution parameters for elements Z = 1 to Z = 54 in the photoelectron energy range 100-5000 eV,” *Atomic Data and Nuclear Data Tables*, vol. 77, p. 97, 2001.

[48] M.P. Seah and G.C. Smith, “Quantitative AES and XPS: Determination of the electron spectrometer transmission function and the detector sensitivity energy dependencies for the production of true electron emission spectra in AES and XPS,” *Surface and Interface Analysis*, vol. 15, p. 751, 1990.

[49] M.P. Seah and W.A. Dench, “Quantitative Electron Spectroscopy of Surfaces: A Standard Data Base for Electron Inelastic Mean Free Paths in Solids,” *Surface and Interface Analysis*, vol. 1, p. 2, 1979.

[50] S. Tougaard, *QUASES-IMFP-TPP2M*. 2002.

[51] S. Tanuma, C. J. Powell, and D.R. Penn, “Calculations of electron inelastic mean free paths. V. Data for 14 organic compounds over the 50–2000 eV range,” *Surface and Interface Analysis*, vol. 21, p. 165, 1994.

[52] D. Briggs and M.P. Seah, *Practical Surface Analysis: Auger and X-ray photoelectron spectroscopy*, Wiley, 1983.

[53] National Institute of Standards and Technology, “NIST X-ray Photoelectron Spectroscopy (XPS) Database.” [Online]. Available: http://srdata.nist.gov/xps/Default.aspx.

[54] J.J. Olivero and R.L. Longbothum, “Empirical fits to the Voigt line width: a brief review,” *Journal of Quantitative Spectroscopy and Radiative Transfer*, vol. 17, p. 233, 1977.

[55] J. Humlíček, “Optimized computation of the Voigt and complex probability functions,” *Journal of Quantitative Spectroscopy and Radiative Transfer*, vol. 27, p. 437, 1982.

[56] M. Wojdyr, "Fityk: a general-purpose peak fitting program," *Journal of Applied Crystallography*, vol. 43, p. 1126, 2010.

[57] N.V. Smith and D.P. Woodruff, "Inverse Photoemission from Metal Surfaces," *Progress Surface Science*, vol. 21, p. 295, 1986.

[58] F. Schedin, G. Thornton, and R.I.G. Uhrberg, "Windows and photocathodes for a high resolution solid state bandpass ultraviolet photon detector for inverse photoemission," *Review of Scientific Instruments*, vol. 68, p. 41, 1997.

[59] V. Dibeler, J.A. Walker, K.E. McCulloh, and H. Rosenstock, "Effect of hot bands on the ionization of some diatomic halogen molecules," *International Journal of Mass Spectrometry and Ion Physics*, vol. 7, p. 209, 1971.

[60] D. Attwood, *Soft X-rays and Extreme Ultraviolet Radiation*, Cambridge, New York, 1999.

[61] D.H. Tomboulin and P.L. Hartman, "Spectral and Angular Distribution of Ultraviolet Radiation from the 300-MeV Cornell Synchrotron,"*The Physical Review*, vol. 102, p. 1423, 1956.

[62] Advanced Light Source, "High Resolution and Flux for Materials and Surface Science Beamline 8.0.1," 2009. [Online]. Available: http://www.als.lbl.gov/als/als_users_bl/8.0.1-Overview.pdf.

[63] J.J. Jia, T.A. Callcott, J. Yurkas, A.W. Ellis, F.J. Himpsel, M.G. Samant, J. Stöhr, D.L. Ederer, J.A. Carlisle, E.A. Hudson, L.J. Terminello, D.K. Shuh, and R.C.C. Perera, "First experimental results from IM/TNN/TULANE/LLNL/LBL undulator beamline at the advanced light source," *Review of Scienific Instruments*, vol. 66, p. 1394, 1995.

[64] Advanced Light Source, "Soft X-ray Flourescence (SXF) Spectrometer. Beamline 8.0.1," 2009. [Online]. Available: http://www.als.lbl.gov/als/als_users_bl/8.0.1-Overview.pdf.

[65] M. Boots, *ALS sxedaq*. University of Saskatchewan.

[66] M. Blum, L. Weinhardt, O. Fuchs, M. Bär, Y. Zhang, M. Weigand, S. Krause, S. Pookpanratana, T. Hofmann, W. Yang, J.D. Denlinger, E. Umbach, and C. Heske, "Solid and liquid spectroscopic analysis (SALSA)-a soft x-ray spectroscopy endstation with a novel flow-through liquid cell," *Review of Scientific Instruments*, vol. 80, p. 123102, 2009.

[67] SPring-8, "BL15XU(WEBRAM) OUTLINE," 2014. [Online]. Available: http://www.spring8.or.jp/wkg/BL15XU/instrument/lang-en/INS-0000000354/instrument_summary_view.

[68] S. Ueda, Y. Katsuya, M. Tanaka, H. Yoshikawa, Y. Yamashita, S. Ishimaru, Y. Matsushita, and K. Kobayashi, "Present Status of the NIMS Contract Beamline BL15XU at SPring-8," *AIP Conference Proceedings*, vol. 1234, p. 403, 2010.

[69] T.A. Calcott, *Vacuum Ultraviolet Spectroscopy II (Experimental Methods in the Physical Sciences)*, Academic Press, San Diego, 1998.

[70] Calculated using attenuation lengths from B. L. Henke, E. M. Gullikson, and J. C. Davis, “X-Ray Interactions: Photoabsorption, Scattering, Transmission, and Reflection at E = 50-30,000 eV, Z = 1-92,” *Atomic Data and Nuclear Data Tables*, vol. 54, no. 2, pp. 181–342, Jul. 1993; http://wwwcxro.lbl.gov/optical_constants/atten2.html.

[71] S. R. Wasserman, “The analysis of mixtures: Application of principal component analysis to XAS spectra,” *Journal de Physique IV*, vol. 7, p. 203, 1997.

[72] S. R. Wasserman, P. G. Allen, D. K. Shuh, J. J. Bucher, N. M. Edelstein, “EXAFS and principal component analysis: A new shell game,” *Journal of Synchrotron Radiation*, vol. 6, p. 284, 1999.

[73] M.-P. Isaure, A. Laboudigue, A. Manceau, G. Sarret, C. Tiffreau, P. Trocellier, G. Lamble, J.-L. Hazemann, and D. Chateigner, “Quantitative Zn speciation in a contaminated dredged sediment by μ-PIXE, μ-SXRF, EXAFS spectroscopy and principal component analysis,” *Geochimica et Cosmochimica Acta.*, vol. 66, p. 1549, 2002.

[74] O. Keski-Rahkonen, and M. O. Krause, “Total and Partial Atomic-level Widths,” *Atomic Data and Nuclear Data Tables*, vol. 14, p. 139, 1974.

[75] “X-Ray Fluorescence Spectrometer ZSX Primus II,” *The Rigaku Journal*, vol. 22, p. 42, 2005.

[76] J.L. Pankove, *Optical processes in semiconductors, vol. 1*, Dover Publications, Inc., New York, 1975.

[77] P. Kubelka, “New Contributions to the Optics of Intensely Light-Scattering Materials. Part I,” *Journal of the Optical Society of America*, vol. 38, p. 448, 1958.

[78] “Applications and Use of Integrating Spheres With the LAMBDA 650 and 850 UV/Vis and LAMBDA 950 UV/Vis/NIR Spectrophotometers,” *APPLICATION NOTE: UV/VIS AND UV/VIS/NIR SPECTROSCOPY*, PerkinElmer Life and Analytical Sciences, p. 1, 2004.

[79] P. Sigmund, “Mechanisms and theory of physical sputtering by particle impact,” *Nuclear Instruments and Methods in Physics Research Section B: Beam Interactions with Materials and Atoms*, vol. 27, p. 1, 1987.

[80] “EX05: Differentially Pumped, Scanning Ion Gun,” *Thermo Scientific*, 2008.

[81] Nonsequitur Technologies, “Ion Guns: Model 1402-Low Energy Perfomance,” 2014. [Online]. Available: http://nonsequitur-ion-gun.com/Model_1402.html.

[82] H. Rodriguez-Alvarez, “Growth mechanisms of $CuInS_2$ formed by the sulfurization of thin metallic films,” PhD thesis, Technischen Universität Berlin, 2010.

[83] M. Bär, I. Repins, M. A. Contreras, L. Weinhardt, R. Noufi, and C. Heske, “Chemical and electronic surface structure of 20%-efficient Cu(In,Ga)Se_2 thin film solar cell absorbers,” *Applied Physics Letters*, vol. 95, p. 052106, 2009.

[84] B. J. Stanbery, C. H. Chang, and T. J. Anderson, “Engineered phase inhomogeneity for CIS device optimization,” in *Ternary and Multinary Compounds: Proceedings of the 11th International Conference*, R. D. Tomlinson, A. E. Hill, and R. D. Pilkington, Eds. Bristol: Iop Publishing Ltd, p. 915, 1998.

[85] V. Nadenau, G. Lippold, U. Rau, and H.-W. Schock, “Sodium induced secondary phase segregations in $CuGaSe_2$ thin films,” *Journal of Crystal Growth*, vol. 233, p. 13, 2001.

[86] G. Rossi, I. Lindau, L. Braicovich, and I. Abbati, “Cooper-minimum effects in the photoionization cross sections of 4d and 5d electrons in solid compounds,” *Physical Review B*, vol. 28, p. 3031, 1983.

[87] K.K. Chin, K. Miyano, R. Cao, T. Kendelewicz, J. Yeh, I. Lindau, and W.E. Spicer, “Summary Abstract: Chemical reaction at the In on GaAs (110) interface: A synchrotron radiation photoemission study,” *Journal of Vacuum Science & Technology B: Microelectronics and Nanometer Structures*, vol. 5, p. 1080, 1987.

[88] I. Repins, M.A. Contreras, B. Egaas, C. DeHart, J. Scharf, C.L. Perkins, B. To, and R. Noufi, “19.9%-efficient ZnO/CdS/$CuInGaSe_2$ solar cell with 81.2% fill factor,” *Progress in Photovoltaics: Research and Applications*, vol. 16, p. 235, 2008.

[89] A. Meeder, L. Weinhardt, R. Stresing, D. Fuertes Marrón, R. Würz, S.M. Babu, T. Schedel-Niedrig, M.Ch. Lux-Steiner, C. Heske, and E. Umbach, “Surface and bulk properties of $CuGaSe_2$ thin films,” *Journal of Physics and Chemistry of Solids*, vol. 64, p. 1553, 2003.

[90] C. Julien, M. Eddrief, K. Kambas, and M. Balkanski, “Electrical and optical properties of In_2Se_3 thin films,” *Thin Solid Films*, vol. 137, p. 27, 1986.

[91] M. Bär, L. Weinhardt, C. Heske, H.-J. Muffler, M.Ch. Lux-Steiner, E. Umbach, and Ch.-H. Fischer, “Cd^{2+}/NH_3 treatment of Cu(In,Ga)(S,Se)$_2$ thin-film solar cell absorbers: a model for the performance-enhancing processes in the partial electrolyte,”*Progress in Photovoltaics: Research and Applications*, vol. 13, p. 571, 2005.

[92] C. Heske, D. Eich, R. Fink, E. Umbach, T. van Buuren, C. Bostedt, L.J. Terminello, S. Kakar, M.M. Grush, T.A. Callcott, F.J. Himpsel, D.L. Ederer, R.C.C. Perera, W. Riedl, and F. Karg, “Observation of intermixing at the buried CdS/Cu(In,Ga)Se_2 thin film solar cell heterojunction,” *Applied Physics Letters*, vol. 74, p. 1451, 1999.

[93] L. Weinhardt, M. Bär, S. Pookpanratana, M. Morkel, T.P. Niesen, F. Karg, K. Ramanathan, M.A. Contreras, R. Noufi, E. Umbach, and C. Heske, “Sulfur gradient-driven Se diffusion at the CdS/CuIn(S,Se)$_2$ solar cell interface,” *Applied Physics Letters*, vol. 96, p. 182102, 2010.

[94] P.J. Cumpson, “The Thickogram: a method for easy film thickness measurement in XPS,” *Surface and Interface Analysis*, vol. 29, p. 403, 2000.

[95] L. Baker, A.S. Cavanagh, J. Yin, S.M. George, A. Kongkanand, and F.T. Wagner, “Growth of continuous and ultrathin platinum films on tungsten adhesion layers using atomic layer deposition techniques,” *Applied Physics Letters*, vol. 101, p. 111601, 2012.

[96] M. Polak, “X-ray photoelectron spectroscopic studies of CdSe0.65 Te0.35,” *Journal of Electron Spectroscopy and Related Phenomena*, vol. 28, p. 171, 1982.

[97] S.W. Gaarenstroom and N. Winograd, “Initial and final state effects in the ESCA spectra of cadmium and silver oxides,” *The Journal of Chemical Physics*, vol. 67, p. 3500, 1977.

[98] H. Seyama and M. Soma, “X-ray photoelectron spectroscopic study of montmorillonite containing exchangeable divalent cations,” *Journal of the Chemical Society, Faraday Transactions 1*, vol. 80, p. 237, 1984.

[99] M. Bär, L. Weinhardt, O. Fuchs, J. Klaer, J. Peiser, H.-W. Schock, and C. Heske, “Chemical Bath Deposition of CdS Thin Films on $CuInS_2$ and Si Substrates - A Comparative X-Ray Emission Study,” in *Conference Record of the 2006 IEEE 4th World Conference on Photovoltaic Energy Conversion*, vol. 1, p. 416, 2006.

[100] D. Hariskos, R. Menner, P. Jackson, S. Paetel, W. Witte, W. Wischmann, M. Powalla, L. Bürkert, T. Kolb, M. Oertel, B. Dimmler, and B. Fuchs, “New reaction kinetics for a high-rate chemical bath deposition of the Zn(S,O) buffer layer for $Cu(In,Ga)Se_2$-based solar cells,” *Progress in Photovoltaics: Research and Applications*, vol. 20, p. 534, 2012.

[101] J.J. Yeh and I. Lindau, “Atomic subshell photoionization cross sections and asymmetry parameters parameters: $1 \leq Z \leq 103$,” *Atomic Data and Nuclear Data Tables*, vol. 32, p. 1, 1985.

[102] J.H. Hubbell, P.N. Trehan, Nirmal Singh, B. Chand, D. Mehta, M.L. Garg, R.R. Garg, Surinder Singh, and S. Puri, “A Review, Biblioghraphy, and Tabulation of *K, L*, and Higher Atomic Shell X-Ray Fluorescence Yields,” *Journal of Physical and Chemical Reference Data*, vol. 23, p. 339, 1994.

[103] L. Zhou, T.A. Callcott, J.J.Jia, D.L. Ederer, and R. Perera, “Sulfur $L_{2,3}$ and zinc $M_{2,3}$ soft-x-ray fluorescence spectra in CdS and ZnS,” *Physical Review B*, vol. 55, p. 5051, 1997.

[104] L. Weinhardt, O. Fuchs, A. Fleszar, M. Bär, M. Blum, M. Weigand, J.D. Denlinger, W. Yang, W. Hanke, E. Umbach, and C. Heske, “Resonant inelastic soft x-ray scattering of CdS: A two-dimensional electronic structure map approach,” *Physical Review B*, vol. 79, p. 165305, 2009.

[105] C. Barglik-Chory, D. Buchold, M. Schmitt, W. Kiefer, C. Heske, C. Kumpf, O. Fuchs, L. Weinhardt, A. Stahl, E. Umbach, M. Lentze, J. Geurts, and G. Müller, “Synthesis, structure and spectroscopic characterization of water-soluble CdS nanoparticles,” *Chemical Physics Letters*, vol. 379, p. 443, 2003.

[106] U. Winkler, D. Eich, Z. H. Chen, R. Fink, S. K. Kulkarani, and E. Umbach, "Thermal behaviour of CdS nanoparticles investigated by high resolution photoelectron spectroscopy," *Physica Status Solidi (a)*, vol. 173, p. 253, 1999.

[107] U. Winkler, D. Eich, Z.H. Chen, R. Fink, S.K. Kulkarani, and E. Umbach, "Detailed investigation of CdS nanoparticle surfaces by high-resolution photoelectron spectroscopy," *Chemical Physics Letters*, vol. 306, p. 95, 1999.

[108] J. Nanda, Beena Annie Kuruvilla, and D.D. Sarma, "Photoelectron spectroscopic study of CdS nanocrystallites," *Physical Review B*, vol. 59, p. 7473, 1999.

[109] H. Döllefeld, C. McGinley, S. Almousalami, T. Möller, H. Weller, and A. Eychmüller, "Radiation-induced damage in x-ray spectroscopy of CdS nanoclusters," *The Journal of Chemical Physics*, vol. 117, p. 8953, 2002.

[110] R. Colin, and J. Drowart, "Mass Spectrometric Determination of Dissociation Energies of Gaseous Indium Sulphides, Selenides and Tellurides," *Journal of the Chemical Society, Faraday Transactions*, vol. 64, p. 2611, 1968.

[111] G. Moiseev, and J. Šesták, "Thermochemical and thermodynamical properties of some compounds in the system Ga-Sb-S," *Journal of Thermal Analysis*, vol. 43, p. 539, 1995.

[112] S. Pookpanratana, I. Repins, M. Bär, L. Weinhardt, Y. Zhang, R. Félix, M. Blum, W. Yang, and C. Heske, "CdS/Cu(In,Ga)Se_2 interface formation in high-efficiency thin film solar cells," *Applied Physics Letters*, vol. 97, p. 074101, 2010.

[113] J.R. Waldrop, R.W. Grant, S.P. Kowalczyk, and E.A. Kraut, "Measurement of semiconductor heterojunction band discontinuities by x-ray photoemission spectroscopy," *Journal of Vacuum Science & Technology A: Vacuum, Surfaces, and Films*, vol. 3, p. 835, 1985.

[114] S.H. Wei and A. Zunger, "Band offsets and optical bowings of chalcopyrites and Zn-based II-VI alloys," *Journal of Applied Physics*, vol. 78, p. 3846, 1995.

[115] C. Argile, and G. E. Rhead, "Adsorbed layer and thin film growth modes monitored by Auger electron spectroscopy," *Surface Science Reports*, vol. 10, p. 277, 1989.

[116] F. Erfurth, B. Hußmann, A. Schöll, F. Reinert, A. Grimm, I. Lauermann, M. Bär, T. Niesen, J. Palm, S. Visbeck, L. Weinhardt, and E. Umbach, "Chemical structure of the $(Zn_{1-x},Mg_x)O/CuIn(S,Se)_2$ interface in thin film solar cells," *Applied Physics Letters*, vol. 95, p. 122104, 2009.

[117] I. Lauermann, M. Bär, and C.-H. Fischer, "Synchrotron-based spectroscopy for the characterization of surfaces and interfaces in chalcopyrite thin-film solar cells," *Solar Energy Materials and Solar Cells*, vol. 95, p. 1495, 2011.

[118] E. Janocha, "Electronic Properties of ALD Zinc Oxide Interfaces and its Implication for Chalcopyrite Absorber Materials," PhD thesis, Technische Universität Berlin, 2011.

[119] M. Bär, A. Ennaoui, J. Klaer, T. Kropp, R. Sáez-Araoz, S. Lehmann, A. Grimm, I. Lauermann, C. Loreck, S. Sokoll, H.-W. Schock, C.-H. Fischer, M.C. Lux-Steiner, and C. Jung, "Intermixing at the heterointerface between ZnS/Zn(S,O) bilayer buffer and $CuInS_2$ thin film solar cell absorber," *Journal of Applied Physics*, vol. 100, p. 064911, 2006.

[120] R.A. Soref and H.W. Moos, "Optical Second-Harmonic Generation in ZnS-CdS and CdS-CdSe Alloys," *Journal of Applied Physics.*, vol. 35, p. 2152, 1964.

[121] M. Bär et al., *Proc. 39th IEEE PVSC*, Tampa, FL, June 16-21, 2013.

[122] M.M. El-Nahass, A. Qusti, B. Dakhel, H.S. Soliman, "Growth and optical properties of $ZnIn_2Se_4$ films," *Optica Pura y Aplicada*, vol. 24, p. 117, 1991.

[123] S. Lazzez, K.B. Ben Mahmoud, S. Abroug, F. Saadallah, and M. Amlouk, "A Boubaker polynomials expansion scheme (BPES)-related protocol for measuring sprayed thin films thermal characteristics," *Current Applied Physics*, vol. 9, p. 1129, 2009.

[124] M. Bär, N. Barreau, F. Couzinié-Devy, L. Weinhardt, R. G. Wilks, J. Kessler, and C. Heske, *to be published*.

[125] C.-H. Fischer, N. Allsop, S. E. Gledhill, T. Köhler, M. Krüger, R. Sáez-Araoz, Y. Fu, R. Schweiger, J. Richter, P. Wohlfart, P. Bartsch, N. Lichtenberg, and M. C. Lux-Steiner, "The spray-ILGAR (ion layer gas reaction) method for the deposition of thin semiconductor layers: Process and applications for thin film solar cells," *Solar Energy Materials and Solar Cells*, vol. 95, p. 1518, 2011.

[126] M. Powalla, G. Voorwinden, D. Hariskos, P. Jackson, and R. Kniese, "Highly efficient CIS solar cells and modules made by the co-evaporation process," *Thin Solid Films*, vol. 517, no. 7, p. 2111, 2009.

[127] M.C. Hanna and A.J. Nozik, "Solar conversion efficiency of photovoltaic and photoelectrolysis cells with carrier multiplication absorbers," *Journal of Applied Physics*, vol. 100, p. 074510, 2006.

[128] I. Luck, J. Kneisel, K. Siemer, J. Bruns, R. Scheer, N. Klenk, and D. Bräuning, "Influence of Na on the properties of Cu-rich prepared $CuInS_2$ thin films and the performance of corresponding $CuInS_2$/CdS/ZnO solar cells," *Solar Energy Materials & Solar Cells*, vol. 67, p. 151, 2001.

[129] V. Probst, F. Karg, J. Rimmasch, W. Riedl, W. Stetter, H. Harms, and O. Eibl, "Advanced Stacked Elemental Layer Process for $Cu(InGa)Se_2$ Thin Film Photovoltaic Devices," *Materials Research Society, Symposium Proceedings*, vol. 426, p. 165, 1996.

[130] R. Kimura, T. Mouri, T. Nakada, S. Niki, Y. Lacroix, T. Matsuzawa, K. Takahashi, A. Kunioka, "Photoluminescence Properties of Sodium Incorporated in $CuInSe_2$ Thin Films," *Japanese Journal of Applied Physics*, vol. 38, p. L289, 1999.

[131] M. Ruckh, D. Schmid, M. Kaiser, R. Schäffler, T. Walter, H.-W. Schock, "Influence of Substrates on the Electrical Properties of $Cu(In,Ga)Se_2$ Thin Films," *Proceedings of the First World Conference on Photovoltaic Energy Conversion, Hawaii*, p. 156, 1994.

[132] L. Weinhardt, C. Heske, E. Umbach, T.P. Niesen, S. Visbeck, and F. Karg, "Band alignment at the i-ZnO/CdS interface in Cu(In,Ga)(S,Se)$_2$ thin-film solar cells," *Applied Physics Letters*, vol. 84, p. 3175, 2004.

[133] A. Roche, H. Montes, J. Brissot, M. Romand, P. Josseaux, and A.K. De Mesmaeker, *Applied Surface Science*, vol. 21, p. 12, 1985.

[134] L. Weinhardt, T. Heim, O. Fuchs, C. Heske, E. Umbach, M. Bär, C.-H. Fischer, M.C. Lux-Steiner, Y. Zubavichus, T.P. Niesen, and F. Karg, "CdS and Cd(OH)$_2$ formation during Cd treatments of Cu(In,Ga)(S,Se)$_2$ thin-film solar absorbers," *Applied Physics Letters*, vol. 82, p. 571, 2003.

[135] S. Lehmann, M. Rusu, A. Grimm, I. Kötschau, I. Lauermann, P. Pistor, S. Sokoll, T. Schedel-Niedrig, M. C. Lux-Steiner, C. -H. Fischer, L. Weinhardt, C. Heske, and C. Jung, "Cd^{2+}/NH$_3$ treatment-induced formation of a CdSe surface layer on CuGaSe$_2$ thin-film solar cell absorbers," *Applied Physics Letters*, vol. 86, p. 222107, 2005.

[136] K. Otte, G. Lippold, F. Frost, A. Schindler, F. Bigl, M. V. Yakushev, and R. D. Tomlison, "Low energy ion beam etching of CuInSe$_2$ surfaces," *Journal of Vacuum Science and Technology A*, vol. 17, no. 1, p. 19, 1999.

[137] M. Bär, J. Klaer, L. Weinhardt, R.G. Wilks, S. Krause, M. Blum, W. Yang, C. Heske, and H.-W. Schock, "Cu$_{2-x}$S Surface Phases and Their Impact on the Electronic Structure of CuInS$_2$ Thin Films – A Hidden Parameter in Solar Cell Optimization," *Advanced Energy Materials*, vol. 3, p. 777, 2013.

[138] E. Niemi and L. Stolt, "Characterization of CuInSe$_2$ Thin Films by XPS," *Surface and Interface Analysis*, vol. 15, p. 422, 1990.

[139] R. Scheer and H. J. Lewrenz, "Photoemission study of evaporated CuInS$_2$ thin films. II. Electronic surface structure," *Journal of Vacuum Science and Technology A*, vol. 12, p. 56, 1994.

[140] S. Andres, C. Lehmann, and C. Pettenkofer, "Epitaxial growth of ZnO on CuInS$_2$ (112)," *Thin Solid Films*, vol. 518, p. 1032, 2009.

[141] M. Bär, J. Klaer, R. Félix, N. Barreau, L. Weinhardt, R.G. Wilks, C. Heske, and H.-W. Schock, "Surface Off-Stoichiometry of CuInS$_2$ Thin-Film Solar Cell Absorbers," *IEEE Journal of Photovoltaics*, vol. 3, p. 828, 2013.

[142] A. Klein and W. Jaegermann, "Fermi-level-dependent defect formation in Cu-chalcopyrite semiconductors," *Applied Physics Letters*, vol. 74, p. 508, 1999.

[143] P. Pistor, N. Allsop, W. Braun, R. Caballero, C. Camus, C.-H. Fischer, M. Gorgoi, A. Grimm, B. Johnson, T. Kropp, I. Lauermann, H. Mönig, S. Schorr, A. Weber, and R. Klenk, "Cu in In$_2$S$_3$: interdiffusion phenomena analysed by high kinetic energy X-ray photoelectron spectroscopy," *Physica Status Solidi (a)*, vol. 206, p. 1059, 2009.

[144] M. Bär, N. Barreau, F. Couzinié-Devy, S. Pookpanratana, J. Klaer, M. Blum, Y. Zhang, W. Yang, J.D. Denlinger, H.-W. Schock, L. Weindhardt, J. Kessler, and C. Heske,

"Nondestructive depth-resolved spectroscopic investigation of the heavily intermixed In_2S_3/Cu(In,Ga)Se_2 interface," *Applied Physics Letters*, vol. 96, p. 184101, 2010.

[145] L. Weinhardt, "Elektronische and chemische Eigenschaften von Grenzflächen und Oberflächen in optimierten Cu(In,Ga)$(S,Se)_2$ Dünnschichtsolarzell," PhD thesis, Bayerischen Julius-Maximilians-Universität, 2005.

[146] *Landolt-Börnstein*, edited by K.-H. Hellwege and O. Madelung, (Springer Berlin, 1985), vol. 17.

[147] N. Guezmir, J. Ouerfelli, and S. Belgacem, "Optical properties of sprayed $CuInS_2$ thin layers," *Materials Chemistry and Physics*, vol. 96, p. 116, 2006.

[148] M. Bashahu and A. Habyarimana, "Review and test of methods for determination of the solar cell series resistance," *Renewable energy*, vol. 6, p. 127, 1995.

[149] D. Psych, A. Mette, and S.W. Glunz, "A review and comparison of different methods to determine the series resistance of solar cells," *Solar Energy Materials and Solar Cells*, vol. 91, p. 1698, 2007.

[150] K. Bouzidi, M. Chegaar, and A. Bouhemadou, "Solar cells parameters evaluation considering the series and shunt resistance," *Solar Energy Materials and Solar Cells*, vol. 91, p. 1647, 2007.

[151] M.K. El- Adawi and I.A. Al- Nuaim, "A method to determine the solar cell series resistance from a single I-V characteristic curve considering its shunt resistance – new approach," *Vacuum*, vol. 64, p. 33, 2002.

[152] S. Sadewasser, "Surface potential of chalcopyrite films measured by KPFM," *Physica Status Solidi (a)*, vol. 203, p. 2571, 2006.

[153] D. Liao and A. Rockett, "Cu depletion in $CuInSe_2$ surface," *Applied Physics Letters*, vol. 82, p. 2829, 2003.

[154] R. Klenk, J. Klaer, Ch. Köble, R. Mainz, S. Merdes, H. Rodriguez-Alvarez, R. Scheer, and H.-W. Schock, "Development of $CuInS_2$-based solar cells and modules ," *Solar Energy Materials and Solar Cells*, vol. 95, p. 1441, 2010.

[155] R. Scheer, "Activation energy of heterojunction diode currents in the limit of interface recombination," *Journal of Applied Physics*, vol. 105, p. 104505, 2009.

[156] M. Bär, B.-A. Schubert, B. Marsen, R.G. Wilks, S. Pookpanratana, M. Blum, S. Krause, T. Unold, W. Yang, L. Weinhardt, C. Heske, and H.-W. Schock, "Cliff-like conduction band offset and KCN-induced recombination barrier enhancement at the CdS/Cu_2ZNSnS_4 thin-film solar cell heterojunction," *Applied Physics Letters*, vol. 99, p. 222105, 2011.

[157] M. Bär, J. Klaer, R. Félix, L. Weinhardt, R. G. Wilks, C. Heske, and H.-W. Schock, *to be published*.

[158] M. Bär, “Neuartige Cd-Freie Fensterstruktur für Chalkopyrit-Dünnschichtsolarzellen,” PhD thesis, Technischen Universität Berlin, 2004.

[159] S. Pookpanratana, “Chemical and Electronic Structure of Surfaces and Interfaces in Compound Semiconductors,” PhD thesis, Univsersity of Nevada, Las Vegas, 2010.

[160] C. Heske, “Characterization of the Electronic and Chemical Structure at the Thin Film Solar Cell Interfaces,” Subcontract Report NREL/SR-520-46434, Sep. 2009.

[161] M. Bär, S. Nishiwaki, L. Weinhardt, S. Pookpanratana, O. Fuchs, M. Blum, W. Yang, J.D. Denlinger, W.N. Shafarman, and C. Heske, “Depth-resolved band gap in $Cu(In,Ga)(S,Se)_2$ thin films,” *Applied Physics Letters*, vol. 93, p. 244103, 2008.

[162] N.G. Dhere, S.R. Ghongadi, M.B. Pandit, A.H. Jakagirdar, and D. Scheiman, “$CIGS_2$ Thin-Film Solar Cells on Flexible Foils for Space Power,” *Progress in Photovoltaics: Research and Applications*, vol. 10, p. 407, 2002.

[163] I.H. Campbell, S. Rubin, T.A. Zawodzinski, J.D. Kress, R.L. Martin, D.L. Smith, N.N. Barashkov, and J.P. Ferraris, “Controlling Schottky energy barriers in organic electronic devices using self-assembled monolayers,” *Physical Review B*, vol. 54, p. R14321, 1996.

[164] S. Braun, W.R. Salaneck, and M. Fahlman, “Energy-Level Alignment at Organic/Metal and Organic/Organic Interfaces,” *Advanced Materials*, vol. 21, p. 1450, 2009.

[165] E. Moons, M. Bruening, L. Burstein, J. Libman, A. Shanzer, and D. Cohen, “Molecular Approach to Surface Control of Chalcogenide Semiconductors,” *Japanese Journal of Applied Physics*, vol. 32, suppl. 32-33, p. 730, 1993.

[166] S. Lehmann, D. Fuertes Marrón, M. Bär, I. Lauermann, H. Mönig, and M.Ch. Lux-Steiner, “Tailoring the Work Function of Chalcopyrite Thin Films with Self-Assembled Monolayers of Thiols,” *Materials Research Society Symposium Proceedings*, vol. 1012, p. 1012-Y13-08, 2007.

[167] S. Bastide, R. Butruille, D. Cahen, A. Dutta, J. Libman, A. Shanzer, L. Sun, A. Vilan, “Controlling the Work Function of GaAs by Chemisorption of Benzoic Acid Derivatives,” *The Journal of Physical Chemistry B*, vol. 101, p. 2678, 1997.

[168] D.M. Alloway, M. Hofmann, D.L. Smith, N.E. Gruhn, A.L. Graham, R. Colorado, V.H. Wysocki, T. Randall Lee, P.A. Lee, and N.R. Armstrong, “Interface Dipoles Arising from Self-Assembled Monolayers on Gold: UV-Photoemission Studies of Alkanethiols and Partially Fluorinated Alkanethiols,” *The Journal of Physical Chemistry B*, vol. 107, p. 11690, 2003.

[169] J. Stettner, “Self assembled monolayer formation of alkanethiols on gold: Growth from solution versus physical vapor deposition,” PhD thesis, Graz University of Technology, 2010.

[170] C.D. Balin, E.B. Troughton, Y.T. Tao, J. Evall, G.M. Whitesides, R.G. Nuzzo, "Formation of monolayer films by the spontaneous assembly of organic thiols from solution onto gold," *Journal of the American Chemical Society*, vol. 111, p. 321, 1989.

[171] F. Schreiber, "Structure and growth of self-assembling monolyers," *Progress in Surface Science*, vol. 65, p. 151, 2000.

[172] J. Gong, and C.B. Mullins, "Structure and growth of self-assembling monolyers," *Journal of the American Chemical Society Communications*, vol. 130, p. 16458, 2008.

[173] X. Liu, B. Xu, J. Haubrich, R.J. Madix, and C.M. Friend, "Surface-Mediated Self-Coupling of Ethanol on Gold," *Journal of the American Chemical Society Communications*, vol. 131, p. 5757, 2009.

[174] T. Solomun, K. Christmann, and H. Baumgärtel, "Interaction of Acetonitrile and Benzonitrile with the Au(100) Surface," *The Journal of Physical Chemistry*, vol. 93, p. 7199, 1989.

[175] R. Haerle, E. Riedo, A. Pasquarello, and A. Baldereschi, "sp^2/sp^3 hybridization ratio in amorphous carbon from C 1s core-level shifts: X-ray photoelectron spectroscopy and first-principles calculation," *Physical Review B*, vol. 65, p. 045101, 2001.

[176] A. Nikitin, H. Ogasawara, D. Mann, R. Denecke, Z. Zhang, H. Dai, K. Cho, and A. Nilsson, "Hydrogenation of Single-Walled Carbon Nanotubes," *Physical Review Letters*, vol. 95, p. 225507, 2005.

[177] P. Ruffieux, O. Gröning, M. Bielmann, P. Mauron, L. Schlapbach, and P. Gröning, "Hydrogen adsorption on sp^2-bonded carbon: Influence of the local curvature," *Physical Review B,* vol. 66, p. 245416, 2002.

[178] K. Ihm, T.-H. Kang, J.H. Han, S. Moon, C.C. Hwang, K.-J. Kim, H.-N. Hwang, C.-H. Jeon, H.-D. Kim, B. Kim, C.-Y. Park, "Hydroxyl group-induced adsorptions of 4-nitro benzoic acid on the Si(100) surface," *Journal of Electron Spectroscopy and Related Phenomena,* vol. 144-147, p. 397, 2005.

[179] M. Fahlman, A. Crispin, X. Crispin, S.K.M. Henze, M.P. de Jong, W. Osikowicz, C. Tengstedt, and W.R. Salaneck, "Electronic structure of hybrid interfaces for polymer-based electronics," *Journal of Physics:Condensed Matter,* vol. 19, p. 183202, 2007.

[180] W. Osikowicz, M.P. de Jong, S. Braun, C. Tengstedt, M. Fahlman, and W.R. Salaneck, "Energetics at Au top and bottom contacts on conjugated polymers,"*Applied Physics Letters*, vol. 88, p. 193504, 2006.

[181] K. Hong, J.W. Lee, S.Y. Yang, K. Shin, H. Jeon, S.H. Kim, C. Yang, and C.E. Park, "Lower hole-injection barrier between pentacene and a 1-hexadecanethiol-modified gold substrate with a lowered work function," *Organic Electronics*, vol. 9, p. 21, 2008.

[182] Y. Wan, Y. Li, Q. Wang, K. Zhang, and Y. Wi, "The Relationship of Surface Roughness and Work Function of Pure Silver by Numerical Modeling," *International Journal of Electrochemical Science*, vol. 7, p. 5204, 2012.

[183] G.A. Sim, J. Monteath Robertson, and T.H. Goodwin, “The Crystal and Molecular Structure of Benzoic Acid,” *Acta Crystallographica*, vol. 8, p. 157, 1955.

[184] R.C.C.M. Micaroni, M.I.M.S. Bueno, and W.F. Jardin, “Degradation of Acetonitrile Residues Using Oxidation Processes,” *Journal of the Brazilian Chemical Society*, vol. 15, p. 509, 2004.

[185] M. Addamo, V. Augugliaro, S. Coluccia, A. Di Paola, E. Garcia-López, V. Loddo, G. Marci, G. Martra, and L. Palmisano, “The Role of Water in the Photocatalytic Degradation of Acetonitrile and Toluene in Gas-Solid and Liquid-Solid Regimes,” *International Journal of Photoenergy*, vol. 2006, p. 1, 2006.

[186] T. Glatzel, M. Rusu, S. Sadewasser, and M.C. Lux-Steiner, “Surface photovoltage analysis of thin CdS layers on polycrystalline chalcopyrite absorber layers by Kelvin probe force microscopy,” *Physica Status Solidi (a)*, vol. 203, p. 2571, 2006.

Publications

S. Pookpanratana, I. Repins, M. Bär, L. Weinhardt, Y. Zhang, R. Félix, M. Blum, W. Yang, and C. Heske, “CdS/Cu(In,Ga)Se$_2$ interface formation in high-efficiency thin film solar cells,” Applied Physics Letters, vol. 97, p. 074101, Aug. 2010.

M. Wimmer, M. Bär, D. Gerlach, R.G. Wilks, S. Scherf, C. Lupulescu, F. Ruske, R. Félix, J. Hüpkes, G. Gavrila, M. Gorgoi, K. Lips, W. Eberhardt, and B. Rech, “Hard x-ray photoelectron spectroscopy study of the buried Si/ZnO thin-film solar cell interface: Direct evidence for the formation of Si–O at the expense of Zn-O bonds,” Applied Physics Letters, vol. 99, no. 15, pp. 152104–152104–3, Oct. 2011.

X. Song, R. Caballero, R. Félix, D. Gerlach, C.A. Kaufmann, H.-W. Schock, R.G. Wilks, and M. Bär, “Na incorporation into Cu(In,Ga)Se$_2$ thin-film solar cell absorbers deposited on polyimide: Impact on the chemical and electronic surface structure,” Journal of Applied Physics, vol. 111, p. 034903, Feb. 2012.

S. Pookpanratana, R. France, R. Félix, R. Wilks, L. Weinhardt, T. Hofmann, L. Tati Bismaths, S. Mulcahy, F. Kronast, T.D. Moustakas, M. Bär, and C. Heske, “Microstructure of vanadium-based contacts on n-type GaN,” Journal of Physics D: Applied Physics, vol. 45, p. 105401, Mar. 2012.

R.G. Wilks, I. Repins, M.A. Contreras, R. Félix, J. Herrero-Albillos, L. Tati-Bismaths, F. Kronast, R. Noufi, and M. Bär, “Intergrain variations of the chemical and electronic surface structure of polycrystalline Cu(In,Ga)Se$_2$ thin-film solar cell absorbers,” Applied Physics Letters, vol. 101, p. 103908, Sep. 2012.

D. Gerlach, D. Wippler, R.G. Wilks, M. Wimmer, M. Lozac’h, R. Félix, S. Ueda, H. Yoshikawa, K. Lips, B. Rech, M. Sumiya, K. Kobayashi, M. Gorgoi, J. Hüpkes, and M. Bär, “p-type a-Si:H/ZnO:Al and μc-Si:H/ZnO:Al Thin-film Solar Cell Structures – A Comparative Hard X-ray Photoelectron Spectroscopy Study,” IEEE Journal of Photovoltaics, vol. 3, pp. 483-487, Jan. 2013.

M. Bär, J. Klaer, R. Félix, F. Erfurth, R. Félix, N. Barreau, L. Weinhardt, R.G. Wilks, C. Heske, and H.-W. Schock, “Surface Off-Stoichiometry of CuInS$_2$ Thin-Film Solar Cell Absorbers,” IEEE Journal of Photovoltaics, vol. 3, pp. 828-832, Apr. 2013.

M. Bär, J.-P. Theisen, R.G. Wilks, F. Erfurth, R. Félix, D. Gerlach, S. Haas, L. Tati-Bismaths, F. Reinert, F. Kronast, T.P. Niesen, J. Palm, S. Visbeck, and L. Weinhardt, “Lateral inhomogeneity of the Mg/(Zn+Mg) composition at the (Zn,Mg)O/CuIn(S,Se)$_2$

thin-film solar cell interface revealed by photoemission electron microscopy," Journal of Applied Physics, vol. 113, p. 193709, May 2013.

D. Gerlach, R.G. Wilks, D. Wippler, M. Wimmer, M. Lozac'h, R. Félix, A. Mück, M. Meier, S. Ueda, H. Yoshikawa, M. Gorgoi, K. Lips, B. Rech, M. Sumiya, J. Hüpkes, K. Kobayashi, and M. Bär, "The silicon/zinc oxide interface in amorphous silicon-based thin-film solar cells: Understanding an empirically optimized contact," Applied Physics Letters, vol. 103, p. 023903, Jul. 2013.

M. Wimmer, D. Gerlach, R.G. Wilks, S. Scherf, R. Félix, C. Lupulescu, F. Ruske, G. Schondelmaier, K. Lips, J. Hüpkes, M. Gorgoi, W. Eberhardt, B. Rech, and M. Bär, "Chemical interaction at the buried silicon/zinc oxide thin-film solar cell interface as revealed by hard x-ray photoelectron spectroscopy," Journal of Electron Spectroscopy and Related Phenomena, vol. 190, pp. 309-313, Oct. 2013.

Conferences

R. Félix, N. Barreau, F. Couzinié-Devy, F. Erfurth, J.P. Theisen, S. Pookpanratana, Y. Zhang, M. Blum, R. Wilks, W. Yang, J.D. Denlinger, C. Heske, F. Reinert, J. Kessler, and M. Bär, “Chemical and Electronic Structure of the $(In,Al)_2S_3/Cu(In,Ga)Se_2$ Interface,” *European Materials Research Society 2010 Spring Meeting*, Strasbourg, France, Jun. 2010. - Poster presentation

R. Félix, J. Klaer, R.G. Wilks, and M. Bär, “Tuning the electronic structure of the $CdS/CuInS_2$ heterojunction via organic dipole layers,” *European Materials Research Society 2012 Spring Meeting*, Strasbourg, France, May 2012.

- Poster presentation

R. Félix, A. Weber, O. Zander, H. Rodriguez-Alvarez, B.-A. Schubert, J. Klaer, R.G. Wilks, R. Mainz, H.-W. Schock, and M. Bär, “Surface selenization of $CuInS_2$ thin-film solar cell absorbers by rapid thermal processing,” *The Energy & Materials Research Conference*, Torremolinos, Spain, Jun. 2012.

- Oral presentation

Acknowledgements

I would like to acknowledge the support of the many people and institutions that have made this work possible.

I am grateful to the Deutscher Akademischer Austauschdienst (DAAD) for their financial support during my doctoral studies.

To Prof. Dieter Schmeißer I would like to thank for accepting to be my Doktorvater at BTU Cottbus and for his supervision and comments throughout my doctoral work.

To Prof. Marcus Bär, my mentor and supervisor, I will always be indebted for the opportunity of forming part of the Young Investigator Group Interface Design (EN-1) at the HZB, for his continued guidance, support and patience throughout (and even before the start of) this work.

I deeply appreciate Prof. Hans-Werner Schock's kind disposition to read and comment on this dissertation, as well as assessing in multiple occasions the progress of my doctoral work.

I am thankful to Dr. Regan Wilks for his many helpful insights in analyzing and improving the presention of data, and for always being available to provide me feedback during the writing of this work.

Dr. Dominic Gerlach was a great fellow PhD-student, who will always be linked to my memories of this particular period of time. I wish him much success in all his future pursuits, as I do for the present and past members of the E-N1 group. Thank you for the good times!

I am grateful toWolfram Witte from the ZSW and Jo Klaer from the HZB for providing me with samples and for their valuable input. Likewise, I thank Prof. Andreas Klein and Dr. Tobias Adler for their kind willingness to share data for evaluation and discussion purposes.

To the "extended Clemens Heske group" I thank for the spectroscopic "tool chest" collaboration, which allowed for the carrying out of many of the experiments here presented.

I am much obliged to Dr. Roland Mainz and his group, especially Dr. Humberto Rodriguez-Alvarez and Dr. Alfons Weber, for their assistance with RTP experiments and the fruitful discussions stemming from the obtained results. Likewise, I also thank Björn Schubert for performing XRF measurements on RTP-treated samples.

I am appreciative of Dr. Alejandra Ramírez-Caro’s assistance with UV-Vis spectrophotometry measurements, and Carola Kelch and Michael Kirsch’s help with CdS chemical bath deposition treatments and the fabrication of solar cell devices.

Counting with the uplifting support of longtime friends Dr. Timo Hofmann and Dr. Sujitra Pookpanratana was also crucial during the writing of this dissertation.

My special thanks go to the following friends who have made me feel as part of their own families during the time of this work: the Ávila-Mejía Family, Michael Köhler, the Langenbacher Family, the López-Félix Family, the Rojas-Ramírez Family, and the Schöngut-Zambrana Family.

To my parents, Ana and Roberto, and my brothers, Alexander and David, I am bound for the love and support they have constantly shown me throughout my life. Whatever goal I may reach, I will always owe it to them.